How taming "jumping genes" could help treat disease p. 244

Visualizing a protein stalled during mitochondrial import p. 303

Global distribution of toxic metal soil pollution p. 316

Science

$15
18 APRIL 2025
science.org

AAAS

CARBONATES ON MARS

Evidence of an ancient carbon cycle pp. 251 & 292

NOMIS & Science
YOUNG EXPLORER AWARD 2025

Research at the intersection of the social and life sciences

Unconventional. Interdisciplinary. Bold.

The NOMIS & *Science* Young Explorer Award recognizes and rewards early-career M.D., Ph.D., or M.D./Ph.D. scientists who perform research at the intersection of the social and life sciences. Essays written by these bold researchers on their recent work are judged for clarity, scientific quality, creativity, and demonstration of cross-disciplinary approaches to address fundamental questions.

A cash prize of up to USD 15,000 will be awarded to essay winners, and their engaging essays will be published in *Science*. Winners will also be invited to share their work and forward-looking perspective with leading scientists in their respective fields at an award ceremony.

Apply by May 15, 2025
at www.science.org/nomis

NOMIS FOUNDATION
Creating the Spark

Science
AAAS

CONTENTS

18 APRIL 2025
VOLUME 388
ISSUE 6744

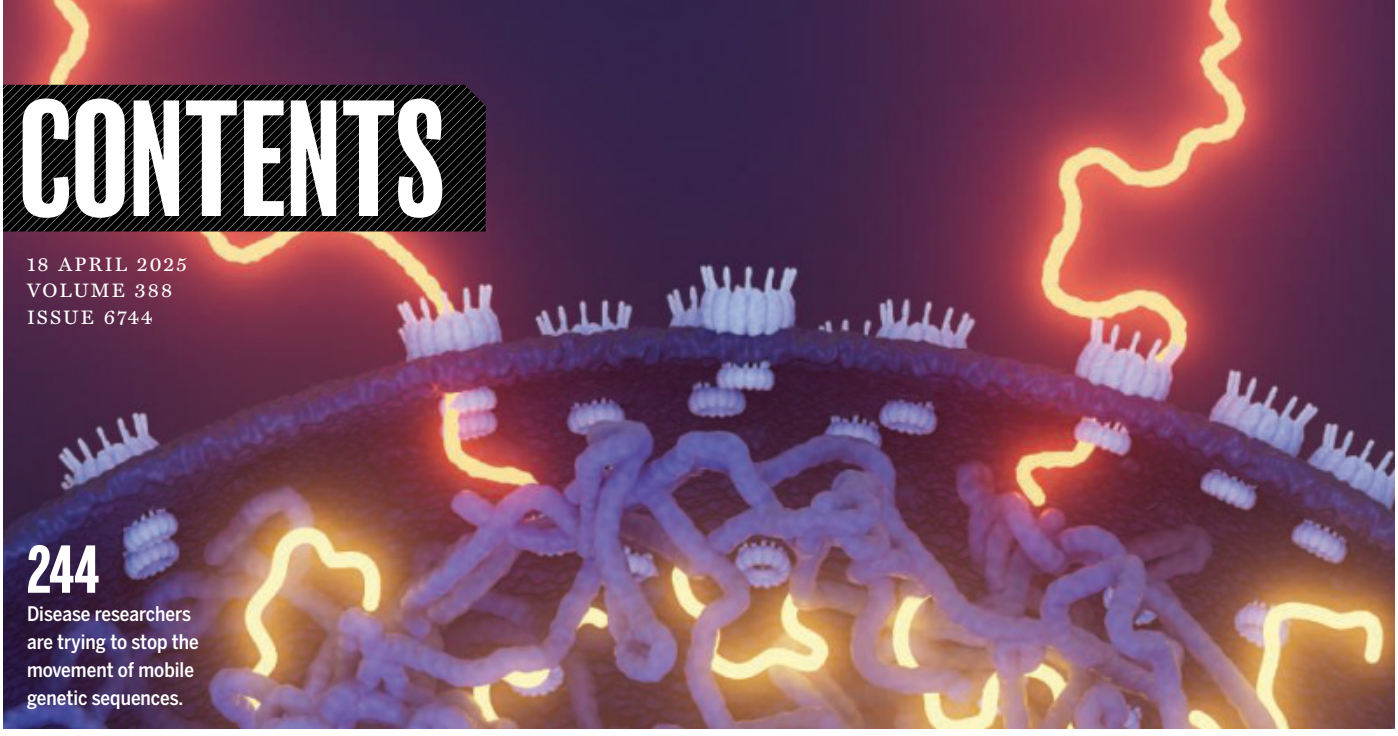

244
Disease researchers are trying to stop the movement of mobile genetic sequences.

NEWS

IN BRIEF

IN DEPTH

FEATURES

INSIGHTS

POLICY FORUM

PERSPECTIVES

BOOKS *ET AL.*

LETTERS

257

RESEARCH

IN BRIEF

RESEARCH ARTICLES

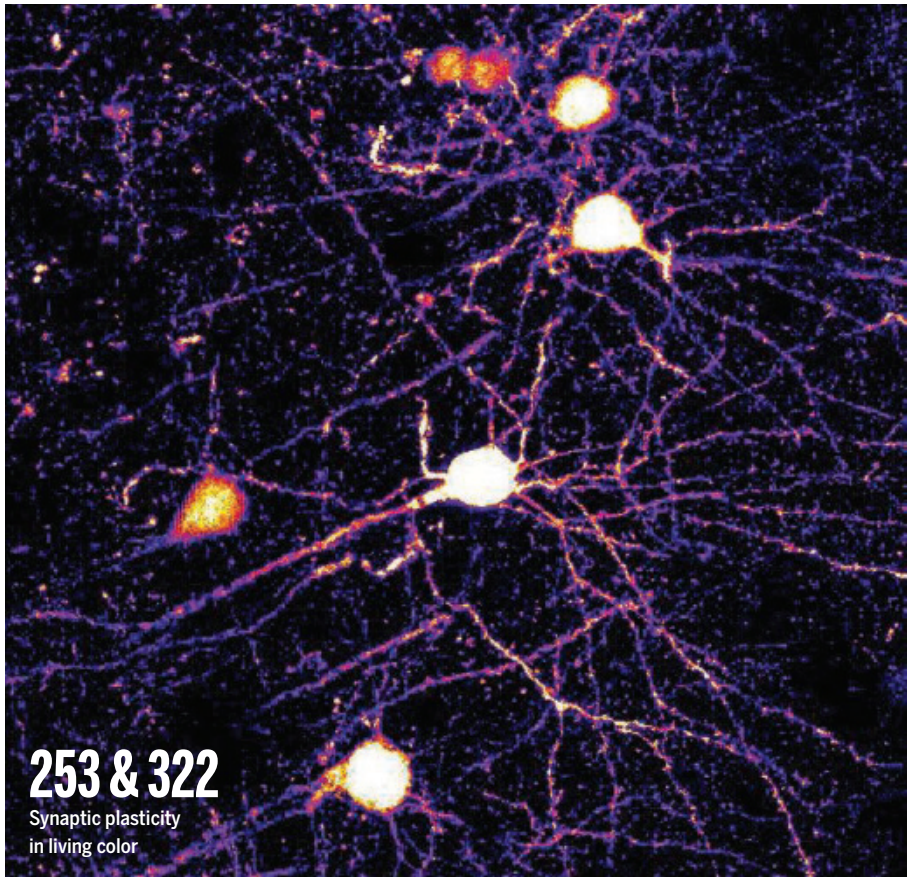

253 & 322
Synaptic plasticity in living color

DEPARTMENTS

ON THE COVER

This photograph of Gale crater, Mars, was taken by the Curiosity rover at the Ubajara drill site. The rover's 40-cm-wide tracks are visible in the foreground. The rover drilled a rock sample at this location, which was found to contain substantial amounts of siderite, an iron carbonate mineral. The siderite likely played a role in an ancient carbon cycle that affected Mars' surface climate. See pages 251 and 292. *Credit: NASA/JPL-Caltech/MSSS*

IMAGE: WILLIAM J. WRIGHT

SCIENCE (ISSN 0036-8075) is published weekly on Friday, except last week in December, by the American Association for the Advancement of Science, 1200 New York Avenue, NW, Washington, DC 20005. Periodicals mail postage (publication No. 484460) paid at Washington, DC, and additional mailing offices. Domestic individual membership, including subscription (12 months): $165 ($74 allocated to subscription). Domestic institutional subscription (51 issues): $2865; Foreign postage extra: Air assist delivery: $135. First class, airmail, student, and emeritus rates on request. Canadian rates with GST available upon request, GST #125488122. Publications Mail Agreement Number 1069624. **Printed in the U.S.A.**
Change of address: Allow 4 weeks, giving old and new addresses and 8-digit account number. **Postmaster:** Send change of address to AAAS, P.O. Box 96178, Washington, DC 20090–6178. **Single-copy sales:** $15 each plus shipping and handling available from backissues.science.org; bulk rate on request. **Authorization to reproduce** material for internal or personal use under circumstances not falling within the fair use provisions of the Copyright Act can be obtained through the Copyright Clearance Center (CCC), www.copyright.com. The identification code for *Science* is 0036-8075. *Science* is indexed in the *Reader's Guide to Periodical Literature* and in several specialized indexes.

EDITORIAL

When state support for science fails

Antonio Lazcano is a professor in the Facultad de Ciencias at the Universidad Nacional Autónoma de México, Mexico City, Mexico, and member of El Colegio Nacional, Mexico City, Mexico. alar@ciencias.unam.mx

The establishment and growth of scientific communities require long-term planning, political backing, and social and economic support. In many Latin American countries, these entities have been repeatedly shaken by monetary catastrophes, political attacks, and the lack of national and regional developmental strategies that include science and technology. Such volatility has taken its toll on the region's scientific enterprise, because science cannot advance under the vagaries of economic uncertainty, political violence, and unpredictable investment.

In the 1970s, the burgeoning scientific communities of several South American countries, such as Chile, Uruguay, Brazil, and Argentina, were severely damaged by coups d'état that closed universities and sent to prison or into exile hundreds of young scientists and top-level researchers. Reconstruction of academic life has been slow and uneven. Further complicating the ascension of Latin American science is the fact that it is a heterogeneous region in which patches of modernity and wealth coexist with conditions of dismal poverty, and organized crime has made field work dangerous in many localities.

> "...science cannot advance under the vagaries of economic uncertainty, political violence, and unpredictable investment."

The scientific landscape of Latin America today is still reeling from multiple setbacks. The list includes Argentinian President Javier Milei's decision to drastically reduce science funding; former Brazilian President Jair Bolsonaro's policies that undermined the autonomy of the country's universities and academic research; Nicaraguan President Daniel Ortega's takeover of universities and of the National Academy of Sciences; and the rapidly declining state of science and higher education in Venezuela and Mexico, where the countries' respective leader and former leader, Nicolas Maduro and Andrés Manuel López Obrador, have accused scientists of constituting a nefarious elite engaged in useless research. Political populism, which underlies many of these actions, is a global threat that will not fade away in the near future, and its expansion and radicalization represent major challenges to the scientific enterprise.

Scientists and students have reacted to these assaults with protests and have received considerable support from the independent media and, in Argentina and Mexico, from the National Scientific and Technical Research Council (CONICET) and the National Autonomous University of Mexico (UNAM), respectively. Many Nicaraguans and Venezuelan researchers have had to go into exile but continue to collaborate from abroad with their colleagues. In countries where governments undermined public health measures intended to control the spread of COVID-19, scientists took matters into their own hands, creating outreach groups that used digital platforms to counter pandemic misinformation. In Brazil, despite Bolsonaro's refusal to acknowledge the damages wrought by deforestation, environmental specialists and citizens alike have continued to speak out in defense of the Amazon rainforest, often at great personal peril.

There is an urgent need to resolve the rift between Latin American governments and scientific communities. In the meantime, there have been some encouraging attempts to forge new collaborations to better support the region's scientific interests. For example, the Mexican National Commission for the Knowledge and use of Biodiversity (CONABIO)—a semi-autonomous research center—was, until recent government encroachment, a vital sustainability platform connecting academia, the government, and civil society. Uruguay's National Research and Innovation Agency (ANII) has similarly worked to ensure stable backing for research through a mix of public and private support. And initiatives such as the Amazon Fund, financed largely by Norway and Germany, help insulate Brazilian scientists from domestic political pressures.

The establishment and reinforcement of semi-autonomous research institutions and multinational research networks in the region are a good start, but without sustained support for scientific research, the region will continue to lose talented scientists to countries where faculty positions and funding are more assured. Reversing this course will require the coordinated effort of research institutions, scientific associations, and networks of higher education across Latin America. To do this, these groups will need to leverage the shared history and common cultural backgrounds of the region to develop regional academic strategies that—with international and private support—can diversify funding sources, facilitate the training of the next generation of scientists, strengthen scientific networks, and guarantee scientific freedom.

–Antonio Lazcano

10.1126/science.adx9924

NEWS

> "I was in paradise. I would very much like to stay in paradise."
>
> **Kseniia Petrova, a Russian scientist detained by U.S. Immigration and Customs Enforcement**, to *The New York Times* on her life doing research at Harvard Medical School.

IN BRIEF

Edited by **Shraddha Chakradhar**

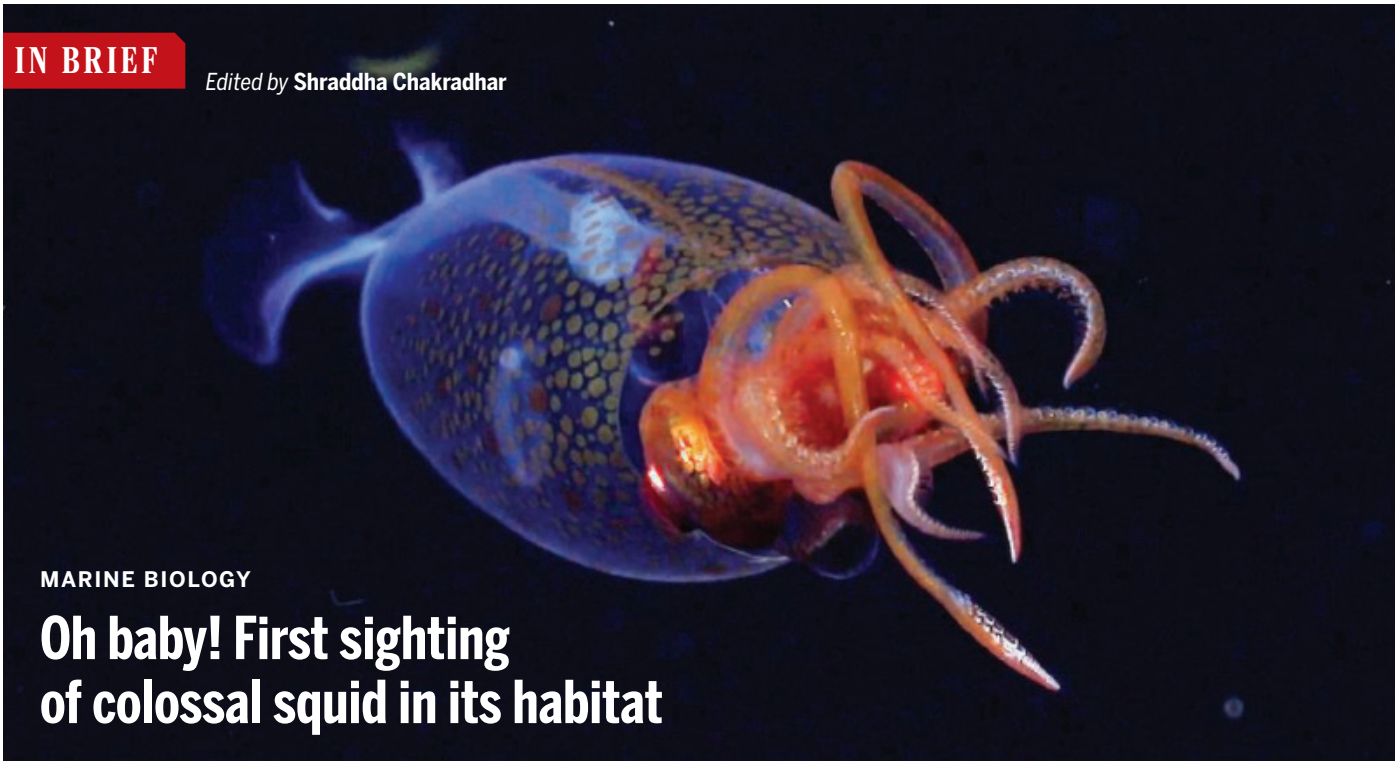

MARINE BIOLOGY

Oh baby! First sighting of colossal squid in its habitat

A team of researchers this week debuted the first video taken of the colossal squid (*Mesonychoteuthis hamiltoni*) in its natural deep-water habitat. This unprecedented sighting of the elusive species, which is the largest known invertebrate, comes from a team of biologists aboard the Schmidt Ocean Institute's *R/V Falkor (too)* in the South Atlantic Ocean as part of an expedition to survey marine life. A remotely operated vehicle 600 meters below sea level captured video of a 30-centimeter-long juvenile squid that was identified later by experts as *M. hamiltoni*. The species was first described 100 years ago by scientists who examined remains found in the stomach of a sperm whale. Since then, a few captures by fishing vessels have revealed more about the squid's size and anatomy, including that it can grow up to 7 meters in length and weigh up to half a ton.

A young colossal squid was filmed for the first time in its natural deep-sea habitat.

PHOTO: ROV SUBASTIAN/SCHMIDT OCEAN INSTITUTE

Pig kidney transplant fails

BIOLOGY | A woman who lived with a gene-edited pig kidney for 130 days—a new record—had the organ removed on 4 April after showing signs of rejection, yet another setback for the long-struggling field of xenotransplantation, which aims to improve the lives of humans with organs from animals. Surgeons at New York University Langone Health had transplanted the kidney to Towana Looney, a 53-year-old Alabama woman, in November 2024, hoping her immune system would not attack the organ thanks to improved immunosuppressive drugs and 10 edits to the donor pig's genome. Revivicor, the company that engineered the pigs, and Looney's doctors say the rejection may have occurred because an unrelated infection led them to reduce her dosage of immunosuppressive drugs shortly before the failure. Looney has since restarted dialysis, her doctors say, and is in good health. Since Looney's transplant last November, two other people have received kidneys from gene-edited pigs made by other companies and are doing well so far.

New German high-tech ministry

SCIENCE POLICY | Germany's incoming government plans a new ministry responsible for research, technology, and aerospace, according to the agreement between a coalition of center-right and center-left parties announced last week. The realignment is one of several nods to science in the 144-page document, unveiled on 9 April, that outlines the coalition's priorities. The plan splits the current Ministry of Research and Education, sending the education portfolio to the ministry for family, seniors, women,

and youth and shifting technology and aerospace from the economics ministry to the new science-focused ministry. The agreement lists as priorities research on artificial intelligence, quantum technologies, biotechnology, security and defense, and fusion energy. It also plans a program called 1000 Minds to attract international talent and "maintain Germany as an attractive destination" for researchers during an era of polarization.

New antibiotic for gonorrhea

INFECTIOUS DISEASE | Gepotidacin, an antibiotic pill that last month received approval from the U.S. Food and Drug Administration (FDA) to treat urinary tract infections, is also effective against gonorrhea, a study published this week in *The Lancet* shows. The current front-line antibiotics for gonorrhea, a combination of injections and pills, don't work against increasingly prevalent drug-resistant strains of the bacterium *Neisseria gonorrhoeae*. If left untreated or treated insufficiently, *N. gonorrhoeae*, which annually infects more than 80 million people worldwide, can lead to chronic pelvic and urinary pain as well as infertility. In the new study, which enrolled 600 people in Europe, the United States, and Mexico, gepotidacin proved just as effective as the front-line drugs and also worked against resistant strains. If gepotidacin wins approval for gonorrhea—its maker, GSK, says it will soon file the paperwork with FDA—it would be the first new drug against the sexually transmitted infection since the 1990s.

Mütter Museum director ousted

SCIENTIFIC COMMUNITY | Kate Quinn, who became the Mütter Museum's executive director in September 2022, is no longer working at the Philadelphia institution famous for medical oddities and unique specimens. The College of Physicians of Philadelphia, the museum's parent organization, confirmed her last day was 7 April. During her controversial tenure, Quinn initiated a review of the museum's policies on handling and displaying human remains. It led to a project that sought out community input on ethical considerations regarding the museum's 6600 human specimens, because many of the human remains housed there were obtained without consent and as a result of medical racism. However, staff and museum fans felt that changes under Quinn's leadership—including the removal of hundreds of online photos and videos deemed possibly disrespectful—risked harming the museum's unique character. The college said two science historians will take over Quinn's duties.

TRUMP TRACKER

NASA BUDGET THREATS The White House is expected to ask Congress to cut NASA's science programs by nearly 50% in its upcoming 2026 budget request, according to documents reported on by *Ars Technica*. President Donald Trump's administration wants to cut nearly $5 billion from NASA's $25 billion budget, $3.6 billion of which would come from the agency's science office, whose budget would be roughly halved to $3.9 billion. Planetary science spending would drop by $800 million, or about 30%, and earth science spending would be cut by $1 billion, or about half. If approved by Congress—which is not certain—such cuts would likely require NASA to close laboratories and shut down some Earth-observing satellites. The agency would also be forced to abandon the almost fully assembled Nancy Grace Roman Space Telescope. Scheduled to launch in 2027, it would explore exoplanets and look for sources of dark energy.

HARVARD FUNDING FROZEN The Trump administration froze $2.2 billion in federal research grants and a $60 million unidentified contract to Harvard University this week, hours after the school announced it would not give in to a list of White House demands. The administration had placed nearly $9 billion in Harvard's federal funding under "review"—a move that is separately being challenged in court by two groups representing Harvard professors—but the school is now the first threatened university to stand up publicly to the president's pressure. In an 11 April letter, government lawyers outlined a series of demands, including that Harvard allow external audits of academic programs; do away with diversity, equity, and inclusion programs; and "reform" fields that "lack viewpoint diversity" among faculty or students. In its response, the university said the demands were illegal and unconstitutional, encroaching on its First Amendment rights. "No government—regardless of which party is in power—should dictate what private universities can teach, whom they can admit and hire, and which areas of study and inquiry they can pursue," Harvard President Alan Garber said in a public letter.

FOGARTY DIRECTOR BOOTED Add Kathleen Neuzil to the growing list of leaders at the National Institutes of Health (NIH) who have been removed and offered an unspecified new job with the Indian Health Service (IHS). Neuzil, an infectious disease and vaccine specialist who headed the Fogarty International Center since May 2024, received an email on 11 April from the Department of Health and Human Services that immediately put her on administrative leave and, at press time, she had yet to decide whether she wanted to accept an IHS posting far away from the center's Maryland home. Fogarty has a $95 million budget and supports global health research and training of scientists around the world. Two-thirds of its grants typically go to U.S. institutions that partner with groups in low- and middle-income countries.

ANIMAL TESTING ROLLBACKS Two federal agencies are moving away from testing drugs and environmental chemicals in animals, opting instead for alternative methods such as computer modeling or devices that mimic human tissues. On 10 April, U.S. Food and Drug Administration (FDA) Director Martin Makary said in a statement that his agency is dropping animal testing requirements for "monoclonal antibody therapies and other drugs," immediately for companies applying to study drug candidates. Makary added that FDA will also evaluate real-world safety data on potential drugs already tested in people in other countries. That same day, *The Washington Times* reported that Environmental Protection Agency (EPA) Director Lee Zeldin said his agency will reinstate a 2019 policy phasing out animal testing. Former President Joe Biden's administration rescinded the EPA policy in 2024, saying its deadlines of reducing testing on mammals by 30% by this year and phasing it out entirely by 2035 were not based in science.

LGBTQ QUESTIONS CUT U.S. researchers responding to a flagship census of Ph.D. recipients will no longer be invited to share information about their sexual orientation, and their options for gender will be binary: male or female. Prompted by recent executive orders from Trump, the move by the National Science Foundation—approved last week—reverses changes made last year to its annual Survey of Earned Doctorates to enable researchers and policymakers to examine how many sexual and gender minorities are in STEM. The current iteration of the survey, which is completed by roughly 55,000 respondents annually, began in July 2024 and will wrap up in June. The agency declined to comment when asked what will happen to data collected before the change took effect.

IN DEPTH

TRUMP ADMINISTRATION

NIH bars Chinese scientists, others from databases

Trump administration escalates efforts to keep sensitive data from foreign adversaries

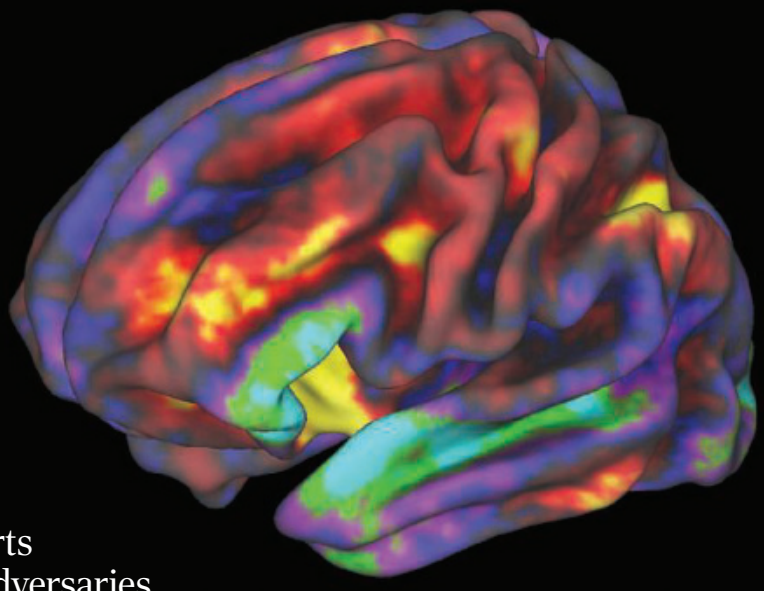

Imaging data from the Adolescent Brain Cognitive Development Study are now off-limits to researchers in six countries.

By **Richard Stone**

The U.S. National Institutes of Health (NIH) has barred scientists in China and five other "countries of concern" from accessing 21 biomedical databases, which hold information on cancer cases, brain diseases, and more. The 2 April move by President Donald Trump's administration, which ramps up a longer running effort to prevent foreign access to data deemed sensitive, also halts projects involving the databases that include collaborators in the named countries.

"At a time when the study of genetic variation is fundamental to pinpointing the causes and cures of diseases, this seems like a pointless expression of spite," says Pedro Antonio Valdés Sosa, a neuroinformaticist at the University of Electronic Science and Technology of China who has used an affected database on child brain development for his research. Targeted databases include ones that are "crucial to understand brain disorders," he says.

The other countries shut out of the databases are Cuba, Iran, North Korea, Russia, and Venezuela. "This could be really devastating to the few remaining good scientists in Venezuela," says Gladys Maestre, a Venezuelan-born neuroscientist at the University of Texas Rio Grande Valley who collaborates on Alzheimer's disease research with scientists in her home country. "You need real data from real people to test your hypotheses."

Former President Joe Biden had imposed some restrictions on foreign access to the databases, but the new regulation posted this month tightens them significantly. It is a "technical update" to a rule issued by the U.S. Department of Justice (DOJ) on 8 January seeking to better secure all kinds of sensitive information—including biometric and genomic data, health care records, and geolocation data—from foreign adversaries. DOJ warned that hostile intelligence services could use such data for blackmail and coercion, identifying high-risk government personnel and sensitive locations, and offensive cyber operations. And access to "bulk human genomic data" might help adversaries develop new bioweapons, the agency said.

Chinese researchers told *Science* in October 2024, during the Biden administration, that they were already being intermittently denied access to the Adolescent Brain Cognitive Development (ABCD) Study database. Launched in 2018, the study follows some 11,880 children, enrolled at age 9 or 10, into adulthood, tracking how sleep patterns, smoking, and experiences such as using social media and playing sports and video games affect brain development. China embarked on a similar longitudinal study in 2023 that aims to enroll 26,624 children.

Now, Chinese scientists are entirely shut out of the ABCD database, says a brain researcher from China who requested anonymity because he hopes there will eventually be exceptions to the policy. "The high quality of ABCD data is a yardstick for scientists around the world," he says. "Now we are deprived of an important comparison for our own work."

Since 4 April, thousands of Chinese scientists have also been locked out of the Surveillance, Epidemiology and End Results Program, a database of U.S. cancer cases and the largest such repository in the world, according to the *South China Morning Post*.

Cuban biomedical scientists, who had been tapping the now-restricted databases, are also lamenting the move. "This new blockade will definitely set back our understanding of many diseases and potentially affect patients," says Tania Crombet Ramos, medical director of the Center of Molecular Immunology in Havana.

Beyond blocking database access, NIH is "ending any remaining ongoing projects" involving the repositories if they include researchers or institutions in the countries of concern, Andrew Nixon, communications director for the U.S. Department of Health and Human Services, NIH's parent agency, said in a statement. "NIH takes oversight of security including confidentiality, integrity, and availability of participant data very seriously," he said. Nixon did not respond to a query from *Science* about how many projects are being shuttered or whether NIH has a mechanism for issuing waivers.

In a statement, BGI Group, a genomics powerhouse in Shenzhen, China, noted that Chinese scientists contributed data to some of the databases that are now off-limits, such as the National Center for Biotechnology Information's database of Genotypes and Phenotypes. That repository, which includes genomewide association studies and medical sequencing data, "represents a shared human legacy that … benefits all of humanity," the company said. (The U.S. Department of Commerce in 2023 added three BGI Group firms to a trade blacklist out of concern their technologies might be used for surveillance of minority groups in China—an assertion BGI Group dismissed as misinformation.)

"I want to think NIH's action is a circumstance of the geopolitical moment," Maestre says. She says she understands the need to secure data—but worries blanket restrictions could lead other countries to retaliate and shut U.S. scientists out of overseas databases. ■

IMAGE: RICHARD WATTS

TRUMP ADMINISTRATION

NASA, NOAA face major climate science cuts

National Climate Assessment is at risk, as are scores of other research programs

By **Paul Voosen**

The assault on climate science by President Donald Trump's administration has been taken to a new level, as two federal agencies appear ready to eliminate long-standing, major climate research and policy efforts.

NASA last week terminated the contract that supports two dozen technical staff at the U.S. Global Change Research Program (USGCRP), the White House office that coordinates research among the federal agencies. The move will hollow out the staff relied on to assist volunteer scientists in the production of the quadrennial U.S. National Climate Assessment (NCA), potentially leaving that report delayed, diminished, or as a venue for climate misinformation.

Moreover, the Trump administration is seeking to end nearly all of the climate research conducted by the U.S. National Oceanic and Atmospheric Administration (NOAA), one of the country's premier climate science agencies, according to an internal budget document seen by *Science*. The document indicates the White House is ready to ask Congress to eliminate NOAA's climate research centers and cut hundreds of federal and academic climate scientists who track and study human-driven global warming.

Congress could still override Trump's desires on the NOAA cuts, but it's harder to see how the impact on the NCA will be averted. Work on the sixth version of the climate assessment, which is due by 2027 or 2028, began during the end of former President Joe Biden's administration, which had already selected many of its authors, who are drawn from U.S. science agencies and academia. The report, which is congressionally mandated, is the government's premier guide on climate change impacts, providing actionable guidance to U.S. citizens and companies planning for global warming.

On 8 April, word came that NASA, on direction from someone unidentified in the administration, had terminated the contract for ICF International, a consulting firm. ICF supported the production of the past two climate assessments. In 2021, NASA signed it to a 5-year contract, worth up to $34 million, to continue work on the NCA with USGCRP. A NASA spokesperson confirmed the agency was terminating the ICF contract, saying, "NASA is streamlining its support" for the program.

Prior to Trump's inauguration, most of the federal USGCRP staff had been sent back to their home agencies, leaving Heidi Roop, a climate scientist from the University of Minnesota Twin Cities, as USGCRP's acting director. Once Roop, who is on a term-limited contract, returns to her university in the next few months, USGCRP will effectively have no staff.

The White House is taking aim at efforts to understand the impacts of climate change.

PHOTO: KEVIN CARTER/GETTY IMAGES

That could basically end the NCA process, says Donald Wuebbles, a climate scientist at the University of Illinois Urbana-Champaign who led the assessment's fourth version, published in 2017. It's a big loss to the nation, including the many companies that rely on these data, he adds. "The NCA has real value to companies and organizations for figuring out how to adapt."

USGCRP and the NCA have long been targeted by Trump political appointee Russell Vought, who leads the White House's Office of Management and Budget. In the pre-election Project 2025 report produced by the Heritage Foundation that has provided a blueprint for many Trump administration actions, Vought included thoughts on how to remake USGCRP, suggesting it should include more "diverse viewpoints." He also suggested that any USGCRP prepared under the Biden administration should be "critically analyzed" and potentially refused.

Running the NCA is not the only role of USGCRP. Just as important are the monthly meetings the office coordinates between its member agencies, which seek to prevent duplication of effort and flesh out blind spots in studying to the global effects of human-driven climate change, including how deforestation, pollution, and other human influences are changing the world, Wuebbles says. "Losing all that connection is bad for the country."

Preparing the NCA without support staff would make it difficult to produce a document that, while fulfilling the statutory requirement, actually provides useful information to the public. And there is always a risk that such a report could, instead, become a vector for misinformation.

There is concern the White House will publish climate skeptic documents under the imprint of the NCA, allowing them to be used in court challenges of climate-based regulations. "Watch for a rogue's gallery of climate deniers to be put in as agency reps," Andy Miller, a longtime climate scientist at the U.S. Environmental Protection Agency who worked for a decade with USGCRP, wrote in a post on Bluesky.

The future of USGCRP and the NCA will likely reside with congressional responses and any legal action taken to block the contract cancellation, Wuebbles says. "Let the lawsuits begin."

Congress, rather the courts, will have the final say on the proposed NOAA cuts, which would overall eliminate $1.7 billion from the $6.3 billion agency but could still be altered before the administration sends its 2026 budget request to Congress in the coming weeks. The draft budget document seen by *Science* shows a massive funding cut for the agency's research arm, the Of-

fice of Oceanic and Atmospheric Research (OAR), to just over $171 million, a drop of $485 million. Any remaining research funding from previously authorized budgets would be moved to other programs. "At this funding level, OAR is eliminated as a line office," the document states.

The plan would represent a huge blow to efforts to understand climate change, says Craig McLean, OAR's longtime director who retired in 2022. "It wouldn't just gut it. It would shut it down." Scientifically, he adds, obliterating OAR would send the United States back to the 1950s—all because the Trump administration doesn't like the answers to scientific questions NOAA has been studying for a half-century.

The administration's plan would "eliminate all funding for climate, weather, and ocean laboratories and cooperative institutes," the document says. Currently, NOAA operates 10 research labs around the country, including influential ocean research centers on both coasts; five atmospheric science labs; a severe storm lab; and the Geophysical Fluid Dynamics Laboratory, the birthplace of weather and climate modeling.

The proposal would cut NOAA's climate research grants program, which awards roughly $70 million a year to academic scientists. It would end support for collecting regional climate data and information, often used by farmers and other industries. Trump is also seeking to radically rework the next-generation geostationary weather satellites planned by the agency. That includes cutting its planned atmospheric pollution and ocean color instruments because, as the document puts it, the satellites will deliver exclusively "weather" data. The request would also cut funding for the National Center for Environmental Information—the nation's primary archive of climate data—by $18 million.

The White House proposal is only the first stage of the budget process and will face strong opposition from Democrats. "Trump's budget plan for NOAA is both outrageous and dangerous," said Representative Zoe Lofgren (D–CA), the ranking member of the U.S. House of Representatives's science committee, in a statement to *Science*. "This administration's hostility towards research and rejection of climate science will have the consequence of eviscerating the weather forecasting capabilities that this plan claims to preserve."

McLean expressed some hope that the Republican lawmakers running Congress will not approve these cuts, citing how much of NOAA spending is spread throughout their districts. But that's not a sure thing, he says. "It's a very different Congress today." ■

PLANT BIOLOGY

Scientists identify structure that controls seed size

An overlooked "gate" governs nutrient transport to seeds and might one day boost agricultural harvests

By **Erik Stokstad**

Decades of studies have scrutinized a scrawny mustard relative named *Arabidopsis thaliana*, but plant biology's version of the lab rat still retains secrets—including one with potentially major agricultural payoffs. In *Current Biology* last week, a research team describes a never-before-seen mechanism by which the plant's flowers nourish fertilized eggs and help them develop into seeds.

"This discovery lays the foundation for a new approach to controlling seed size," says Tomokazu Kawashima, a developmental biologist at the University of Kentucky who wasn't involved with the study.

Indeed, the team exploited a gene involved in the mechanism to increase the size of mustard seeds by 17% and of rice grains by 9%. It's not necessarily desirable to have larger rice—it can mess with the texture and taste—but many related cereal crops, such as corn and wheat, might benefit from the same gene manipulation.

With only a few exceptions, plant biologists don't understand the physiological mechanisms of genes known to influence seed size. Many interested in how plants make seeds study the part of the flower where the pollen descends down a tiny tube and meets an ovule containing an egg cell. But Nagoya University plant biologist Ryushiro Kasahara, the new study's senior author, focuses instead on where nutrients arrive via a network of tubes called phloem to feed the developing embryo. Adding a blue dye to phloem, his team found callose, a structural molecule that plants use to erect temporary cell walls, forming in cells near where the tubes reach the ovules. The callose created a barrier, shaped like a dinner plate.

The team confirmed that the callose-filled cells serve as a gate to prevent the phloem's nutrients from reaching unfertilized ovules, and that the barrier later disappeared from ovules that had been fertilized. The discovery of this previously unknown structure thrilled Kasahara. "I was so happy and danced around." Kawashima notes that in hindsight, it makes sense that such a structure exists to help plants avoid investing too much into unfertilized ovules.

The team also identified dozens of genes for enzymes that can degrade callose. When the researchers created a version of *Arabidopsis* with a nonfunctional gene for an enzyme called AtBG_ppap, the plant's callose gates remained largely intact even when its ovules were fertilized, leading to seeds that were 8% smaller than normal.

But when the team created another mutant in which the gene is overexpressed, the plant's seeds became larger than normal—presumably because the gates were so readily broken down that a surfeit of nutrients flowed to the fertilized ovules. According to Kasahara, the team has not seen any side effects in the *Arabidopsis* plants modified to have larger seeds. To get a sense of the agricultural potential, the team then similarly tweaked the enzyme's counterpart gene in rice and got larger grains.

Miguel Perez-Amador, a plant biologist at the Polytechnic University of Valencia who wasn't involved with the study, says the findings emphasize how much there is still to learn about even closely studied structures such as the ovule. "There's always room for new discoveries," he says, "no matter how much we think we know!" ■

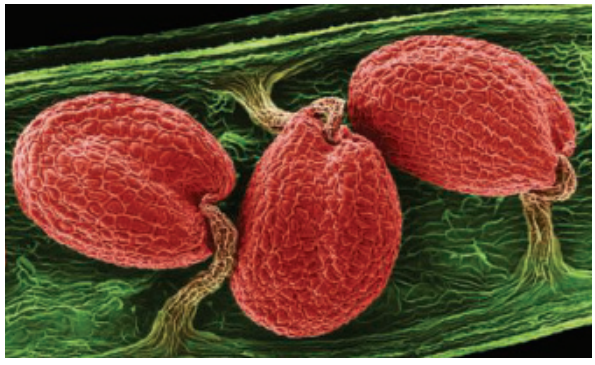

The seeds of *Arabidopsis*, enhanced here with false color, are less than 1 millimeter wide, but they hide a potentially big secret.

IMAGE: DENNIS KUNKEL MICROSCOPY/SCIENCE SOURCE

A cat mummy from ancient Egypt.

EVOLUTION

Cat domestication tied to ancient Egyptian cult

Mass sacrifice of wildcats may have given rise to pet felines

By **David Grimm**

In 2001, archaeologists made a discovery that promised to rewrite the history of cat domestication. Scientists had long believed cats became our friends in ancient Egypt, where they've been immortalized in mummies and art. But when researchers dug beneath a 9500-year-old home in a farming village on the Mediterranean island of Cyprus, they discovered what appeared to be a pet cat buried with a human—more than 4000 years before ancient Egypt even existed.

And so a new story began to take shape. The Cyprus find—along with the discovery of other ancient cat bones across Europe—persuaded many scientists that domestication began when wildcats slunk into the rat-plagued villages of early Mediterranean farmers and eventually evolved into the housecats we know today. As these farmers migrated to new parts of Europe, they brought their cats with them.

Now, two studies—both posted late last month on the preprint server bioRxiv—restore the focus on Egypt. Ancient bones and DNA from cats across Europe and the Mediterranean suggest they may have been domesticated in Egypt after all, possibly as recently as 3000 years ago. The process, one of the new papers theorizes, was a gruesome one: Mass sacrifices of cats tied to a religious cult instilled tameness over many generations. "It's the murder pathway of domestication," says Greger Larson, an evolutionary biologist at the University of Oxford and author on both studies.

That's "a reasonable hypothesis," says Natalie Munro, an archaeozoologist at the University of Connecticut. Still, she and others say, the evidence isn't as clear-cut as it seems.

One of the new studies, led by Sean Doherty, an archaeological scientist at the University of Exeter, took a new look at the Cyprus bones, as well as other remains of supposed domestic cats scattered throughout Europe, comparing their size and shape with skeletal measurements from 2400 wild and domestic felines across Europe and the Mediterranean. All shook out as European wildcats (*Felis silvestris*)—a larger, more robust species not closely related to either domestic cats (*F. catus*) or their direct ancestor, the African wildcat (*F. lybica*).

Nuclear DNA from these specimens (save from the Cyprus animal, whose genetic material is too poorly preserved) confirmed they were European wildcats, according to the second team, overseen by Claudio Ottoni, a paleogeneticist at the University of Rome Tor Vergata.

The analyses make the hypothesis that early farmers domesticated and transported cats "much less compelling," Munro says. "And that means," Doherty says, "we have to start looking elsewhere for epicenters of domestication."

That "elsewhere" brings the story back to ancient Egypt. When Ottoni's team compared the genomes of domestic cats with those of African wildcats from multiple locations, North African wildcats were the closest match. "I would definitely bet on Africa" as the origin of cats, Ottoni says. What's more, without the ancient European "cats" in the equation, the oldest genetically confirmed domestic cats are now mummified Egyptian kitties dated to between 500 and 0 B.C.E.

That timing jibes with a resurgence of a cult worshipping Bastet, an Egyptian goddess of fertility and health. Devotion to her took a bloody form in the first millennium B.C.E.: Pilgrims paid for "votive mummies" of cats as part of their temple visits. As demand for these cat sacrifices soared, the Egyptians established catteries to raise millions of the animals. Herding, as it were, so many cats in one place would have selected for those best suited to live around people and other felines, Larson says. "There was a heavy selection pressure for tameness."

It's a nice story, says Julia Troche, an Egyptologist at Missouri State University, but the timing doesn't quite check out. She notes that the bones of what may be tame cats in predynastic Egypt date back to the early fourth millennium B.C.E., and that art depicting cats in Egyptian homes—such as an image of a feline eating fish under a dining room table—date back to at least 1500 B.C.E. Although it's impossible to say whether these were truly domestic cats, she says, "they were very much a part of the human world" long before the rise of sacrificial cults.

Troche suspects the forces driving cats and humans together in ancient Egypt were the same ones scholars once suspected operated in the fields of early Mediterranean farmers. The ancient Egyptians kept grain in their homes, she notes, which probably attracted rodents, which in turn attracted cats. The tamest cats were the ones most likely to come in, to be protected, and to breed, she says. "There's your domestication pathway."

Today, there are approximately 1 billion cats on Earth and they live on every continent except Antarctica. Credit ritual murder? Rat-plagued farmers? One thing's for sure, Troche says. "There must have been something very special about cats—and not just that they're so freaking cute and adorable." ■

PHOTO: NATURAL HISTORY MUSEUM, LONDON/BRIDGEMAN IMAGES

Yale School of Medicine is backing faculty who propose "a bridge to somewhere."

PHOTO: SPENCER JONES/GHI/UCG/UNIVERSAL IMAGES GROUP VIA GETTY IMAGES

HIGHER EDUCATION

After grant cuts, universities offer faculty a lifeline

"Bridge" programs are seen as temporary help but no substitute for sustained federal funding

By **Jeffrey Mervis**

Last fall, Keith Maggert's grant proposal to the National Institutes of Health (NIH) to extend his work in chromosome biology and gene regulation received a score from reviewers that put it over the threshold for funding. Final approval was due in February, but turmoil at NIH delayed it until late May, leaving him with a gap in supporting his fly genetics lab at the University of Arizona (UA).

On 7 April, however, he received $37,619 in short-term support from another source: his own university. The money will allow him to continue to pay two graduate students and buy needed supplies. Maggert is one of seven UA faculty members to date who have benefited from the university's new "bridge" program, designed for those whose research has been disrupted by the wave of spending cuts and freezes in grantmaking by President Donald Trump and his administration.

Several U.S. universities are taking similar steps to assist their researchers in dire straits. They're experimenting with different flavors of assistance—for example, some are helping faculty reimagine their research programs while others try to ensure their doctoral students are able to complete their degrees. Most schools aren't sharing how much money they are committing to these efforts, though wealthier institutions probably can do more to keep labs afloat. And all bridge programs are likely to be oversubscribed.

Still, the current moment calls for action, administrators say. "This is unprecedented and uncharted waters," says Wendy Hensel, president of the University of Hawaii (UH) System, which has launched a bridge program focused on students in labs whose grants have been cut. "During the COVID pandemic, we received significant support from the federal and state government. The difference here is there will be no one riding to the rescue."

Bridge programs aren't new. Research universities historically have used them when faculty members hit a bump in the road in winning federal grants. But the series of land mines the Trump administration has detonated since 20 January, including the dismantling of several agencies, decrees banning certain types of research, and the threats to some universities' entire research portfolios, raise a new set of challenges.

As universities seek ways to sustain their researchers, Yale School of Medicine is among the most generous. It is making an unspecified amount of money available, on a competitive basis, to faculty members whose existing NIH grant has been "precipitously" terminated or whose pending proposal has been frozen. "The idea is to preserve our investment in individual faculty as well as in their research, and frankly, to preserve the investment of taxpayers as well," says the medical school's dean, Nancy Brown. Faculty can request up to 90% of the amount being blocked, according to a notice posted when the program was announced on 18 February.

Before submitting a proposal, the notice says, applicants must consult with colleagues on how best to "reimagine" their research. The idea is to help faculty "pivot," Brown says, either to a topic the government is more likely to support or to a more receptive federal agency. "It has to be a bridge to somewhere," she explains.

Other institutions are more constrained. As Vassilis Syrmos, vice president for research and innovation at UH, puts it, "We don't have the financial capacity to be a sponsor of the type of research in which we excel."

Instead, UH is focusing on the graduate students of faculty members who have lost grants. It's aided by the UH Foundation, which raises money from private donors. "Of course we care about our faculty and staff, but our primary obligation is to our students," Hensel says. "So priority number one is to find an alternative source of funding that allows them to continue to progress in their research and their degree program."

Syrmos is hoping the foundation will raise $500,000 over the next 6 to 12 months to rescue as many as one-quarter of the 750 UH graduate students in science and engineering who he estimates will be affected by the cutbacks. The university has already received termination and stop-work orders for 32 projects, a number he expects to grow.

At the University of Massachusetts (UMass), students are also likely to be key beneficiaries. Michael Malone, UMass's vice president for research, says he expects requests to pay graduate student stipends will soak up most of the money set aside for its bridge program. He says UMass is also prepared to support requests for additional equipment and supplies if needed for a student to complete their doctoral work.

Most universities with bridge programs have set limits on how much they will contribute. UMass and the University of Michigan both require the faculty member's department to match the university's contribution. At UA, Tomás Díaz de la Rubia, senior vice president for research and innovation,

says the university won't support researchers proposing to move into a new area. And if the federal government reopens the spigot, most institutions will require faculty to return any bridge funding they receive.

Columbia University, where the Trump administration has put hundreds of millions of dollars in federal research grants in jeopardy, declined to say whether it plans any type of competitive bridge program. But in a 4 April letter to the community, acting President Claire Shipman said the university "has made a near-term commitment to pay the salaries and stipends of those affected, as we work to restore funding and consider alternative funding mechanisms."

An institution's endowment may seem like an obvious source of alternative funding; Columbia's amounted to $14.8 billion last year. But college presidents are loath to tap the principal. And university administrators insist that most of the earnings from that pot of money are already earmarked for other purposes, notably student financial aid and construction of new research facilities.

Instead, most universities are turning to the federal funds they receive for providing the facilities and administrative support needed to do research. But those funds, known as indirect costs, are also under attack from the Trump administration and congressional Republicans, who have accused universities of accumulating a "slush fund" by overcharging in negotiating individual payment rates. In February, NIH proposed slashing those rates, potentially depriving grantee institutions of billions of dollars annually. Last week, after a federal judge permanently blocked the move, the government appealed her ruling to a higher court.

The dispute may be one reason most institutions have declined to announce how much they intend to spend on bridge programs. If universities with uncapped bridge programs like Yale's are to fully meet the demand from faculty in the months to come, that could come to millions of dollars. "Nobody wants to look like they have extra money lying around," says one university administrator who requested anonymity to speak freely about the sensitive issue.

Syrmos says UH may increase the share of its indirect cost payments that go into a central pot, now 25%, to boost the potential budget of its bridge program. But he says UH will never be able to make up for the missing federal support. A 2-week cruise for the university's research vessel could eat up the entire sum being raised by the foundation, he notes. "Our bridge program is just a way to provide them with a soft landing while we try to figure out how to solve the problem in the long run," Syrmos says. "And that could require a new business model." ■

BIOMEDICINE

Companies seek second GLP-1 revolution—in pill form

Smaller, easier to make drug compounds could treat obesity and diabetes with fewer side effects

By **Rachel Brazil**

Drugs that mimic glucagonlike peptide-1 (GLP-1), such as semaglutide—marketed as Ozempic or Wegovy—have revolutionized the treatment of obesity and type 2 diabetes, but they have major drawbacks. "[They] are expensive to manufacture, they have to be refrigerated, and they often have to be injected because they cannot go through the gastrointestinal tract without being degraded," explains Alejandra Tomas, a cell biologist at Imperial College London who studies the cellular receptor GLP-1 drugs target. That's all because they consist of peptides, or long chains of amino acids.

A small-molecule version of the therapy, on the other hand, could be given as a daily pill and would be much cheaper to produce. Companies including Eli Lilly, Pfizer, and Roche have launched clinical trials of such compounds. Results from Lilly's first phase 3 trial of its oral drug are expected later this year. But Pfizer announced this week it was halting development of its candidate after signs of liver injury in a trial participant.

The candidates furthest along in development activate the same receptors as peptide drugs do, in much the same way. But several firms are exploring more innovative small molecules that target different sites on those receptors—and could lead to even more effective treatments with fewer side effects.

"In the next 4 or 5 years, this field will mature and more patients ultimately should be able to get these medicines," says Kyle Sloop, a molecular biologist at Lilly Research Laboratories.

By mimicking a natural hormone, semaglutide and other drugs in its class help regulate blood sugar by increasing insulin secretion from the pancreas in response to glucose, and suppress appetite by slowing down digestion. The first generation of peptide drugs were essentially copies of GLP-1, with modifications to prevent the peptide from quickly degrading once in the body. Novo Nordisk first won U.S. approval for semaglutide to treat type 2 diabetes in 2017. It needed to be injected, but in 2019 the company added a pill form, which includes an absorption-enhancing ingredient that allows the peptide to penetrate the stomach wall. However, it requires a high dose and has to be taken while fasting, with minimal liquid.

A small molecule, besides being cheaper, is more easily absorbed. But unlike with hormone-mimicking peptides, "you're essentially starting from scratch" to find an effective compound, says Nick Traggis, founder and CEO of Ambrosia Biosciences.

Typically, companies seeking leads for a small-molecule drug test thousands of compounds in an automated process to find ones that bind to a target receptor in the lab. But because the GLP-1 receptor has a large area of interface with the natural hormone, it's

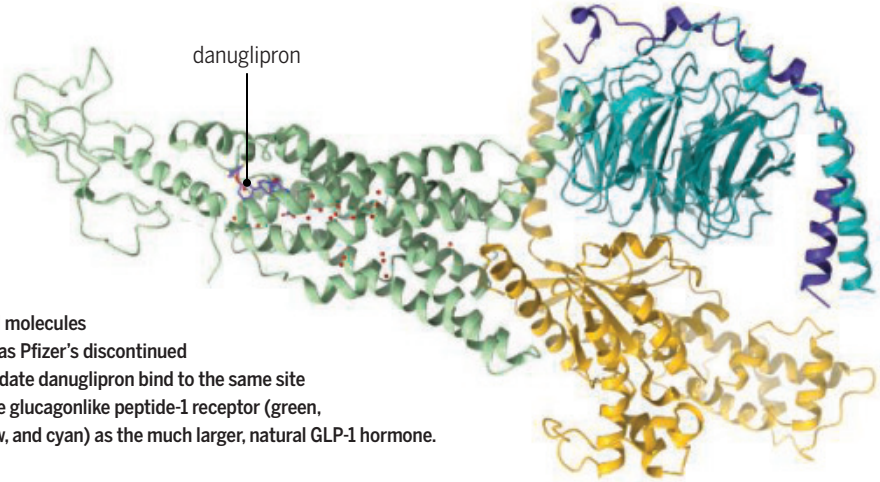

Small molecules such as Pfizer's discontinued candidate danuglipron bind to the same site on the glucagonlike peptide-1 receptor (green, yellow, and cyan) as the much larger, natural GLP-1 hormone.

ILLUSTRATION: ZHANG *ET AL*., *MOLECULAR CELL*, 80:3 (2020)

hard to know which part of this real estate a much smaller compound needs to hit to be effective.

A breakthrough came in 2017, when researchers used cryogenic electron microscopy to work out the 3D molecular structure of the GLP-1 receptor. Researchers can now use computational modeling to simulate how molecules interact with the receptor, Sloop says. That lets them predict the structures most likely to be a fit. "We don't have to make every single molecule" to test its promise.

Lilly's leading oral drug candidate, orforglipron, binds to the same area or "pocket" within the GLP-1 receptor as the natural hormone, Sloop and colleagues reported in December 2024. But this smaller compound attaches via different amino acids within the pocket. "Those interactions are very efficient," and are enough to activate the receptor, Sloop says.

In 2023, the company published results from a phase 2 trial, in which people taking orforglipron once a day showed average body weight reductions of up to 14.7%, roughly comparable to results from semaglutide.

Pfizer's candidate, danuglipron, emerged after screening 2.8 million compounds against a GLP-1 receptor to which another compound was already bound outside the target site, changing its shape and rendering it more sensitive. This so-called positive allosteric modulator allowed the company to identify some weakly binding molecules it could then modify and improve. It's an unusual "but smart" approach, says David Gloriam, an expert in computational drug design from the University of Copenhagen.

But in a 14 April announcement, Pfizer revealed it was dropping danuglipron after one person in a dose-optimization study "experienced potential drug-induced liver injury which resolved after discontinuation of danuglipron." The company said it would continue to pursue a small-molecule treatment for obesity.

A handful of case studies from patients on injectable treatments suggest liver damage could be a very rare side effect of GLP-1 drugs, though they are also under study for potential benefits in certain types of fatty liver disease. "The issue Pfizer saw … seems to be specific" to danuglipron, Traggis says. Ambrosia, which is also developing a small-molecule drug, "remain[s] incredibly bullish on the long-term benefits and safety" of oral GLP-1 therapies, he adds.

Ambrosia and other companies are looking outside the receptor site targeted by the GLP-1 hormone, seeking allosteric sites where a molecule could bind to trigger the receptor's signaling. Ideally, a drug would preferentially activate a cell's insulin-regulating pathway but avoid a second type of signaling that has been linked to side effects seen with the current peptide drugs, such as nausea, vomiting, and diarrhea. "Small molecules targeting novel binding sites might potentially offer improved tolerability," suggests Jeff Finer, CEO of Septerna Therapeutics, "although this remains to be determined."

Septerna has developed a technique that places the GLP-1 receptor in an artificial, membranelike structure, allowing researchers to see its binding and signaling behavior in action. The technique has enabled them to identify a new binding site—and find promising small molecules that can bind to it.

Like peptide drugmakers, teams pursuing small molecules hope to supercharge the treatments' effectiveness by targeting not only GLP-1 receptors, but also others involved in glucose metabolism, such as glucagon receptors and the glucose-dependent insulinotropic polypeptide (GIP) receptor. Lilly's peptide drug, tirzepatide (marketed as Zepbound or Mounjaro), which targets both GLP-1 and GIP receptors, reduced weight more than semaglutide in a head-to-head trial; it won U.S. approval in 2022 for diabetes and in 2023 for weight loss. Other multireceptor-targeting drugs are in clinical trials.

Developing a small molecule that hits multiple receptors is "technically challenging," Sloop says, "but there is evidence that it can happen." Septerna's novel binding pocket may help identify such molecules, Finer says, because 80% to 90% of the pocket's genetic sequence is shared among GLP-1, GIP, and the glucagon receptor. But there remains uncertainty about how these additional receptors work and how they should be drugged—for example, there's a debate about whether it's more beneficial to activate GIP receptors or block them. "As good as we all are at chemistry, we're all still learning the biology," Traggis says.

At Ambrosia, Traggis and his colleagues are developing separate small molecule drugs for each receptor. They plan to develop these into multiple pills, "where you can then tailor the dosing to each person," a strategy that may help minimize side effects, Traggis says.

In the next 5 years, some researchers predict small-molecule drugs that are cheaper and easier to administer than their peptide cousins will have a shot at similar blockbuster status. But Finer suspects these options will coexist with the injectables, not supplant them. "The enormity of the patient population affected by obesity and diabetes—estimated to be more than 800 million people worldwide—suggests there's room for multiple therapeutic approaches." ■

Rachel Brazil is a science journalist based in London.

ENERGY RESEARCH

Lawsuit challenges DOE indirect costs cut

Judge blocked NIH from making a similar move

By **Jeffrey Mervis**

A coalition of universities and higher education groups this week asked a federal judge to block a move by the U.S. Department of Energy (DOE) to unilaterally cut in half its overhead rate on academic grants. The lawsuit calls DOE's policy, announced on 11 April, "a virtual carbon copy" of an indirect cost cap proposed in February by the National Institutes of Health (NIH) that a judge has ruled violated federal law.

"The purpose of [DOE] funding to colleges and universities is to support scientific research—not foot the bill for administrative costs and facility upgrades," Secretary of Energy Chris Wright said in announcing DOE's new 15% rate for indirect cost reimbursement. The department currently pays universities an average overhead rate of 30%—in other words, an additional 30 cents for every dollar of direct research it funds—although each school negotiates its own rate. DOE says a 15% cap will save an estimated $405 million in an annual external research grants budget of $2.5 billion.

NIH had claimed that its identical 15% cap would have saved $4 billion a year. But on 4 April a federal judge issued a permanent injunction against the change, finding NIH had ignored federal statutes and a congressional directive banning such unilateral changes to its rates.

DOE's action has elicited similar criticism from research advocates. "This is a ruinous policy," says Matt Owens of COGR. "First it was NIH. Now it is DOE. Bad policy is bad policy, and doubling down on it doesn't make it better."

In the lawsuit filed on 14 April, the Association of American Universities and 10 other plaintiffs argue DOE's "arbitrary and capricious" move violated a federal law that requires agencies to fully explain the reasoning behind a policy change and seek public comment before implementing it. ■

eppendorf & Science

PRIZE FOR NEURO BIOLOGY

2024 Winner
Laura Seeholzer, Ph.D.
University of California San Francisco, School of Medicine, USA

For research on airway neuroendocrine cells responding to external threats

Application Deadline
June 15, 2025

Call for Entries 2025

Eppendorf & Science Prize for Neurobiology
The annual Eppendorf & Science Prize for Neurobiology is an international prize which honors young scientists for outstanding neurobiological research based on methods of molecular, cellular, systems, or organismic biology. If you are 35 years of age or younger and doing great research, now is the time to submit an entry for this prize.
It's easy to apply! Write a 1,000-word essay and tell the world about your work.

eppendorf.com/prize

As the winner, you could be next to receive
> Prize money of US$25,000
> Publication of your work in *Science*
> Full support to attend the Prize Ceremony held in conjunction with the Annual Meeting of the Society for Neuroscience in the USA
> 10-year AAAS membership and online subscription to *Science*
> Complimentary products worth US$1,000 from Eppendorf
> An invitation to visit Eppendorf in Hamburg, Germany

eppendorf Science AAAS

FEATURES

RISKY MOVES

Can blocking "jumping genes" treat diseases and aging?

By **Mitch Leslie**

Bess Frost was thrilled when her genetically engineered fruit flies began taking longer strolls. The insects develop features of Alzheimer's disease, and as they age their neurons perish and their walking deteriorates. But Frost, a cell and molecular biologist then at University of Texas (UT) Health San Antonio, and her colleagues found that a drug called 3TC slowed or reversed the changes.

The 2018 result bolstered the idea that targeting transposons, restive DNA sequences that jump around the genome, might help treat Alzheimer's and a wide range of other conditions. That's because 3TC, developed to fight HIV, also gets transposons to stay put.

Still, Frost's friend Campbell Sullivan, a neuropsychologist also at UT Health who studies people with Alzheimer's, told her not to get too excited. "She said, 'My patients wouldn't be impressed by this,'" recalls Frost, who is now at Brown University.

The pair decided to conduct a clinical trial that could be more compelling. In 12 people with early Alzheimer's who took 3TC for 6 months, the drug didn't boost cognitive abilities. But other indicators suggested some benefits, as Frost, Sullivan, and their colleagues revealed last month in *npj Dementia*. For instance, levels of one key neurodegeneration indicator dipped, suggesting 3TC protects patients' brain cells. "That was the change I was most excited to see," Frost says.

Their recent study was the first clinical test of an antitransposon strategy for Alzheimer's to reach the finish line. But it's just one of a growing number of trials launched by academic researchers and biotechs to gauge the effects of throttling transposons—so-called jumping genes. These vagrant sequences, some of which are relics of viruses that invaded cells long ago or may even be derived from symbiotic bacteria, make up more than 40% of the human genome but were once seen as largely harmless. However, a variety of evidence from human cell lines, lab animals, and epidemiological studies has implicated their antics in illnesses such as lupus, amyotrophic lateral sclerosis (ALS), Parkinson's disease, and cancer, as well as in aging.

ILLUSTRATION: A. FISHER/*SCIENCE*

When retrotransposons (yellow) replicate, their mobile RNA versions (orange) may foster health problems.

Encouraging results are trickling in. In 2022, a phase 2 trial determined that 3TC halted tumor growth in some patients with colorectal cancer. Last year, Transposon Therapeutics revealed that a different drug that stymies replication of these sequences slowed one sign of physical decline in people with ALS or another neurodegenerative disease, frontotemporal dementia. "It's really amazing how quickly the story has developed," says John Sedivy, a molecular biologist at Brown and the company's co-founder.

Besides testing hand-me-down drugs such as 3TC, researchers are crafting compounds specifically to block the main troublemaking transposon in humans, LINE-1. ROME Therapeutics has developed a slew of LINE-1–focused drugs and hopes to reveal its first clinical trial results within 18 to 24 months, according to the company's chief scientific officer, Heike Keilhack.

Researchers say the clinical trials of transposon inhibitors are important not just to identify potential treatments, but also to test whether jumping genes do drive human diseases. "It's now clear that LINE-1 is important in lots of common diseases. What's not clear is how much it matters," says Brown biochemist Martin Taylor.

BIOLOGISTS HAVE UNDERSTOOD that genomes contain segments that can move around for about 80 years, since geneticist Barbara McClintock's pioneering work on such transposable elements in corn, which earned her a Nobel Prize in Physiology or Medicine in 1983. Many transposons simply cut themselves out of a chromosome and travel to a new location. But retrotransposons like LINE-1 can reproduce. A retrotransposon DNA sequence in one location can spawn an RNA copy that then becomes the template for a new DNA doppelganger that inserts itself elsewhere (see graphic, p. 246).

Retrotransposons constitute a large share of the human genome—LINE-1 alone accounts for 17%. For comparison, conventional genes make up only about 2% of the genome. "It is humbling to think that we are much more retrotransposons than we are human," says immunologist Tomas Mustelin of the University of Washington.

Some retrotransposons are the remnants of RNA viruses that infected our ancestors. Others apparently formed when cells accidentally made DNA versions of normal RNA molecules that slipped into the genome. LINE-1, which dates back more than 1 billion years, resembles sequences in bacteria. Its ancestors may have infiltrated the genome when the ancient bacteria that gave rise to mitochondria, cells' energy-producing organelles, took up residence.

Most of the 500,000 copies of LINE-1 in our genome have deteriorated over time and become immobile. However, about 100 copies of the retrotransposon, scattered through the chromosomes, can trick cells into replicating them and shoehorning the duplicates into our DNA at new positions. Over life's history, LINE-1 and its counterparts have been a creative force, Mustelin says. "Retrotransposons have been instrumental in the evolution of multicellular life. They brought a lot of genome innovation and have contributed to the growth in the size of the genome."

In the short term, however, recent findings suggest their effects can be baleful. Researchers knew transposons hop around in mammalian cells during embryonic development. But they thought that after this burst of activity, cells mostly kept transposons in check. Adult animal cells cinch up the parts of the genome where the parasitic sequences reside, locking out the enzymes needed to copy them.

But Sedivy and other researchers have found more recently that transposons escape these restraints in many nonembryonic cells. He and his colleagues chanced on the effect in 2013 while studying cellular senescence, a semidormant state in which aged or damaged cells lose the ability to divide. They noticed that the levels of LINE-1 RNA—an indicator of the transposon's activity—shot up after human cells entered senescence. Sedivy had been working on senescence since the 1990s, but he says this finding changed the course of his career. "I kind of took a detour into retrotransposons."

Later research confirmed that aging stirs up latent transposons and that they also mobilize in adult cells in a long list of inflammatory and neurodegenerative diseases. Some parts of the body seem to be especially vulnerable. "It's getting more and more clear that the central nervous system is particularly permissive for LINE-1 activation," Sedivy says. In addition, "We definitely know they are more active in a large number of cancers," says cancer biologist David Ting of Massachusetts General Hospital. One study found transposons were on the move in at least 31% of tumors.

These conditions are diverse, but there may be a common thread, says molecular biologist Vera Gorbunova of the University of Rochester Medical Center. Like our jowls and abs, parts of our genome loosen as we get older. "We lose the mechanism

that keeps transposons in check," she says. This genomic unraveling occurs not just as we age, but also in diseases such as Alzheimer's, ALS, cancer, and lupus.

The process can cause harm in unexpected ways. For many years, conventional wisdom held that relocation of a transposon was only a problem if it altered DNA at its landing site, creating mutations in existing genes or disrupting genetic control sequences. Such changes could contribute to cancer or, if they occurred in reproductive cells, lead to genetic diseases.

But researchers have found that active retrotransposons can also cause trouble when their RNA copies are released into the cytoplasm. Many of the sequences "have molecular patterns that are indistinguishable from viral sequences," says cancer biologist Daniel De Carvalho of the Princess Margaret Cancer Center. In 2015, he and other researchers reported that retrotransposon RNAs, which can fold into double-stranded shapes that resemble a viral genome, trip cells' virus detectors. The RNAs can further spawn other types of molecules, including double-stranded DNA and RNA-DNA hybrids, that can also set off cells' invasion alarms.

The upshot is that cells in which transposons are active often behave as if they were under viral attack. One of the countermeasures they take is to churn out type I interferons, proteins that orchestrate an assortment of defensive responses. They can also spark inflammation, which contributes to a range of diseases and is a feature of aging. Sedivy says this discovery came as a surprise. He and other scientists trying to understand the impact of transposons "weren't thinking about interferons," he says. "We thought about DNA damage."

TO SUPPRESS THE CELLULAR MAYHEM, researchers and biotechs are aiming at a protein crucial to LINE-1's mobility: ORF2p. Encoded by the transposon's DNA, the protein serves, among other things, as a reverse transcriptase, making a DNA copy of the transposon RNA so that LINE-1 can insert itself into the genome. Because some RNA viruses such as HIV and the hepatitis B virus rely on versions of reverse transcriptase to infect cells, researchers have already developed multiple drugs, known as reverse transcriptase inhibitors, that block these enzymes.

These inhibitors wouldn't stop LINE-1 from making an initial RNA copy, but they could short-circuit rounds of replication and curtail formation of the DNA-RNA hybrids and double-stranded DNA that can set off viral detectors. And some work suggests the inhibitors also thwart a cellular control center that promotes inflammation. So researchers hope the drugs will stem release of type I interferons and reduce inflammation.

For their fly study, Frost and her colleagues chose an approved HIV reverse transcriptase inhibitor. Transposon Therapeutics resurrected a different compound, which its developer had abandoned for financial reasons after phase 2 clinical trials against HIV. "It was kind of sitting on the shelf in Japan," Sedivy says. The drug, known as TPN-101, turned out to be more potent against LINE-1 than against HIV.

Last year, the company announced promising results from phase 2 trials of TPN-101 for three neurodegenerative diseases in which LINE-1 is on the move: progressive supranuclear palsy, ALS, and frontotemporal dementia. In progressive supranuclear palsy, the drug knocked down levels of neurofilament light (NfL), a protein released by dead or dying neurons, and reduced indicators of inflammation. In ALS and fronto-

Restless DNA

About 100 copies of the LINE-1 transposon are capable of copying themselves and colonizing new places in our genome. These jumps rely on cellular enzymes and proteins encoded by LINE-1's own DNA. Because this activity can contribute to disease, researchers and biotech companies are looking for ways to block it.

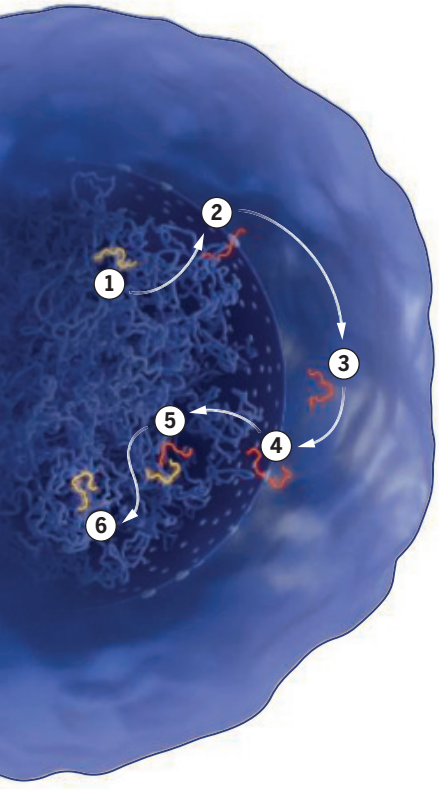

1 Switching to RNA
Inside the cell nucleus, enyzmes make an RNA version of LINE-1's DNA.

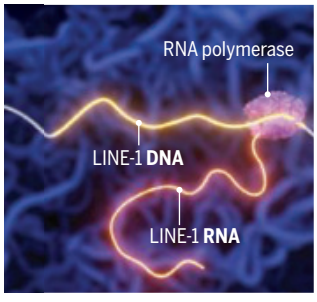

2 Departure
The LINE-1 RNA slips into the cytoplasm, where it may lead to inflammation.

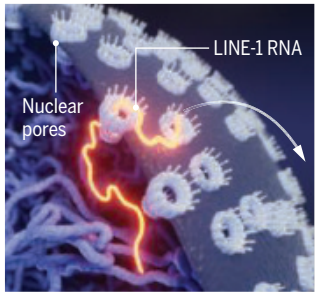

3 Reading the RNA
Cellular ribosomes read LINE-1's RNA, making two proteins.

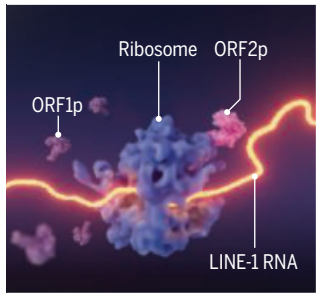

4 Return to the nucleus
ORF1p helps usher ORF2p and the LINE-1 RNA back into the nucleus.

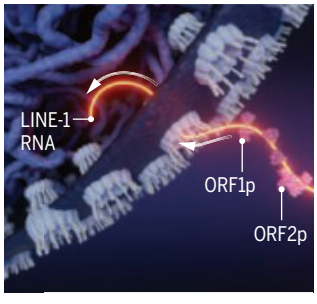

5 Reconversion
ORF2p reverts LINE-1 RNA back into DNA, a process drugs can block.

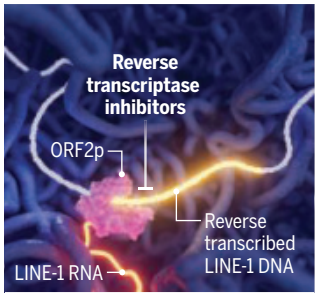

6 Settling down
When LINE-1 establishes a new genomic location, it can break up genes.

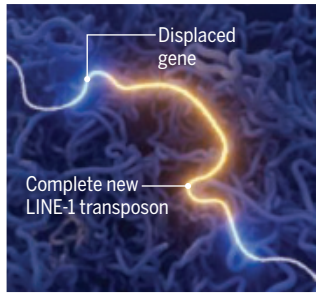

GRAPHIC: A. FISHER/*SCIENCE*

temporal dementia, TPN-101 both lowered NfL levels and cut by 50% the decline in vital capacity, a measure of respiratory muscle strength that falls in the disorders.

Computational biologist Benjamin Greenbaum of Memorial Sloan Kettering Cancer Center notes, however, that existing drugs like TPN-101 "were not designed for the purpose" of inhibiting LINE-1. That's why he and Ting co-founded ROME. It has developed several hundred new compounds tailored to block LINE-1's ORF2p, Keilhack says. Rome hasn't started any clinical trials, but it has presented positive results from studies of lab animals and human cells. Last year, for instance, the company unveiled findings that suggested one of its compounds improved survival of brain cells in mice that model Parkinson's.

Two 2024 studies, both published in *Nature*, could help researchers devise better inhibitors of ORF2p by providing the first high-resolution views of the protein's 3D structure. The two teams worked independently but had to contend with the same problem—amassing enough ORF2p to study. One group genetically modified insect cells to make the protein. Each cell could only safely manufacture a tiny amount of ORF2p, however. "The bottleneck is that the enzyme is very toxic to cells," says molecular and structural biologist Akanksha Thawani of the University of California, Berkeley.

She and her colleagues needed 20 liters of cells to synthesize a sufficient amount of the protein. Using a protein mapping method called cryo–electron microscopy, they determined that when ORF2p is ready to make a DNA version of LINE-1's RNA, it latches onto the tail of the RNA molecule. Blocking that interaction may offer a new opportunity to stymie the protein, she says.

In the second study, Taylor, Greenbaum, and colleagues genetically modified bacteria to crank out enough of ORF2p's core to make crystals of it for analysis. They found an explanation for why some reverse transcriptase inhibitors that stall HIV don't work against LINE-1. HIV's reverse transcriptase contains a pocket where these drugs can lodge, jamming the enzyme. However, ORF2p lacks that feature, the scientists reported—another clue that might help drug developers come up with better LINE-1 blockers.

Researchers are eager to try the drugs in illnesses beyond neurodegenerative diseases and cancer. Lupus, a common autoimmune disease, is one. Not only do patients typically produce high levels of type I interferons, but their blood cells can also teem with transposon RNA. "We don't have definitive proof" that transposon activity drives the disease, says molecular immunologist J. Michelle Kahlenberg of the University of Michigan. But compounds targeting LINE-1 might quell symptoms. And they might be easier on patients than current lupus drugs, which broadly suppress the immune system and are "basically a sledgehammer," she says.

Kahlenberg and colleagues have already tested some of ROME's LINE-1 inhibitors on cells from lupus patients. Type I interferons turn on a host of genes, but in 2024 the scientists showed that two of the drug candidates halted the increase in gene activity in samples of skin tissue. However, Kahlenberg cautions, "It's early days."

> **"It is humbling to think that we are much more retrotransposons than we are human."**
>
> **Tomas Mustelin**
> University of Washington

Another tempting target is aging. One hint that arresting LINE-1 might slow the physical deterioration that comes with the years is a 2022 finding in mice mimicking a condition called Hutchinson-Gilford progeria syndrome (HGPS), which produces symptoms resembling premature aging. When the researchers used small molecular strands known as antisense oligonucleotides to cut the levels of LINE-1 transposons in the mice, the animals lived about 25% longer than untreated rodents, they reported in *Science Translational Medicine*. One of the team's leaders was stem cell biologist Juan Carlos Izpisua Belmonte, who had just left the Salk Institute for Altos Labs, a startup devoted to "cellular rejuvenation" that launched with some $3 billion in backing. Altos hasn't publicly confirmed it is pursuing the same approach, but Izpisua Belmonte says the transposon-targeting antisense oligonucleotides are a "compelling candidate for promoting health span, warranting further investigation into their potential for aging interventions."

For antiaging researchers, it's a long way from mouse studies to humans, where confirming that a drug extends life span would take decades, Gorbunova says. But she notes that shorter studies that show positive changes in aging indicators, such as the patterns of methyl groups on DNA that can serve as aging clocks, might provide crucial evidence. Researchers tackling aging, Gorbunova says, "need something new, and inhibiting transposons shows great promise."

The new approach won't yield blockbuster cures, many researchers say. The diseases and conditions they are targeting are too complex, with multiple pathological mechanisms. In Alzheimer's, for example, "transposable elements are definitely not the only thing going wrong," Frost says. The same thing is likely true in cancer. When Ting and colleagues tested 3TC in patients with colorectal cancer, they found the drug curbed tumor growth but didn't kill abnormal cells. The drugs may be most useful, he says, to boost current treatments. "My hope has always been to give [transposon-inhibiting] drugs in combination with chemotherapy and see what happens."

The idea of dosing people with transposon inhibitors for long periods of time, to combat aging or specific diseases, also worries some researchers in the field. The current generation of reverse transcriptase inhibitors seems to cause few side effects—some patients with HIV have taken them for decades. But more effective transposon inhibitors could have unexpected downsides, especially if the sequences are key to normal functions, Mustelin says. "There is a growing notion in the field that retrotransposons have been co-opted for many physiological processes."

For example, they may help the body generate new blood cells. A 2024 study in *Science* (8 November, p. 637) revealed that retrotransposon activity, possibly by boosting type I interferon release, helped awaken dormant stem cells in the bone marrow of mice that were pregnant or had lost a lot of blood, allowing the animals to increase blood cell production.

Mustelin doesn't want the clinical research on transposon inhibitors to slow down, but he thinks researchers need to watch carefully for serious side effects in patients whose jumping genes have been shackled. "Until clinical trials are completed, we can speculate all we want, but we won't have any definitive evidence." ■

Solar photovoltaic module products are produced in Hefei, China, in October 2024.

POLICY FORUM

SUSTAINABLE DEVELOPMENT

Developing countries locked out of low-carbon technology trade

More than 90% of all low-carbon technology trade is between high-income countries and China

By **Praveena Bandara, Rebecca Ray, Jiaqi Lu, Kevin P. Gallagher**

A new class of low-carbon goods and services forms the essential inputs for the transition to lower-carbon and climate-resilient economic growth paths. By constructing a new dataset of such low-carbon technology (LCT) trade, we found that the vast majority of emerging market and developing countries (not including China) are not part of LCT trade. For the small amount of LCT trade in which developing countries engage, most are net importers. Because developing countries are left out of the production chains for LCT, they struggle to afford to import these technologies and have little chance at building capabilities to produce and export their own LCT. Without considerable technological transfer and long-run affordable investment, the developing world could be locked out of the climate transition in a manner that could lock in a new structure of global inequality.

ASYMMETRICAL GLOBAL MARKET

Power-generation technologies such as solar and wind, energy-storage technologies such as batteries, and clean transportation options such as electric vehicles are what are commonly referred to as LCTs. In addition to these new technologies, LCTs also include environment protection equipment and energy efficiency–improving technologies such as heating and insulation systems for buildings, waste disposal, air purifying, and recycling systems that address environmental pollution and even solar-powered energy-efficient consumer appliances. Trade data in LCTs can be a valuable tool in assessing international consumption and production patterns of LCTs, and, more importantly, the lack of trade flows may point to the mismatch between needs and purchasing and productive

Global Development Policy Center, Boston University, Boston, MA, USA. Email: jl1@bu.edu

PHOTO: NURPHOTO VIA GETTY IMAGES

Sectoral breakdown of regional low-carbon technology export and import patterns

Regions with high-income (HI), developed countries (●) participate in low-carbon technology trade more than regions composed of predominantly low-, low middle–, or upper middle–income (LMI) countries (●). China, an upper middle–income country and notable exception, is shown in gray. Regions are shown in descending order on the basis of their share of global exports and imports.

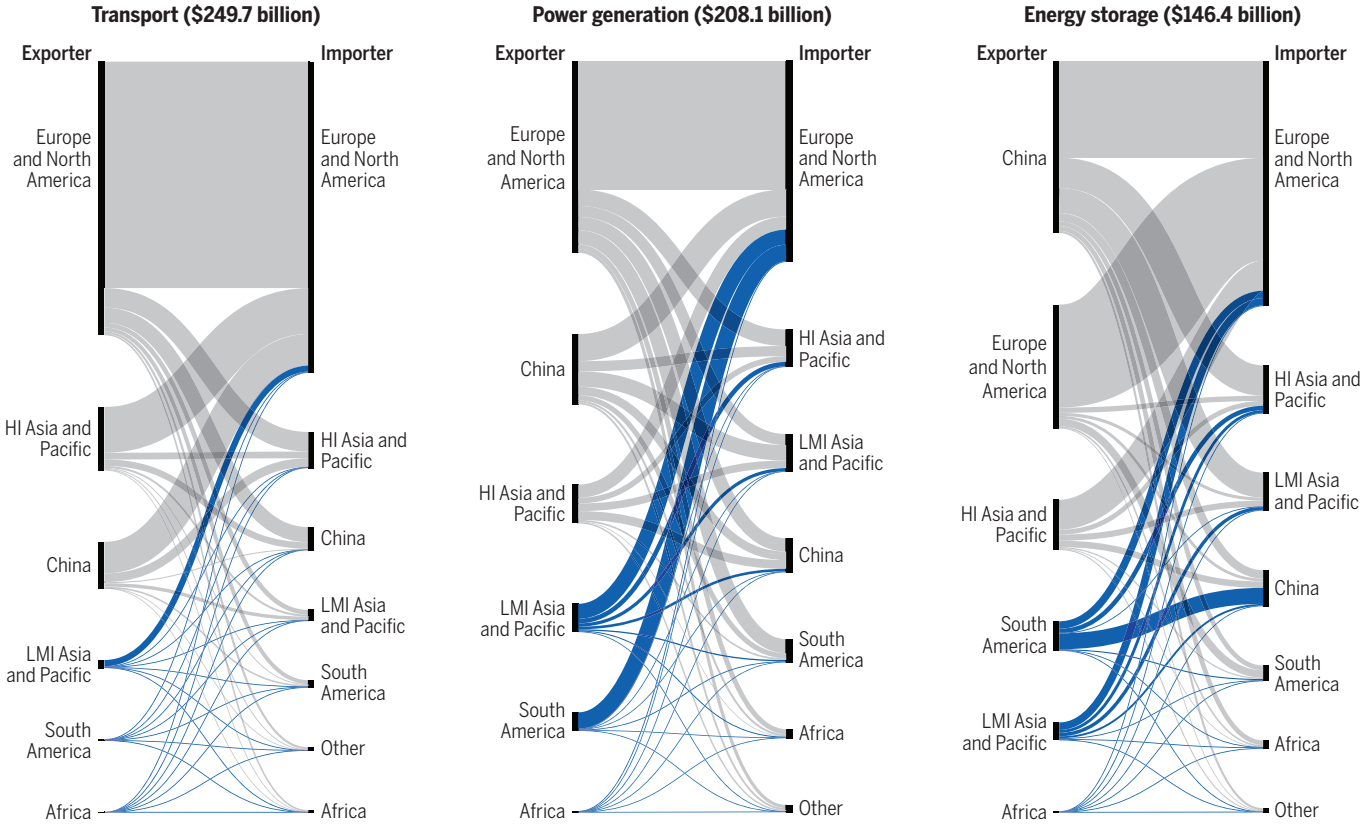

North America and Europe: countries on the continents of North America and Europe; Other: Antarctica, bunkers (offshore stores that supply fuel and provisions for ships and aircraft), and free zones (designated areas, such as export processing zones, within a country that are not treated as part of its customs territory for trade purposes).

CREDITS: (GRAPHIC) V. PENNEY/*SCIENCE*; (DATA) UN COMTRADE DATABASE (COMTRADE) DATABASE; WORLD BANK COUNTRY AND LENDING GROUPS; THE INTERNATIONAL MONETARY FUND'S LOW CARBON TECHNOLOGY HARMONIZED SYSTEM CODES

capacities of developing countries.

We developed a taxonomy for categorizing LCT goods by synthesizing existing lists of these goods [see supplementary materials (SM) for more details on the methodology]. We then used this taxonomy to compile a panel dataset of LCT imports and exports, from 1997 through 2022, at the product-country-year level using United Nations (UN) Comtrade data. The list of LCT goods is primarily composed of end products and intermediate parts but notably excludes critical minerals (except for lithium).

According to our new dataset, the size and structure of the global LCT trade have changed dramatically over the past three decades, growing at a faster pace than total trade. The total value of LCT trade grew by approximately 600%, from $172 billion in 1997 to nearly $1.2 trillion in 2022, whereas total trade grew around 400% from 1997 ($4.7 trillion) to 2022 ($23 trillion).

Our data reaffirms the present understanding of LCT trade patterns, which is that the main players (in order of export value, that is, price multiplied by quantity in 2022) are China, Germany, and the US (see fig. S1A). High-income countries, which traditionally dominated the export market, saw their share decline from 93.8% in 1997 to 62% in 2022. By contrast, China emerged as the main exporter in 2009 and quickly caught up with its Western counterparts within a span of 10 years. Presently, China is the main exporter, accounting for 19% of global LCT exports, whereas the US is the main importer, accounting for 12.8% of global LCT imports in 2022.

These shifts in the import-export market have profoundly affected the trade balance of LCTs for the past 25 years (see fig. S1). China has emerged as the primary surplus country in LCT trade, as well as parts of Europe, with the US having a small deficit. Almost all developing countries indicate no substantial participation in LCT trade or have trade deficits. Many of the emerging markets and developing economies (EMDEs) facing trade deficits in emerging LCT sectors also struggle to afford the economic burden of these trade deficits and, indeed, already face public debt conditions high enough to pose obstacles to their own climate change adaptation and mitigation investments (see fig. S1C). Overall, developing countries are largely omitted from, or paying to participate in, LCT trade—a burden that may make their own sustainability goals less achievable.

SECTORAL TRADE PATTERNS

In addition to estimating LCT trade flows at the country level, we disaggregated LCT trade by sector level, including buildings, energy storage, pollution control, power generation, consumer appliance, transport, and environmental monitoring (see SM). In particular, transport, power generation, and energy storage make up 57% of trading in the seven LCT sectors, accounting for nearly 24, 19, and 14%, respectively (calculated as a percentage of world LCT exports in 2022).

The inter- and intraregional trade patterns in the transport and power-generation sectors for 2022 reveal that trade is still dominated by high-income, European countries trading among each other (see the fig-

ure). China and high-income Asia and Pacific countries account for trade values equal to about half that of their European and North American counterparts in the transport and power generation sectors.

Among the various new LCTs, solar and wind are the dominant alternative technologies facilitating the energy transition from nonrenewable to renewable sources and are an essential part of the new climate economy. Export patterns show that the production of these technologies is gaining traction among many developing countries (see fig. S1B). Yet they are facing severe competition in the global market. China still dominates solar exports, accounting for a little more than 50% of the market (see fig. S2A). Though China exports more to high-income countries, it directs about 40% of its solar exports to other emerging market and developing countries. The global wind export market remains dominated by high-income countries, which account for 56% of exports, followed by China with 24%. Together, they account for 80% of total global exports (see fig S2B). Like solar exports, a nonnegligible share of these exports is also directed to EMDEs.

The energy-storage sector, which is essential for addressing renewable energy intermittency and transportation electrification, also shows China and high-income Asia and Pacific countries commanding more than half of exports (43.6 and 12.8%, respectively), indicating a strong production capacity, whereas Europe and North America lead in imports (62.1%). This pattern suggests the substantial role of China and high-income Asia and Pacific countries in manufacturing energy-storage goods to meet the growing demand from Europe and North America as they accelerate their energy transition.

GETTING ON TRACK

The present period of global economic transformation and transition presents EMDEs with opportunities for growth and building resilience, along with substantial challenges. In the short term, economic development pathways for developing countries will broaden or narrow depending on the extent to which they can participate in the newly emerging supply chains, thereby generating crucial export revenue, particularly for countries presently dependent on fossil fuel energy commodity production (*1*). Importing LCT goods and deploying them in a timely manner will also be a short- to medium-term goal for these countries. Finally, there is a growing trend toward deploying green industrial policies with the long-term goal of fostering green industrial development among EMDEs and advanced economies alike (*2*). However, whether EMDEs decide to pursue one or many of these ambitious goals, they will face major financial obstacles with competing interests vying for limited financial resources.

Several factors will need to be addressed to combat global climate change and improve the development prospects of the world's poorer nations. First, there is a lack of resource mobilization that will allow the developing world to invest and take part in the global transition to a low-carbon and climate-resilient economy. Although multilateral development banks (MDBs) and the Group of 20 (G20) have pledged to have MDBs mobilize trillions of dollars for such countries, they lack the level of capital to make a stepwise increase (*3*). Second, external shocks due to COVID-19, war and sanctions, and climate change itself have put many EMDEs in such debt distress that the ability to harness the resources for importing or investing in homegrown LCTs is out of reach (*4*, *5*). Third, although the transition to LCTs reduces the dependence on fossil fuel imports and leads to long-term savings, it requires considerable upfront investment in the short term. This mismatch creates a need for innovative financial instruments, such as loans that can be repaid through future savings from avoiding fossil fuel imports. Furthermore, the need for foreign currency and/or further borrowing to import these technologies on top of existing debt burdens (also often denominated in foreign currency) puts EMDEs at risk of macroeconomic instability, including exchange and currency crises, which in turn may have knock-on effects on foreign investment. Finally, policies to subsidize new industries and/or require foreign investors to transfer LCTs, or tax foreign fossil fuel companies, are not permissible under numerous trade and investment agreements (*6*). Moreover, incumbent firms can file monetary damages for such actions that will enhance their fiscal positions (*7*).

These factors are accentuated by the increasingly strong interplay between trade policies and climate change. Notably, measures such as the European Union's Carbon Border Adjustment Mechanism are poised to discriminate against high-carbon content products, potentially stripping emerging economies of economic opportunities if their domestic manufacturing fails to decarbonize quickly enough (*8*). At the same time, rising interstate trade tensions could further raise the cost of some LCTs in the world economy and put debates over the level of climate financing in gridlock. It is unlikely that two trading countries would come to an agreement to address these issues at the World Trade Organization, given its nonoperational appellate body.

During the 2024 29th United Nations (UN) Climate Change Conference (COP29) in Baku, developed countries committed to mobilizing $300 billion annually over the next decade for climate finance—three times the present level but still substantially below the more than $1 trillion that economists say is needed (*9*). In July 2025, the UN will host the Fourth International Conference for Financing for Development, and later in the year, Brazil will host COP30 and South Africa the G20 summit. It is imperative that global climate action be the centerpiece of such discussions and that a stepwise increase in new, long-term, and low-cost financing and technological transfer is made available to enable the developing world to participate in the climate transition. The health of the climate, the prospects of billions of people in poorer nations, and the legitimacy of the higher-income nations and China in the multilateral system are at stake. ■

REFERENCES AND NOTES

1. E. Espagne *et al*., "Cross-border risks of a global economy in mid-transition," Working paper, International Money Fund (IMF), 8 September 2023.
2. European Bank for Reconstruction and Development (EBRD), "Transition report 2024-25: Navigating industrial policy" (EBRD, 2024).
3. K. P. Gallagher, M. Zucker-Marques, R. R. Bhandary, N. Marins, "Energizing MDB financing capacity: Identifying and filling the gaps to raise ambition for the 2030 agenda and beyond" (Boston University Global Development Policy Center, 2024); https://www.bu.edu/gdp/files/2024/10/G20-MDBs-Report-FIN.pdf.
4. M. Zucker-Marques *et al*., "Defaulting on development and climate: Debt sustainability and the race for the 2030 agenda and Paris Agreement" (Boston University Global Development Policy Center, 2024); https://www.bu.edu/gdp/files/2024/04/DRGR-Report-2024-FIN.pdf.
5. K. P. Gallagher, R. Ray, R. R. Bhandary, L. Ramos, *One Earth* **6**, 1291 (2023).
6. R. D. Thrasher, *Constraining Development: The Shrinking of Policy Space in the International Trade Regime*, Anthem IGLP Rethinking Global Law and Policy Series (Anthem Press, 2020).
7. K. Tienhaara, R. Thrasher, B. A. Simmons, K. P. Gallagher, *Science* **376**, 701 (2022).
8. G. Magacho, E. Espagne, A. Godin, *Clim. Policy* **24**, 243 (2024).
9. UN Climate Change, "COP29 UN Climate Conference agrees to triple finance to developing countries, protecting lives and livelihoods" (UN Climate Change, 2024); https://unfccc.int/news/cop29-un-climate-conference-agrees-to-triple-finance-to-developing-countries-protecting-lives-and.
10. P. Bandara, R. Ray, J. Lu, K. P. Gallagher, Data and code for "Developing countries locked out of low carbon–technology trade" (2025); https://www.bu.edu/gdp/files/2025/02/Data-and-Code.zip.

ACKNOWLEDGMENTS

All data and code used in the presented analyses can be accessed at (*10*). The authors thank A. Iaia for excellent research assistance. The authors also acknowledge support from the European Climate Foundation, Hewlett Foundation, Rockefeller Brothers Fund, and Climate Works Foundation.

SUPPLEMENTARY MATERIALS

science.org/doi/10.1126/science.adu7731

10.1126/science.adu7731

PERSPECTIVES

The layered deposits of Mount Sharp in Gale crater contain the rich geochemical history of Mars.

PHOTO: NASA/JPL-CALTECH/MSSS

GEOSCIENCE

Catching a glimpse of ancient Mars

Exposed minerals hint at the evolution of geochemical conditions on early Mars

By **Janice L. Bishop**[1] *and* **Melissa D. Lane**[2]

Minerals that are revealed on the surface of Mars can provide clues about its ancient geological history. These deposits are formed in specific geochemical environments involving water. Over the past three decades, contradicting views have been proposed about the climate on early Mars. The planet has been described to have had a warm and wet (*1*) or cold and dry (*2*) climate, with intermittent warm intervals supporting liquid water (*3*, *4*) and transient Earth-like conditions that are required to form some of the observed minerals (*5*). Analyzing minerals on Mars may solve this long-standing puzzle. On page 292 of this issue, Tutolo *et al.* (*6*) report the observation of pure siderite—an iron carbonate that forms under neutral to alkaline pH—in a sample analyzed by the Curiosity rover in 2024. Detection of this new carbonate contributes to understanding the geochemical history of Mars.

Mars once had a dense atmosphere that stabilized liquid water on its surface (*4*). By contrast, modern Mars barely has an atmosphere. It is much thinner than on Earth's highest mountains, making Mars a frigid and dry desert covered with rocks, sand, and dust. This immense transition challenges modeling of the thick atmosphere that existed on early Mars. Fortuitously, abundant minerals—including clays, carbonates, and sulfates that formed ~4 billion years ago—can provide clues about the early climate. Meteorite impacts and wind have churned up and scoured the surface over time, exposing these ancient, once-buried minerals. These deposits reveal active aqueous chemistry on early Mars.

Previous studies proposed that subsurface or subaqueous magnesium smectite clay formed from hydrothermal groundwater at neutral to alkaline pH (*7*, *8*). Remote-sensing analyses that used data from the Compact Reconnaissance Imaging Spectrometer for Mars (CRISM) of Mawrth Vallis—a region with abundant clays and channels carved by flowing water—also discovered the presence of magnesium smectite under a thick unit of iron-rich smectite (*9*). This layering and morphology of minerals suggested that the magnesium smectite partially converted to iron-rich smectite (*9*) through sedimentary processes (*10*). In addition, sulfates and sulfate-bearing precipitates that formed under mildly acidic conditions were found between the iron-rich smectite layer and an overlying aluminum-rich clay (*11*). These discoveries reflect a changing geochemistry in ancient Mars that includes periods of acidic environments. However, it is challenging to garner a complete picture of the chemical composition of the Martian surface through measurements acquired from orbit.

Tutolo *et al.* analyzed minerals directly

[1]SETI Institute, Mountain View, CA, USA. [2]Fibernetics, Lititz, PA, USA. Email: jbishop@seti.org; lane@fibergyro.com

with instruments on the Curiosity rover at Mount Sharp in Gale crater—a large impact crater thought to have once held an ancient lake. The authors suggest that the subsurface siderite could have been widespread on ancient Mars. Curiosity observed that siderite is mixed with sulfates and iron oxide–bearing minerals. This points to the presence of a once acidic environment that partially dissolved siderite to form these mineral assemblages. A large volume of carbon dioxide released from this reaction may have thickened the atmosphere and stabilized water on the surface.

Folding together the Mawrth Vallis alteration scenario with the siderite-to-sulfate progression described by Tutolo *et al.* enables consideration of the following global hypothesis for the evolution of early Mars' geochemistry (see the figure). About 4 billion years ago, widespread magnesium smectite and siderite formed on Mars in a neutral to mildly alkaline environment. Later alteration of the surface by acidic water partially dissolved siderite, forming sulfates and releasing iron ions (Fe^{2+}) into the surrounding clay deposits. Some of these ions oxidized and formed iron-rich magnesium smectite and nontronite (Fe^{3+}- containing smectite), whereas other iron ions precipitated as ferric oxide or ferric hydroxide.

This synopsis is consistent with mineral assemblages that have been observed across Mars. The decrease in siderite and simultaneous increase in other minerals such as ferric oxide, ferric hydroxide, and sulfate were seen at Mount Sharp (*6*). Global CRISM observations of magnesium-iron-calcium carbonates (*12*) could also reflect geochemical reactions after the dissolution of siderite. Further, the Perseverance rover observed siderite and magnesium-rich carbonate near smectite clay and sulfate in Jezero crater—a region previously flooded by water (*13*). The Opportunity rover at the light-toned sedimentary plains of Sinus Meridiani reported ferric oxide concretions within ancient sulfate-bearing rock (*14*), which could have also resulted from siderite dissolution. As details of Mars' geochemistry are discovered through orbital and rover investigations around the planet, additional clues are revealed about the diversity of potentially habitable environments. When the samples collected by the Perseverance rover are returned to Earth for analyses, they will fully share their scientific secrets. ■

Early martian geology

Analyzing exposed minerals on the surface can provide a comprehensive picture of geochemical processes that took place on early Mars.

~4 billion years ago

Mars had abundant amounts of siderite (iron carbonate) and Mg-smectite in a neutral-to-alkaline environment.

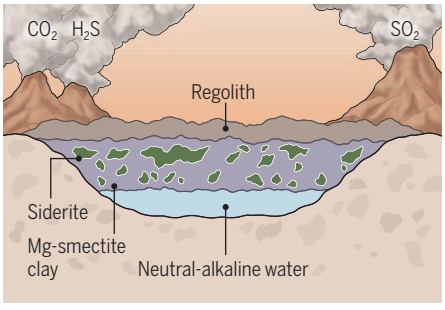

~3.8 to 4 billion years ago

Surface alteration with acidic water partially dissolved siderite. The leached Fe ions reacted to form ferric oxide and ferric hydroxide and Fe-rich Mg-smectite with Mg- and Ca-sulfates, CO_2, and water as by-products.

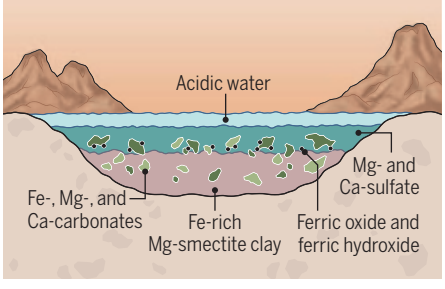

~3.8 billion years ago

The excess CO_2 may have thickened the atmosphere to stabilize water on the surface.

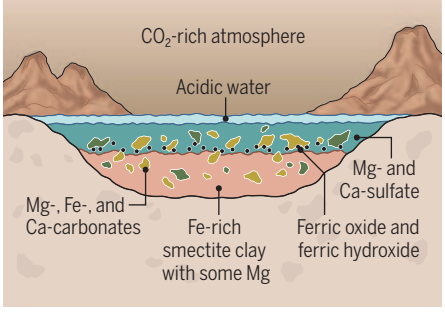

Ca, calcium; CO_2, carbon dioxide; Fe, iron; H_2S, hydrogen sulfide; Mg, magnesium; SO_2, sulfur dioxide.

REFERENCES AND NOTES

1. J. B. Pollack, J. F. Kasting, S. M. Richardson, K. Poliakoff, *Icarus* **71**, 203 (1987).
2. F. Forget *et al.*, *Icarus* **222**, 81 (2013).
3. M. H. Carr, *J. Geophys. Res.* **100**, 7479 (1995).
4. R. Wordsworth *et al.*, *Nat. Geosci.* **14**, 127 (2021).
5. J. L. Bishop *et al.*, *Nat. Astron.* **2**, 206 (2018).
6. B. M. Tutolo *et al.*, *Science* **388**, 292 (2025).
7. B. L. Ehlmann *et al.*, *Nature* **479**, 53 (2011).
8. J. R. Michalski *et al.*, *Nat. Geosci.* **6**, 133 (2013).
9. J. D. McNeil *et al.*, *Nat. Geosci.* **18**, 124 (2025).
10. D. R. Lowe, J. L. Bishop, D. Loizeau, J. J. Wray, R. A. Beyer, *Bull. Geol. Soc. Am.* **132**, 17 (2020).
11. J. L. Bishop *et al.*, *Icarus* **341**, 113634 (2020).
12. J. J. Wray *et al.*, *J. Geophys. Res.* **121**, 652 (2016).
13. E. Clavé *et al.*, *J. Geophys. Res. Planets* **128**, e2022JE007463 (2023).
14. S. W. Squyres *et al.*, *Science* **306**, 1709 (2004).

10.1126/science.adw4889

MICROBIOLOGY

How bacteria subvert plant immunity

To prevent their detection, bacteria inhibit plant enzymes with a small molecule

By **Frank C. Schroeder**

Early detection of the enemy is a central tenet of an immune system's fight against microbial pathogens. For this purpose, plants and animals have evolved dedicated receptors to detect pathogen-associated molecular patterns (PAMPs) that trigger a host of defense responses (*1*). These ancient and conserved surveillance systems detect equally conserved PAMPs, which have diverse chemical structures, including bacterial flagellin and lipopolysaccharides. The ability of plants and animals to recognize such microbial signatures has driven the evolution of sophisticated countermeasures by pathogens to evade detection. On page 297 of this issue, Sanguankiattichai *et al.* (*2*) report that pathogenic bacteria undermine plant perception of flagellin by producing an iminosugar, called glycosyrin, that inhibits a plant glycosidase required for flagellin detection and thereby suppresses plant immune responses. The finding has broad implications for the role of glycobiology in plant-microbe interactions and also drug discovery.

Flagellin, the primary protein component of propeller-like filaments called flagella that bacteria use for movement, represents a quintessential PAMP that is recognized by both plant and animal immune systems. Plants detect a conserved 22–amino acid epitope (flg22) through the pattern-recognition receptor FLS2, whereas mammals recognize flagellin through Toll-like receptor 5 (TLR5). However, flg22 and other bacterial elicitor motifs are buried under a coat of oligosaccharide chains and need to be exposed before they can be detected by immune receptors. In 2019, it was reported that *Nicotiana benthamiana*, a close relative of tobacco and an important model system for studying plant-pathogen interactions,

Boyce Thompson Institute and Department of Chemistry and Chemical Biology, Cornell University, Ithaca, NY, USA. Email: schroeder@cornell.edu

GRAPHIC: A. FISHER/*SCIENCE*

secretes β-galactosidase 1 (BGAL1) into the apoplast (the extracellular space), where this enzyme strips flagellin of its sugar coat to enable its perception by receptors and activation of defense responses (*3*). The same study also suggested that the pathogenic bacterium *Pseudomonas syringae* can fight back. The bacteria appeared to produce a small molecule that inhibits BGAL1 and thereby antagonizes detection of flg22 by the plant (*3*). However, the structure of this inhibitor could not be determined, in part because it seemed to be chemically unstable, complicating its isolation and identification by means of conventional spectroscopic analysis.

To tackle this challenge, Sanguankiattichai *et al.* deployed an innovative strategy. Instead of relying on chromatographic fractionation to isolate the inhibitor produced by *P. syringae*, the authors used cryogenic electron microscopy, which revealed a near-perfect snapshot of the small-molecule inhibitor captured in the active site of a galactosidase. Moreover, the images revealed that the inhibitor represents an unusual iminosugar, consisting of a pyrrolidine ring bearing a hydrated aldehyde. This structure—glycosyrin—mimics sugar moieties in glycosides, enabling it to inhibit not only BGAL1 but also other plant glycosidases involved in immune responses.

"...this multipronged attack relies on the biosynthesis of a single small molecule..."

Iminosugars are produced by many plants and bacteria and have been studied extensively as glycosidase inhibitors (*4*). However, most natural iminosugars contain six-membered rings that resemble glucose or galactose, in contrast to the five-membered ring in glycosyrin. Given that iminosugars are also used to treat human disease, such as type II diabetes and lysosomal storage disorders (*5*), glycosyrin's unusual structure may also provide inspiration for drug development.

Sanguankiattichai *et al.* found that bacterial glycosyrin production interferes with plant defense and enhances bacterial virulence through at least three mechanisms. By inhibiting BGAL1, it prevents the deglycosylation of immunogenic flagellin peptides, suppressing pathogen recognition. Inhibition of BGAL1 and possibly other glycosidases also alters the pattern of sugars attached to proteins more broadly, which could perturb structures and functions of plant cell wall components and secreted proteins needed for pathogen defense. In addition, glycosidase inhibition by glycosyrin induced accumulation of osmolytes such as trehalose and galactosylglycerol in the apoplast (extracellular space), creating conditions that favor bacterial colonization while dampening plant defense responses. The authors also speculate that glycosyrin may block the release of major plant defense hormones such as salicylic acid from their inactive sugar conjugates. That this multipronged attack relies on the biosynthesis of a single small molecule with a fairly simple structure—glycosyrin—shows the level of sophistication that pathogens use to manipulate host physiology.

Sanguankiattichai *et al.* show that expression of the glycosyrin biosynthesis gene cluster (*gsn*) in *P. syringae* is controlled by pathways that also regulate bacterial virulence, establishing a direct link between pathogenicity and iminosugar production. Notably, the *gsn* cluster is also found in a range of other plant pathogenic bacteria, suggesting that glycosidase inhibition is a broadly conserved virulence strategy. However, iminosugar-based inhibition of plant defenses may be even more widespread. Glycosyrin incorporates phosphoribosylamine, an intermediate from the purine biosynthesis pathway, in contrast to other iminosugar biosynthesis pathways that rely on sugar-phosphate precursors and aminotransferases (*6*). This divergence highlights the metabolic flexibility of bacteria and indicates that other, yet uncharacterized iminosugars may exist in pathogens that lack all or parts of the *gsn* cluster. This suggests that glycobiology plays a much greater role in plant-microbe interactions than previously appreciated. Because inhibition of deglycosylation seems to be a general virulence mechanism, targeting iminosugar biosynthesis or enhancing plant glycosidase activity might provide routes to disease management.

Glycosylation of microbial PAMPs also affects their recognition by the human immune system. For example, glycosylation of flagellin in *Burkholderia cenocepacia*, a bacterial pathogen that causes opportunistic infections in individuals with weakened immune systems, impairs its ability to stimulate TLR5 signaling (*7*, *8*). Thus, immune evasion by modulating PAMP glycosylation may represent a virulence mechanism also in animal-pathogen interactions. It could be interesting to reexamine the metabolomes of human pathogens for compounds that regulate host glycosidases. ■

REFERENCES AND NOTES

1. C. Zipfel, *Trends Immunol.* **35**, 345 (2014).
2. N. Sanguankiattichai *et al.*, *Science* **388**, 297 (2025).
3. P. Buscaill *et al.*, *Science* **364**, eaav0748 (2019).
4. I. Conforti, A. Marra, *Org. Biomol. Chem.* **19**, 5439 (2021).
5. R. J. Nash *et al.*, *Future Med. Chem.* **3**, 1513 (2011).
6. H. E. Beal, N. A. Horenstein, *AMB Express* **11**, 120 (2021).
7. K. Khim *et al.*, *Vaccines* **8**, 139 (2023).
8. A. Hanuszkiewicz *et al.*, *J. Biol. Chem.* **289**, 19231 (2014).

10.1126/science.adx0288

NEUROSCIENCE

Dendritic arbors structure memories

Synapses on different dendritic domains store distinct types of information

By **Ayelén I. Groisman**[1] *and* **Johannes J. Letzkus**[1,2,3]

One of the most notable differences between neurons and most other cells in the body is the complex and intricate morphology of their dendritic arbors. These elaborate, treelike processes receive the lion's share of a neuron's synaptic inputs. Electrical dendritic recordings (*1*) combined with computer modeling (*2*) have uncovered a wealth of mechanisms whereby dendrites can shape information processing and storage. Despite thus gaining deep insights into their computational capacities, much less is known about how dendritic mechanisms enable the brain to instruct meaningful behavior. On page 322 of this issue, Wright *et al.* (*3*) report that synapses impinging onto different dendritic domains undergo plasticity (activity-induced changes in strength) according to distinct rules, indicating that dendritic arbors differentially control which type of information they select for storage.

The constant acquisition, storage, and retrieval of memories are among the most essential and fascinating features of the brain. For instance, memory formation is a marvel of efficiency: The storage capacity of the human brain—running on approximately 20 watts of power—is estimated to fall into the petabyte range (*4*), whereas supercomputers handling such data volumes consume megawatts of power. As such, the neuronal implementation of memory has been under intense scientific scrutiny for many decades. One highly successful entry point for investigation was provided by the observation that the strength of synaptic connections can be changed by neuronal activity, an effect called synaptic plastic-

[1]Institute for Physiology, Faculty of Medicine, University of Freiburg, Freiburg, Germany. [2]BrainLinks-BrainTools, Intelligent Machine-Brain Interfacing Technology (IMBIT), University of Freiburg, Freiburg, Germany. [3]Center for Basics in NeuroModulation, University of Freiburg, Freiburg, Germany. Email: johannes.letzkus@physiologie.uni-freiburg.de

ity. This established an experimental model for determining the likely cellular substrate of memory formation, leading to the identification and dissection of a markedly diverse set of synaptic plasticity mechanisms (*5*, *6*). Furthermore, this line of study revealed that the location of a synaptic input within the dendritic arbor can be a fundamental determinant of its plasticity (*7*, *8*).

Typical experiments on synaptic plasticity have been conducted on just a handful of model neuron types, under controlled conditions and in in vitro preparations that lack the native structure of the brainwide neuronal network. Conversely, bona fide memories are generated through the intricate interplay among diverse neuron types with ongoing activity patterns that change over the sleep-wake cycle and are moreover subject to control by several factors only present in the intact brain (e.g., neuromodulation and synaptic inhibition).

To address which forms of plasticity are recruited during the formation of such real-world memories, and to determine whether dendritic synapse location plays a role, Wright *et al.* used a combination of structural and functional in vivo imaging as mice learned a motor task. They focused on a type of neuron previously implicated in the behavior (pyramidal neurons in layer 2/3 of the motor cortex) and examined both the synaptic input to individual dendritic spines (small membrane protrusions that receive synaptic signals) and the resulting postsynaptic activity. This was performed in two dendritic domains—the basal area close to the cell soma in layer 2/3 and the apical dendrites in layer 1 close to the surface of the neocortex.

Wright *et al.* found that the pre- and postsynaptic activity patterns that occur during learning have a differential effect on synaptic plasticity in apical and basal dendrites. In apical dendrites, spines that displayed high coactivity with their neighbors subsequently became strengthened (i.e., potentiated). This indicates that learning-related plasticity is governed by local interactions between nearby synaptic inputs in apical dendrites. Conversely, inputs to basal dendrites were strengthened or weakened as a function of their coactivity with the global output of the entire neuron in the form of action potentials (see the figure). In line with this observation, chronically reducing the activity of a neuron reduced potentiation in basal dendrites while leaving apical plasticity intact.

Two types of plasticity in one neuron

During motor learning, synaptic inputs impinging on apical dendrites of pyramidal neurons in layer 2/3 of the motor cortex are strengthened (potentiated) by coactivity with their local neighbors (●). By contrast, potentiation of basal synapses is controlled by coactivity with the neuron's global action potential output (●). Notably, the two dendritic compartments also receive largely distinct input streams.

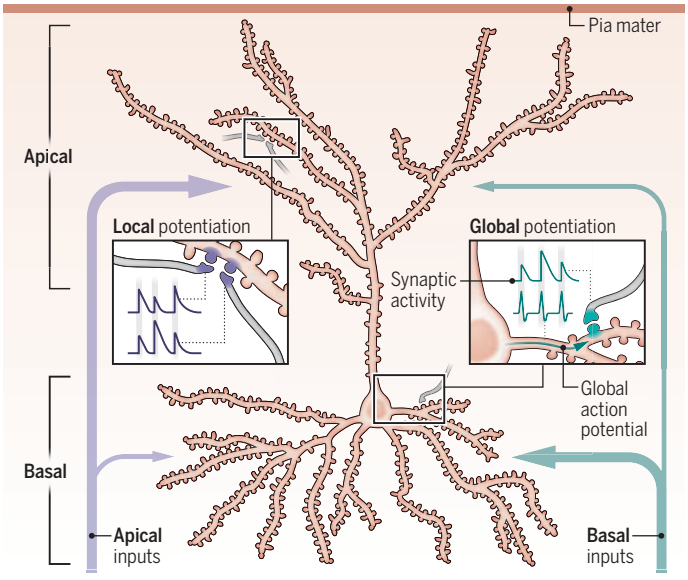

These results demonstrate that dendritic arbors compartmentalize synaptic plasticity underlying memories. Mechanistically, they support the long-held notion that the electrical properties of dendrites shape plasticity: Action potentials attenuate as they back-propagate from the soma into the dendrites and therefore predominantly affect the relatively proximal basal synapses. Conversely, distal apical dendrites have greater electrical resistance, translating to stronger local depolarization by synaptic input (*1*) and thereby favoring cross-talk between neighboring inputs (*9*, *10*).

Functionally, the findings of Wright *et al.* suggest a number of intriguing implications as well as several key questions for future work. Notably, the two dendritic domains receive inputs from different brain areas that convey largely distinct types of information (*11*). The mechanisms uncovered by the authors now provide a framework for how the postsynaptic neuron extracts different information content from these inputs for storage. Specifically in apical dendrites, an important open question is whether cooperation between afferents from different brain areas is required for plasticity induction, as has been suggested (*12*). Future work imaging the activity of defined afferents to individual apical dendritic segments may be used to uncover the logic of these heterosynaptic learning rules.

The plasticity of basal synapses observed by Wright *et al.* follows a classical Hebbian learning rule, in which inputs that contribute to action potential firing in the postsynaptic neuron are strengthened (*5*, *6*). Conversely, distal apical input plasticity is largely independent of global output, pinpointing a fundamentally different function (*13*). The apical learning rule favors the formation of functional clusters of spines, which can in turn cooperatively elicit dendritic spikes (a localized form of dendritic action potential). These events are notable because they may represent the only way for apical inputs to affect somatic activity (*1*, *2*). The spatial clustering of inputs could furthermore enable each dendritic branch to operate as an independent memory unit, greatly increasing the information storage capacity of single neurons (*2*). Apical plasticity can likely also occur in the absence of somatic output. Such "offline learning" may have a particularly prominent function for memory consolidation during sleep, which is associated with electrical decoupling of apical dendrites from the soma (*14*, *15*). The methodology developed by Wright *et al.* will enable future research on these and other key issues pertaining to dendritic compartmentalization of memory. ■

REFERENCES AND NOTES

1. G. J. Stuart, N. Spruston, *Nat. Neurosci.* **18**, 1713 (2015).
2. P. Poirazi, A. Papoutsi, *Nat. Rev. Neurosci.* **21**, 303 (2020).
3. W. J. Wright *et al.*, *Science* **388**, 322 (2025).
4. T. M. Bartol Jr. *et al.*, *eLife* **4**, e10778 (2015).
5. J. C. Magee, C. Grienberger, *Annu. Rev. Neurosci.* **43**, 95 (2020).
6. P. R. Roelfsema, A. Holtmaat, *Nat. Rev. Neurosci.* **19**, 166 (2018).
7. P. J. Sjöström *et al.*, *Physiol. Rev.* **88**, 769 (2008).
8. R. C. Froemke *et al.*, *Front. Synaptic Neurosci.* **2**, 29 (2010).
9. C. D. Harvey, K. Svoboda, *Nature* **450**, 1195 (2007).
10. J. K. O'Hare *et al.*, *Science* **375**, eabm1670 (2022).
11. M. B. Pardi *et al.*, *Trends Neurosci.* **46**, 20 (2023).
12. J. Sohn *et al.*, *Sci. Adv.* **8**, eabm0531 (2022).
13. S. d'Aquin *et al.*, *Science* **376**, eabf7052 (2022).
14. M. Aime *et al.*, *Science* **376**, 724 (2022).
15. J. Aru, M. Suzuki, M. E. Larkum, *Trends Cogn. Sci.* **24**, 814 (2020).

ACKNOWLEDGMENTS

The authors thank A. Marmelshtein for discussion and acknowledge the German Research Foundation (LE3804/3-1, LE3804/4-1, LE3804/7-1, LE3804/8-1, TRR 384/1 2024, and 514483642) and EMBO (ALTF157-2022) for support.

10.1126/science.adx0640

GRAPHIC: N. BURGESS/*SCIENCE*

BATTERIES

Cracking the failure of lithium batteries

Prolonged operation accumulates damage that is similar to fatigue in an electrode

By **Jagjit Nanda**[1,2] *and* **Sergiy Kalnaus**[3]

Lithium batteries that use a solid electrolyte have the potential to improve safety and increase the amount of stored energy. This makes solid-state electrochemical cells a promising option for electric vehicles and wearable devices. However, nonuniform plating or stripping of lithium at the interface between an anode (negative electrode) and the electrolyte during charging and discharging leads to growth of detrimental lithium filaments (dendrites) that short-circuit the battery cell. This problem even occurs when the battery operates at small currents. The underlying mechanism of this failure is not well understood. On page 311 of this issue, Wang *et al.* (*1*) report that structural defects accumulate in the lithium metal anode under repeated charging and discharging at a small current. This is similar to mechanical fatigue that is observed over longer periods of intermittent straining of a material. The observation could guide the design of lithium batteries with increased life span.

When a material undergoes repeated mechanical loading, cracks start to form and propagate, resulting in a failure below the critical stress that causes breaking of the material. Similar damage accumulation can happen in an electrochemical cell. Applying a small current in one direction may not lead to failure, but cycling (repeated cycles of charging and discharging) can form structural defects, such as cracks, slip bands, and voids. This fatigue-like process of damage accumulation depends on the materials that constitute the electrode. For example, failure of brittle oxide particles that are embedded in an electrode is described as quasi-brittle damage (*2*), whereas damage to a ductile metal electrode is proportional to the plastic (irreversible) strain energy per each electrochemical cycle (*3*).

It is difficult to examine the origin of cyclic stress in an electrode because of the way that solid-state electrochemical cells operate. The anode undergoes continuous volumetric changes as lithium strips away from the electrode during charging and then redeposits on the anode surface (plating) during discharging of the battery. This also causes changes in the pressure applied to the electrode, which dictates plastic deformation of the material. The stress state of the lithium layer primarily depends on its thickness. A thin layer experiences more hydrostatic pressure than a thick one because of volumetric constraint from friction with the solid electrolyte. This has been confirmed by observations of decreases in creep strain (time-dependent permanent deformation) and strain rate in the anode (*4*). Although static properties of lithium metal in connection with battery operation have been studied, the effect of cyclic current on the material has been largely neglected.

"...Wang *et al.* provide an important connection between electrochemical and mechanical fatigue..."

Wang *et al.* show that even at a cyclic current that is below one-tenth of the critical current density—the maximum current that a material can carry without damage—fatigue-like processes in a lithium metal anode cause degradation at the interface of the solid electrolyte, resulting in failure. The authors used empirical laws of fatigue to calculate the fatigue life of the electrode with respect to the applied current. Traditional models that are commonly used for mechanical fatigue are based on the relationship between the fatigue life of a material and the applied force. For example, the Coffin-Manson model relates the plastic strain caused by the number of cycles of mechanical loading and unloading to failure by using a simple power law under a controlled strain. By contrast, the Basquin law connects elastic (reversible) strain to the fatigue life in a similar power law relationship under a controlled applied stress. Wang *et al.* combined these two relationships to calculate the number of charging and discharging cycles that lead to failure (short circuit) under a specific cyclic current density.

Wang *et al.* established a fatigue-limited current that is analogous to the endurance limit in mechanical fatigue. This value reflects the magnitude of cyclic current under which the battery does not fail at a sufficiently large number of charge and discharge cycles. Although Wang *et al.* provide an important connection between electrochemical and mechanical fatigue, a direct application of the traditional multiaxial fatigue models to an electrochemical system is challenging because of the continuous variation in the volume (mass) of the electrode during the electrochemical cycling. The continuum mechanics theory is built on a fundamental principle that the plastic deformation responsible for fatigue damage is isochoric (having a constant volume). However, the cyclic plating and stripping of lithium violates this principle. Further improvements on the relationship between fatigue life and applied current density could be made by using a more advanced fatigue model. Additionally, mean stress—an equivalent value of static stress superimposed on the cyclic stress—can dictate the fatigue life of a material. The Morrow fatigue model includes a correction for the mean stress and would be useful for scenarios when external compressive force from the battery's internal components influences fatigue, particularly at longer cycling periods.

The work of Wang *et al.* recognizes the importance of fatigue in the performance of lithium metal anodes in solid-state batteries. The authors equate applied current density with the stress magnitude to obtain fatigue life. Further investigations should follow to describe the complex stress-strain state of lithium, including cycle rate, length scale, and temperature (*5*). The fatigue principles of Wang *et al.* could also extend to the failure of a cathode (positive electrode), in which ceramic-like oxide undergoes repeated (de)intercalation of lithium with varying degrees of strains driven by structural transformation (*6*). ■

[1]SLAC-Stanford Battery Center, Applied Energy Division, SLAC National Accelerator Laboratory, Menlo Park, CA, USA. [2]Materials Science and Engineering, Stanford University, Stanford, CA, USA. [3]Computational Sciences and Engineering Division, Oak Ridge National Laboratory, Oak Ridge, TN, USA. Email: jnanda@slac.stanford.edu; kalnauss@ornl.gov

REFERENCES AND NOTES

1. T. Wang *et al.*, *Science* **388**, 311 (2025).
2. S. Kalnaus, K. Rhodes, C. Daniel, *J. Power Sources* **196**, 8116 (2011).
3. A. Fatemi, N. Shamsaei, *Int. J. Fatigue* **33**, 948 (2011).
4. C. G. Haslam, J. B. Wolfenstine, J. Sakamoto, *J. Power Sources* **520**, 230831 (2022).
5. E. G. Herbert, N. J. Dudney, M. Rochow, V. Thole, S. A. Hackney, *J. Mater. Res.* **34**, 3593 (2019).
6. C. Xu *et al.*, *Nat. Mater.* **20**, 84 (2021).

10.1126/science.adw9437

BOOKS *et al.*

TECHNOLOGY

What we owe the present

A physicist issues an urgent call to deflate the world-shaping power of tech billionaires

More Everything Forever: AI Overlords, Space Empires, and Silicon Valley's Crusade to Control the Fate of Humanity
Adam Becker
Basic Books, 2025. 384 pp.

By **Àlex Gómez-Marín**

More Everything Forever—the title of astrophysicist Adam Becker's new book—is a perfect encapsulation of the sinister ideology that has come to possess the heart of Silicon Valley. Determined to control the future of our species, tech oligarchs posture to create a posthuman race. Even if they are bluffing, Becker argues that their ideas, as the book's publisher puts it, "pervert public discourse and distract us from real social problems." But only if we allow them to.

Becker articulates a timely and informed wake-up call: "If we don't want tech billionaires setting those terms, we need to understand their ideas about the future: their curious origins, their horrifying consequences, and their panoply of ethical gaps and scientific flaws." His vehement critique is fundamental to diminishing their power.

Becker provides the reader with much-needed literacy to navigate the dominant tenets professed by the tech elite. It is a mouthful of entangled isms: effective altruism, longtermism, transhumanism, rationalism, etc. This is what they entail.

Silicon Valley's obsession with future humans jeopardizes today's societies.

First, championed by the Scottish philosopher William MacAskill among others, we have effective altruism, a modern movement that seeks to optimize philanthropic efforts. When coupled with longtermism—a radical form of utilitarian ethics that prescribes current actions to maximize scenarios far in the future—morality turns into an optimization problem that easily goes off the rails. Hypothetical future humans—conjured ageless silicon minds traveling through empty space—matter more than the lives of real people here today, reinforcing the escalating accumulation of wealth and power by a selected club. Philanthropy (etymologically, mankind-loving) then becomes sweetened plutocracy and, ultimately, misanthropy.

Another peculiar crowd, the transhumanists, promise to redeem the world by means of a spooky hybrid of tech-fiction and technocracy. Apparently unconcerned with the reality that exponential growth ultimately saturates, they prophesy a practically inevitable (and morally imperative) utopia: the singularity. Very soon, soothsays the American inventor Ray Kurzweil, we will literally merge with our machines, whose computing power will be so colossal that what it means to be human will be transfigured or, perhaps, disfigured. Such an obsession to copy, paste, and edit the human condition is a pseudo-religion concealed under the rhetoric of techno-scientific progress.

Next, Becker addresses a movement that buys into the gospel of an inevitable singularity but fears dystopia on our way to utopia. If transhumanists shine in the gloom of *The Matrix*, rationalists inhabit the doom of *Terminator*. To avoid a "paperclip apocalypse"—a thought experiment by Swedish philosopher Nick Bostrom—rationalists are devoted to aligning artificial intelligence so that it is friendly to human interests. There is no middle ground here either: We go to tech-bro heaven, or we miserably die.

Silicon Valley's convoluted, implausible, and arguably immoral "solutions" to existential risks distract us from existing ones. Poor education, unsafe foods, political polarization, prospects of nuclear war, engineered pandemics, privacy invasion, the end of democracy, and so on, all look like minor disquietudes to this network of influential people, companies, institutes, and think tanks.

Uncovering this act of misdirection is one of Becker's major goals. I agree that we are facing a double-helix of dangerous bullshit. Becker emphasizes the triple core of such faulty ideas: systematic "reduction" of any problem to a technological one, humongous "profit" afforded by the gospel of growth, and misplaced "transcendence" encouraging the disregard of all limits and limitations, including death.

Powerful, intelligent, rich people with poor ideas can be terribly dangerous indeed. That is why this is a serious issue rather than a "quirky tour of wacky ideas." We must rightfully protest: Who has appointed these deranged individuals to be the stewards of mankind?

Toward the end of the book, Becker suggests that the solution lies in "eliminating billionaires" as "an investment in the political stability that makes prosperity possible." His diagnosis seems far deeper than his prognosis. Perhaps reluctant to dive into anthropological, metaphysical, and even spiritual waters, the best he can offer is a sensible but ultimately facile critique of wild capitalism as the root of all evil.

At the end of the day, rather than "more everything forever," the world could do with a little bit more kindness here and now. This is what we owe the present: fewer prophets and more poets, fewer technocrats and more dancers, less Silicon Valley and more Monty Python. Riffing on a fabled slogan, it is time to make humanity humane again, so that the values that guide our actions sing a love letter to our granddaughters. ■

The reviewer is at the Instituto de Neurociencias, Consejo Superior de Investigaciones Científicas–Universidad Miguel Hernández de Elche, Alicante, Spain.
Email: agomezmarin@gmail.com

10.1126/science.adu3202

ILLUSTRATION: NASA/AMES RESEARCH CENTER/RICK GUIDICE

A child interacts with a sensory-stimulating lamp during a therapy session.

PHOTO: ANDREA OBZEROVA/ALAMY STOCK PHOTO

NEUROSCIENCE

Widening the autism spotlight

Underrepresentation of girls and women in studies warps our understanding of the condition, argues a neuroscientist

By **Meng-Chuan Lai**

What is it like to be an autistic girl or woman? In *Off the Spectrum*, Gina Rippon tackles this question, weaving together a compelling critical history of autism's conceptual evolution with a crash course in social and developmental neuroscience. A neuroscientist renowned for challenging sex and gender stereotypes about the brain, Rippon incisively dissects the origins and "self-fulfilling prophecy" of long-standing male biases about autism and synthesizes the story of the contemporary rediscovery of how autism presents in females with analysis of the social conditioning that often renders autistic girls and women invisible in the "male spotlight."

In 1925 to 1927, readers learn, Soviet psychiatrist Grunya Efimovna Sukhareva documented detailed observations of six boys and five girls, noting their shared traits—aligning with what we now conceptualize as autism—as well as their differences. Her research, particularly on girls, was largely overlooked in the West. Instead, the "discovery" of autism has long been attributed to Leo Kanner and Hans Asperger, on the basis of their respective reports on mostly male individuals in 1943 and 1944.

Off the Spectrum: Why the Science of Autism Has Failed Women and Girls
Gina Rippon
Seal Press, 2025. 352 pp.

The near omission of autistic girls created cycles of biases in the conceptualization, assessment, recognition, and understanding of autism, argues Rippon. She outlines the harmful downstream effects of this underrepresentation and illustrates how including autistic girls and women in contemporary studies and understanding the ways they camouflage autistic presentations can offer valuable insight into how "a biological script play[s] out on a social stage."

Rippon masterfully weaves the life stories of autistic girls and women together with historical critique and neuroscientific insights. She boldly argues that both the "Kanner group," those traditionally seen as unmistakably autistic, and the "Chameleons" (*1*), those who mask their traits and whose autism remains debated in the public's eyes, are part of the same spectrum.

Building on psychiatrist Lorna Wing's taxonomy of different social motivation and coping styles in autistic people (*2*), Rippon's depiction of Chameleons can be seen as autistic individuals who seem like "loners" but actually long to belong. Notably, while the term "female autism" appears throughout the book, Rippon rightly cautions against the trap of sex essentialism. The nuanced experience of being a Chameleon among autistic girls and women can also be shared by autistic boys, men, and gender-diverse people.

Skeptics with a more orthodox view of autism may consider Chameleons not as autistic but instead as individuals who incorrectly identify with the autistic label as a result of social contagion, but this perspective overlooks a core principle of identity—people recognize each other as part of the same tribe precisely because they share fundamentally similar biological and social traits.

Clinicians have, understandably, sought to define autism reliably on the basis of measurable, observable behaviors. But Rippon encourages readers to question whether this obsessive conviction that "seeing is believing" is truly rational, scientific, and equitable. To this end, *Off the Spectrum* not only addresses Rippon's central question—"What is it like to be autistic?"—but also delves into the fundamental inquiry: "What is autism?" Her answer reveals an unsettling reality: Both the overwhelming underrepresentation of female individuals in autism research and the incomplete understanding of autism neuroscience stem from how easily minorities are overlooked, misunderstood, and assumed to be the same as the majority.

This is not a new problem in scientific research. A similar pattern has played out, for example, in the male-centric field of pain biology for decades (*3*). Fortunately, through open science, collaboration, and dedicated efforts, research is now better equipped to identify sex-dependent brain features of autism (*4, 5*) and explore how autistic brain development intersects with sex differentiation and gender socialization (*6*). The insights learned so far, however, are largely drawn from brain scans of the same autistic females who have generously participated in research over the past two decades. And most of these individuals, who number less than 300, are white and from high-income countries. We have a long way to go toward properly understanding "what it is like to be autistic" across diverse global contexts.

With intellectual rigor, deep empathy, and a masterful balance of science and storytelling, *Off the Spectrum* reveals Rippon as a humble scientist, compassionate humanist, and effective knowledge translator. Far from being a "sex differences denier," as critics have called her, she meticulously attends to sex and gender nuances in this book, challenging stereotypes, exposing oversights, and illuminating individual differences and the life stories of autism's lost people. ■

The reviewer is at the Department of Psychiatry, Temerty Faculty of Medicine, University of Toronto, Toronto, Ontario, Canada. Email: mengchuan.lai@utoronto.ca

REFERENCES AND NOTES

1. B. Cook, "The Chameleons: Women with Autism," posted 5 May 2015 by SBS The Feed, YouTube; https://youtu.be/VJHa9xk16Hw?si=iiBTFau0LxZWB2N5.
2. L. Wing, *Lancet* **350**, 1761 (1997).
3. A. N. Plumb *et al.*, *Pain* **164**, 1775 (2023).
4. S. A. Bedford *et al.*, *Biol. Psychiatry* **97**, 517 (2025).
5. D. S. Andrews *et al.*, *Mol. Psychiatry* **29**, 3440 (2024).
6. D. L. Floris et al., Am. J. Psychiatry 180, 50 (2023).

10.1126/science.adw7642

Seawater intrusion has become more frequent and extreme in China's coastal cities, including Yantai.

PHOTO: NUR PHOTO/GETTY IMAGES

Edited by **Jennifer Sills**

Prevent coastal seawater intrusion in China

From October to November 2024, multiple coastal cities in China experienced a historic, large-scale seawater intrusion, during which an abnormal and extreme rise in tide water took place for an extended period of time (*1*). Seawater poured into houses, farmland, and aquaculture ponds, increasing the salinity of freshwater resources and resulting in heavy losses to China's coastal communities and aquaculture farmers (*2*). If China does not take preventive measures, the losses caused by seawater intrusions will increase.

China has about 143,900 km^2 of coastal areas with an altitude of 5 m or below that are at risk of storm surges and seawater intrusion (*3*). These areas have a combined population of more than 70 million people, accounting for about 27% of the total population worldwide that is at risk of such disasters (*3*). Seawater intrusion and associated tidal flooding can cause long-term damage to agricultural production, underground freshwater resources, coastal wetlands, and human health (*1*, *4*).

From 1980 to 2023, the rate of sea level rise along China's coast accelerated to 4.0 mm per year—higher than the global average of 3.4 mm per year over the same period (*5*). This trend may increase the frequency of seawater intrusion in the future (*2*). China urgently needs to enact policies that anticipate these changes.

Since 2016, China has taken steps to mitigate damage from marine disasters by protecting and restoring coastal ecosystems (*6*–*8*), but these efforts have not taken into account the effect of climate change. In addition, in 2017, China launched the National Seawall Construction Plan, which aims to build new seawalls and reinforce existing structures (*9*), but even China's new seawalls will be unlikely to effectively withstand extreme flooding. Most seawalls are constructed for present-day flood and tide control management rather than for future extremes resulting from sea level rises (*10*). Outdated construction specifications, including seawall width and slope protection, remain in use (*9*). The seawalls also weaken ecological services by separating land and sea ecosystems instead of incorporating vegetation and spaces that enhance ecosystem functions (*11*). Because they are inadequately maintained, many older seawalls suffer from settlement, leakage, and damage to sluice gates, which puts nearby communities, especially in rural areas, at increased risk (*9*, *10*).

To prepare for warming temperatures and rising sea levels, China should comprehensively identify potential seawater intrusion areas and conduct more-refined seawater intrusion risk assessment and spatial zoning for coastal communities. Additionally, the government should use high-precision topographic data to update the construction specifications for coastal city seawalls on the basis of simulation data of seawater intrusion and then reevaluate and reinforce traditional seawall infrastructure accordingly. Finally, to raise awareness about the risks of seawater intrusion, China should conduct public education campaigns.

Chao Liu[1], Ping Li[2], Dahai Liu[3]*
[1]Key Laboratory of Coastal Science and Integrated Management, First Institute of Oceanography, Ministry of Natural Resources, Qingdao, China. [2]Institute of Marine Development of Ocean University of China, Qingdao, China. [3]School of Public Administration and Policy, Renmin University of China, Beijing, China.
*Corresponding author. Email: dahai@ruc.edu.cn

REFERENCES AND NOTES

1. "China Focus: Seawater intrusion incurs waterlogging on China's northern coasts," *Xinhua* (2024); https://english.news.cn/20241022/ed228957dfa546a6876a8ff650a56804/c.html.
2. J. Jing, "More frequent seawater intrusions are causing alarm in coastal regions," *Beijing Review* (2024); https://english.chinatoday.com.cn/China/202412/t20241209_800386549.html.
3. D. K. Chen *et al.*, *Adv. Earth Sci.* **28**, 10 (2013) [in Chinese].
4. R. J. Nicholls, A. Cazenave, *Science* **328**, 1517 (2010).
5. National Climate Centre, *Blue Book on Climate Change of China 2024* (Science Press, 2024) [in Chinese].
6. National Development and Reform Commission and National Forestry and Grassland Administration, "National Project Plan for the Construction of Coastal Sheltering Forest System (2016–2025)" [in Chinese] (2017); https://www.gov.cn/xinwen/2017-05/16/5194348/files/8cfb540b5ff744518f1f05abdd201bdd.pdf.
7. National Development and Reform Commission and Ministry of Natural Resources, "National Plan for Major Conservation and Restoration Projects of Important Ecosystems (2021-2035)" (2020); https://www.ndrc.gov.cn/xxgk/zcfb/tz/202006/P020200611354032680531.pdf [in Chinese].
8. National Marine Hazard Mitigation Service, "Four handbooks on ecosystem restoration for coastal hazard mitigation, focusing on salt marshes, seagrass beds, oyster reefs, and sandy coasts" [in Chinese] (2024); https://www.nmhms.org.cn/details/F3VH9K_KD.html.
9. National Development and Reform Commission and Ministry of Water Resources, "National Sea Wall Construction Plan" [in Chinese] (2017); https://www.gov.cn/xinwen/2017-08/21/5219341/files/ca80da2e-6b404a788a6c0f47ccc8ca8e.pdf.
10. Y. Li, "Rising Seas Threaten China's Long, Low, and Crowded Coast," *Sixth Tone* (2020); https://www.sixthtone.com/news/1006652.
11. Z. Ma *et al.*, *Science* **346**, 912 (2014).

10.1126/science.adv5677

Disposal of anesthetics threatens ecosystems

To prevent the abuse of anesthetic drugs, such as fentanyl and propofol, hospitals dispose of unused anesthetics. In countries such as the United Arab Emirates, Japan,

and China, some hospitals abide by local policies by dumping these unused anesthetics into sewers (*1*–*3*). This disposal method contravenes environmental principles and threatens public health. These countries should implement policies to require and regulate the safe disposal of anesthetics by hospitals.

Wastewater treatment systems cannot eliminate anesthetics (*4*), and their presence in the water supply could cause harm. Even at low concentrations, fentanyl-like drugs may exert toxic effects on fish and other aquatic organisms (*5*, *6*). Pharmaceutical substances may enter the human body through the food chain (*7*). Water contamination by anesthetics also affects the accuracy of illicit drug monitoring in wastewater (*8*, *9*), thereby interfering with public safety management.

Safer, eco-friendly disposal methods for anesthetics are essential. Some countries use strategies that better protect the environment, although each is associated with trade-offs. In Australia, the law requires hospital staff to seal anesthetics in vials and place them in sharps containers for disposal. This strategy carries the risk of recovery of the substances for illegal use (*10*). In the United States, anesthetic disposal methods include incineration or the use of agents that solidify liquids. These processes prevent illegal use of drugs, but they are costly (*11*).

To prevent anesthetics from entering aquatic ecosystems, legislation should prohibit their direct discharge into sewer systems, ensure environmental supervision of hospital activities, and require regular monitoring of drug concentrations in hospital wastewater. Countries worldwide should promote safe, green, accessible, and affordable disposal technology, such as molecular adsorption containers (*12*), to prevent anesthetic drug retrieval. Government subsidies can ease the associated financial load on medical facilities. Finally, health authorities should ensure that all health care providers receive environmental education that promotes responsible drug disposal.

Xin Liu[1], Ruolin Hou[1]*, Chengyi Liu[2], Wei Shen[1], Kezhen Wang[3], Changzhen Zhang[4]
[1]The Third People's Hospital Health Care Group of Cixi, Ningbo, China. [2]Jiangxi University of Chinese Medicine, Nanchang, China. [3]Xianju People's Hospital, Taizhou, China. [4]Ningbo No. 2 Hospital, Ningbo, China.
*Corresponding author.
Email: ruolinhou93@163.com

REFERENCES AND NOTES

1. Tokyo Metropolitan Government Bureau of Public Health, "Guidelines for the Proper Disposal of Medical Narcotics" [in Japanese] (2022); https://www.hokeniryo.metro.tokyo.lg.jp/documents/d/hokeniryo/r04haikihouhou.
2. Dubai Health City Authority, "Narcotic, Controlled & Semi-controlled Medications Management" (2023); https://dhcc.ae/gallery/NarcoticControlledandSemi-controlledMedicationsManagement.pdf.
3. Health Commission of Hubei Province, "Regulations for the Management of Anesthetic Drugs and Schedule I Psychotropic Substances in Hubei Province Medical Institutions" [in Chinese] (2021); https://wjw.hubei.gov.cn/zfxxgk/zc/gfwj/202109/t20210901_3733168.shtml.
4. L. Chen, C. Guo, Z. Sun, J. Xu, *Environ. Res.* **200**, 111362 (2021).
5. H. Falfushynska *et al.*, *Pharmaceuticals* **17**, 537 (2024).
6. B. Wang *et al.*, *PeerJ* **10**, e14524 (2022).
7. A. Kock *et al.*, *Sci. Total Environ.* **878**, 162939 (2023).
8. M. Kostrubiak *et al.*, *J. Med. Syst.* **44**, 169 (2020).
9. E. Zuccato *et al.*, *Environ. Health Perspect.* **116**, 1027 (2008).
10. New South Wales Ministry of Health, "Medication Handling in NSW Public Health Facilities" (2022); https://www.health.nsw.gov.au/pharmaceutical/Pages/medication-handling-pubhealth.aspx.
11. D. Gordon, S. M. McGarry, *ASA Monitor* **82**, 18 (2018).
12. S. Chauhan, T. Shafi, B. K. Dubey, S. Chowdhury, *Waste Dispos. Sustain. Energy* **5**, 37 (2023).

10.1126/science.adv3820

Overcoming roadblocks to a global plastic pact

In December 2024, the global community expected the parties at the fifth Intergovernmental Negotiating Committee (INC-5) meeting in Busan, South Korea, to produce a landmark treaty to address the planet's plastic pollution crisis. The event was intended to be the final opportunity for more than 170 United Nations (UN) member states to craft an ambitious pact (*1*). However, after week-long heated discussions, negotiators failed to develop a consensus. Before the next meeting, scheduled for August 2025 in Geneva, Switzerland, the negotiating parties should work to understand and overcome the factors that stalled the talks (*2*).

Deep division among member states obstructed consensus. Fossil fuel exporters such as Russia, Iran, and Saudi Arabia formed a coalition to push for a treaty centered solely on waste management (*3*) and opposed production constraints. Norway and Rwanda cochaired a coalition that relentlessly supported a globally binding accord that could cap production. Escalating geopolitical tensions and involvement of petrochemical-producing nations such as the United States, Russia, Iran, and other Middle East countries in conflicts may further split the parties apart, jeopardizing the chances of achieving consensus.

An unjust representation of the key stakeholders further stalled progress toward consensus. Petrochemical lobbyists overshadowed other crucial voices, including scientists. Their dominance and privileged access to private events raised concerns about transparency (*4*). Some national delegations included lobbyists despite serious reservations from other stakeholders, undermining trust in the negotiations.

The absence of strong leadership also stymied the negotiations. Countries such as the United States and China did not push for meaningful progress on production caps (*5*), allowing fossil fuel producers and lobbyists to dominate the process. The United States has historically been a major force behind environmental regulations (*6*). China, an emerging leader that has started striving for stringent environmental protection policies domestically, exercised less influence than expected (*5*).

The failure to forge consensus at this pivotal moment is a costly setback that exacerbates the plastic crisis (*7*), but the upcoming meeting, dubbed INC-5.2, has sparked renewed hopes of success. Given that the Trump administration is unlikely to lead on this issue (*8*, *9*), progress hinges on the extent to which the European Union (EU) and countries such as China embrace their leadership responsibilities. China, EU, and other countries with economic power can steer negotiations under the UN's umbrella by setting strict standards for eliminating domestic and global plastic pollution while fostering innovative research, multilateral collaborations, and financial support. With support from the "Coalition of the Willing," an ambitious and determined alliance of more than 100 nations (*10*) that formed at the INC-5.1, these leaders can use their diplomatic reach to take a decisive role in resolving conflicts, to help develop consensus on contentious issues such as production caps and chemicals of concern, and to curb the undue sway of industrial lobbyists.

Farooq Shah[1,2] and Wei Wu[1]*
[1]School of Breeding and Multiplication (Sanya Institute of Breeding and Multiplication), Hainan University, Sanya, China. [2]Department of Agronomy, Abdul Wali Khan University, Mardan, Khyber Pakhtunkhwa, Pakistan.
*Corresponding author.
Email: weiwu@hainanu.edu.cn

REFERENCES AND NOTES

1. UN, "UNEP/Closing of INC-5 In Busan Korea" (2024); https://media.un.org/unifeed/en/asset/d331/d3316357.
2. UN Environment Programme, "Second Part of the Fifth Session (INC-5.2)" (2025); https://www.unep.org/inc-plastic-pollution/session-5.2.
3. *Nature* **628**, 474 (2024).
4. Center for International Environmental Law, "Fossil fuel lobbyists flood final scheduled round of global plastics treaty negotiations" (2024); https://www.ciel.org/news/inc-5-lobbyist-analysis.
5. L. R. Gonçalves *et al.*, *Camb. Prisms Plast.* **2**, e26 (2024).
6. R. D. Kelemen, T. Knievel, *Int. J. Const. Law* **13**, 945 (2015).
7. A. S. Pottinger *et al.*, *Science* **386**, 1168 (2024).
8. N. Jones *et al.*, *Nature* **637**, 532 (2025).
9. J. Tollefson, *Nature* **546**, 198 (2017).
10. T. Farrelly *et al.*, *Camb. Prisms Plast.* **3**, e6 (2025).

10.1126/science.adv0976

CALL FOR PAPERS

SPJ
SCIENCE PARTNER JOURNALS

emdria
EMDR International Association

Journal of EMDR Practice and Research

The *Journal of EMDR Practice and Research* is a peer-reviewed journal that publishes articles on all aspects of EMDR therapy and Adaptive Information Processing (AIP) theory. It's an online-only, Open Access journal published in affiliation with the EMDR International Association (EMDRIA) and distributed by the American Association for the Advancement of Science (AAAS).

Topics of particular interest include, but are not limited to: empirical research evidence based on EMDR therapy and the AIP model, mechanisms of action and dismantling studies, early EMDR interventions, and EMDR therapy in the framework of psychotherapy integration.

Submit your manuscripts to *Journal of EMDR Research* today!

Learn more: **spj.science.org/jemdr**

The Science Partner Journals (SPJ) program was established by the American Association for the Advancement of Science (AAAS), the non-profit publisher of the Science family of journals. The SPJ program features high-quality, online-only, Open-Access publications produced in collaboration with international research institutions, foundations, funders, and societies. Through these collaborations, AAAS furthers its mission to communicate science broadly and for the benefit of all people by providing top-tier international research organizations with the technology, visibility, and publishing expertise that AAAS is uniquely positioned to offer as the world's largest general science membership society. Visit us at **spj.science.org**

@SPJournals **@SPJournals** **@SPJournals**

OPEN ACCESS

ARTICLE PROCESSING FEES WAIVED THROUGH DECEMBER 2026

SCIENCE SHAPING TOMORROW

AAAS ANNUAL MEETING
Boston, MA | February 13–15, 2025

2025 AAAS Annual Meeting Posters

PRESENTED BY Georgia Tech · Ivan Allen College of Liberal Arts School of Public Policy

2025 AAAS Student E-poster Competition Winners

The AAAS Student E-poster competition recognizes the individual efforts of students actively working toward an undergraduate, graduate or doctoral-level degree. The winners' presentations displayed originality and understanding, setting them apart from their peers. Eligible students can apply to present at the 2026 E-poster Competition starting late Spring 2025.

BIOCHEMISTRY AND MOLECULAR BIOLOGY

Graduate Student First Place: **Pascal Kunz,** Harvard University, *Development of Monoclonal Antibodies Targeting Blood Group Antigens*

Graduate Student Honorable Mention: **Deng Li,** Northeastern University, *Computational Investigation of The Role of Water Models in Protein-Glycan Dynamics*

Undergraduate Student First Place: **Madeline Bono,** Temple University, *STAT2 Promotes Colorectal Cancer Independently of Type I IFN Receptor Signaling*

Undergraduate Student Honorable Mention: **Julia Vazquez,** University of California, San Diego, *Thermostable Marine Protease Globupain with Potential for Biotechnology Application*

BRAIN AND BEHAVIOR

Graduate Student First Place: **Aleksei Krotov,** Northeastern University, *Control and Embodiment of Complex Tools: Hitting a Target with a Bullwhip*

Graduate Student Honorable Mention: **Bryce Axe,** Northeastern University, *Developmental Impacts of Adolescent LSD and Psilocybin Exposure on Brain Function*

Undergraduate Student First Place: **Devon Borg,** University of Florida, *Parkinson's Paradox: A-Syn's Selective Strike on SNc Dopamine Neurons Over VTA*

Undergraduate Student Honorable Mention: **Majed Al Shaheen,** Kuwait University, *Estrous Cycle Patterns in an Alzheimer's Disease Model: Implications for Cognition*

CELL BIOLOGY

Graduate Student First Place: **Miles Arnett,** University of Pennsylvania, *Epigenetic Reprogramming Exploits an Acquired Vulnerability in Drug-Resistant Cancer*

Graduate Student Honorable Mention: **Layla Alnoumas,** Strathclyde University, *Understanding the Metabolic Response of Breast Cancer Cells to Olaparib*

Undergraduate Student First Place: **Finn Creeggan,** McGill University, *Decoding The Multiomic Reactive Ependymal Cell Landscape In Multiple Sclerosis*

Undergraduate Student Honorable Mention: **Akaash Surendra,** Arizona State University, *Assessing Effects of CDK4/6i on Glioblastoma Cell State Markers and Cell Viability*

DEVELOPMENTAL BIOLOGY GENETICS AND IMMUNOLOGY

Graduate Student First Place: **Nika Mehrnia,** Harvard University, *Enhanced Alveolar Bone Regeneration with SPM Releasing Graft Using 3D-Printing Technology*

Graduate Student Honorable Mention: **Jakub Baczyński-Keller,** Gdansk University of Technology, *Deep Dive into Macrophages' Role in Regenerative Response to Zebrafish Spine Injury*

Undergraduate Student First Place: **Ben Sheirbon,** Seattle Pacific University, *Treating Gammaherpesvirus Infections With Nucleotide Metabolism Inhibitors*

Undergraduate Student Honorable Mention: **Maren Ritterbuck,** Northeastern University, *Characterizing The Functional Role Of Trpv4 Ion Channel In Axoltl Limb Regeneration*

ENVIRONMENT AND ECOLOGY

Graduate Student First Place: **Emerson Conrad-Rooney,** Boston University, *Effects of Growing Season Warming and Winter Freeze/Thaw Cycles on Tree Growth*

Graduate Student Honorable Mention: **Madison McMinn,** Northeastern University, *In-depth Chemical Profiling of Tire and Artificial Turf Crumb Rubber*

Undergraduate Student First Place: **Michael Skibsted,** University of Georgia, *Fewer Native Turtles in Areas with More People*

Undergraduate Student Honorable Mention: **Davis Huber,** University of Georgia, *25 Years of Climate Change Threaten to Shrink Georgia's Barrier Islands and Marshes*

MEDICINE AND PUBLIC HEALTH

Graduate Student First Place: **Alexis Wilkinson,** Rice University, *Extraction-Free Sample Preparation for LAMP-Based HPV Testing at the Point-of-Care*

Graduate Student Honorable Mention: **Leonora Blodgett,** Northeastern University, *Movement as a Vital Sign for Predicting Health and Development in Preterm Infants*

Undergraduate Student First Place: **Ruth Berkun,** Caltech University, *Quantitative Reflex Tests Using a Novel Acoustic-Based Sensing System*

Undergraduate Student Honorable Mention: **Tiffany Ho,** Berkeley University, *Quantitative Analyses of Metals and Lithogenicity of Human Urine*

PHYSICAL SCIENCES

Graduate Student First Place: **Pranamita Chakraborti,** University of North Carolina at Charlotte, *Mechanistic Basis of the Voltage Sensitivity of Thiazolothiazole Dyes*

Graduate Student Honorable Mention: **Joydeep Naskar,** Northeastern University, *Towards a Complete Classification of Holographic Entropy Inequalities*

Undergraduate Student First Place: **Maritza Sanchez,** CT State Community College - Gateway, *Palladium-catalyzed Carbonylation of an Acyclic Methylene-Bridged-Arene Trimer*

Undergraduate Student Honorable Mention: **Simon Zhang,** University of California, San Diego, *Functionalized Indigo as Annihilators for Triplet-Triplet Annihilation Upconversion*

SCIENCE IN SOCIETY

Graduate Student First Place: **Tasneem Mohammed,** Arizona State University, *The Impact of Aspects of Academia on Science Faculty Depression*

Graduate Student Honorable Mention: **Denissa Sari Darmawi Purba,** University of Illinois Urbana-Champaign, *Vulnerability Assessment of Electric Vehicles and Charging Stations in Evacuations*

Undergraduate Student First Place: **Aubrey Pinteric,** Arizona State University, *Uterine Technologies: Social Implications from Past to Future*

Undergraduate Student Honorable Mention: **Emily Foreman,** San Jose State University, *Assessing Physicists' Influence on New Nuclear Weapons Policies*

SOCIAL SCIENCES

Graduate Student First Place: **Celestial Jynx Pigart,** Arizona State University, *Depression Over Time in Science Graduate Programs*

Graduate Student Honorable Mention: **Katie Coscia,** Middle Tennessee State University, *Training Undergraduates How to Talk About Controversial Topics With Others*

Undergraduate Student First Place: **Isaac Zaragoza-Oldendorff,** Tecnologico de Monterrey, *Food Insecurity in Mexico: Food is a Right, Not a Privilege*

Undergraduate Student Honorable Mention: **Dongim Lee,** Franklin W. Olin College of Engineering, *Linguistic Bias in Automatic Speech Recognition for People Who Stutter*

TECHNOLOGY, ENGINEERING AND MATH

Graduate Student First Place: **Anoop Kiran,** Brown University, *Mutual Aerodynamic Interactions between Aerial Robots in Close Proximity*

Graduate Student Honorable Mention: **Tanner Honnef,** Clark University, *The Total Operating Characteristic Requires Updates to Its Use and Software*

Undergraduate Student First Place: **Madeline Szoo,** *Vascularized Patient Model of Diffuse Intrinsic Pontine Glioma To Study Drug Delivery*

Undergraduate Student Honorable Mention: **Grace Jansen,** Northeastern University, *In-Situ Observation of Mn3O4 Formation in Alkaline MnO2 Electrodes*

Photo Credit:
Robb Cohen Photography and Video

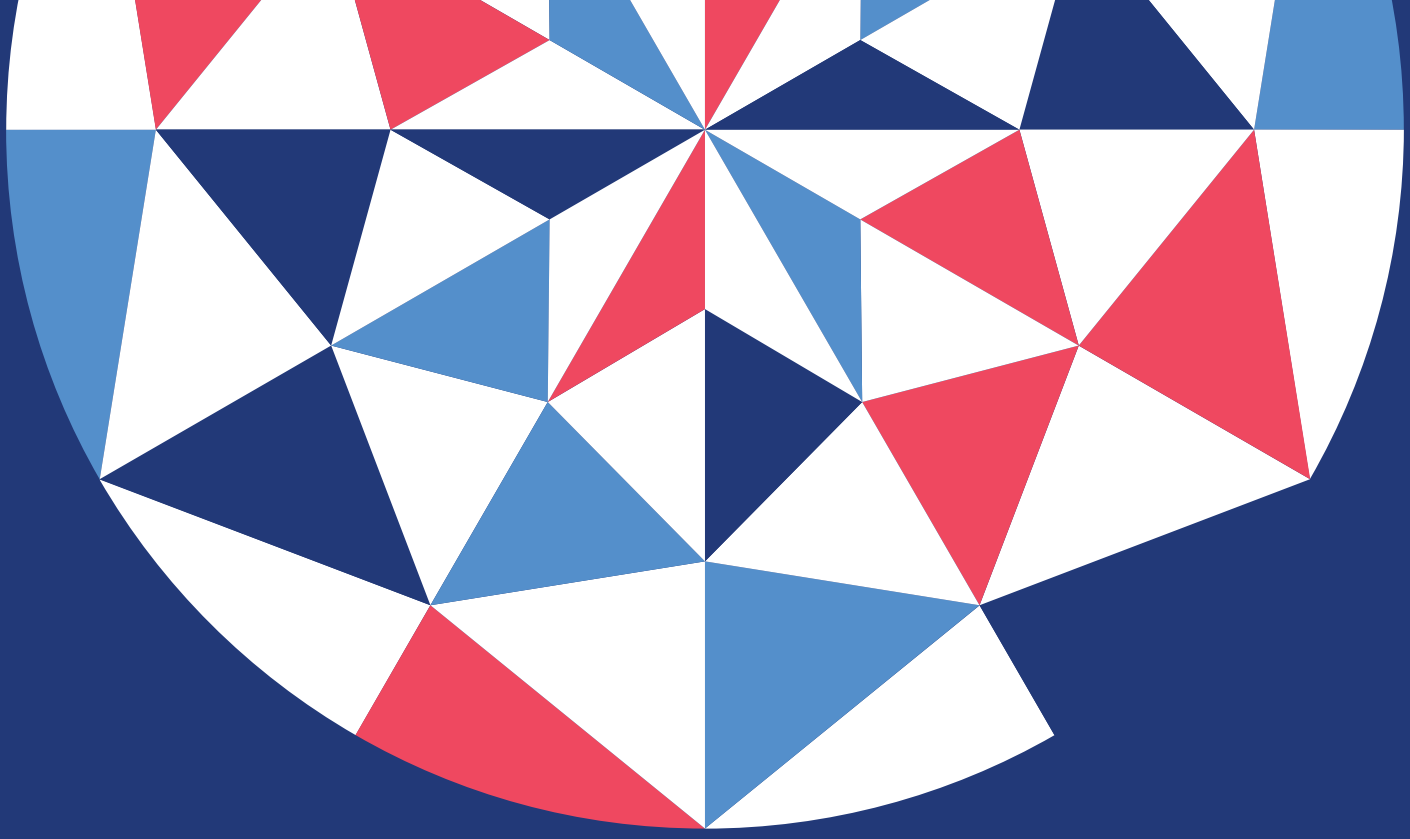

SCIENCE @ SCALE

AAAS | **ANNUAL MEETING**
Phoenix, AZ | February 12–14, 2026

Present your groundbreaking research, lead engaging workshops, and connect with a diverse community of experts.
Be a part of the 2026 AAAS Annual Meeting!

Propose a session or workshop by Tuesday, May 6, 2025
Visit aaas.org/meetings for more information.

RESEARCH

IN *SCIENCE* JOURNALS

Edited by **Michael Funk**

PHOTO: PAL SZILAGYI PALKO/ALAMY STOCK PHOTO

ENVIRONMENTAL SCIENCE

Mapping metals

Metals and metalloids are ubiquitous in soils, originating from bedrock and from human activities and infrastructure. These compounds can be toxic to humans and other organisms, and their soil distribution and concentrations at global scale are not well known. Hou *et al*. analyzed data from more than 1000 regional studies to identify areas of metal toxicity and explore drivers of these trends. They estimate that 14 to 17% of cropland exceeds agricultural thresholds for at least one toxic metal. Climate and topography, along with mining activity and irrigation, predicted which soils would exceed metal thresholds. Soil metal pollution is a global issue that will likely increase with the growing demand for toxic metals in new technologies. —Bianca Lopez *Science* p. 316, 10.1126/science.adr5214

Historic and current human activities, such as copper mining near this tailing pond in Romania, pose serious threats to soil health globally.

ORGANIC CHEMISTRY

A cone to make chiral amines

Forging carbon-nitrogen bonds in just one of two mirror image orientations is essential to the preparation of numerous pharmaceuticals and agrochemicals. Many catalysts have been developed for this purpose, but they usually rely on specific binding sites on the substrate to dictate the reaction choreography. Zhang *et al*. report the theory-guided design of an enveloping cone-shaped ligand for copper-catalyzed carbon-nitrogen bond formation with alkyl iodides that lack well-differentiated binding sites. The reaction produces a wide range of chiral amines with high selectivity. —Jake S. Yeston

Science p. 283, 10.1126/science.adu3996

BATTERIES

Observing mechanical fatigue during cycling

Lithium dendrite formation and porosity effects caused by high current density are known reasons for the failure of lithium metal batteries. However, there is an open question of why failure can occur at a current density much lower than the critical current density upon cycling. Wang *et al*. propose that mechanical fatigue of the lithium metal is the primary cause of cycle degradation (see the Perspective by Nanda and Kalnaus). Using in operando scanning electron microscopy, they showed that reversible plating and stripping of lithium generates cyclic stresses, even at low current densities, and these stresses lead to defects, microcracks, and microvoids that cause interface degradation. In conjunction with simulation, the authors showed that they could determine the cycle life of solid-state batteries as a function of current density. —Marc S. Lavine

Science p. 311, 10.1126/science.adq6807; see also p. 255, 101126/science.adw9437

2D MATERIALS

Dragging along

A pair of two-dimensional (2D) systems, one featuring electron carriers and the other featuring hole carriers, separated by a thin insulating layer can host correlated interlayer excitons. Such excitons are predicted to exhibit superfluidity, as well as the so-called perfect Coulomb drag, in which the current in one layer causes an equal but opposite current in the other layer. Two studies have now observed nearly perfect drag at low temperatures in heterostructures consisting of molybdenum

diselenide and tungsten diselenide layers separated by hexagonal boron nitride. Nguyen *et al*. used transport measurements, whereas Qi *et al*. relied on an optical technique. The studies enable further exploration of exciton transport in such heterostructures, including searching for superfluidity. —Jelena Stajic

Science p. 274, 10.1126/science.adl1829; p. 278, 10.1126/science.adl1839

STRUCTURAL BIOLOGY

PINK1 at the mitochondrial membrane

Damaged mitochondria must be recycled and replaced to maintain proper cell function. The ubiquitin kinase PINK1 plays a key role in this process by detecting depolarized mitochondria and starting a signaling pathway that marks these organelles for autophagy. Callegari *et al*. determined the structure of PINK1 in complex with the translocase of the outer membrane complex, which imports proteins, including PINK1, into the mitochondria, and a pair of voltage-dependent anion channels. This structure revealed how stalling of PINK1 during import and oxidation of surface cysteine residues establishes a dimeric preactive complex that is prepared to initiate downstream signaling. —Michael A. Funk

Science p. 303, 10.1126/science.adu6445

NEUROSCIENCE

Translation at the junction

The development of neuromuscular junctions involves the selective pruning of muscle fiber–innervating axons such that only one axon innervates each muscle fiber. Van der Hoorn *et al*. monitored translation, the process of active protein synthesis from messenger RNAs, in motor neurons in early postnatal mice and characterized the "translatome" that emerges and changes during synaptic pruning. The results highlight the role of neural metabolism and posttranscriptional regulation in muscle innervation and provide a foundation for understanding the physiology and pathophysiology of neuromuscular disease. —Leslie K. Ferrarelli

Sci. Signal. (2025) 10.1126/scisignal.adr0176

ALLERGY

"Mann"-aging allergy

Allergen immunotherapy given subcutaneously or sublingually has demonstrated potential for controlling allergic reactions, but real-world results are mixed. An attractive approach is to target allergens to the immune-tolerant environment of the liver. Gómez Medellín *et al*. developed a liver-targeted immunotherapy using mannosylated allergens, which reduce the risk of anaphylaxis. A model immunotherapy elicited antigen-specific regulatory T cells in vivo and controlled airway reactivity after antigen challenge in mice. An engineered immunotherapy against a house dust mite allergen showed similar benefits. —Courtney Malo

Sci. Transl. Med. (2025) 10.1126/scitranslmed.adl0406

MARS GEOLOGY

Curiosity finds carbonates in Gale crater

The Curiosity rover is gradually climbing a mountain located in Gale crater on Mars. Higher levels of the stratigraphy expose rocks that formed at later times. Tutolo *et al*. studied the composition of drill samples taken from a sulfate-rich layer (see the Perspective by Bishop and Lane). They found that the rocks contained abundant iron carbonate, which was invisible in previous orbital observations. If there are similar abundances of carbonate in other sulfate-rich layers across Mars, then those layers may contain a substantial reservoir of carbon dioxide extracted from the atmosphere. The carbonates found by the authors have partially decomposed, returning some carbon dioxide to the atmosphere: an ancient carbon cycle. —Keith T. Smith

Science p. 292, 10.1126/science.ado9966; see also p. 251, 10.1126/science.adw4889

IN OTHER JOURNALS

Edited by **Corinne Simonti** *and* **Jesse Smith**

STELLAR ASTROPHYSICS

Activity statistics of RCB stars

R Coronae Borealis–type variable stars (RCB stars) are a rare class of hydrogen-poor and carbon-rich supergiant stars. They undergo unpredictable dimming events known as declines, in which the stellar brightness abruptly drops by more than 95%, then gradually recovers over the following months or years. Declines are thought to be due to the sudden formation of carbon-rich dust in the RCB star's atmosphere. Crawford *et al.* performed a statistical study of declines in 162 RCB stars, finding that cooler stars generally have more frequent declines than warmer ones. For most of their targets, the timing of declines was stochastic, which they attributed to convection in the stellar atmosphere. One target showed a link between declines and its pulsation period. —Keith T. Smith

Mon. Not. R. Astron. Soc. (2025) 10.1093/mnras/staf215

R Coronae Borealis–type variable stars are prone to dramatic, unpredictable dimming events.

IMAGE: ESO

HIV

Geographical misalignment

More than 25 million people in Africa are living with HIV. For many, access to health care is very challenging, especially for women in rural communities. Ponce *et al.* present geospatial and geostatistical modeling showing what influences access to antiretroviral therapy (ART) and applied this information to conditions in Malawi. They found that in this area, geographical access to ART is profoundly influenced by the availability of transportation, resulting in such a patchy distribution of access to medical services that treatment "deserts" were evident. These gaps mean that a range of health care issues, as well as HIV and its comorbidities, are inadequately addressed in Malawi, and that rural people living in poverty have shorter life expectancies than their peers in urban centers. —Caroline Ash

Nat. Med. (2025) 10.1038/s41591-025-03561-6

MUTUALISM

Robbers and thieves

Mutualisms, exchanges that benefit both interacting species, form the basis of ecologically and economically important processes such as pollination. Mutualisms can be exploited, however, such as when animals take nectar by creating a hole in the flower's corolla ("robbing") or entering flowers without transferring pollen ("theft"). Leal *et al.* performed a meta-analysis to understand how nectar robbing and theft affect nectar quality, pollinator visitation, and plant reproduction. They found that whereas both behaviors reduced nectar quality, only theft reduced pollinator visitation rates and plant reproductive success. Although robbing appears to be a clear case of exploitation, it also sometimes pollinates flowers or triggers flowers to create more nectar, thus producing a net benefit for the plant. —Bianca Lopez *Ecology* (2025) 10.1002/ecy.70036

Nectar robbers such as this carpenter bee, *Xylocopa virginica*, steal nectar without pollinating the flower.

MACHINE LEARNING

Modeling chemical processes in solutions

Solvent molecules can substantially influence the stability of chemical species, reaction kinetics, and product ratios. However, performing accurate atomistic simulations of complex condensed-phase chemical processes that incorporate explicit solvent molecules remains challenging and computationally demanding. Pultar *et al.* demonstrated that combining an anisotropic message-passing formalism for neural network potentials with an electrostatic embedding scheme in hybrid quantum–mechanical/molecular-mechanical simulations can efficiently reduce computational costs. It also enables sampling of dynamic systems containing hundreds of solvent molecules and tens of thousands of atoms over hundreds of nanoseconds, showing excellent agreement with experimental thermodynamic properties. The proposed approach has the potential to facilitate efficient routine modeling of complex chemical reactions in solutions. —Yury Suleymanov

J. Am. Chem. Soc. (2025) 10.1021/jacs.4c17015

CHEMOTHERAPY

Prenatal exposure to chemotherapy

Chemotherapy can be given to pregnant woman with cancer after the first trimester, but the potential risks posed to the developing fetus are not clear. Struys *et al.* investigated whether prenatal exposure to maternal chemotherapy treatment affects fetal hematopoietic (blood) stem cells. The researchers performed single-cell analysis of human cord blood (as a source of neonatal DNA) from women treated with chemotherapy during pregnancy. Compared with cord blood samples from untreated pregnant patients with cancer and healthy pregnant women, prenatal exposure to chemotherapy regimens during pregnancy was correlated with increased accumulation of somatic mutations in fetal blood cells. These data highlight the need for larger-scale studies that monitor the long-term impact of neonatal exposure to genotoxic stress. —Priscilla N. Kelly

Cancer Discov. (2025) 10.1158/2159-8290.CD-24-1368

BIOMATERIALS

Reproducing key cues for bone growth

The hierarchical structure of growing bone requires a microenvironment generated by a complex mixture of physical and chemical cues that makes it challenging to reproduce in vitro. Zhu *et al.* developed a hydrogel based on DNA and methacrylated gelatin (GelMA) that forms a dual network structure, to which they added enzymatically prepared amorphous calcium phosphate. The structured gel promoted cell migration and the formation of a woven bone organoid in a three-dimensional culture over 21 days, which showed dynamic mineralization and remodeling. After a 4-week subcutaneous placement in mice, the cultured organoids encouraged the formation of well-vascularized mineralized bone tissue. —Marc S. Lavine

Adv. Mat. (2025) 10.1002/adma.202501254

NEUROSCIENCE

Can sweeteners make you hungry?

Noncaloric sweeteners such as sucralose are widely used in foods and beverages to provide a sweet taste without the calories of sucrose. However, some studies suggest that these sweeteners can stimulate appetite. Chakravartti *et al*. gave 75 young adults a drink containing sucralose, sucrose, or water in a randomized crossover trial and used functional magnetic resonance imaging to study blood flow to the hypothalamus, a brain structure that has an important role in appetite. Compared with sucrose, the consumption of sucralose stimulated hypothalamic blood flow and produced greater hunger responses. The findings highlight the complexity of the neural mechanisms controlling appetite and indicate that future work is needed to understand the long-term health implications of sweetener use. —Sarah Lemprière

Nat. Metab. (2025) 10.1038/s42255-025-01227-8

RESEARCH ARTICLE SUMMARY

STRUCTURAL BIOLOGY

Structural basis for nucleolin recognition of *MYC* promoter G-quadruplex

Luying Chen, Jonathan Dickerhoff, Ke-wei Zheng, Satchal Erramilli, Hanqiao Feng, Guanhui Wu, Buket Onel, Yuwei Chen, Kai-Bo Wang, Megan Carver, Clement Lin, Saburo Sakai, Jun Wan, Charles Vinson, Laurence Hurley, Anthony A. Kossiakoff, Nanjie Deng, Yawen Bai, Nicholas Noinaj, Danzhou Yang*

INTRODUCTION: G-quadruplexes (G4s) are DNA or RNA secondary structures formed in guanine (G)–rich sequences with significant functional roles. These globular structures form under physiological conditions and are stabilized by cellular potassium or sodium ions (K^+ or Na^+). G4s in oncogene promoters regulate gene transcription and are promising anticancer drug targets. The *MYC* oncogene, particularly, contains a G4-forming region in its proximal promoter NHE III_1, which controls 75 to 85% of transcription. In K^+ solution, the *MYC* NHE III_1 forms two parallel-stranded G4s, Myc121 and Myc161. Parallel G4 structures are robust and commonly found in promoter regions and RNA G4s.

RATIONALE: Numerous proteins have been reported to interact with G4s, but only a few structures of G4-protein complexes have been resolved. They all involve processive helicases that unfold G4, generating full access to external G tetrads for stacking interactions. However, genomic G4 recognition cannot be solely attributed to G tetrad–stacking interactions, as flanking regions within continuous duplex DNA hinder access to external G-tetrads.

Nucleolin was identified in 2009 as a major binding protein of the *MYC* promoter G4 (M3ycG4) and functions as a transcriptional repressor. This modular protein features a central DNA or RNA binding domain consisting of four RNA binding domains [RBDs or RNA-recognition motifs (RRMs)] interconnected by three linkers. Notably, nucleolin has a higher affinity for MycG4 than for its well-established substrate, the stem-loop nucleoin recognition element (NRE) RNA. However, structural information of the G4-nucleolin complex is unavailable.

RESULTS: We resolved the crystal structure of the 1:1 nucleolin-MycG4 complex at 2.6 Å, facilitated by a de novo NCL-MycG4 complex-specific fragment antigen-binding region (Fab) and an optimized Myc161 sequence. All four RBDs of nucleolin are essential for high-affinity binding to MycG4, unlike its interaction with NRE RNA, which involves only two RBDs. Nucleolin prefers the Myc161 G4 (dissociation constant K_d ~3 nM). In the complex structure, the Myc161 G4 adopts a folded parallel-stranded topology with two K^+ ions between three G tetrads, closely resembling the nuclear magnetic resonance (NMR) solution structure of free Myc161, including a similar 5′ DNA triad capping structure.

The four RBDs of nucleolin wrap around MycG4 to form multivalent interactions with its three loops and 5′ flanking region for specific and high-affinity recognition. RBD1, RBD2, and Linker12 extensively interact with the 6–nucleotide (nt) central loop and the 5′ flanking region of Myc161, with Linker12 adopting a highly structured 9–amino acid α helix. RBD3 and RBD4 bind the 1-nt loops of MycG4, as demonstrated by NMR. The complex structure reveals distinct nucleolin-specific nucleobase-recognition motifs located outside the canonical RNP motifs, allowing multivalent binding to multiple individual nucleobases spatially dispersed on the globular G4 substrate. Nucleolin binding to MycG4 inhibits polymerase extension. Cleavage under targets and tagmentation sequencing (CUT&Tag) demonstrates nucleolin binding to the *MYC* promoter G4-forming region in cells. Notably, nucleolin's genome-wide binding sites align closely with G4 loci, suggesting that G4s are nucleolin's primary cellular substrates.

CONCLUSION: We report the first high-resolution structure of a G4 in complex with a regulating protein. Our structure reveals the first G4 conformation–based protein recognition. The globular G4 structure, with its multiple loops and flanking regions, provides an ideal platform for multivalent interactions with the modular nucleolin protein. The specific and high-affinity recognition of MycG4 requires all four RBDs of nucleolin. Nucleolin shows little interactions with the buried G tetrad core but recognizes the exposed loop and flanking regions of the globular G4, which may be a general feature of G4 interactions for nonhelicase proteins. Our findings suggest that G4s are nucleolin's primary cellular substrates and indicate a G4-based epigenetic transcriptional regulation. The specific and high-affinity binding of the MycG4 by nucleolin can block the binding of other transcription factors to the same promoter region or recruit regulatory proteins. Further, the nucleolin-MycG4 complex structure will help G4-targeted drug discovery. ■

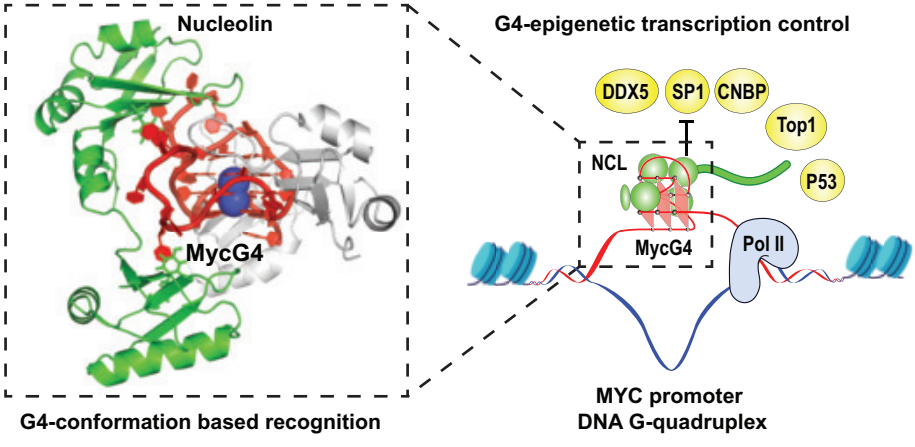

G4 conformation–based protein recognition for G4 epigenetic transcription control. Modular nucleolin (NCL) protein binds the globular MycG4 through G4 conformation–based recognition through multivalent interactions with MycG4 loops and flankings, enabling specific and high-affinity binding. Nucleolin binds the *MYC* promoter G4-forming region in cells, and this high-affinity binding suggests a MycG4-epigenetic transcription control by blocking the binding of transcription factors or recruiting regulatory proteins.

The list of author affiliations is available in the full article online.
*Correspoding author. Email: yangdz@purdue.edu
Cite this article as L. Chen *et al.*, *Science* **388**, eadr1752 (2025). DOI: 10.1126/science.adr1752

READ THE FULL ARTICLE AT
https://doi.org/10.1126/science.adr1752

RESEARCH ARTICLE SUMMARY

TISSUE IMAGING

Deep-tissue transcriptomics and subcellular imaging at high spatial resolution

Valentina Gandin†, Jun Kim†, Liang-Zhong Yang, Yumin Lian, Takashi Kawase, Amy Hu, Konrad Rokicki, Greg Fleishman, Paul Tillberg, Alejandro Aguilera Castrejon, Carsen Stringer, Stephan Preibisch, Zhe J. Liu*

INTRODUCTION: Understanding how gene expression and subcellular structures are spatially organized within tissues is fundamental to biology and disease research. However, conventional fluorescence imaging is limited by color channels, restricting the simultaneous visualization of multiple molecular components. Although in situ spatial transcriptomics has expanded molecular imaging capabilities, it struggles to resolve high-abundance targets and dense cellular structures in thick specimens. Additionally, existing methods often require complex processing steps or suffer from signal loss in deeper regions. To overcome these challenges, we developed cycle hybridization chain reaction (HCR), a highly multiplexed RNA and protein imaging method that enables high-resolution transcriptomics and subcellular structure imaging in thick tissues.

RATIONALE: Existing spatial transcriptomics approaches often rely on cross-round barcoding, which requires precise spot registration across imaging cycles. These techniques are generally limited to thin tissue sections and are prone to errors in dense molecular environments. Conversely, single-shot signal amplification methods such as HCR amplification excel at deep-tissue imaging of both sparse and dense targets; however, they lack high-throughput capacity. To address these limitations, we developed cycleHCR, which integrates multicycle DNA barcoding with HCR amplification. This approach enables high-throughput three-dimensional (3D) spatial analysis of RNA and protein distributions in thick tissue specimens, facilitating precise molecular mapping across multiple spatial scales.

RESULTS: We applied cycleHCR to whole-mount mouse embryo transcriptomics, imaging 254 lineage-specific genes in E6.5-7.0 embryos. By integrating automated imaging and computational pipelines, we achieved precise 3D gene expression and cell fate mapping across a specimen depth of ~310 μm. Cluster analysis of single-cell gene expression data identified nine distinct cell populations, corresponding to known developmental lineages, with well-defined spatial organization. Our data enabled spatial analysis of gene expression gradients and heterogeneity, providing single-cell resolution insights into how gene expression varies across embryonic structures.

Beyond transcriptomics, cycleHCR was combined with expansion microscopy to visualize 10 distinct subcellular structures in mouse embryonic fibroblasts. We observed complex nuclear and cytoplasmic architectures with enhanced spatial resolution. Moreover, the platform enabled unified multiplex RNA and protein imaging in mouse hippocampal slices, uncovering intricate gene expression gradients and cell-type–specific nuclear structural variations.

CONCLUSION: By overcoming the limitations of traditional fluorescence imaging and existing spatial transcriptomics methods, cycleHCR offers key advantages: (i) Single-shot imaging enables robust deep-tissue in situ transcriptomics for both sparse and dense targets. (ii) The resulting empirical images allow immediate validation and visualization of molecular targets. (iii) A barcode system supports joint RNA and protein imaging, enabling cross-modality spatial analysis of cell types and subcellular organization.

As a scalable spatial omics platform, cycleHCR is poised to advance developmental biology, neuroscience, and systems biology. Its adaptability across different specimen types highlights its potential as a next-generation imaging tool for deciphering the spatial arrangement of molecular components within intact tissues. Further optimization of microscopy modalities and sample preparation will enhance imaging depth and throughput, with promising applications in disease research and precision diagnostics. ■

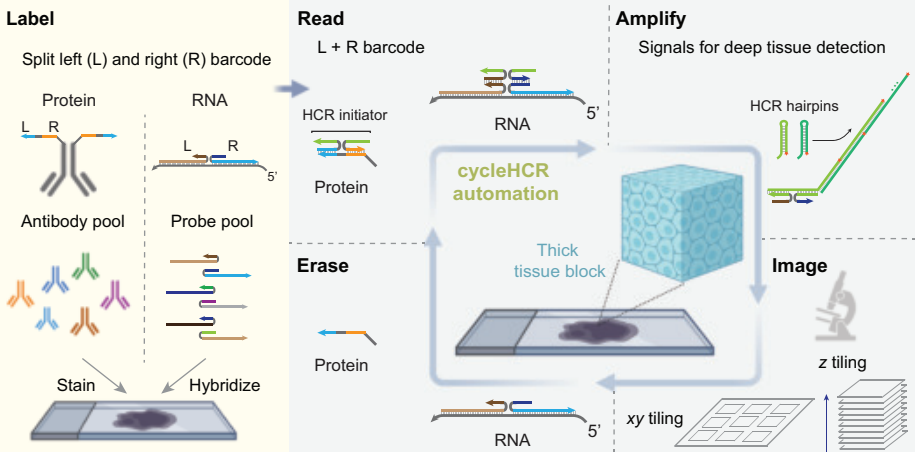

Unified multiplex RNA and protein imaging through cycleHCR. Samples are first labeled with antibody and probe pools, where each target is uniquely barcoded with a split left (L) and right (R) barcode. The cycleHCR automation pipeline then reads targets using distinct L + R readout probes equipped with split HCR initiators. Signals are amplified through HCR, enabling deep tissue detection. After volumetric imaging, readout probes are instantly erased using chemical treatment, allowing for the next round of detection. Arrowheads indicate the 3′ end of DNA or RNA.

The list of author affiliations is available in the full article online.
*Corresponding author. Email: liuz11@hhmi.org
†These authors contributed equally to this work.
Cite this article as V. Gandin *et al.*, *Science* **388**, eadq2084 (2025). DOI: 10.1126/science.adq2084

READ THE FULL ARTICLE AT
https://doi.org/10.1126/science.adq2084

RESEARCH ARTICLE SUMMARY

EVOLUTION

Adaptation repeatedly uses complex structural genomic variation

Zachariah Gompert*, Jeffrey L. Feder, Thomas L. Parchman, Nicholas P. Planidin, Frederick J. H. Whiting, Patrik Nosil*

INTRODUCTION: The fit of organisms to their environment is a hallmark of adaptive evolution and can lead to the emergence of new species and thus create biological diversity. Therefore, understanding the genetic basis of local adaptation remains a major goal in biology. Structural genetic elements such as chromosomal inversions, insertions, deletions, and translocations are widespread across genomes and have increasingly been shown to shape evolution. However, the complexity of such elements and their role in repeatedly driving local adaptation remain unclear. Comparisons of haplotype-resolved or phased genome assemblies from multiple individuals provide new opportunities to understand how structural variation contributes to evolution, particularly in regard to the repeatability of evolution.

RATIONALE: *Timema cristinae* is a wingless, plant-feeding stick insect that exhibits two color-pattern morphs that are divergently adapted to two different plant species. On the plant *Adenostoma fasciculatum*, one often finds a striped color-pattern morph of *T. cristinae* that is green but also bears a longitudinal, white stripe on its dorsal surface. Past work has shown that this morph is cryptic on the thin needle-like leaves of *A. fasciculatum*. On an alternative host, the larger and more tree-like *Ceanothus spinosus*, one often finds an unstriped morph that is green but lacks the dorsal stripe, making it cryptic against the broad leaves of *C. spinosus*. Thus, the color-pattern morphs are adaptations to different hosts that promote camouflage and survival in the face of visual predation by birds and lizards. Both these morphs are found on two different mountains (Refugio and Highway 154) near Santa Barbara, California. In this work, we leveraged phased genome assemblies of each morph from each mountain to dissect the genetic basis of color-pattern polymorphism. We coupled these genomes with population genetics data to infer the evolutionary history of the morphs and the roles of selection, present gene flow, and historical introgression in their origin and maintenance.

RESULTS: Phased genome assemblies show that adaptive divergence in cryptic color pattern is repeatedly underlain by structural variation, but not a simple chromosomal inversion. We found that color pattern in populations on two different mountains is associated with translocations that have also been inverted. These complex structural variants span ~43 and ~15 mega–base pairs on the two mountains and contain 299 and 97 genes, respectively. The translocations arose independently on each mountain, representing repeated evolution. Although the translocations differ in size and origin on each mountain, they overlap partially such that the inverted region and a small segment of the colinear region of the translocation on one mountain coincide with the colinear region of the translocation on the other mountain. Consequently, these structural variants contain some of the same gene regions, including candidate color-pattern genes. We also provide evidence that this structural variation is subject to divergent selection along a geographic cline and arose without introgression between species. The results thus show how the origin of complex structural variation provides a mechanism for repeated bouts of adaptation.

CONCLUSION: We report structural variation underlying an adaptive polymorphism in a stick insect. Related results reported in other plants and animals point to a general role for structural variation in adaptive evolution. However, we show here that such structural variation can be complex and diverse, not always representing a simple chromosomal inversion, with differences among populations of a single species. Structural variation may be regularly available as a substrate for evolution, yet its importance may be presently underestimated because scientists have lacked powerful tools to detect it. Thus, accumulating examples of inversions and supergenes may only be the beginning. Indeed, our findings suggest that structural variation could be an abundant, diverse, and widespread source of genetic variation, providing fuel for evolution. Moreover, such variation may arise repeatedly to provide an element of predictability to adaptive evolution. Ongoing advances in genomics will allow this idea to be tested in a wide range of organisms and contexts. ■

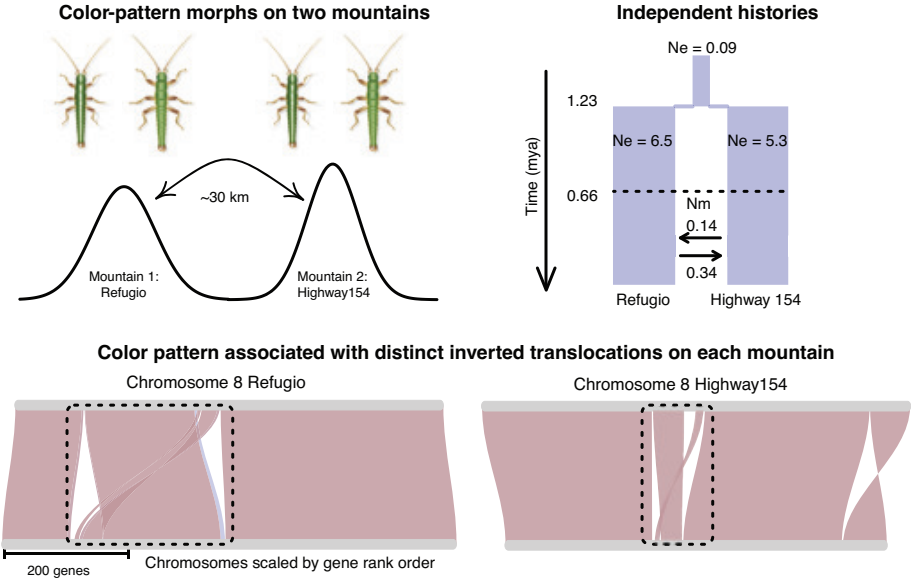

Adaptive divergence in cryptic color pattern in *T. cristinae* stick insects is repeatedly underlain by complex structural variation. *T. cristinae* exhibits two color-pattern morphs—striped and green—that are divergently adapted to two different plant species. Color pattern in populations of these stick insects on each of two different mountains is associated with large translocations that have also been inverted. These translocations differ in size and origin on each mountain, but they overlap partially and are associated with some of the same genes. mya, million years ago; Ne, effective population size; Nm, number of migrants per generation.

The list of author affiliations is available in the full article online.
*Corresponding author. Email: zach.gompert@usu.edu (Z.G.); patrik.nosil@cefe.cnrs.fr (P.N.)
Cite this article as Z. Gompert *et al.*, *Science* **388**, eadp3745 (2025). DOI: 10.1126/science.adp3745

READ THE FULL ARTICLE AT
https://doi.org/10.1126/science.adp3745

RESEARCH ARTICLE SUMMARY

ENZYME DESIGN

Computational design of serine hydrolases

Anna Lauko†, Samuel J. Pellock*†, Kiera H. Sumida†, Ivan Anishchenko, David Juergens, Woody Ahern, Jihun Jeung, Alexander F. Shida, Andrew Hunt, Indrek Kalvet, Christoffer Norn, Ian R. Humphreys, Cooper Jamieson, Rohith Krishna, Yakov Kipnis, Alex Kang, Evans Brackenbrough, Asim K. Bera, Banumathi Sankaran, K. N. Houk, David Baker*

INTRODUCTION: Enzymes efficiently accelerate the chemical reactions that sustain all living systems using complex and atomically precise molecular architectures that are extremely challenging to design. Previous efforts to design enzymes have largely focused on finding geometric matches between model active sites and preexisting protein structures, an approach akin to buying a suit from a thrift store; it is unlikely the fit will be perfect. Most previous enzyme design efforts have also primarily focused on simplified active sites designed for a single state, even for enzymes that use multistep reaction mechanisms. These design limitations have limited the geometric precision and preorganization of the active site, key features of highly efficient enzymes. New approaches that generate protein structures tailored to a complex enzyme active site and assess the structural compatibility of the resulting design with each state along the reaction coordinate are needed to improve enzyme design.

RATIONALE: We reasoned that rather than searching for geometric matches between designed active sites and fixed protein backbones, we could instead leverage deep learning–based generative models to construct proteins that are tailor-made for the desired active site. Once generated, we could use deep learning–based ensemble modeling to structurally assess the compatibility of a designed enzyme with each step in a catalytic cycle. We reasoned that ester hydrolysis by serine hydrolases would serve as an excellent model reaction because the reaction mechanism requires a complex active site made up of intricate hydrogen bond networks to activate the serine nucleophile that can accommodate multiple transition states and intermediates throughout the reaction cycle, including the acyl-enzyme intermediate (AEI) and two tetrahedral intermediates (TI1, TI2).

RESULTS: We used RFdiffusion denoising trajectories starting from completely random residue distributions to generate protein backbones housing active sites that span a range of catalytic residue compositions and geometries and assigned amino acid sequences to these backbones using LigandMPNN. Experimental characterization of the resulting designs revealed multiple serine hydrolases with high structural accuracy to the predicted models (Cα root mean square deviations <1 Å between design and crystal structures), catalytic efficiencies as high as 2.2×10^5 M^{-1} s^{-1}, and folds distinct from natural hydrolases. Designs filtered for structural compatibility and preorganization across the catalytic cycle using a newly developed ensemble modeling method, PLACER, had considerably improved success rates and catalytic activities. Characterization of designs with increasingly complex active sites revealed structural and compositional features essential for catalysis: minimal active sites composed of Ser-His dyads yielded proteins containing reactive serines capable of covalent labeling with phosphonate probes and ester substrates, but the full Ser-His-Asp triad and two-component oxyanion hole are necessary for catalytic turnover. Rather than performing rounds of directed evolution, we were able to improve catalysis through explicit optimization of catalytic geometries. The RFdiffusion calculations sample a considerable range of folds and structures, enabling an analysis of the geometric determinants of catalysis that complements structural studies of native serine hydrolases.

CONCLUSION: We demonstrate that RFdiffusion can scaffold complex active sites with higher accuracies, success rates, and catalytic activities than previous computational methods. Deep learning–based assessment of active site preorganization at each step in a multistep reaction can considerably increase design success rates for enzymes with complex catalytic mechanisms. The enzyme structure generation and active site evaluation methods described here should be broadly applicable to the design of multistep enzymes for a wide variety of chemical reactions. ■

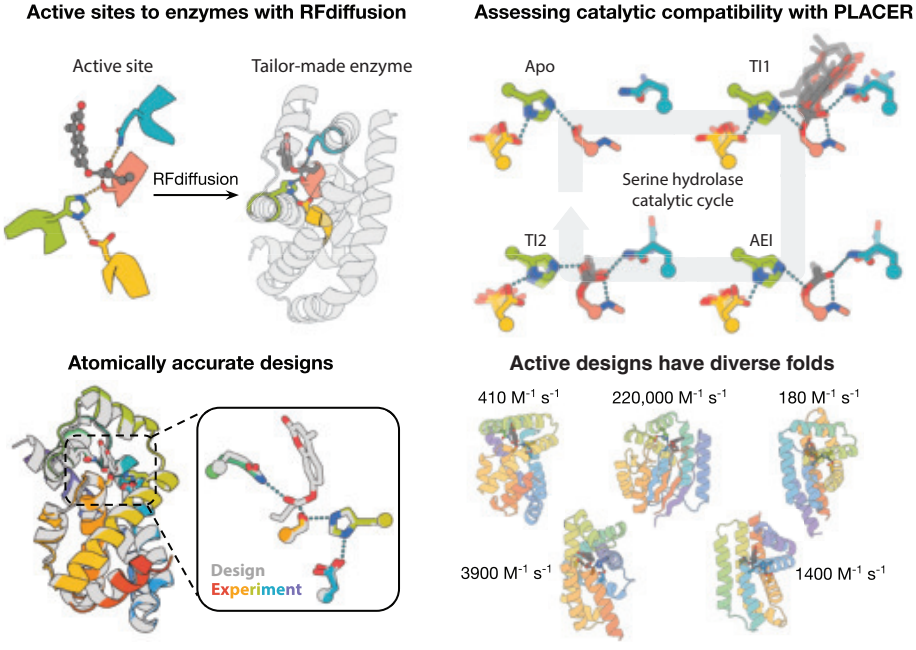

Computational design of serine hydrolases. RFdiffusion generates enzymes tailor-made for a given active site (top left). Assessing design compatibility across the catalytic cycle with the PLACER neural net. Conformational ensembles for each step of the reaction are shown (top right). Comparison with crystal structures shows that designs made with RFdiffusion and filtered with PLACER are atomically accurate (bottom left). Designed serine hydrolases expand the fold space of this ancient enzyme family (bottom right, catalytic efficiencies listed).

The list of author affiliations is available in the full article online.
*Corresponding author. Email: spellock@uw.edu (S.J.P.); dabaker@uw.edu (D.B.)
†These authors contributed equally to this work.
Cite this article as A. Lauko *et al.*, *Science* **388**, eadu2454 (2025). DOI: 10.1126/science.adu2454

READ THE FULL ARTICLE AT
https://doi.org/10.1126/science.adu2454

RESEARCH ARTICLE SUMMARY

PLANT GENETICS

The genetic architecture of cell type–specific cis regulation in maize

Alexandre P. Marand*, Luguang Jiang, Fabio Gomez-Cano, Mark A. A. Minow, Xuan Zhang, John P. Mendieta, Ziliang Luo, Sohyun Bang, Haidong Yan, Cullan Meyer, Luca Schlegel, Frank Johannes, Robert J. Schmitz*

INTRODUCTION: Noncoding genetic variants are a major driver of phenotypic diversity. In *Zea mays* (maize), genetic variation within cis-regulatory regions accounts for ~40% of phenotypic variability in agronomically important traits. Missing from past studies, however, is the role of cell context in shaping regulatory variant effects and a clear definition of the molecular mechanisms underlying phenotypic variation. Thus, resolving the genetic and molecular principles that give rise to phenotypic diversity in a cell state–aware framework is paramount to advancing crop improvement efforts.

RATIONALE: Single-cell genomic methods offer a powerful approach for understanding the genetic sources of gene expression and chromatin accessibility variation. We generated and analyzed single-cell assay for transposase-accessible chromatin sequencing (scATAC-seq) and single-nuclei RNA sequencing (snRNA-seq) data across 172 genetically and phenotypically diverse inbred maize lines for insight into the regulatory mechanisms underlying phenotypic variability.

RESULTS: Our single-cell dataset comprises >700,000 nuclei from 33 distinct cell states. We first used this resource to investigate the extent of cis-regulatory variation among diverse genetic backgrounds, identifying binding sites for specific transcription factor (TF) families as being critical determinants of regulatory sequence conservation and functional activity. Through comparisons with 21 teosinte (a progenitor of modern maize) genomes, we identified 1587 accessible chromatin regions that were unique and fixed in the domesticated maize lineage. These accessible chromatin regions were enriched for *hAT* and *PIF/Harbinger* transposons, implicating co-option of transposon cis-regulatory elements as a major source of new regulatory sequences specific to domesticated maize.

By applying the principles of population genetics, we identified 107,623 cis chromatin accessibility quantitative trait loci (cis-caQTL) within accessible chromatin regions and validated their effects on enhancer activity using self-transcribing active regulatory region sequencing (STARR-seq). We found that cell state–specific cis-caQTL are common and often overlap with phenotype-associated variants identified by genome-wide association studies (GWASs). Deep investigation of caQTL indicated that variants within TEOSINTE BRANCHED1/CYCLOIDEA/PROLIFERATING CELL FACTOR (TCP)–binding sites are strong determinants of chromatin accessibility. Moreover, all caQTL variants with decreased TCP-binding affinity were concomitant with loss of chromatin accessibility. Construction of cell state–specific gene-regulatory networks indicated that TCP TFs are highly cell state specific and controlled by master cell identity regulators. Analysis of caQTL affecting distal accessible chromatin regions further implicated TCP TFs as being major contributors toward chromatin accessibility variation and, as a result, chromatin interactions.

Through transcriptome-wide association mapping, chromatin accessibility–wide association mapping, and integration of caQTL with expression QTL and GWAS variants, we found that caQTL were commonly associated with flowering-related phenotypes. We hypothesized that the transition of modern maize from tropical to temperate climates may have been a significant contributor of extant chromatin accessibility variation. Indeed, we found that caQTL are associated with signatures of population differentiation, and that these population-divergent variants occur within binding sites for TFs previously implicated in flowering time and floral morphology nonuniformly among cell states.

CONCLUSIONS: These analyses advance our understanding of how cell context and molecular diversity contribute to innovations in phenotype, providing the blueprints for future crop improvement efforts. ■

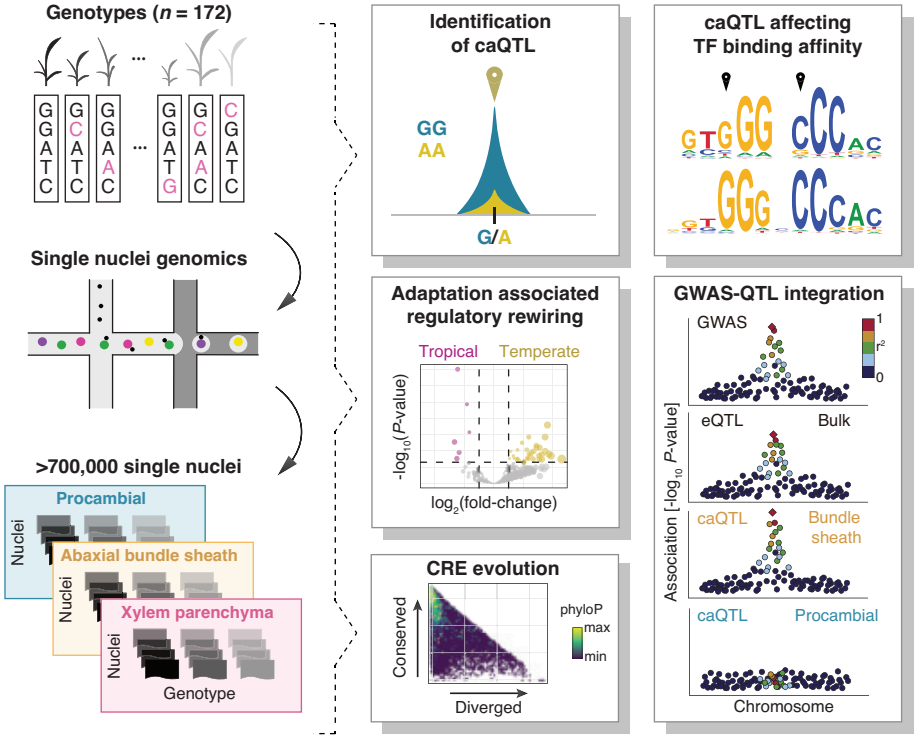

Single-nuclei caQTL mapping and investigation of cell context–specific effects. scATAC-seq profiles from >700,000 single nuclei across 172 maize inbred lines were used to identify >100,000 cis-caQTL within accessible chromatin regions. This study uncovered TF–binding site perturbations with effects on chromatin accessibility, caQTL colocalized with GWAS and eQTL, regulatory evolution associated with maize domestication, and local adaptation–associated regulatory rewiring at cell type resolution.

The list of author affiliations is available in the full article online.
*Corresponding author. Email: amarand@umich.edu (A.P.M.); schmitz@uga.edu (R.J.S.)
Cite this article as A. P. Marand *et al.*, *Science* **388**, eads6601 (2025). DOI: 10.1126/science.ads6601

RESEARCH ARTICLE SUMMARY

DEVELOPMENT

Casz1 is required for both inner hair cell fate stabilization and outer hair cell survival

Yuwei Sun, Minhui Ren, Yu Zhang, Shuting Li, Zhengnan Luo, Suhong Sun, Shunji He, Guangqin Wang, Di Zhang, Suzanne L. Mansour, Lei Song, Zhiyong Liu*

INTRODUCTION: The auditory organ, the cochlea, houses two subtypes of sound receptor hair cells (HCs): inner HCs (IHCs) and outer HCs (OHCs), which have distinct morphologies and functions. Both IHCs and OHCs have stereocilia on their cell surface, where the mechanoelectrical transduction channel components are located. Both cell types play critical roles in sound perception, with IHCs serving as the primary sensory cells that form synapses with auditory neurons, and OHCs functioning as sound amplifiers. HCs are highly vulnerable to degeneration caused by various ototoxic insults, which, in mammals, leads to permanent hearing loss. Birds and fish, unlike mammals, can regenerate HCs by activating key genes underlying HC development in supporting cells (SCs), which then transdifferentiate into HCs, restoring hearing.

RATIONALE: Transcriptomic comparisons between mammalian IHCs and OHCs have begun to identify IHC- and OHC-specific genes and some of the genetic signaling pathways governing IHC and OHC development. There has been some success in using this knowledge to promote mammalian HC regeneration. Currently, however, the regenerated IHCs or OHCs in mouse models are dysfunctional and exhibit defective stereocilia. Thus, it is of critical importance to identify additional HC subtype–specific genes, especially those encoding transcription factors, and genetically perturb their functions to uncover their roles in HC subtype development and survival.

RESULTS: We previously identified *Casz1*, encoding a zinc finger transcription factor, as enriched in IHCs but not OHCs. In this study, we found that *Casz1* is persistently expressed in IHCs and transiently expressed in OHCs and that *Casz1* plays a pivotal role in stabilizing the fate of early-differentiating IHCs and regulating OHC survival. Deletion of *Casz1* in embryonic cochlear progenitor cells did not affect IHC production or specification; however, the fate of these IHCs became unstable, and *Casz1*-deficient IHCs began exhibiting OHC-like characteristics, including up-regulation of OHC-specific genes, down-regulation of IHC-specific genes, and a reduction in presynaptic proteins. Additionally, *Casz1* deletion did not impair OHC production but eventually resulted in OHC degeneration. Furthermore, both *Casz1*-deficient IHCs and OHCs had abnormal stereocilia morphology, suggesting that Casz1 might play a direct role in stereocilia formation. Consequent to the IHC and OHC defects, mice with *Casz1* deletion exhibited severe hearing impairment. Through full-length single-cell transcriptomic analysis and genetic rescue experiments, we further found that Gata3 is a key downstream effector of Casz1. Restoration of Gata3 significantly alleviated the phenotypes observed in *Casz1*-deficient IHCs and, to a lesser extent, mitigated OHC degeneration and partially restored hearing. Moreover, we found that *Tbx2*, another transcription factor gene crucial for IHC development, is epistatic to *Casz1* for IHC fate stabilization. Finally, we found that Casz1 does not have a critical function at postnatal stages.

CONCLUSION: We found that Casz1, although not directly involved in IHC or OHC fate specification, is critical for stabilizing IHC identity and regulating OHC survival as well as promoting normal stereocilia morphology. Casz1 exerts its function by regulating the downstream effector Gata3, whose overexpression can ameliorate the phenotypic defects observed in *Casz1*-deficient IHCs and OHCs and improve hearing in *Casz1*-deleted mice. Given the significance of Casz1 during early HC development, our findings highlight a genetic pathway that could be targeted for developing hearing restoration therapies. ■

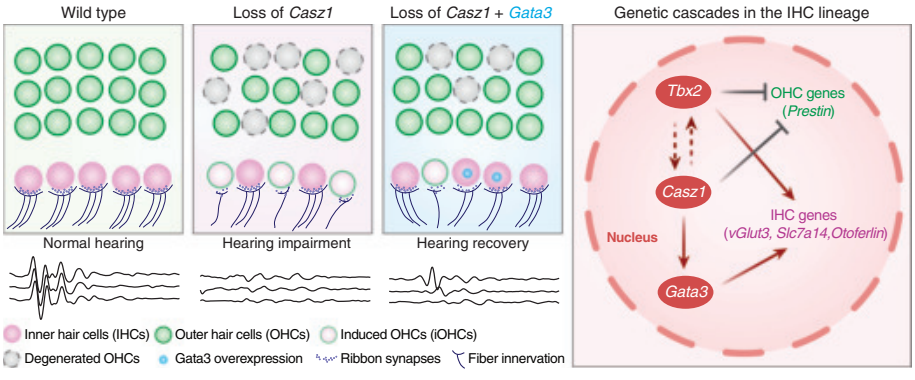

Genetic regulation of cochlear HC development. Loss of *Casz1* leads to transdifferentiation of IHCs into induced OHCs (iOHCs) and OHC degeneration, with iOHCs exhibiting reduced ribbon synapses and fiber innervation. Gata3 is a downstream effector of Casz1, and Gata3 overexpression alleviated the phenotypes of *Casz1*-deficient HCs. Although *Tbx2* is epistatic to *Casz1* in promoting IHC genes and repressing OHC genes, they may also regulate each other.

The list of author affiliations is available in the full article online.
*Corresponding author. Email: liuzhiyong@nibs.ac.cn or zhiyongliu@ion.ac.cn
Cite this article as Y. Sun *et al.*, *Science* **388**, eado4930 (2025). DOI: 10.1126/science.ado4930

RESEARCH ARTICLES

2D MATERIALS

Perfect Coulomb drag in a dipolar excitonic insulator

Phuong X. Nguyen[1,2]†, Liguo Ma[1]†‡, Raghav Chaturvedi[1]†, Kenji Watanabe[3], Takashi Taniguchi[3], Jie Shan[1,2,4]*, Kin Fai Mak[1,2,4]*

Excitonic insulators (EIs) are a solid-state prototype for bosonic phases of matter that can support charge-neutral exciton currents. However, demonstration of exciton transport in EIs is difficult. In this work, we show that the strong interlayer excitonic correlation at equal electron and hole densities in $MoSe_2/WSe_2$ double layers separated by a 2-nanometer barrier yields perfect Coulomb drag under zero magnetic field: A charge current in one layer induces an equal but opposite drag current in the other layer at low temperatures. The drag current ratio remains above 0.9 up to about 20 kelvin. As exciton density increases above the Mott density, the excitons dissociate into an electron-hole plasma abruptly, and only frictional drag is observed. Our experiment may lead to the realization of exciton circuitry and superfluidity.

Excitonic insulators (EIs) arise in semiconductors when the electron-hole binding energy exceeds the bandgap (*1*, *2*). Unlike the charged excitations that are frozen and unable to transport current, the neutral electron-hole pairs (excitons) are free to move in EIs. However, it is intrinsically difficult to demonstrate exciton transport in bulk EI candidates because separate electrical contacts cannot be made to the electrons and holes. This difficulty is overcome in Coulomb-coupled electron-hole double layers. Perfect Coulomb drag—a manifestation of pure exciton transport—has been demonstrated in Coulomb-coupled quantum wells (*3*–*5*) and graphene double layers (*6*–*9*) but only in the quantum Hall regime. The electron-hole binding becomes negligible in the absence of a magnetic field in these systems; only a frictional and/or energy drag has been reported (*10*–*14*). The recently discovered dipolar EIs based on Coulomb-coupled atomic double layers (*15*, *16*) open the possibility to realize perfect Coulomb drag under zero magnetic field. The strong exciton binding and the dispersive excitonic band in this system also present an unexplored regime for the studies of exciton transport (*17*–*20*).

The dipolar EI of interest is realized in double-layer structures made of two semiconducting transition metal dichalcogenide (TMD) monolayers that support a type-II band alignment (*15*, *16*, *21*–*25*) (Fig. 1A). The two TMD monolayers, which are separated by a thin dielectric spacer, are separately contacted by metallic electrodes and form the two plates of a parallel-plate capacitor (Fig. 1B). The application of an interlayer bias voltage V_b splits the electron and hole chemical potentials by eV_b and reduces the charge gap to $\varepsilon_G - eV_b$ for quasiparticle excitations from the zero-bias bandgap ε_G of the double layer (Fig. 1A). (Here, e is the elementary charge.) When the charge gap becomes smaller than the exciton binding energy, $\varepsilon_G - eV_b < \varepsilon_b$, spontaneous formation of dipolar (interlayer) excitons is favorable (*1*, *26*, *27*). An EI has been demonstrated by recent thermodynamic measurements (*15*, *16*). The platform provides an opportunity to realize strongly correlated bosonic phases of matter (*21*, *28*–*35*). The separate electron and hole contacts to the EI, which are lacking in bulk EI candidates (*36*–*41*), also provide an electrical reservoir for dipolar excitons with continuously tunable density n_X and chemical potential eV_b (*22*, *23*).

The Coulomb drag effect is a sensitive probe of the correlation effect between two spatially separated conductors (*42*). The Coulomb interactions between the two layers enable an electric current flowing in one layer (I_{drive}) to induce a drag current (I_{drag}) in the other layer if the second layer is part of a closed circuit (Fig. 1C). Similarly, a voltage drop (V_{drag}) is developed if the second layer is an open circuit (Fig. 1D). We show perfect Coulomb drag in the dipolar EI based on TMD electron-hole double layers at low temperatures; a large drag current ratio remains above 0.9 up to about 20 K. We also demonstrate an equilibrium exciton Mott transition, in contrast to earlier studies of the transition under nonequilibrium settings, such as under optical pumping (*43*, *44*).

Device operation and EI

Our sample consists of Coulomb-coupled $MoSe_2/WSe_2$ double layers with nearly symmetric top and bottom gates (Fig. 1B). Details of the device design and fabrication are described in the supplementary materials (*45*). Compared with the earlier compressibility study (*15*), multiple contacts to each TMD layer with substantially reduced contact resistances have been fabricated. The devices are divided into the channel and contact regions, in which the two TMD monolayers are separated by thin (5 to 6 layers) and thick (10 to 20 nm) hexagonal boron nitride (hBN) spacers, respectively. The TMDs are angle-misaligned to further suppress interlayer tunneling in the channel region. The $MoSe_2$ (Mo) and WSe_2 (W) layers are contacted by bismuth and platinum electrodes for electron and hole transport, respectively. The interlayer bias voltage V_b is applied to inject electron-hole pairs into the channel and tune the pair density n_P. The top and bottom gate voltages (V_{tg} and V_{bg}, respectively) further allow independent control of the electron-hole density imbalance in the double layer through the symmetric combination, $V_g = (V_{tg} + V_{bg})/2$, and the perpendicular electric field through the antisymmetric combination, $\Delta = (V_{bg} - V_{tg})/2$. In the channel region, the electric field reduces the bandgap; however, in the contact regions, because of the much thicker hBN spacer, the electric field heavily electron (hole) dopes the Mo (W) layer to substantially reduce the metal-semiconductor junction resistances. Junction resistances on the order of several kilohms at 1.5 K have been achieved. The contact regions are thus charge reservoirs for exciton injection into the channel region (*15*).

We identify the EI phase of the double layer using the capacitance measurements (fig. S2) as reported in an earlier study (*15*). Both the penetration capacitance (C_P, capacitance between the two gates) and the interlayer capacitance (C_I, capacitance between the TMD monolayers) are measured as a function of V_g and V_b at Δ = 5.5 V and 1.5 K. They characterize the charge and exciton compressibilities (*15*), respectively. Figure 2A illustrates C_P normalized by its geometric value (C_{gg}). The large penetration capacitance at small bias voltages marks the *ii* region, with both layers being charge neutral. Its boundary, denoted by two black dashed lines, traces the band edge of the electron and hole layers (the band edge of the hole layer is fixed at V_g = 0 because the hole layer is grounded). Varying the gate voltage across each boundary introduces doping in one of the layers (the *pi* and *in* regions). For sufficiently large bias voltages, both layers are doped (the *pn* region). Further, the simultaneous interlayer capacitance measurement (fig. S2B) identifies the dash-dotted line, above which the electron-hole pairs are injected into the channel. The enclosed triangular region is an EI, which is charge insulating at low temperatures but hosts an

[1]School of Applied and Engineering Physics, Cornell University, Ithaca, NY, USA. [2]Kavli Institute at Cornell for Nanoscale Science, Ithaca, NY, USA. [3]National Institute for Materials Science, Tsukuba, Japan. [4]Laboratory of Atomic and Solid State Physics, Cornell University, Ithaca, NY, USA.
*Corresponding author. Email: jie.shan@cornell.edu (J.S.); kinfai.mak@cornell.edu (K.F.M.)
†These authors contributed equally to this work.
‡Present address: Zhejiang Key Laboratory of Micro-nano Quantum Chips and Quantum Control, School of Physics, Zhejiang University, Hangzhou, China.

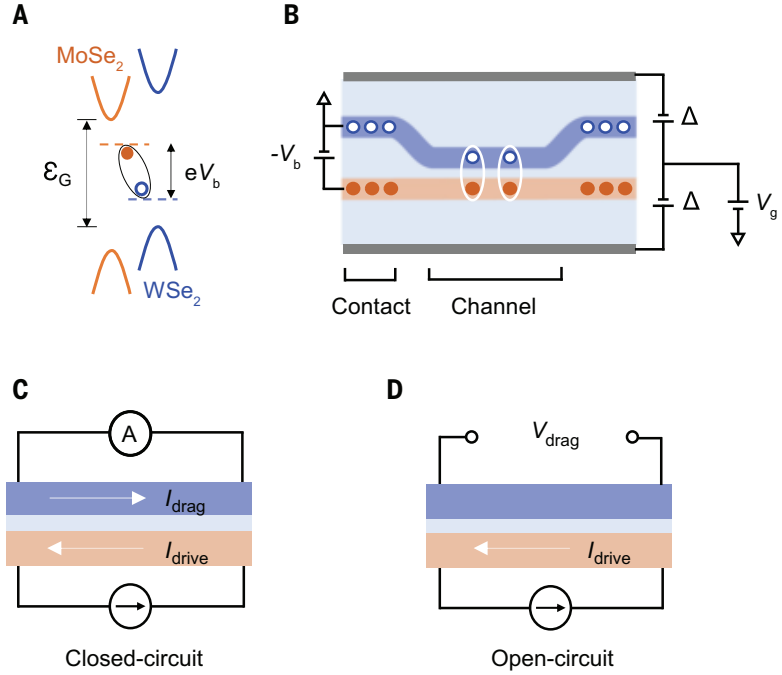

Fig. 1. Coulomb drag measurements in a dipolar EI. (**A**) Type-II band alignment of $MoSe_2/WSe_2$ heterostructures with an interlayer bandgap ε_G. An interlayer bias voltage V_b is applied to separate the electron (filled circle) and hole (empty circle) chemical potentials. An EI spontaneously forms when the charge gap, $\varepsilon_G - eV_b$, is smaller than the exciton binding energy ε_b. (**B**) Cross-sectional schematic of dual-gated WSe_2/hBN/$MoSe_2$ transport devices. The W layer, Mo layer, graphite gates, and hBN dielectrics are colored in blue, orange, gray, and light blue, respectively; V_g and Δ are the symmetric and antisymmetric combinations of the top and bottom gate voltages. Under a large perpendicular electric field $\propto \Delta$, the contact regions with a thick hBN spacer (~10 to 20 nm) are heavily doped with free electrons and holes, allowing exciton injection into the channel region with a thin BN spacer (~2 nm). (**C** and **D**) Schematic for the closed-circuit (C) and open-circuit (D) drag measurements. A bias current I_{drive} is applied to the Mo layer. The W contacts are shorted through an ammeter to measure the drag current I_{drag} in (C) and are connected to a voltmeter to measure the open-circuit drag voltage V_{drag} in (D).

equilibrium dipolar exciton fluid. The exciton binding energy, $\varepsilon_b \approx 30$ meV, is approximately given by the difference between the bias voltage at the tip of the triangle (0.52 V), beyond which the excitons dissociate into free electrons and holes, and the base of the triangle (0.49 V), at which excitons are just injected into the double-layer channel. The channel bandgap ε_G is reduced from the intrinsic value of 1.6 eV to 0.52 eV by antisymmetric gating Δ.

Perfect Coulomb drag

We study Coulomb drag in our devices using the drag counterflow geometry (Fig. 1C). We drive an electron current in the Mo layer using a small ac in-plane bias (5 to 10 mV) and measure the drag current in the W layer (*45*). Figure 2, B and C, shows the V_g and V_b dependences of the drive and drag currents at 1.5 K (see fig. S3 for results from driving the W layer). As expected, a finite I_{drive} is observed whenever the Mo layer is turned on—that is, in the *in*, *pn*, and EI regions. The current increases with increasing electron density. The discrepancy between the transport and capacitance results near the Mo band edge in the *in* region (with small V_b) is likely related to the large contact resistance in the Mo layer (*45*) (fig. S5). By contrast, a I_{drag} hotspot is observed only near the EI region; it decays rapidly with both increasing V_b and V_g, which increase the exciton density and the electron-hole density imbalance, respectively. In addition, I_{drag} always flows in the opposite direction of I_{drive} (fig. S4).

Below, we focus on the case of equal electron and hole densities in the double layer

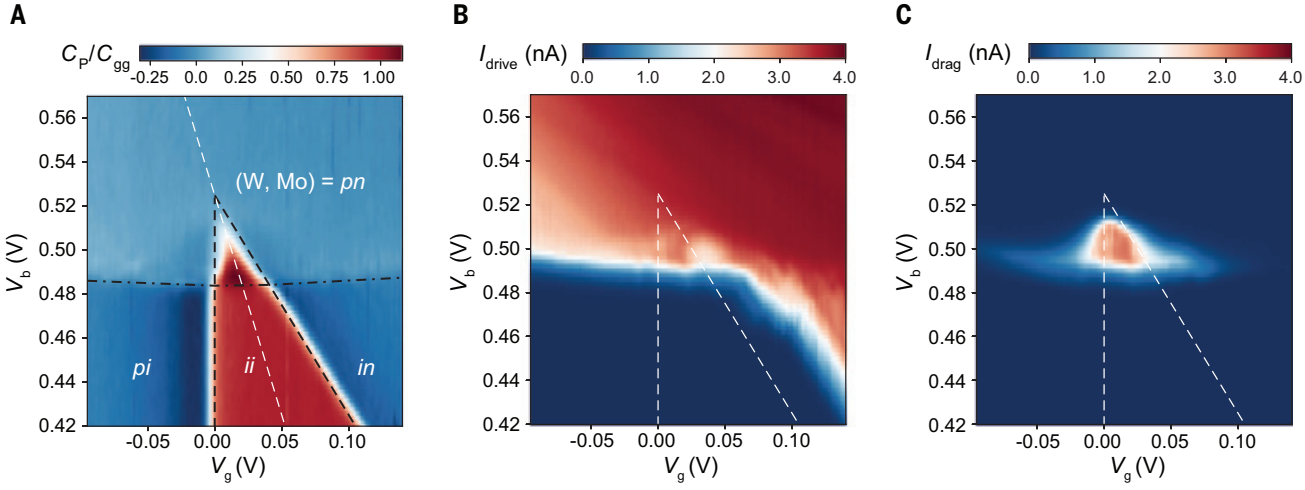

Fig. 2. Exciton transport and electrostatics phase diagram. (**A**) Normalized penetration capacitance C_P/C_{gg} as a function of V_b and V_g, where C_{gg} is the gate-to-gate geometric capacitance. The five distinct regions are separated by the black dashed and dash-dotted lines; the dashed lines correspond to the TMD band edges [see (*15*) for details]. Here *i*, *p*, and *n* denote, respectively, an intrinsic, hole-doped, and electron-doped layer. The double layer is incompressible in the *ii* region, where both layers are intrinsic, and in the EI region (the triangular area enclosed by the black dashed and dash-dotted lines), where an equilibrium exciton fluid emerges. The white dashed line marks equal electron and hole densities. (**B** and **C**) Drive current in the Mo layer (B) and drag current in the W layer (C) as a function of V_b and V_g. The white dashed lines are reproduced from the black dashed lines in (A). The Mo layer is turned on in the *in*, *pn*, and EI regions. Large drag current is observed in the EI region. A weaker drag current is also observed in a slightly electron- and hole-doped EI. All measurements were carried out at 1.5 K.

(along the white dashed line in Fig. 2A). The more general case of a finite electron-hole density imbalance, involving a Bose-Fermi mixture (*46*, *47*) and screened excitonic interactions, is responsible for the nonzero I_{drag} outside the EI region and will be examined in future studies. Figure 3A shows the current amplitude in two layers at 1.5 K as a function of V_b or n_P. The pair density is obtained from the interlayer capacitance measurement $n_P = \int \frac{C_I}{e} dV_b$ (fig. S2C). The drive current turns on sharply at $V_b \approx (\varepsilon_G - \varepsilon_b)/e$, when excitons are first injected into the channel, followed by a moderate increase with increasing V_b. The small deviations of the drive current from a smooth monotonic V_b dependence are device specific and are likely related to the junction imperfections. Notably, I_{drag} is nearly identical to I_{drive} (but with opposite direction) until the bias reaches a threshold $V_b \approx \varepsilon_G/e$, beyond which I_{drag} vanishes abruptly. The corresponding pair density is the Mott limit, $n_M \approx 4.0 \times 10^{11}$ cm^{-2} (see fig. S17 for calibration). Figure 3A also shows that the tunneling current I_{tunnel} between the two layers is negligible and cannot compromise the drag measurements (*45*). This contrasts with the nonequilibrium exciton fluid reported by Wang *et al.* (*24*), in which the observed I_{tunnel} was orders of magnitude higher.

The bottom panel of Fig. 3A shows the drag current ratio, I_{drag}/I_{drive}, at 1.5 K. It displays perfect Coulomb drag in the EI region and negligible Coulomb drag ($I_{drag}/I_{drive} < 0.001$) for pair density above n_M. The temperature and pair density dependences of the drag current ratio are summarized in Fig. 3B, and representative density line cuts are illustrated in Fig. 3C. In general, Coulomb drag decreases with increasing temperature and pair density except for the region near n_M at low temperatures, where the temperature dependence is nonmonotonic. A large drag current ratio remains above 0.9 up to about 20 K at low pair densities.

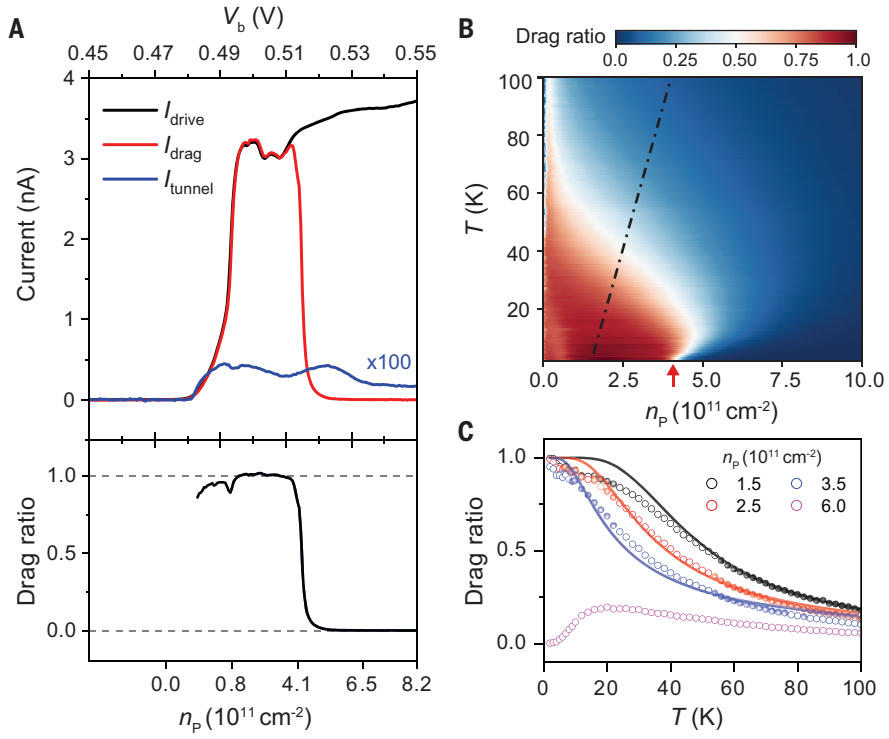

Fig. 3. Perfect Coulomb drag. (**A**) (Top) Drive current, drag current, and tunneling current (multiplied by 100) as a function of V_b (upper axis) and pair density n_P (lower axis) at 1.5 K. (Bottom) The corresponding drag current ratio. Pair density is calibrated from the interlayer capacitance with a systematic uncertainty of ~0.5 × 10^{11} cm^{-2}. Perfect drag is observed in the EI region, where the tunneling current is negligible. The drag current ratio quickly drops to zero outside the EI region. (**B**) Drag current ratio as a function of pair density n_P and temperature T. The dotted-dashed line marks the degeneracy temperature T_d, evaluated from the exciton compressibility peak. The red arrow denotes the Mott density, $n_M \approx 4.0 \times 10^{11}$ cm^{-2}. (**C**) Temperature dependence of the drag current ratio at selected pair densities. Empty symbols and solid lines are the experimental data and the theoretical fits described in the main text and the supplementary materials (*45*), respectively. The drag current ratio remains above 0.9 at low pair densities up to about 20 K. All data were acquired along the white dashed line in Fig. 2A.

When exciton transport dominates over free carrier transport in the channel, perfect Coulomb drag is expected because a steady current of electrons driven through one layer must be accompanied by an equal current of holes in the other layer (*3*). By contrast, when the electrons and holes are unbound, only small frictional drag is expected (*42*). In the case of Fermi liquids, the phase space of electrons and holes available for Coulomb drag increases with temperature, and the drag current ratio scales quadratically with temperature at low temperatures (*42*). The observed perfect Coulomb drag in our experiment therefore demonstrates the dominance of exciton transport in the EI region at low temperatures. Its temperature dependence can be largely captured by a simple model (Fig. 3C, solid lines) of exciton thermal dissociation (*48*), in which the frictional drag and the contact resistance of the drag layer are ignored and the exciton-to–charge carrier mobility ratio is the only fitting parameter and is assumed to be temperature independent (*45*). (These simple assumptions likely cause the observed discrepancy between experiment and theory at low temperatures.) The excitons can also be ionized into an electron-hole plasma at low temperatures by the state filling effect when the pair density exceeds the Mott density (*2*, *48*). The latter corresponds to the abrupt vanishing of the drag current near n_M at low temperatures, where n_M is the Mott density (we estimate $n_M a_B^2 \approx 0.4$, with a_B denoting the exciton Bohr radius). Above the Mott density, the negligible Coulomb drag at 1.6 K implies near-complete exciton ionization; I_{drag}/I_{drive} increases quadratically with temperature at low temperatures by the phase space argument ($n_P = 6 \times 10^{11}$; Fig. 3C).

EI-to-metal transition

We measure the drag resistance of our devices to directly probe the transition from an EI to an electron-hole plasma using the open-circuit geometry shown in Fig. 1D. We bias I_{drive} in the Mo layer and measure the drag voltage drop in the W layer, V_{drag}, using a voltmeter with 100-megohm input impedance. The drag resistance, $R_{drag} = V_{drag}/I_{drive}$, reflects the charge resistance of the double layer (see the circuit model in fig. S1D) (*45*). It is closely connected to the drag current described above. In the EI region at low temperatures (where the exciton conductivity is expected to far exceed the charge conductivity and the frictional drag conductivity), the two quantities are related, $\frac{I_{drag}}{I_{drive}} = \frac{1}{1+R_{WC}/R_{drag}}$, by the contact resistance (R_{WC}) in the drag layer (fig. S1F). The good agreement between the measured drag current ratio and the inferred one from R_{drag} using $R_{WC} \approx 7$ kilohm (fig. S7) supports the validity of this simple relation for a wide range of temperatures and pair densities. The

contact resistance is also independently verified by the two-terminal resistance measurement in the W layer (fig. S5).

Figure 4A shows the temperature dependence of R_{drag} at varying pair densities. As temperature decreases, R_{drag} increases for small densities (an insulating behavior) and decreases for large densities (a metallic behavior). A variation in R_{drag} by nearly six orders of magnitude is observed at 1.5 K. On the metallic side, a Fermi liquid frictional drag, $R_{drag} \approx AT^2$, is observed in the low-temperature limit (*42*, *49*) (fig. S6); a nonmonotonic temperature dependence is also visible near the Mott density. The nonmonotonic dependence demonstrates a crossover from a low-temperature coherent transport regime to a high-temperature incoherent (or classical) regime that occurs near the Fermi temperature of the TMD monolayers (*50*). The Fermi temperature (near the R_{drag} maximum) vanishes continuously as pair density approaches n_M from the metallic side. Notably, such a nonmonotonic dependence has been qualitatively captured in earlier theoretical studies (*51*–*53*), which take into account density- and temperature-dependent screening of electron-hole binding near the exciton Mott transition.

We further analyzed the observed insulator-to-metal transition following the procedures outlined by Dobrosavljevic *et al.* (*54*). We first identified the resistance curve at the critical density, R_c, as the one that displays a power-law temperature dependence (Fig. 4A, dashed line); the corresponding density agrees well with the Mott density. We then normalized the temperature-dependent R_{drag} at other densities by R_c. We can collapse all the normalized resistances into two groups with insulating and metallic behavior, respectively, by normalizing T using a density-dependent temperature T_0 (Fig. 4A, inset). The parameter T_0 vanishes continuously toward n_M from both sides (fig. S9). It is well correlated with the EI charge gap $\left[\approx\int(C_P/C_{gg})dV_g\right]$ obtained from the penetration capacitance measurement on the insulating side (Fig. 4B). In Fig. 4B, we summarize the coefficient A from fitting the temperature-dependent R_{drag} to AT^2 at low temperatures on the metallic side. The coefficient increases by three orders of magnitude as pair density approaches n_M. Together, the continuously vanishing charge gap (and T_0) and the diverging A coefficient with pair density approaching the Mott density from two sides suggest a possible continuous EI-to-metal transition (*55*).

We also observed that the coefficient A scales with pair density as $A \propto (n_P - n_M)^{-3}$ (Fig. 4B, solid line). This resembles, but at the same time differs from, the theoretical prediction of $A \propto (n_P)^{-3}$ for frictional drag from the interlayer Coulomb scattering (*42*, *56*). The reset of the pair density by the Mott density suggests a diverging electron/hole effective mass at n_M (*42*, *56*), consistent with the vanishing electron/hole Fermi temperature at n_M discussed above. The reset is beyond the current understanding. Future theoretical studies taking into account the BEC-BCS crossover (*57*) and the possible Mott transition at n_M are needed to understand the density dependence of A (BEC and BCS stand for Bose-Einstein condensation and Bardeen-Cooper-Schrieffer, respectively).

Discussion and outlook

We illustrate the experimental phase diagram for the exciton fluid in Fig. 3B. The degeneracy temperature T_d (Fig. 3B, dashed line) is obtained from the exciton compressibility peak in the temperature-dependent interlayer capacitance measurement (*15*, *58*–*60*). The exciton fluid is in the degenerate quantum limit below T_d. The degeneracy temperature (*21*) is substantially enhanced by the strong exciton-exciton interactions (*15*, *60*). The exciton fluid is also expected to transition to a superfluid at the Berezinskii-Kosterlitz-Thouless transition temperature lower than T_d (*21*, *60*). However, the Coulomb drag measurements are insensitive to spontaneous phase coherence and superfluid phase transition. The seemingly continuous exciton Mott transition near n_M observed in our experiment is inconsistent with mean-field theories (*21*, *22*, *61*), which have predicted an abrupt transition. On the other hand, density matrix renormalization group (DMRG) and random phase approximation (RPA) with dynamical screening methods have suggested a smooth crossover with exponentially suppressed exciton binding near n_M (*57*, *62*), which would explain an insulator-to-metal transition at finite temperatures but cannot explain the $A \propto (n_P - n_M)^{-3}$ divergence near n_M. The nature of the exciton Mott transition remains to be settled by further theoretical and experimental studies.

Finally, we comment on the effect of disorders. The disorder density in monolayer TMDs is estimated to be $n_d \approx 10^{11}$ cm^{-2} (fig. S13). (It is expected to be lower in the double layers because of extra screening of the disorder potentials by the other TMD layer.) The excitons are expected to be localized for $n_P < n_d$; they become delocalized (and possibly a superfluid) for $n_d < n_P < n_M$. This density window for interesting bosonic phases of matter can be further enlarged by a perpendicular magnetic field that strengthens the exciton binding (fig. S16).

We have demonstrated perfect Coulomb drag at low temperatures, with the drag current ratio remaining above 0.9 up to about 20 K, in a gate-tunable EI realized in TMD atomic double layers separated by a thin hBN barrier. The drag resistance measurement has further revealed an EI-to-metal transition at the Mott density. These studies are enabled by successfully establishing separate electrical contacts to the electron and hole components of the EI. The perfect Coulomb drag demonstrates pure exciton transport across the EI.

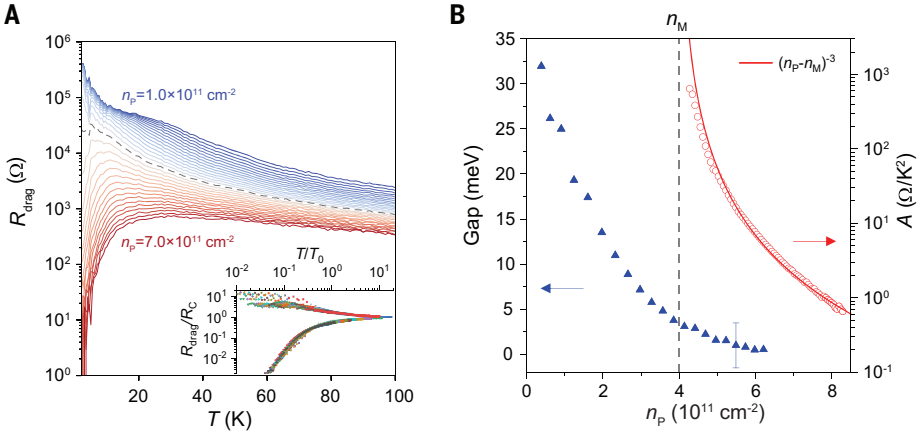

Fig. 4. EI-to-metal transition. (**A**) Temperature dependence of the drag resistance at varying pair densities n_P from 1 to 7 × 10^{11} cm^{-2} with a step size of 0.2 × 10^{11} cm^{-2}. The critical resistance curve R_c (dashed line) at the Mott density $n_M \approx 4.0 \times 10^{11}$ cm^{-2} separates the insulating behavior at low pair densities and the metallic behavior at high pair densities. (Inset) Critical scaling of resistance around n_M. The temperature-dependent resistances normalized by R_c collapse into two groups (with insulating and metallic behavior) when the temperature is scaled by a density-dependent temperature T_0. (**B**) EI charge gap (filled triangles) and coefficient A (empty circles) as a function of pair density n_P. The charge gap is obtained from the penetration capacitance measurement (*45*); the error bar represents the systematic uncertainty induced by the finite ac bias voltage in the measurement. The coefficient A is obtained by fitting the temperature-dependent frictional drag ($R_{drag} = AT^2$) for $n_P > n_M$ (fig. S6). The solid red line plots the scaling $A \propto (n_P - n_M)^{-3}$. The vertical dashed line marks the Mott density n_M.

However, the relatively large contact resistance in the Mo layer of the current devices hinders settling whether the exciton transport is dissipationless—that is, whether there is exciton superfluidity. Future four–exciton terminal measurements that can drive an exciton current and simultaneously measure the exciton chemical potential drop along the channel should be able to set a limit on dissipation occurring in the exciton channel.

REFERENCES AND NOTES

1. D. Jérome, T. M. Rice, W. Kohn, *Phys. Rev.* **158**, 462–475 (1967).
2. N. F. Mott, *Philos. Mag.* **6**, 287–309 (1961).
3. D. Nandi, A. D. K. Finck, J. P. Eisenstein, L. N. Pfeiffer, K. W. West, *Nature* **488**, 481–484 (2012).
4. L. Tiemann *et al*., *Phys. Rev. B* **77**, 033306 (2008).
5. J. P. Eisenstein, A. H. Macdonald, *Nature* **432**, 691–694 (2004).
6. X. Liu, K. Watanabe, T. Taniguchi, B. I. Halperin, P. Kim, *Nat. Phys.* **13**, 746–750 (2017).
7. Y. Zeng *et al*., Evidence for a Superfluid-to-solid Transition of Bilayer Excitons. arXiv:2306.16995 [cond-mat.mes-hall] (2023).
8. J. I. A. Li, T. Taniguchi, K. Watanabe, J. Hone, C. R. Dean, *Nat. Phys.* **13**, 751–755 (2017).
9. X. Liu *et al*., *Science* **375**, 205–209 (2022).
10. J. A. Seamons, C. P. Morath, J. L. Reno, M. P. Lilly, *Phys. Rev. Lett.* **102**, 026804 (2009).
11. A. Gamucci *et al*., *Nat. Commun.* **5**, 5824 (2014).
12. A. F. Croxall *et al*., *Phys. Rev. Lett.* **101**, 246801 (2008).
13. J. I. A. Li *et al*., *Phys. Rev. Lett.* **117**, 046802 (2016).
14. K. Lee *et al*., *Phys. Rev. Lett.* **117**, 046803 (2016).
15. L. Ma *et al*., *Nature* **598**, 585–589 (2021).
16. R. Qi *et al*., *Nat. Commun.* **14**, 8264 (2023).
17. Z. Sun, T. Kaneko, D. Golež, A. J. Millis, *Phys. Rev. Lett.* **127**, 127702 (2021).
18. A. V. Balatsky, Y. N. Joglekar, P. B. Littlewood, *Phys. Rev. Lett.* **93**, 266801 (2004).
19. J. Hu, A. F. Rigosi, D. B. Newell, Y. P. Chen, *Phys. Rev. B* **102**, 235304 (2020).
20. S. K. Banerjee, L. F. Register, E. Tutuc, D. Reddy, A. H. MacDonald, *IEEE Electron Device Lett.* **30**, 158–160 (2009).
21. M. M. Fogler, L. V. Butov, K. S. Novoselov, *Nat. Commun.* **5**, 4555 (2014).
22. F.-C. Wu, F. Xue, A. H. MacDonald, *Phys. Rev. B* **92**, 165121 (2015).
23. M. Xie, A. H. MacDonald, *Phys. Rev. Lett.* **121**, 067702 (2018).
24. Z. Wang *et al*., *Nature* **574**, 76–80 (2019).
25. G. W. Burg *et al*., *Phys. Rev. Lett.* **120**, 177702 (2018).
26. B. I. Halperin, T. M. Rice, *Rev. Mod. Phys.* **40**, 755–766 (1968).
27. L. V. Keldysh, Y. V. Kopaev, *Fiz. Tverd. Tela* **6**, 2791–2798 (1964).
28. J.-J. Su, A. H. MacDonald, *Nat. Phys.* **4**, 799–802 (2008).
29. Y. E. Lozovik, V. I. Yudson, *Sov. Phys. JETP* **44**, 389–397 (1976).
30. X. Zhu, P. B. Littlewood, M. S. Hybertsen, T. M. Rice, *Phys. Rev. Lett.* **74**, 1633–1636 (1995).
31. L. V. Butov, *J. Phys. Condens. Matter* **16**, R1577–R1613 (2004).
32. P. López Ríos, A. Perali, R. J. Needs, D. Neilson, *Phys. Rev. Lett.* **120**, 177701 (2018).
33. S. Conti *et al*., *Phys. Rev. Lett.* **130**, 057001 (2023).
34. Y. N. Joglekar, A. V. Balatsky, S. Das Sarma, *Phys. Rev. B* **74**, 233302 (2006).
35. M. A. Baranov, M. Dalmonte, G. Pupillo, P. Zoller, *Chem. Rev.* **112**, 5012–5061 (2012).
36. H. Cercellier *et al*., *Phys. Rev. Lett.* **99**, 146403 (2007).
37. A. Kogar *et al*., *Science* **358**, 1314–1317 (2017).
38. Y. Wakisaka *et al*., *Phys. Rev. Lett.* **103**, 026402 (2009).
39. L. Du *et al*., *Nat. Commun.* **8**, 1971 (2017).
40. B. Sun *et al*., *Nat. Phys.* **18**, 94–99 (2022).
41. Y. Jia *et al*., *Nat. Phys.* **18**, 87–93 (2022).
42. B. N. Narozhny, A. Levchenko, *Rev. Mod. Phys.* **88**, 025003 (2016).
43. J. Wang *et al*., *Phys. Rev. Lett.* **126**, 106804 (2021).
44. J. Wang *et al*., *Sci. Adv.* **5**, eaax0145 (2019).
45. See the supplementary materials for details.
46. D. D. Dai, L. Fu, *Phys. Rev. Lett.* **132**, 196202 (2024).
47. I. Amelio, N. D. Drummond, E. Demler, R. Schmidt, A. Imamoglu, *Phys. Rev. B* **107**, 155303 (2023).
48. G. Manzke, D. Semkat, H. Stolz, *New J. Phys.* **14**, 095002 (2012).
49. R. V. Gorbachev *et al*., *Nat. Phys.* **8**, 896–901 (2012).
50. S. Das Sarma, E. H. Hwang, *Phys. Rev. B* **68**, 195315 (2003).
51. D. Semkat *et al*., *Phys. Rev. B* **80**, 155201 (2009).
52. D. Snoke, *Solid State Commun.* **146**, 73–77 (2008).
53. K. Asano, T. Yoshioka, *J. Phys. Soc. Jpn.* **83**, 084702 (2014).
54. V. Dobrosavljevic, N. Trivedi, J. M. Valles, Eds., *Conductor-Insulator Quantum Phase Transitions* (Oxford Univ. Press, 2012).
55. T. Li *et al*., *Nature* **597**, 350–354 (2021).
56. E. H. Hwang, R. Sensarma, S. Das Sarma, *Phys. Rev. B* **84**, 245441 (2011).
57. D. Vu, S. Das Sarma, *Phys. Rev. B* **108**, 235158 (2023).
58. Yu. Kagan, V. A. Kashurnikov, A. V. Krasavin, N. V. Prokof'ev, B. V. Svistunov, *Phys. Rev. A* **61**, 043608 (2000).
59. Y. E. Lozovik, I. L. Kurbakov, G. E. Astrakharchik, J. Boronat, M. Willander, *Solid State Commun.* **144**, 399–404 (2007).
60. Z. Hadzibabic, J. Dalibard, *Riv. Nuovo Cim.* **34**, 389–434 (2011).
61. V. V. Nikolaev, M. E. Portnoi, *Superlattices Microstruct.* **43**, 460–464 (2008).
62. G. J. Sreejith, J. D. Sau, S. Das Sarma, *Phys. Rev. Lett.* **133**, 056501 (2024).
63. P. X. Nguyen *et al*., Perfect Coulomb drag in a dipolar excitonic insulator, dataset, Zenodo (2025).

ACKNOWLEDGMENTS

We thank A. MacDonald, L. Fu, S. Das Sarma, P. Littlewood, and E. Mueller for fruitful discussions. **Funding:** This work was supported by the US National Science Foundation (NSF) under DMR-2004451 (capacitance measurement) and the Department of Energy (DOE), Office of Science, Basic Energy Sciences (BES), under award no. DE-SC0022058 (transport measurement). It was also funded in part by the Gordon and Betty Moore Foundation (grant no. GBMF11563). Growth of the hBN crystals was supported by the Elemental Strategy Initiative of MEXT, Japan and CREST (JPMJCR15F3), JST. This work was performed in part at the Cornell NanoScale Science and Technology Facility, a National Nanotechnology Coordinated Infrastructure (NNCI) member supported by NSF grant NNCI-2025233. We also acknowledge support from the David and Lucille Packard Fellowship (K.F.M.) and the Kavli Institute at Cornell (KIC) Engineering Graduate Fellowship (P.X.N.). **Author contributions:** P.X.N., L.M., and R.C. fabricated the devices, performed the measurements, and analyzed the data. K.W. and T.T. grew the bulk hBN crystals. K.F.M. and J.S. designed the scientific objectives and oversaw the project. All authors discussed the results and commented on the paper. **Competing interests:** The authors declare no competing interests. **Data and materials availability:** All data shown in the main text and supplementary materials are available in the Zenodo data repository (*63*).

SUPPLEMENTARY MATERIALS

science.org/doi/10.1126/science.adl1829
Materials and Methods
Supplementary Text
Figs. S1 to S19
References (*64*–*68*)

Submitted 3 October 2023; accepted 25 February 2025
10.1126/science.adl1829

2D MATERIALS

Perfect Coulomb drag and exciton transport in an excitonic insulator

Ruishi Qi[1,2]†, Andrew Y. Joe[1,2,3]†*, Zuocheng Zhang[1], Jingxu Xie[1,2], Qixin Feng[1,2], Zheyu Lu[1,2], Ziyu Wang[1,4], Takashi Taniguchi[5], Kenji Watanabe[6], Sefaattin Tongay[7], Feng Wang[1,2,8]*

Strongly coupled electron-hole bilayers can host quantum states of interlayer excitons, such as high-temperature exciton condensates at zero magnetic field. This state is predicted to feature perfect Coulomb drag, where a current in one layer is accompanied by an equal but opposite current in the other. We used an optical technique to probe the electrical transport of correlated electron-hole bilayers based on $MoSe_2$/hBN/WSe_2 heterostructures. We observed perfect Coulomb drag in the excitonic insulator phase at low temperatures; the counterflow resistance of interlayer excitons remained finite. These results indicate the formation of an exciton gas that does not condense into a superfluid. Our work demonstrates that dynamic optical spectroscopy provides a powerful tool for probing exciton transport behavior in correlated electron-hole fluids.

An electron-hole bilayer—a two-dimensional electron gas (2DEG) and a two-dimensional hole gas (2DHG) coupled together by Coulomb interactions while remaining electrically isolated—provides a highly tunable platform to study strongly correlated electron-hole fluids. In the strong coupling regime where the interlayer distance is small compared with intralayer particle spacing, the electrons and holes in adjacent layers pair into indirect excitons, and the system is expected to host quantum states including correlated excitonic insulators (*1*, *2*), exciton supersolids (*3*), high-temperature exciton Bose-Einstein condensates (BECs) (*2*, *4*–*6*), and superfluids (*7*–*10*). Such bilayer exciton condensates are characterized by a gapped energy spectrum, spontaneous interlayer phase coherence, and

dissipationless exciton transport (*4*, *11*). The interlayer coherence is expected to manifest itself as counterflow superconductivity with perfect Coulomb drag in transport measurements—a current in one layer must be accompanied by an equal but opposite current in the other (*12*, *13*), with a vanishing exciton resistance.

Evidence of exciton condensation and perfect Coulomb drag has been reported in quantum Hall bilayers in semiconductor double quantum wells (*12*, *14*) and graphene systems (*15*–*17*), but the formation of quasi-electrons and quasi-holes in the quantized Landau levels requires a strong external magnetic field, and the excitons only form at very low temperatures (*18*, *19*). Recently, the research focus has shifted toward searching for an exciton condensate in electron-hole bilayers in the absence of a magnetic field (*1*, *4*, *8*, *20*).

Electron-hole bilayers in semiconducting transition metal dichalcogenide (TMD) heterostructures have attracted special interest because of their strong Coulomb interaction and large exciton binding energy (hundreds of milli–electron volts) (*21*–*24*). Consequently, the strong coupling regime becomes accessible (*20*, *25*). When the bandgap energy is electrically tuned below the exciton binding energy, strongly correlated excitonic insulator states have been experimentally achieved (*1*, *26*). Theoretical study of such systems predicts an exciton BEC that persists until a high-temperature Berezinskii-Kosterlitz-Thouless transition (a fraction of the exciton binding energy) (*8*, *11*). Below this temperature, the interlayer excitons are expected to form an exciton superfluid, in which the exciton transports with zero viscosity, similar to the dissipationless transport of Cooper pairs in conventional superconductors. Electrical transport measurements are therefore highly desired to observe these exotic quantum states. However, most semiconducting TMDs have poor electrical contact to common metals due to a large Schottky barrier.

We have developed an optical technique to measure exciton transport behavior without the need to pass any current through contacts. This allows Coulomb drag measurements and quantitative determination of exciton flow resistance. We show that a TMD-based electron-hole bilayer features perfect Coulomb drag—a drive current in one layer induces an equal current in the other layer—at equal electron and hole densities, which becomes nonperfect but remains strong when additional charges are present. Unexpectedly, our exciton transport measurements show the absence of an exciton superfluid for temperatures down to 2 K, which is in contradiction to many theoretical predictions.

Optical measurement of resistance and Coulomb drag

Figure 1A schematically shows the device structure and the experimental setup. We choose molybdenum diselenide ($MoSe_2$) as the electron layer and tungsten diselenide (WSe_2) as the hole layer for their type II band alignment. They are separated by a 3-nm thin hexagonal boron nitride (hBN) tunneling barrier to ensure equilibrium electron-hole fluids with negligible interlayer tunneling (fig. S1) (*27*). The heterostructure is encapsulated by dielectric hBN on both sides and gated by a few-layer graphene top gate (TG) and two bottom gates (BG1 and BG2). This dual-gated electron-hole

[1]Department of Physics, University of California, Berkeley, CA, USA. [2]Materials Sciences Division, Lawrence Berkeley National Laboratory, Berkeley, CA, USA. [3]Department of Physics and Astronomy, University of California, Riverside, CA, USA. [4]School of Physics, Xi'an Jiaotong University, Xi'an, China. [5]Research Center for Materials Nanoarchitectonics, National Institute for Materials Science, Tsukuba, Japan. [6]Research Center for Electronic and Optical Materials, National Institute for Materials Science, Tsukuba, Japan. [7]School for Engineering of Matter, Transport and Energy, Arizona State University, Tempe, AZ, USA. [8]Kavli Energy NanoScience Institute, University of California, Berkeley, and Lawrence Berkeley National Laboratory, Berkeley, CA, USA.
***Corresponding author. Email: andrew.joe@ucr.edu (A.Y.J.); fengwang76@berkeley.edu (F.W.)**
†These authors contributed equally to this work.

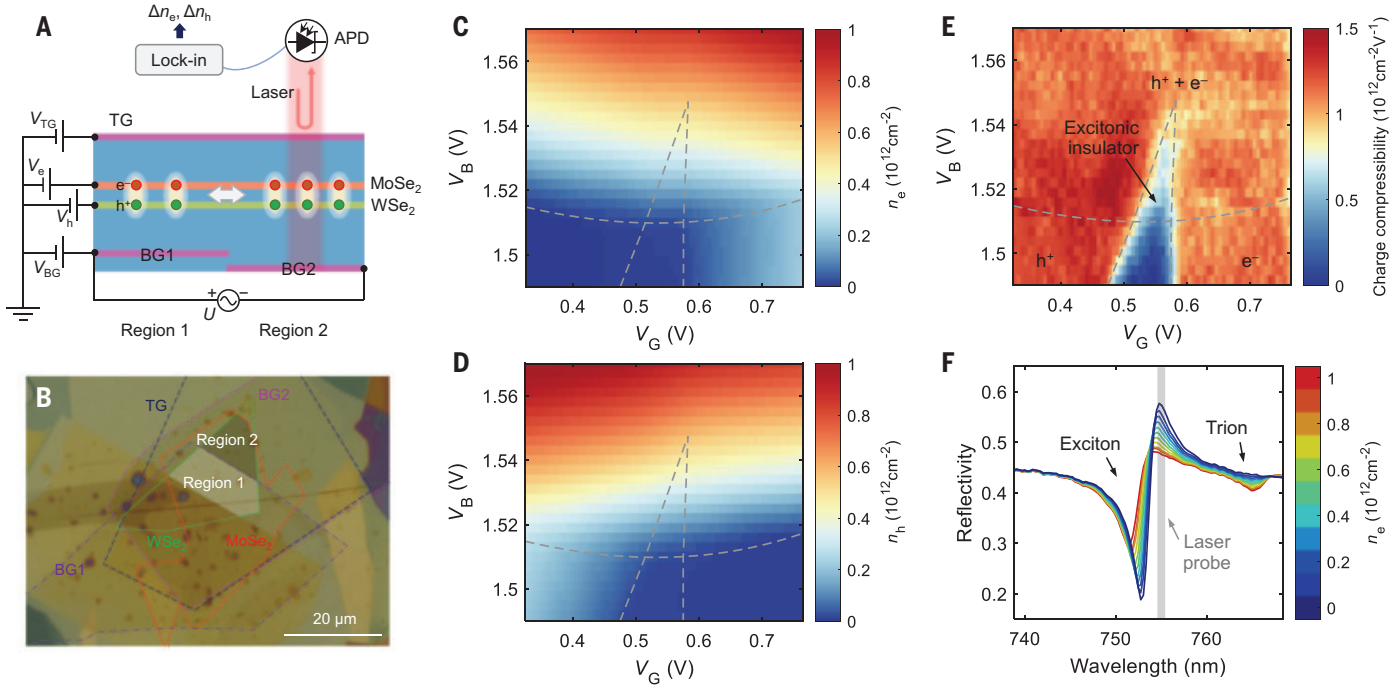

Fig. 1. Correlated electron-hole bilayer device. (**A**) Schematic cross section of device D1, the $MoSe_2$/hBN/WSe_2 heterostructure. The magenta, orange, green, and blue layers denote graphite gates, $MoSe_2$ monolayer, WSe_2 monolayer, and hBN flakes, respectively. The heterostructure has two regions controlled by independent bottom gates (BG1 and BG2). Red and green circles represent electrons and holes, respectively. APD, avalanche photodiode. (**B**) An optical image of device D1, with flake boundaries outlined. (**C** and **D**) Experimentally determined electron (C) and hole (D) density of the electron-hole bilayer in region 2, measured at temperature T = 2 K (*27*). (**E**) Charge compressibility from numerical derivative of electron-hole density imbalance with respect to gate voltage, $\partial(n_e - n_h)/\partial V_G$. The dashed lines are a guide to the eye tracing the boundary of different doping regimes. (**F**) Reflectivity spectrum as a function of electron doping density in the $MoSe_2$ layer. The gray line marks the wavelength of the laser probe.

bilayer device has two regions controlled by separate BGs, each easily tunable with electrical voltages. We began by considering region 1. We kept the electron layer grounded (V_e = 0) and applied voltages on the gates and the hole layer. The gate voltage $V_G \equiv V_{TG} + V_{BG1}$ tunes the Fermi level and thus the net charge density (electron-hole imbalance). The hole-electron voltage difference $V_h - V_e$ and the vertical electric field $V_{TG} - V_{BG1}$ both tune the band alignment. Therefore, the effective interlayer bias voltage $V_B \equiv (V_h - V_e) + \frac{t_m}{t_t+t_m+t_b}(V_{TG} - V_{BG1})$, where t_t, t_m, and t_b are top, middle, and bottom hBN thicknesses in region 1, respectively, controls the effective charge gap. Figure 1B is an optical image of such a device (D1), whose detailed structure is given in fig. S2. We define all the electrical voltages using region 1 and scale the dc voltage on BG2 appropriately such that regions 1 and 2 remain in the same gating and electric field conditions, and thus the electron and hole densities remain homogeneous [details in (*27*)]. Unless otherwise specified, the data discussed hereafter are taken from D1 at a temperature T = 2 K. Similar data have been obtained on device D2, as summarized in fig. S3.

Using reflectance spectroscopy, we were able to determine the doping densities of electrons (n_e) and holes (n_h) as a function of V_G and V_B (*26*, *27*), as shown in Fig. 1, C and D. At low bias voltages, the system has a finite type II bandgap, so only one type of charge can enter the system at a time. When the bias voltage exceeds the gap energy of ~1.51 eV, electrons and holes enter the system at the same time, forming correlated electron-hole fluids that consist of interlayer excitons and possibly extra charges (*1*, *26*). In particular, when the bias voltage reduces the single-particle bandgap to be smaller than the exciton binding energy but still nonzero, an excitonic insulator phase emerges that consists of only interlayer excitons, while no extra unpaired charges are allowed to exist owing to the finite single-particle gap (*1*, *26*). The charge compressibility map (*26*) in Fig. 1E reveals this charge-incompressible triangle region at finite and equal electron and hole densities. In this phase, perfect interlayer correlation is expected at zero temperature. The Coulomb drag is therefore expected to become perfect—any current flow in one layer is necessarily accompanied by an equal but opposite current in the other layer.

In standard electrical transport measurements, multiple contacts are made to each layer to pass currents and measure the resulting voltage drop. However, the contact resistance for TMD layers in the low doping regime is usually orders of magnitude larger than the sheet resistance, and therefore such transport measurements are very challenging. To overcome this problem, we did not drive currents through contacts. Instead, we capacitively drove current between the two heterostructure regions (*28*) in our device by applying a small voltage modulation U = 5 mV (root-mean-square voltage) at angular frequency ω between BG1 and BG2, as illustrated in Fig. 1A. This ac voltage generates an oscillating potential that drives charges and excitons to flow back and forth, leading to an ac particle density change at ω. We then optically detected the density change. The optical absorption of the TMD layers is known to depend sensitively on its local charge density (*29*, *30*). For example, Fig. 1F shows the density dependence of the device reflectivity spectrum near the $MoSe_2$ A-exciton wavelength. With increasing electron density, the intralayer exciton peak loses its oscillator strength, and an additional absorption peak, commonly known as a trion, appears at lower energy (*29*–*31*). We focused a monochromatic laser probe at region 2 (Fig. 1, A and B) and used an avalanche photodiode to read out the reflected light intensity, whose ac component is proportional to the local electron density oscillation Δn_e. Similarly, when the laser wavelength is tuned to the WSe_2 absorption peak, hole density response Δn_h can be measured. The current flow between the two regions, $I_{e/h}$, is directly proportional to the optically measured density change, $I_{e/h} \propto \omega \Delta n_{e/h}$. The optical response therefore provides a probe for charge and exciton transport behavior for the electron-hole bilayer system.

Perfect Coulomb drag

Figure 2, A and B, shows the real part of the hole and electron density oscillation averaged over the low-frequency modulation regime (ω = 0.082 to 41 kHz). The imaginary part is essentially zero at low frequencies (see fig. S4 for a complete dataset). When the bias voltage is small (V_B < 1.51 V), the system forms a 2DEG or a 2DHG with only one type of charge present. The gate modulation will directly drive the charges in the active layer. The holes (electrons) have a well-defined positive (negative) response, owing to their opposite charge. When a high bias voltage closes the gap and both electrons and holes are present, the experiment turns into a Coulomb drag measurement, where the holes are directly capacitively coupled to the bottom gate modulation and drag the electrons with them. If there were no interlayer coupling and both layers acted as perfect metals, the hole layer would completely screen the gate modulation, and the electron layer would have no response. However, the experimental data show that Δn_e is very strong when both layers are doped, indicating strong interlayer interactions in the electron-hole bilayer. Such strong Coulomb drag, where the drag signal is comparable to the drive signal, is unusual, as most coupled bilayer systems have a drag response that is on the order of a percent or less (*32*–*34*). We note that the sign of Δn_e becomes positive in this regime, in contrast to the negative response when there are only electrons in the system. This supports the notion of electrons moving together with holes. For the hole response, the sign remains the same regardless of the electron doping, but the magnitude changes for different doping conditions.

Figure 2C shows the drag ratio $\Delta n_e/\Delta n_h$. Noticeably, the drag ratio features a very strong enhancement when the electron and hole densities are equal. In the excitonic insulator phase, we observe substantially increased drag response and decreased drive response. The drag ratio approaches unity in this triangle region, which is consistent with an excitonic insulator phase that does not allow unpaired charges at low temperatures.

Charge and exciton transport

We next investigated a horizontal linecut at constant bias V_B = 1.52 V (Fig. 3A). Here, the constant V_B leads to nearly constant $n_e + n_h \approx 0.3 \times 10^{12}$ cm^{-2}, and V_G tunes the electron-hole imbalance $n_e - n_h$. At net charge neutrality $n_e = n_h$, the drag signal reaches its peak value, whereas the drive layer has reduced response. Up to our experimental uncertainty, a drag ratio of unity is observed, demonstrating the dominance of exciton transport in the excitonic insulator. When the system is doped with additional electrons or holes, the drag signal decreases rapidly. At zero temperature, the additional electrons or holes are expected to pair with interlayer excitons to create interlayer trions (*35*, *36*), three-particle bound states that resemble hydrogen anions. However, the trion binding energy is likely on the order of 0.1 meV at 3-nm interlayer distance (*35*, *37*, *38*), which is comparable to or smaller than the thermal energy at our base temperature. We do not observe strong peaks in the drag signal at density ratio n_e:n_h of 1:2 or 2:1, presumably because most trions undergo thermal ionization. The drag behaviors at $n_e \neq n_h$ stem largely from the transport of excitons and ionized electrons or holes.

The frequency-dependent density change of the hole and the electron layers is displayed in Fig. 3, B and C, respectively. The gate dependence of the signal shows an abrupt change across the net charge neutrality point, indicating strong excitonic effects in the electron-hole bilayer. The responses remain frequency independent below 100 kHz and start to show frequency dependence when further increasing modulation frequency. The frequency dependence can be understood with the effective ac circuit shown in Fig. 3D. Each heterostructure region forms three geometric capacitances (between TG and $MoSe_2$, between $MoSe_2$ and WSe_2, and between WSe_2 and BG). Ignoring the weak interlayer trion effect, the two heterostructure regions are connected by three

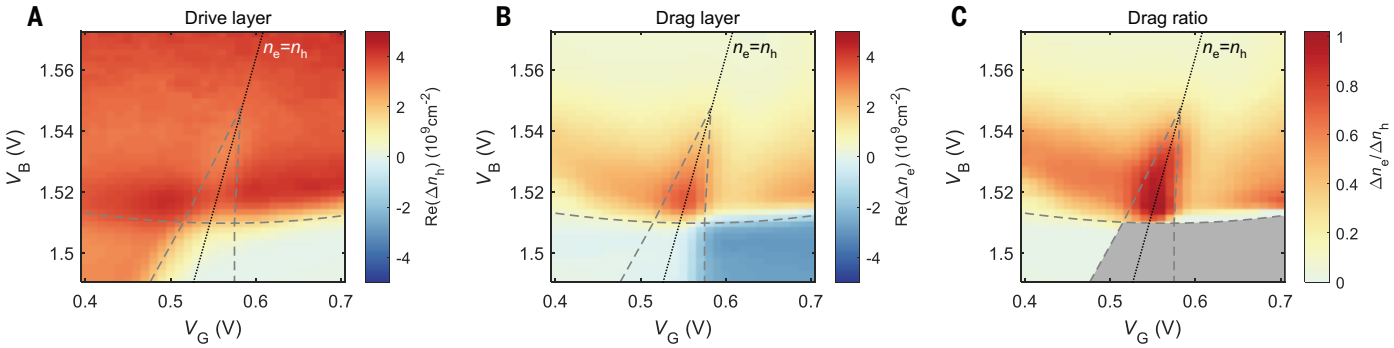

Fig. 2. Strong Coulomb drag in the electron-hole bilayer. (**A** and **B**) Density change of the drive layer (A) and the drag layer (B) under a low-frequency voltage modulation (averaged for ω = 82 Hz to 41 kHz), measured at temperature T = 2 K. (**C**) Drag ratio $\Delta n_e/\Delta n_h$ as a function of gate and bias voltages. The bottom-right region is grayed out because Δn_h is zero when the hole layer is not doped.

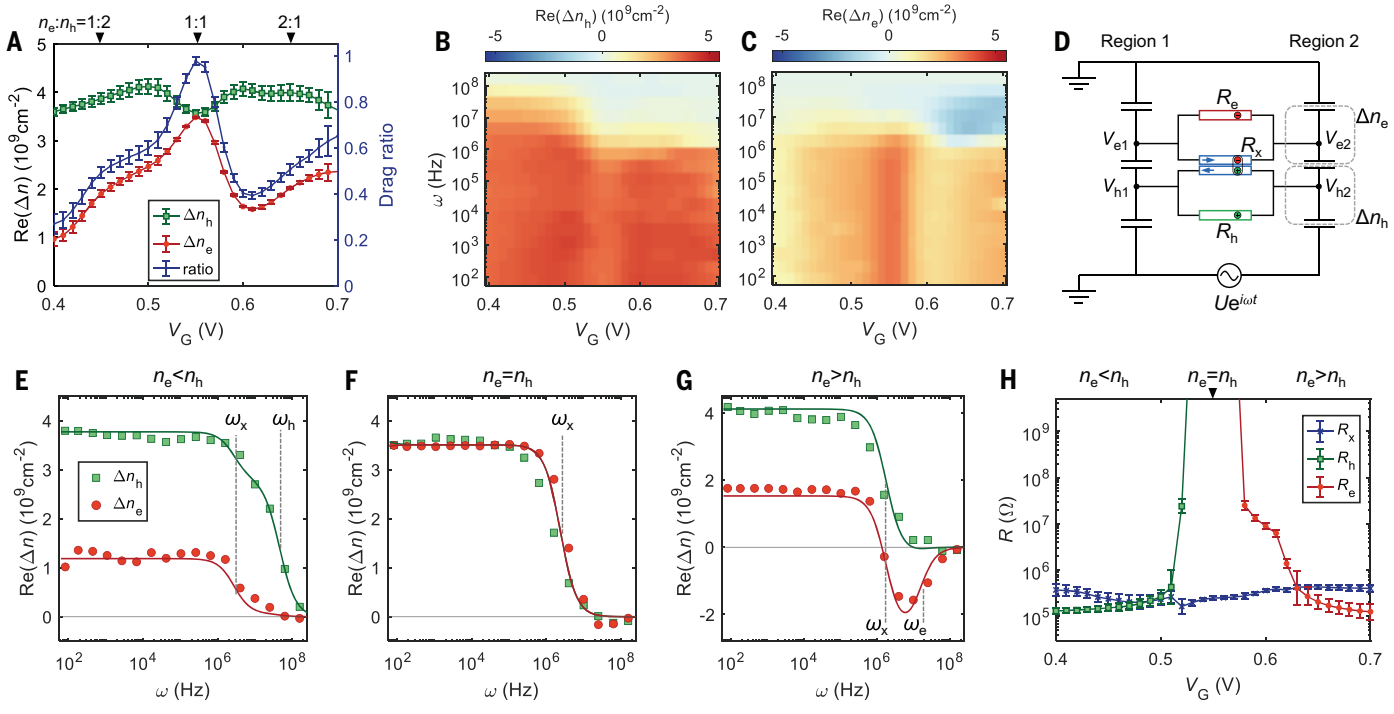

Fig. 3. Exciton and charge transport. (**A**) Drive (green) and drag (red) layer density change as a function of gate voltage at constant V_B = 1.52 V. Right axis (blue): the ratio between Δn_e and Δn_h, revealing perfect Coulomb drag at net charge neutrality. (**B** and **C**) Drive and drag layer density change as a function of V_G under different driving frequencies ω. (**D**) Effective circuit model for transport measurements. (**E** to **G**) Frequency sweeps at V_G = 0.42, 0.55, and 0.63 V, corresponding to three typical doping conditions $n_e < n_h$, $n_e = n_h$, and $n_e > n_h$, respectively. Squares and circles are experimental data for Δn_h and Δn_e, respectively. Solid lines are fitting results from the effective circuit model (*27*). (**H**) Fitted resistance of unpaired electrons (R_e), unpaired holes (R_h), and interlayer excitons (R_x), as a function of V_G. All data are measured at temperature T = 2 K.

effective resistors, corresponding to the transport of unpaired electrons R_e, unpaired holes R_h, and interlayer excitons R_x. Let $V_{ij}(i \in \{e, h\}, j = 1, 2)$ denote the electrochemical potential of layer i and region j. The transport of unpaired electrons and holes can be described by standard resistors R_e and R_h, with current flow $\frac{V_{e1}-V_{e2}}{R_e}$ and $\frac{V_{h1}-V_{h2}}{R_h}$, respectively. The excitons effectively connect the two regions with a special resistor R_x that carries opposite currents for the two layers, $\pm\frac{V_{h1}-V_{h2}-V_{e1}+V_{e2}}{R_x}$, with the WSe_2 layer taking the plus sign and the $MoSe_2$ layer taking the minus sign. In general, the system forms a resistor-capacitor (RC) circuit with three RC time constants set by R_e, R_h, and R_x. As the gate modulation frequency increases, each RC system exhibits a characteristic cutoff frequency, beyond which the corresponding carrier motion becomes ineffective. This occurs because the modulation period becomes shorter than the time required for the carriers to complete a full cycle of motion. Therefore, the frequency-dependent response shows a steplike decay behavior. Depending on the order of the three RC constants, the frequency dependence of the charge density response Δn can have multiple steplike features, each step corresponding to the freeze-out of one type of carrier.

The experimentally measured frequency-dependent density response Δn can be fitted to the effective circuit model to extract the values of R_e, R_h, and R_x. In a strongly coupled bilayer system, the current-voltage relation is determined by a 2-by-2 conductance matrix. The total current, including the contributions

from both excitons and unpaired charges, in the $MoSe_2$ layer and the WSe_2 layer is

$$[I_e I_h] = \begin{bmatrix} \frac{1}{R_e}+\frac{1}{R_x} & -\frac{1}{R_x} \\ -\frac{1}{R_x} & \frac{1}{R_h}+\frac{1}{R_x} \end{bmatrix} \begin{bmatrix} V_{e1}-V_{e2} \\ V_{h1}-V_{h2} \end{bmatrix} \quad (1)$$

With this current-voltage relation, the (Δn_h, Δn_e) response of the circuit can be solved from basic circuit laws as a function of R_e, R_h, and R_x and fitted to the experimental data to get R_e, R_h, and R_x (*27*). Figure 3, E to G, displays the experimental data (symbols) and corresponding fitting results (solid lines) at three typical doping conditions, $n_e < n_h$, $n_e = n_h$, and $n_e > n_h$, respectively. We observe qualitatively distinct behavior among the three doping conditions.

When $n_e = n_h$ (Fig. 3F), the electron and hole responses are identical, with the same amplitude and same cutoff frequency. This demonstrates perfect Coulomb drag in dynamic transport, where the drive current and drag current are identical at all frequencies. The single-step RC decay behavior (determined by R_x) is consistent with the excitonic insulator phase that does not have unpaired electrons or holes. When either type of additional charge is present, the responses of the two layers are no longer identical. When $n_e < n_h$ (Fig. 3E), Δn_e decays at a lower frequency (ω_x) of a few megahertz, but the Δn_h signal survives until a higher cutoff frequency (ω_h) at tens of megahertz. Here ω_x is set by exciton motion, whereas ω_h is determined by the additional unpaired holes. Between ω_x and ω_h, the exciton motion becomes ineffective, so Δn_e drops to nearly zero, but the unpaired holes, being more mobile, can still give rise to finite Δn_h. Similarly, for $n_e > n_h$ (Fig. 3G), there are two steps at different frequencies. The hole layer response Δn_h decays first at a lower frequency ω_x beyond which the exciton motion becomes limited. Above ω_x, the electron response changes its sign because the electron is pushed away from a negative partial gate rather than being dragged by the positive holes during the exciton transport. This pure electron transport then decays at a higher frequency ω_e.

Figure 3H plots the fitted resistances as a function of V_G. The exciton resistance is on the order of hundreds of kilohms and only has a weak gate dependence across the charge neutrality. The unpaired electron and hole resistance change drastically across net charge neutrality, and they do not become conductive at the same time. When $n_e < n_h$, R_e is very large and beyond our measurement range, but when n_e exceeds n_h, it quickly drops below 1 megohm and decreases with increasing electron density. Similar behavior is observed for the hole resistance. This observation indicates that in the low-density regime, the minority carrier cannot exist in the unpaired form, maximizing the number of interlayer excitons. At net charge neutrality, all the electrons and holes pair into bound states of indirect excitons, and the motion of both free charges becomes frozen, leading to perfect Coulomb drag where the current flow can only come from the exciton motion.

Next, we examined the exciton transport at net charge neutrality. Figure 4, A and B, shows the hole and electron density change as a function of pair density n and modulation frequency. At low densities, we observe the same response from the two layers, and the drag ratio (Fig. 4C, right axis) is close to unity for $n \lesssim 0.3 \times 10^{12}$ cm^{-2}. With increased density, the drag ratio gradually decreases owing to the reduced single-particle gap and finite thermal energy. It remains considerable even after the Mott density $n_M \approx 0.8 \times 10^{12}$ cm^{-2} (*1*, *26*). Figure 4D shows the temperature dependence of the drag ratio. At low densities, the Coulomb drag ratio remains larger than 85% up to ~15 K. It keeps decreasing slowly with increased temperature, indicating the coexistence of excitons, unpaired electrons, and unpaired holes at finite temperatures. After complete thermal melting of interlayer excitons at ~70 K (*26*), the drag signal reduces to only ~20% at 80 K. The drag signal does not completely disappear after the quantum dissociation at high exciton density or thermal melting at high temperature, suggesting a considerable drag effect in the

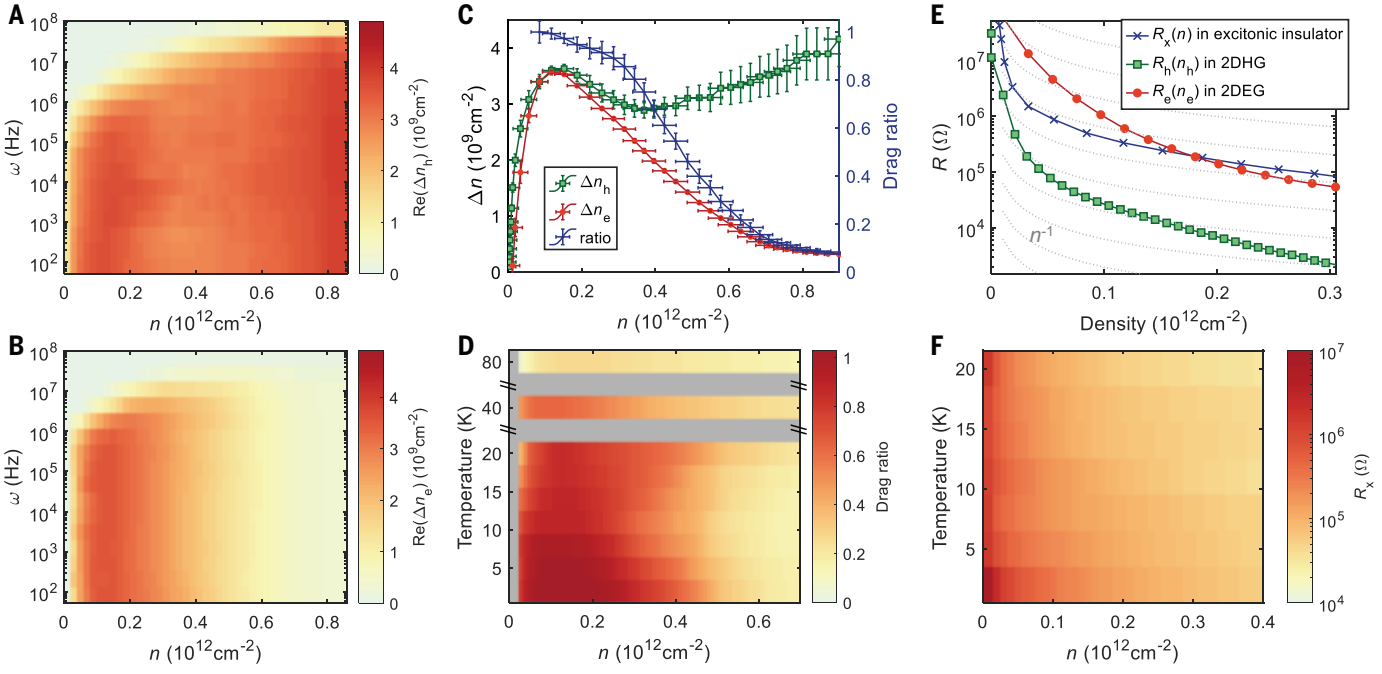

Fig. 4. Drag behavior and exciton transport at charge neutrality. (**A** and **B**) Density and frequency dependence of the drive and drag layer density change at net charge neutrality ($n = n_e = n_h$) at temperature $T = 2$ K. (**C**) Drive (green) and drag (red) layer density change as a function of density n. Right axis (blue): the ratio between Δn_e and Δn_h. (**D**) Density and temperature dependence of the drag ratio at net charge neutrality. (**E**) Fitted exciton resistance R_x as a function of n along the net charge neutrality line shown in blue. Fitted electron (hole) resistance as a function of electron (hole) density in the 2DEG (2DHG) when the opposite charge is not present shown in red (green). Dotted gray lines correspond to constant mobility for reference. (**F**) Density and temperature dependence of the exciton resistance at net charge neutrality.

electron-hole plasma phase caused by strong Coulomb attractions between electrons and holes.

Discussion and outlook

Fitting the electron and hole responses to the effective exciton circuit model yields the exciton resistance R_x as a function of pair density n (Fig. 4E, blue curve). A superfluid transition is not observed. Temperature dependence of the exciton resistance (Fig. 4F) reveals that the exciton resistance decreases with increasing temperature. Contrary to previous theoretical predictions of high-temperature superfluidity in this system (*4*, *6*, *8*), we do not observe any signature of an exciton superfluid down to our base temperature T = 2 K. This could possibly be due to disorders in the samples that might destroy the phase coherence between the excitons or an unexpectedly low superfluid transition temperature (*11*).

Figure 4E compares the resistance of the exciton gas in the excitonic insulator phase (blue), the 2DHG in the WSe_2 layer (green), and the 2DEG in the $MoSe_2$ layer (red) as a function of carrier density. The resistance of the 2DHG in WSe_2 measured here is consistent with standard four-probe transport results (*39*), demonstrating the reliability of our optically measured resistance. At similar carrier density, the resistance of excitons in the excitonic insulator phase is always several times higher than that of the 2DHG in the WSe_2 layer and is overall closer to the resistance of the 2DEG in the $MoSe_2$ layer. Notably, the exciton resistance shows a different density dependence compared with unpaired electrons or holes. The resistance of the 2DHG and the 2DEG both increase substantially faster than $1/n$ at low density, indicating a reduction of mobility potentially caused by interaction-driven Wigner crystallization or unscreened charge defects (*40*, *41*). In contrast, exciton mobility shows a weaker density dependence. The different scaling behavior suggests a different scattering mechanism for interlayer excitons compared with unpaired charges.

Here, we have demonstrated perfect Coulomb drag in the excitonic insulator phase of the electron-hole bilayer system without any external magnetic field. Our results establish TMD-based electron-hole bilayers as a promising platform for exciton-based electronic devices. Although we did not observe exciton superfluidity in TMD bilayers, our work paves the way for further study of counterflow superconductivity and exciton condensates when the sample quality improves further. The optical technique demonstrated here can provide a way to study transport behaviors in TMD-based systems, especially in the low doping regimes where quantum correlation effects are strong but electrical contacts are difficult to make.

REFERENCES AND NOTES

1. L. Ma *et al*., *Nature* **598**, 585–589 (2021).
2. Y. Zeng, A. H. MacDonald, *Phys. Rev. B* **102**, 085154 (2020).
3. S. Conti *et al*., *Phys. Rev. Lett.* **130**, 057001 (2023).
4. F.-C. Wu, F. Xue, A. H. MacDonald, *Phys. Rev. B* **92**, 165121 (2015).
5. X. Zhu, P. B. Littlewood, M. S. Hybertsen, T. M. Rice, *Phys. Rev. Lett.* **74**, 1633–1636 (1995).
6. Y. E. Lozovik, I. L. Kurbakov, G. E. Astrakharchik, J. Boronat, M. Willander, *Solid State Commun.* **144**, 399–404 (2007).
7. P. Pieri, D. Neilson, G. C. Strinati, *Phys. Rev. B* **75**, 113301 (2007).
8. M. M. Fogler, L. V. Butov, K. S. Novoselov, *Nat. Commun.* **5**, 4555 (2014).
9. J.-J. Su, A. H. MacDonald, *Nat. Phys.* **4**, 799–802 (2008).
10. S. Gupta, A. Kutana, B. I. Yakobson, *Nat. Commun.* **11**, 2989 (2020).
11. B. Debnath, Y. Barlas, D. Wickramaratne, M. R. Neupane, R. K. Lake, *Phys. Rev. B* **96**, 174504 (2017).
12. D. Nandi, A. D. K. Finck, J. P. Eisenstein, L. N. Pfeiffer, K. W. West, *Nature* **488**, 481–484 (2012).
13. B. N. Narozhny, A. Levchenko, *Rev. Mod. Phys.* **88**, 025003 (2016).
14. L. V. Butov, A. Zrenner, G. Abstreiter, G. Böhm, G. Weimann, *Phys. Rev. Lett.* **73**, 304–307 (1994).
15. X. Liu, K. Watanabe, T. Taniguchi, B. I. Halperin, P. Kim, *Nat. Phys.* **13**, 746–750 (2017).
16. J. I. A. Li, T. Taniguchi, K. Watanabe, J. Hone, C. R. Dean, *Nat. Phys.* **13**, 751–755 (2017).
17. X. Liu *et al*., *Science* **375**, 205–209 (2022).
18. J. P. Eisenstein, *Annu. Rev. Condens. Matter Phys.* **5**, 159–181 (2014).
19. J. P. Eisenstein, A. H. Macdonald, *Nature* **432**, 691–694 (2004).
20. Z. Wang *et al*., *Nature* **574**, 76–80 (2019).
21. K. F. Mak, J. Shan, *Nat. Photonics* **10**, 216–226 (2016).
22. G. Wang *et al*., *Rev. Mod. Phys.* **90**, 021001 (2018).
23. J. Wang *et al*., *Sci. Adv.* **5**, eaax0145 (2019).
24. J. Wang *et al*., *Phys. Rev. Lett.* **126**, 106804 (2021).
25. L. A. Jauregui *et al*., *Science* **366**, 870–875 (2019).
26. R. Qi *et al*., *Nat. Commun.* **14**, 8264 (2023).
27. See supplementary materials.
28. E. C. Regan *et al*., *Nature* **579**, 359–363 (2020).
29. K. F. Mak *et al*., *Nat. Mater.* **12**, 207–211 (2013).
30. J. S. Ross *et al*., *Nat. Commun.* **4**, 1474 (2013).
31. G. Scuri *et al*., *Phys. Rev. Lett.* **120**, 037402 (2018).
32. S. Kim *et al*., *Phys. Rev. B* **83**, 161401 (2011).
33. T. J. Gramila, J. P. Eisenstein, A. H. MacDonald, L. N. Pfeiffer, K. W. West, *Phys. Rev. Lett.* **66**, 1216–1219 (1991).
34. A. F. Croxall *et al*., *Phys. Rev. Lett.* **101**, 246801 (2008).
35. O. Witham, R. J. Hunt, N. D. Drummond, *Phys. Rev. B* **97**, 075424 (2018).
36. D. D. Dai, L. Fu, *Phys. Rev. Lett.* **132**, 196202 (2024).
37. R. Qi *et al*., arXiv:2312.03251 [cond-mat.mes-hall] (2023).
38. P. X. Nguyen *et al*., arXiv:2312.12571 [cond-mat.mes-hall] (2023).
39. J. Pack *et al*., *Nat. Nanotechnol.* **19**, 948–954 (2024).
40. T. Smoleński *et al*., *Nature* **595**, 53–57 (2021).
41. Z. Xiang *et al*., arXiv:2402.05456 [cond-mat.str-el] (2024).
42. R. Qi *et al*., Perfect Coulomb drag and exciton transport in an excitonic insulator [Dataset], Dryad (2024); https://doi.org/10.5061/dryad.vhhmgqp3h.

ACKNOWLEDGMENTS

Funding: The optical spectroscopy of exciton transport measurements was supported by the AFOSR award FA9550-23-1-0246. The van der Waals heterostructure fabrication was supported by the US Department of Energy, Office of Science, Office of Basic Energy Sciences, Materials Sciences and Engineering Division, under contract DE-AC02-05-CH11231 (van der Waals heterostructures program, KCWF16). S.T. acknowledges support from DOE-SC0020653, NSF CMMI 1933214, NSF mid-scale 1935994, NSF 1904716, and NSF DMR 1552220 and DMR 1955889. K.W. and T.T. acknowledge support from the JSPS KAKENHI (grants 21H05233 and 23H02052) and World Premier International Research Center Initiative (WPI), MEXT, Japan, for the growth of hBN crystals. **Author contributions:** F.W. conceived of the research. R.Q. fabricated the devices with help from A.Y.J., J.X., Q.F., Z.W., and Z.L. R.Q. and A.Y.J. performed optical measurements assisted by Z.Z. and J.X. R.Q., A.Y.J., and F.W. analyzed the data. S.T. grew WSe_2 and $MoSe_2$ crystals. K.W. and T.T. grew hBN crystals. All authors discussed the results and wrote the manuscript. **Competing interests:** The authors declare that they have no competing interests. **Data and materials availability:** The data from this study are available at the Dryad repository (*42*). **License information:** Copyright © 2025 the authors, some rights reserved; exclusive licensee American Association for the Advancement of Science. No claim to original US government works. https://www.science.org/about/science-licenses-journal-article-reuse

SUPPLEMENTARY MATERIALS

science.org/doi/10.1126/science.adl1839
Materials and Methods
Supplementary Text
Figs. S1 to S6
References

Submitted 3 October 2023; accepted 17 December 2024
10.1126/science.adl1839

ORGANIC CHEMISTRY

Asymmetric amination of alkyl radicals with two minimally different alkyl substituents

Yu-Feng Zhang[1,2]†, Biao Wang[1,2]†, Zheng Chen[1,2]†, Ji-Ren Liu[1,2,3]†, Ning-Yuan Yang[1,2], Jin-Min Xiang[1,2], Juan Liu[1,2], Qiang-Shuai Gu[1], Xin Hong[3]*, Xin-Yuan Liu[1,2]*

Differentiating between similar alkyl groups is a major challenge in asymmetric catalysis. Achieving enantiocontrol over unactivated prochiral alkyl radicals is even more difficult owing to their high reactivity and limited interactions with chiral catalysts. In this study, we report a copper-catalyzed asymmetric amination of unactivated prochiral secondary alkyl radicals, using specifically designed chiral anionic multidentate ligands in a radical substitution reaction. This approach efficiently produces highly enantioenriched α-chiral alkyl amines and facilitates the enantioselective formal synthesis of a series of important drug molecules. Mechanistic studies reveal that bulky peripheral modifications on the ligands help create a truncated cone-shaped chiral pocket, enabling precise enantiodiscrimination through steric hindrance and noncovalent interactions. This strategy holds broad potential for asymmetric transformations involving diverse unactivated prochiral alkyl radicals and nucleophiles.

Carbon-centered radicals are a prominent class of reactive intermediates found in numerous contexts, including not only synthetic chemistry but also biochemical (*1*) and astrochemical systems (*2*). However, their short lifetimes and inherent instability have historically posed challenges in generating them and controlling their reactivity, limiting their synthetic utility (*3*). In the past two decades, radical transformations have experienced a resurgence (*4*), driven by advancements in photochemistry (*5*), electrochemistry

(*6*, *7*), and 3d transition metal catalysis (*8*). Complementing photochemical and electrochemical methods that have expanded our ability to generate diverse organic radicals, transition metal catalysis has proven to be a powerful tool for fine-tuning their reactivity. Despite these breakthroughs, precisely controlling the stereochemistry of carbon-centered radical couplings remains a substantial challenge (*9*, *10*).

Over the past three decades, advancements in rational catalyst design—including Lewis acid catalysis (*11*, *12*), organocatalysis (*13*–*16*), transition metal catalysis (*17*–*21*), and enzyme catalysis (*22*–*24*)—have led to considerable progress in catalytic asymmetric radical reactions involving alkyl radicals. These developments have enabled reactions with exceptional chemo-, regio-, and enantioselectivity, efficiently converting abundant feedstocks into valuable chemicals. Two primary types of prochiral alkyl radicals have been successfully used to construct stereocenters at the radical-bearing carbon atoms. The first type comprises alkyl radicals with α-functional groups, which stabilize radicals through conjugation or by facilitating the formation of relatively stable high-valent organometallic species; examples include phenyl, carbonyl, and boryl groups (*18*, *25*). The second type comprises alkyl radicals with remote directing groups, which assist in forming relatively stable organometallic chelate complexes, such as those containing carbonyl or sulfone groups (*18*). In both cases, the functional groups stabilize the radicals or the high-valent organometallic intermediates, allowing for efficient enantiodiscrimination of the pendent α-substituents. However, despite substantial efforts using various chiral catalysts (*26*–*28*), achieving efficient asymmetric intermolecular functionalization of unactivated prochiral alkyl radicals—those lacking a proximal or directing functional group—remains a challenge, even though these radicals have already had a profound impact on synthetic and medicinal chemistry in their racemic form.

The delayed development in this area arises from two primary challenges. First, achieving enantiodifferentiation between two sterically and electronically similar alkyl groups on a prochiral carbon center, as in alkenes, ketones, ketimines, radicals, and carbocations, is a widely recognized challenge in asymmetric catalysis (*29*–*34*) (Fig. 1A). Second, the absence of a stabilizing vicinal or directing group renders the radicals or corresponding high-valent intermediates highly unstable (*35*) and reactive, leading to uncatalyzed nonstereoselective background reactions (Fig. 1B, left). Moreover, the typically low reaction barriers limit the energetic separation between diastereomeric transition states (*3*) (Fig. 1B, right). The lack of functional groups also precludes many common and robust interactions—such as covalent bonding, coordination, charge-charge interactions, and hydrogen bonding—further compromising enantioselectivity.

In biocatalytic processes, certain enzymes have been found to achieve asymmetric transformations of substrates with simple aliphatic substituents through a network of noncovalent interactions (Fig. 1C). These interactions enable precise recognition between enzyme and substrate, resulting in high stereoselectivity (*27*, *28*, *33*). Biophysical studies show that, in many cases, the substrate is positioned within a well-defined chiral cavity. This structural confinement determines the enzyme's substrate specificity and enantioselectivity because the cavity's size primarily governs substrate recognition (*36*).

Inspired by the exceptional capabilities of these enzymes, and to address the challenge of asymmetric functionalization of unactivated prochiral alkyl radicals with broad substrate scope, we hypothesized that a homogeneous copper catalyst, paired with a well-designed bulky chiral ligand forming a truncated cone-shaped pocket, could mimic this asymmetric transformation (Fig. 1D). In this system, the bulkier alkyl groups of unactivated prochiral secondary alkyl radicals would be positioned toward the outer opening of the pocket as the result of steric hindrance, whereas the smaller ones would occupy the inner space (*37*). Favorable noncovalent interactions between the ligand motifs near the outer rim and the larger alkyl groups would likely assist in localizing the bulkier group, facilitating stereodiscrimination. This confined yet partially open catalyst design would accommodate a broad range of alkyl radicals, offering a practical solution to the long-standing challenge of asymmetric functionalization of unactivated alkyl radicals with two minimally different alkyl groups.

Additionally, α-chiral alkyl amines are ubiquitous in natural products, pharmaceuticals, and materials (*38*). Catalytic asymmetric amination of alkyl radicals with amines and their surrogates has recently emerged as a promising approach for preparing α-chiral alkyl amines, with several pioneering efforts reported (*26*, *39*–*41*). However, like other reactions involving prochiral alkyl radicals, these approaches are limited to radical precursors containing an α-functional or remote directing group. To overcome this limitation and expand the synthetic potential of asymmetric radical amination, we envisioned that our strategy would provide a valuable approach for preparing enantioenriched amines with α-stereocenters attached to two alkyl substituents, without requiring any additional functional group.

Here, we report the development of a series of bulky anionic *N*,*N*,*P*-ligands for a copper-catalyzed asymmetric amination of unactivated racemic secondary alkyl iodides with sulfoximines (Fig. 1E). This reaction exhibits broad substrate compatibility, spanning acyclic alkyl iodides with primary, secondary, or tertiary α-alkyl groups, as well as cycloalkyl iodides, yielding excellent enantioselectivity regardless of functional group presence. This catalytic approach can also be applied to the enantioselective C–H amination of a specifically chosen alkane, demonstrating its nascent potential for advancing catalytic asymmetric C–H transformations of readily accessible alkane substrates. Furthermore, the successful formal synthesis of ibrutinib, one of the top five best-selling Food and Drug Administration (FDA)–approved small-molecule drugs in 2023 (*42*), was achieved with excellent enantioselectivity by using this strategy. Mechanistic studies suggest that the Cu and *N*,*N*,*P*-ligand catalysis enables enantiodiscrimination of unactivated prochiral secondary alkyl radicals through outer-sphere radical substitution within a confined and partially open chiral pocket, facilitated by multiple noncovalent interactions.

Reaction development

At the outset, we investigated the enantioconvergent amination of commercially available racemic 2-iodopentane (**E1**), which features similar *n*-propyl and methyl α-substituents, with sulfoximine (*39*) (Fig. 2). To generate the corresponding unactivated alkyl radical, we used the hypervalent iodine(III) compound Mes_2IBF_4 [bis(2,4,6-trimethylphenyl)iodonium tetrafluoroborate] (*43*, *44*), which first forms aryl radicals that rapidly abstract iodine atoms from **E1**. We initially screened more than 20 ligand backbones in the presence of CuTc [copper(I) thiophene-2-carboxylate], Mes_2IBF_4, and Cs_2CO_3 in $^{i}Pr_2O$ (fig. S1). Unfortunately, among the monodentate, bidentate, and tridentate ligands tested, only a few yielded the desired product **1**, and with minimal enantioselectivity. Despite this, the anionic *N*,*N*,*P*-ligand **L*1** (*45*), previously used for copper-catalyzed asymmetric reactions of activated alkyl radicals with various nucleophiles (*20*, *46*, *47*), showed some promise, delivering 24% enantiomeric excess (ee), albeit with very low conversion (<5% yield). To mitigate undesired coordination of the quinoline group (*48*), we tested the tetrazole-based ligand **L*2**, which slightly improved enantioselectivity (28% ee) but remained inefficient.

[1]Shenzhen Grubbs Institute, Department of Chemistry, and Guangming Advanced Research Institute, Southern University of Science and Technology, Shenzhen, China. [2]Shenzhen Key Laboratory of Cross-Coupling Reactions, Southern University of Science and Technology, Shenzhen, China. [3]Center of Chemistry for Frontier Technologies, Department of Chemistry, State Key Laboratory of Clean Energy Utilization, Zhejiang University, Hangzhou, China.
***Corresponding author. Email: hxchem@zju.edu.cn (X.H.); liuxy3@sustech.edu.cn (X.-Y.L.)**
†These authors contributed equally to this work.

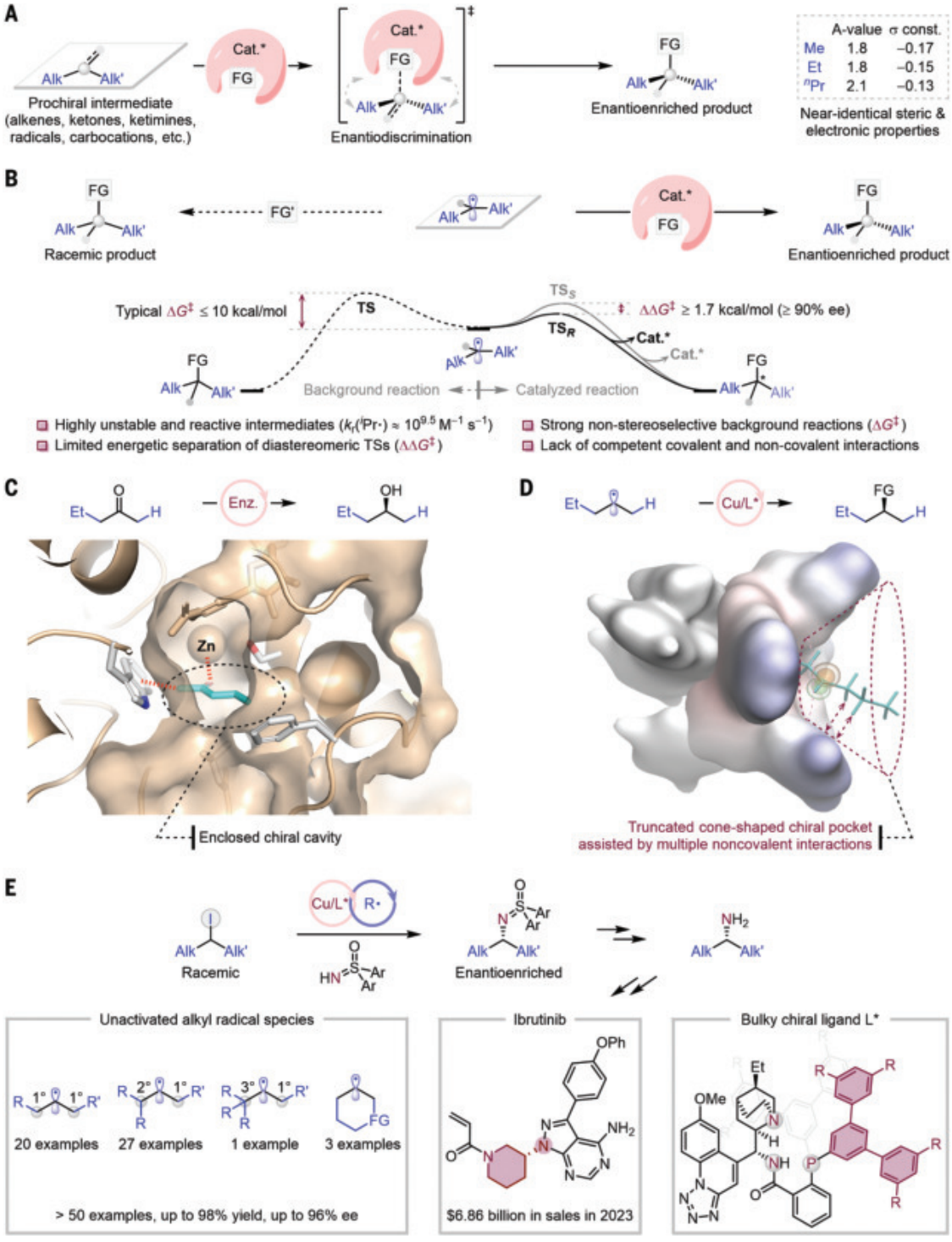

Fig. 1. Context for development of catalytic asymmetric functionalization of unactivated prochiral alkyl radicals. (**A**) Achieving stereodifferentiation between two minimally different alkyl groups is a fundamental challenge in asymmetric catalysis. The steric parameters [A-values, (*62*)] and electronic parameters [σ constants, (*63*)] are extracted from the literature. (**B**) The asymmetric functionalization of unactivated prochiral alkyl radicals with two similar α-alkyl substituents is particularly challenging owing to their high reactivity and the lack of effective interactions with chiral catalysts. The Gibbs free-energy barrier [$\Delta G^{\ddagger}$, (*28*, *64*)], free-energy difference [$\Delta\Delta G^{\ddagger}$, (*65*)], and the radical combination constant for isopropyl radicals [$k_r(^{i}\mathrm{Pr}\cdot)$, (*66*)] are derived or extracted from the literature. (**C**) Enzymatic systems efficiently differentiate between simple aliphatic groups through the formation of a well-defined chiral cavity (*36*). This figure is based on the protein structure of *Geotrichum candidum* acetophenone reductase (Protein Data Bank code: 6ISV). (**D**) We proposed a copper catalyst featuring a truncated cone-shaped chiral pocket, designed to selectively functionalize secondary alkyl radicals with two minimally different α-alkyl substituents. (**E**) Bulky chiral *N*,*N*,*P*-ligands enable copper-catalyzed asymmetric amination of unactivated prochiral secondary alkyl radicals, derived from iodide precursors, independent of functional group presence. This reaction demonstrates broad substrate scope and substantial potential for synthesizing bioactive α-chiral alkyl amines. Alk, alkyl; FG, functional group; Cat.*, chiral catalyst; Et, ethyl; ^{n}Pr, *n*-propyl; const., constant; ee, enantiomeric excess; ^{i}Pr, isopropyl; Enz., enzyme; L*, chiral ligand; Ar, aryl; Ph, phenyl.

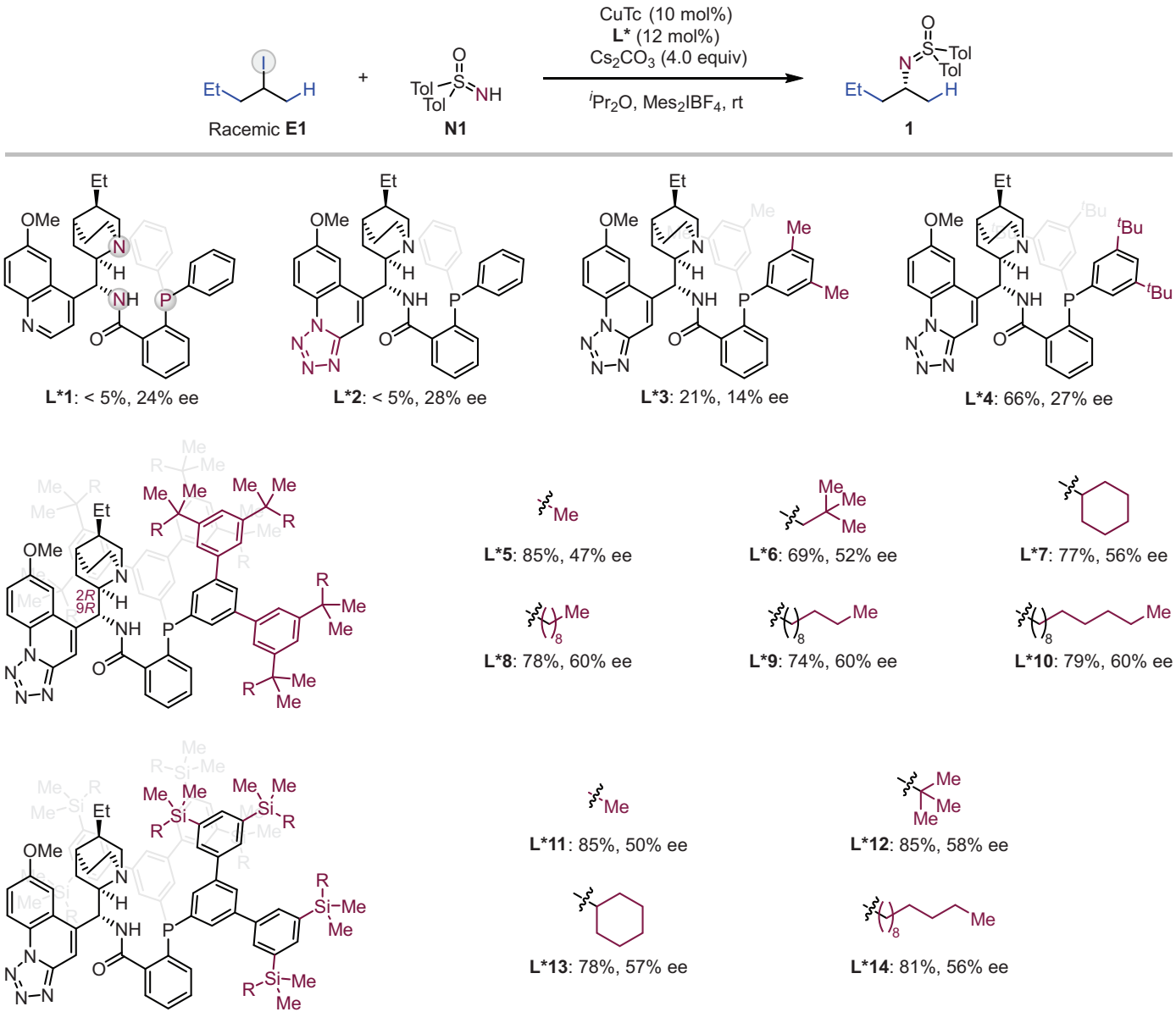

Optimized conditions

Thermal condition A: **1**, 85%, 72% ee

CuTc (10 mol%), **L*9** (12 mol%), Cs_2CO_3 (4.0 equiv), Mes_2IBF_4 (1.5 equiv), $^iPr_2O/CH_2Cl_2$ (50/1), –20 °C.

Photocatalytic condition B: **1**, 52%, 90% ee

CuTc (10 mol%), **L*12** (12 mol%), Cs_2CO_3 (4.0 equiv), toluene/1,3-$F_2C_6H_4$ (1/1), *hν* (390 nm), –78 °C.

Fig. 2. Rationally designed ligands and reaction development. Tol, *p*-tolyl; CuTc, copper(I) thiophene-2-carboxylate; Mes, mesityl; Me, methyl; ^{t}Bu, *tert*-butyl; rt, room temperature. *h*, Planck's constant ($h = 6.626 \times 10^{-34}$ J·s); *ν*, frequency of the radiation.

Inductively coupled plasma mass spectrometry analysis (table S1) suggested that the low efficiency was likely due to poor catalyst solubility (Cu concentration: 0.35×10^{-3} M) when using **L*2**. Recognizing that alkyl groups could enhance the solubility of copper catalysts in nonpolar solvents (*49*), we modified the phosphorus-bound phenyl rings by introducing alkyl substituents in **L*3** and **L*4**, which led to improved reactivity (Cu concentration with **L*4**: 2.7×10^{-3} M). However, enantioselectivity remained low, suggesting that these ligands lacked essential elements for effective enantiocontrol.

Density functional theory (DFT) calculations using a simplified model ligand indicated that C–N bond formation between the unactivated alkyl radical and the LCu(II)–sulfoximinato complex proceeds through an outer-sphere radical substitution mechanism (see below). Unlike inner-sphere reductive elimination from a Cu(III) intermediate, outer-sphere C–N bond formation likely involves enantiodiscrimination at a greater distance from the copper center (*50*, *51*). We hypothesized that introducing bulky peripheral substituents to create a confined chiral pocket could be key to precise

enantiocontrol. With this in mind, we designed ligand **L*5** by replacing the *tert*-butyl groups in **L*4** with larger 3,5-di-*tert*-butyl phenyl groups. This modification markedly improved both enantioselectivity (47% ee) and reactivity (85% yield, Cu concentration: 4.0×10^{-3} M), supporting our ligand design strategy. To further enhance enantioselectivity, we evaluated a series of **L*5** derivatives by replacing one methyl group of the *tert*-butyl substituent with neopentyl (**L*6**), cyclohexyl (**L*7**), and *n*-nonyl (**L*8**) groups. These modifications increased enantioselectivity to 60% ee. However, further elongation of the alkyl chains in **L*9** and **L*10** had negligible impact on the reaction. We hypothesized that the bulky alkyl groups introduced steric effects in the outer coordination sphere and might also engage in noncovalent interactions (*30*, *50*, *52*) with the alkyl substituents of the radical species (fig. S2), optimizing enantiodiscrimination in the outer-sphere radical substitution pathway. Notably, replacing the *tert*-butyl groups in **L*4** with bulkier trimethylsilyl groups slightly improved enantioselectivity, and further increasing the bulkiness of the silyl substituents raised the ee value up to 58%, close to the optimal result achieved with the alkyl-series ligands **L*8** to **L*10**. After further optimizing reaction parameters—such as copper salts, bases, solvents, and reaction temperatures (tables S2 to S5)—we identified optimal conditions with **L*9** as follows: the reaction of **E1** (1.0 equiv) and **N1** (1.0 equiv) in the presence of CuTc (10 mol %), **L*9** (12 mol %), Mes_2IBF_4 (1.5 equiv), and Cs_2CO_3 (4.0 equiv) in a mixture of $^iPr_2O$ and CH_2Cl_2 (50/1 v/v) at –20°C for 3 days, yielding product **1** in 85% yield with 72% ee (Fig. 2 and table S5). The decreased reaction temperature primarily accounted for the enhanced enantioselectivity. To further improve enantioselectivity, we explored photocatalytic conditions, which might enable radical generation at even lower temperatures (*26*, *41*, *53*). Notably, preliminary spectroscopic studies indicated the potential photoactivity of our catalytic system (figs. S3 and S4). Accordingly, we replaced Mes_2IBF_4 with 390-nm light-emitting diode (LED) irradiation and obtained product **1** in 52% yield with 90% ee (Fig. 2 and table S5) at –78°C when using **E1** (1.0 equiv) and **N1** (1.0 equiv) with CuTc (10 mol %), **L*12** (12 mol %), and Cs_2CO_3 (4.0 equiv) for 3 days.

Scope

With the optimal conditions established, we investigated the scope of unactivated alkyl iodides in the asymmetric amination reaction (Fig. 3; figs. S5 and S6 provide details on sulfoximine reagents, product configurations, and catalyst-controlled enantioselectivity). Starting with α-methyl–substituted unactivated alkyl iodides, we found that linear primary α-alkyl substituents, both without (**1** and **2**) and with functional groups—such as chloro (**3**), cyano (**4**), ester (**5** and **7**), phenyl (**6**), azido (**8**), amide (**9**), and trifluoromethyl (**10**)—were compatible. These substrates produced the desired amination products in moderate to good yields with excellent enantioselectivity under photocatalytic conditions. Thermal conditions also proved effective for α-methyl–substituted alkyl iodides, accommodating both functionalized (**11** and **12**) and γ-branched primary α-alkyl groups (**13** to **18**). The length of the alkyl tether had minimal impact on the stereoselectivity of the reaction (e.g., **7** versus **11**; **6** versus **12**). Additionally, both cyclic (**19** to **30**) and acyclic (**31**) secondary α-alkyl substituents were compatible under either photocatalytic or thermal conditions. Functional groups such as carbamate (**19**), ether (**20**), sulfone (**21**), and ketone (**24**) had little effect on the reaction's stereoselectivity. A comparison of thermal and photocatalytic conditions (fig. S7) revealed that enantiocontrol was analogous at the same temperature but that the efficiency of thermal conditions was generally higher. However, as the temperature dropped to –50°C or lower, the efficiency of thermal conditions declined dramatically (table S5). Consequently, for certain substrates (for a typical example, see the results of **1** in Fig. 2 and table S5), photocatalytic conditions were used to achieve better enantiocontrol under such low-temperature conditions. The reaction producing compound **19** was successfully scaled up to the gram scale, with the catalyst loading reduced by half and the reaction time extended to 7 days. Approximately half of the ligand **L*9** was recovered after the reaction. The enantiomer of **19** (*ent*-**19**) was also obtained by using the pseudo-enantiomer of **L*9** [(2*S*,9*S*)-**L*9**], with comparable yield and enantioselectivity. Furthermore, an unactivated alkyl iodide with a bulky adamantyl α-substituent smoothly afforded product **32** in 57% yield and 88% ee. This relatively low sensitivity to the steric bulk of alkyl radicals highlights the versatility of the reaction and is consistent with the proposed outer-sphere C–N bond coupling mechanism.

In addition to α-methyl alkyl iodides, the reaction was also applicable to α-ethyl alkyl iodides. In asymmetric catalysis, distinguishing between linear alkyl groups differing by only a methylene unit becomes increasingly difficult as the chain lengthens. Notably, the catalytic system efficiently differentiated an ethyl group from an *n*-propyl group, delivering product **33** with promising enantioselectivity and demonstrating the system's remarkable enantiocontrol. Even-higher enantioselectivity was observed, with α-ethyl alkyl iodides bearing a γ-branched primary (**34**) or secondary (**35**) alkyl group.

Given the salience of α-chiral cycloalkyl amines in natural products and pharmaceuticals (*54*), we extended our studies to cycloalkyl iodides. Through a straightforward ligand screening process, **L*6** emerged as a privileged ligand. Under optimized conditions, cyclohexyl (**36**) and piperidyl iodides (**37** and **38**) underwent amination with high enantioselectivity (88 to 91% ee) and moderate to excellent yield.

These results demonstrate that various types of unactivated prochiral alkyl radicals—whether generated under photocatalytic or thermal conditions—can be effectively controlled enantioselectively. This not only highlights the broad compatibility of our catalytic system but also suggests its potential for practical applications in the conversion of unactivated prochiral alkyl radicals derived from more complex systems.

Synthetic utility

To enhance the synthetic potential of this catalytic system, we explored the asymmetric radical amination of unactivated C(sp^3)–H bonds, which would allow for the efficient and rapid conversion of low-cost feedstocks into valuable chiral building blocks (*55*). Although this approach is ideal for organic synthesis, asymmetric radical functionalization of unactivated C(sp^3)–H bonds often faces challenges in achieving both regio- and enantioselectivity, particularly in transition metal catalysis (*56*). To mitigate the regioselectivity issue, we used the bulky mesityl (2,4,6-trimethylphenyl) radical, generated in situ from $MesN_2BF_4$, as a relatively selective hydrogen atom abstractor that preferentially targeted the less hindered methylene C–H bonds in 2,2-dimethylpentane (**H1**; fig. S8 provides the results obtained with other alkane substrates), thereby producing the corresponding unactivated alkyl radicals. Using this approach, our catalytic system aminated the alkane, which served as both the C–H substrate and the solvent, yielding the chiral product **17** as the only observable regioisomer in moderate yield (calculated with respect to **N1**). Most of the unreacted **N1** could be recovered. Notably, the enantioselectivity (85% ee) was maintained, comparable to that of the cross-coupling reaction (Fig. 4A and fig. S8), which suggests that radicals formed through alternative pathways can also be effectively controlled enantioselectively within this system.

To further demonstrate the synthetic utility of this catalytic system, the free α-chiral primary amine **39** was readily obtained by deprotecting sulfoximine **38**, with no substantial loss of enantiopurity (Fig. 4B). This magnesium metal–based deprotection protocol is both operationally simple and mild, demonstrating good compatibility with common functional groups such as arenes, isolated alkenes, amides, carbamates, alcohols, and ethers (*39*). However, highly reactive functionalities, such as

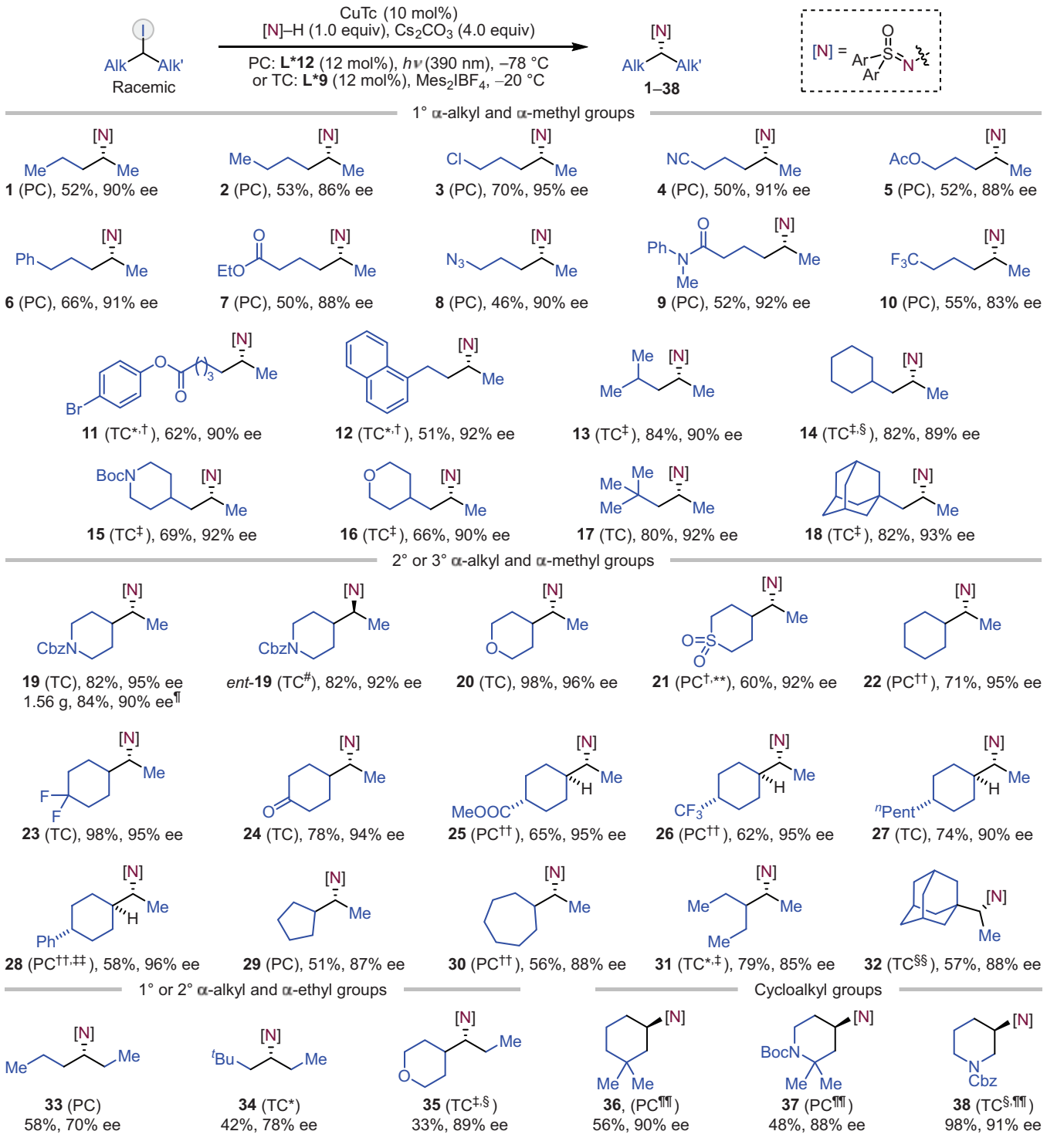

Fig. 3. Scope of racemic unactivated alkyl iodide. Standard conditions: alkyl iodide (0.10 mmol, 1.0 equiv), sulfoximine (0.10 mmol, 1.0 equiv), CuTc (0.010 mmol, 10 mol %), and Cs_2CO_3 (0.40 mmol, 4.0 equiv) in the presence of **L*12** (0.012 mmol, 12 mol %) and 390 nm LEDs at –78°C or **L*9** (0.012 mmol, 12 mol %) and Mes_2IBF_4 (0.15 mmol, 1.5 equiv) at –20°C (additional experimental details provided in supplementary materials). The reported yield is for the isolated product. The ee value was determined by chiral HPLC analysis. *at –40°C; †with **L*14** (12 mol %); ‡with **L*8** (12 mol %); §at –30°C; ¶with CuTc (5.0 mol%) and **L*9** (6.0 mol%) for 7 days; #with (2*S*,9*S*)-**L*9** (12 mol %); **at 5°C; ††at –50°C; ‡‡with **L*14** (15 mol %); §§with CuTc (20 mol %) and **L*8** (24 mol %); ¶¶with **L*6** (12 mol %). PC, photocatalytic conditions; TC, thermal conditions; Ac, acetyl; Boc, *tert*-butyloxycarbonyl; Cbz, benzyloxycarbonyl; ^{n}Pent, *n*-pentyl.

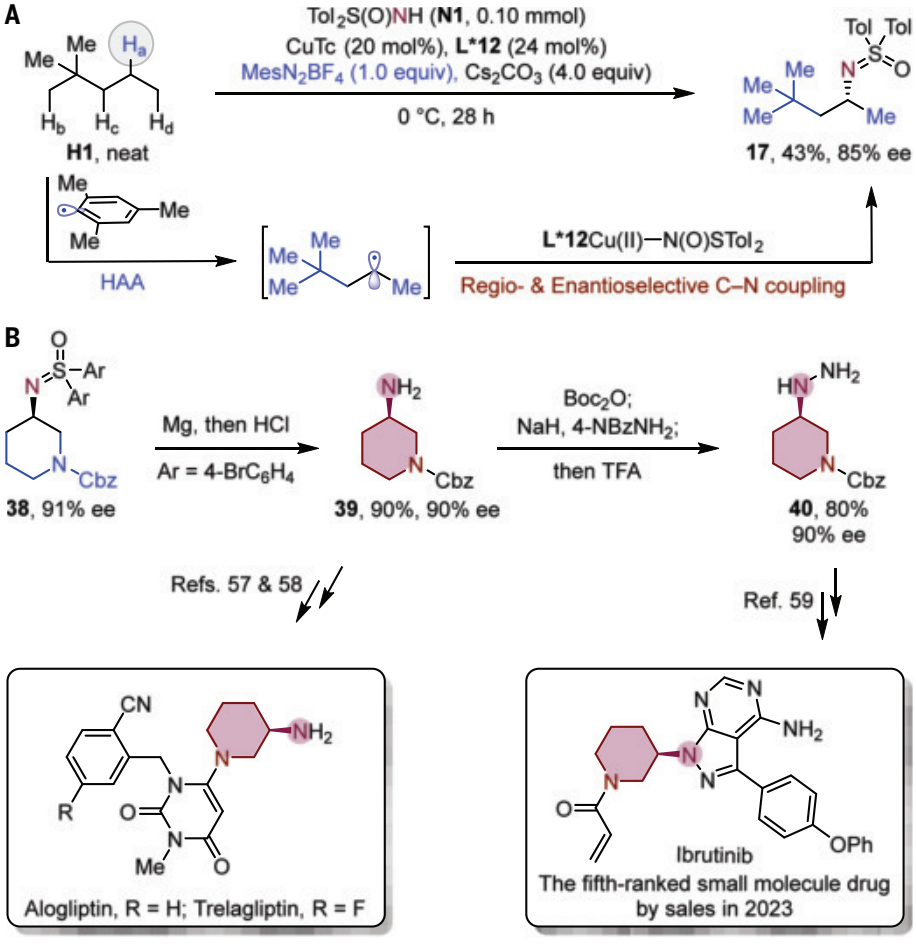

Fig. 4. Asymmetric radical C–H amination of an alkane substrate and synthetic transformations. (**A**) The regioselective and asymmetric radical C–H amination of 2,2-dimethylpentane. (**B**) Facile conversion to α-chiral alkyl primary amines and the formal synthesis of drug molecules. HAA, hydrogen atom abstraction; 4-NBz, 4-nitrobenzoyloxy; TFA, trifluoroacetic acid.

aryl iodides, are unlikely to remain intact under these conditions (fig. S9 provides a more detailed discussion).

Notably, this chiral amine serves as a core motif in nearly 20 approved or prospective drugs (fig. S10). In particular, it has been previously converted into alogliptin (*57*) and trelagliptin (*58*), two drugs used to treat type 2 diabetes. More importantly, simple functional group manipulations of **39** yielded the α-chiral alkyl hydrazine **40**, a key intermediate in the synthesis of ibrutinib (*59*), one of the top-selling small-molecule drugs approved by the FDA in 2023 for the treatment of leukemia and lymphoma (*42*). The absolute configuration of **39** was confirmed by comparison with a commercially available authentic sample, and the configurations of all other cyclic products were assigned by analogy.

Mechanistic investigation

To investigate the reaction mechanism, we conducted control experiments using 6-iodo-1-heptene (**E39**) as a mechanistic probe for radical species under both thermal and photocatalytic conditions (Fig. 5A). These reactions proceeded through tandem cyclization and amination, yielding the coupling product **41** with diastereoselectivity comparable to that of classical free radical cyclization (*60*). Additionally, radical trapping experiments with butylated hydroxytoluene (BHT) led to complete inhibition of the reactions under both conditions, and BHT-trapped products were obtained in considerable yield (fig. S11A). Moreover, the enantiopurity of the products remained consistent over different time intervals, indicating that a uniform mechanism was in operation throughout the reaction and ruling out a kinetic resolution process (fig. S11B). No evidence of enantioenrichment or enantioerosion was observed when enantioenriched alkyl iodide was used, excluding the possibility of dynamic kinetic resolution (fig. S11C). These findings, together with the previously mentioned C–H amination results (Fig. 4A) and the nearly identical enantioselectivity observed under both thermal and photocatalytic conditions (fig. S7), provide strong evidence for the formation of the same unactivated alkyl radical intermediates in both conditions, which are then enantioselectively transformed into the tertiary products (fig. S12 shows the proposed catalytic cycles).

We then performed DFT calculations to gain further insight into the C–N bond formation mechanism and the origins of enantioselectivity. Using the achiral *N*,*N*,*P*-ligand as a model, the mechanism of the C–N bond formation pathway is studied. Starting from the key Cu(II) intermediate **INT-A** and alkyl radical **INT-B**, we identified an outer-sphere radical substitution transition state **TS-C** for C–N bond formation, overcoming a free-energy barrier of 18.1 kcal/mol (Fig. 5B, orange pathway; figs. S13 to S17; tables S6 and S8; and data S1). By contrast, the inner-sphere pathway proceeds through the radical capture transition state **TS-E**, Cu(III) species **INT-F**, and reductive elimination **TS-G**, which requires a higher overall barrier of 22.4 kcal/mol (Fig. 5B, green pathway, and fig. S17). To confirm the nature of radical substitution in **TS-C**, we performed natural bond orbital (NBO) analysis of this transition state, which revealed the interaction between the singly occupied molecular orbital of the alkyl radical and the antibonding orbital of the Cu–N bond (Fig. 5C and fig. S16). This is consistent with the classical free radical substitution mechanism (*61*), and the Mulliken spin distribution analysis also indicated its open-shell singlet electronic configuration (fig. S15).

To explore the origins of enantioselectivity, we modeled the C–N bond formation transition state with the optimal chiral ligand **L*12** (Fig. 5E, figs. S18 to S21, tables S6 and S7, and data S1). The favored transition state **TS-H-**(*R*) leads to the major product **20**, which is 2.6 kcal/mol more favorable than **TS-H-**(*S*), which is consistent with experimental selectivity (Fig. 3). In **TS-H-**(*R*), the bulky cyclohexyl fragment of the alkyl radical occupies the least hindered quadrant of the chiral pocket [Fig. 5D, southeast (SE) quadrant, 28.2% occupied], whereas the smallest hydrogen atom is positioned in the most sterically congested region near the large *P*-substituent [Fig. 5D, southwest (SW) quadrant, 74.2% occupied; and fig. S19, left]. Noncovalent interactions between the 3,5-bissilylphenyl motif of the *P*-substituent and the cyclohexyl group help stabilize the orientation of the alkyl radical (Fig. 5E, left, and fig. S20). Conversely, in **TS-H-**(*S*), the cyclohexyl fragment experiences pronounced steric hindrance from the quinuclidine ring on the ligand (Fig. 5E, right, and fig. S19, right). Further analysis using the distortion and interaction model of these transition states confirmed the combined effects of steric hindrance and

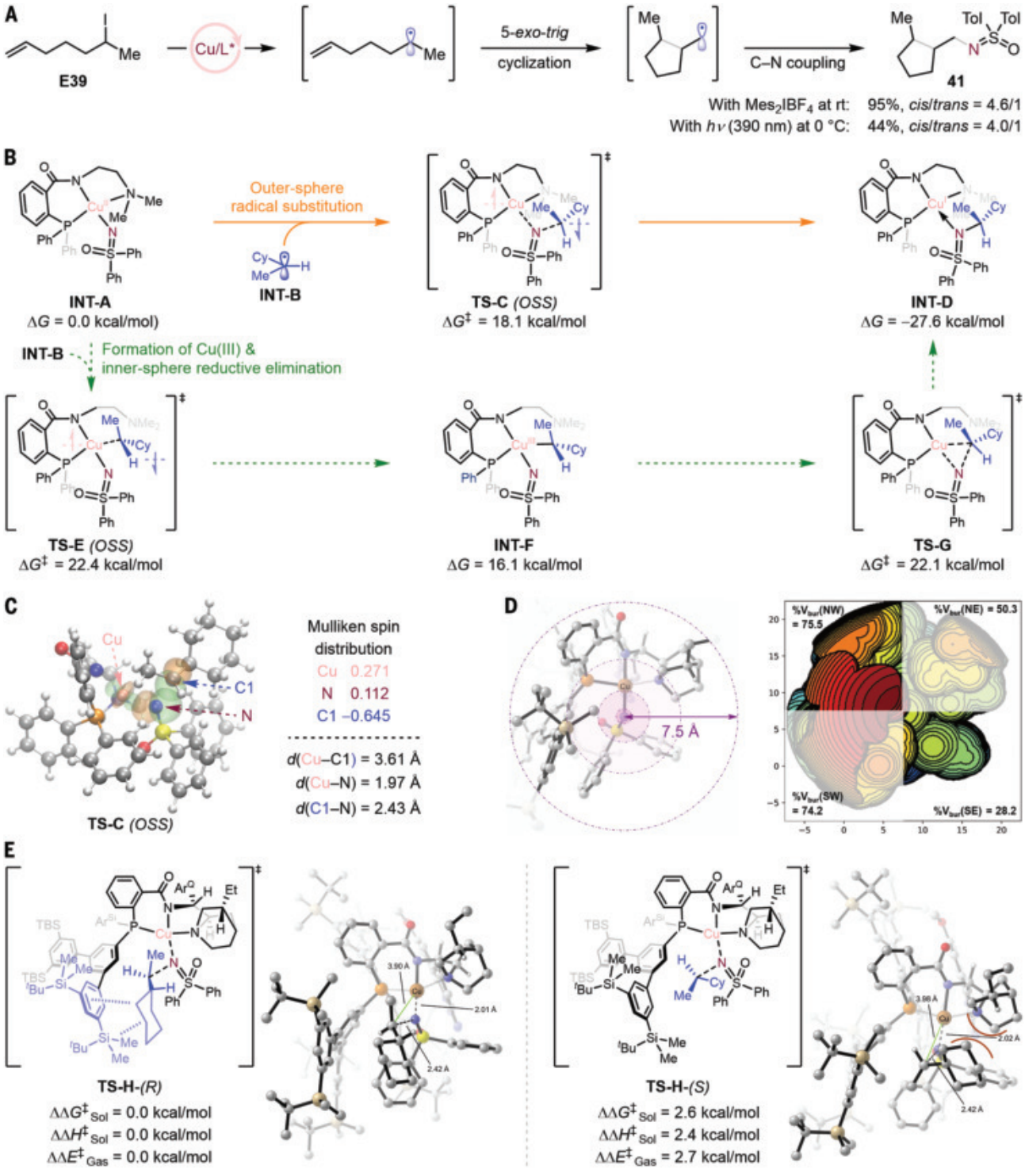

Fig. 5. Mechanistic investigations. (**A**) Radical clock control experiments. (**B**) The DFT-computed free-energy profiles of both outer-sphere and inner-sphere pathways with an achiral model ligand system. (**C**) The three-dimensional (3D) structure, key NBO orbitals, and Mulliken spin distributions of the transition state for radical substitution-type C–N bond formation in an achiral model ligand system. (**D**) A steric map of the chiral pocket derived from the key **L*12**Cu(II)Nu species, which recognizes the prochiral faces of the alkyl radical. (**E**) Enantio-determining transition states for C–N bond formation with **L*12**. Cy, cyclohexyl; OSS, open-shell singlet; $\%V_{bur}$, percent buried volume; NW, northwest; NE, northeast; SW, southwest; SE, southeast; TBS, *tert*-butyldimethylsilyl; Ar^{Q}, 7-methoxytetrazolo[1,5-*a*] quinolin-5-yl; Ar^{Si}, 3,3″,5,5″-tetrakis(*tert*-butyldimethylsilyl)-[1,1′:3′,1″-terphenyl]-5′-yl; Sol, solution; Nu, nucleophile.

weak interactions, which are responsible for the enantiocontrol of the alkyl radical (fig. S21 and table S7). Additionally, preliminary 1D selective gradient nuclear Overhauser effect spectroscopy experiments suggested the potential presence of noncovalent interactions between the alkyl substrates and the alkyl motifs of the ligands. Specifically, a nuclear Overhauser effect signal was observed between the trimethylsilyl group of **L*11** and the alkyl iodide **E13** (fig. S2).

On the basis of these experimental and computational findings, we propose that the enantiocontrol of unactivated prochiral alkyl radicals in this catalytic system originates from the well-defined, truncated cone-shaped pocket, as initially hypothesized. The confined space within the pocket exerts a strong size-exclusion effect, positioning the smaller alkyl group in the congested inner region, while the larger group is pushed outward (Fig. 1D). Additionally, multiple noncovalent interactions provided by the bulky peripheral fragments of the catalyst help control the orientation of the radicals during the free radical substitution process, thereby enhancing enantioselectivity. Accordingly, this catalytic system has successfully achieved highly asymmetric amination of a wide range of unactivated prochiral alkyl radicals.

Conclusions

We have developed a platform involving a copper and chiral anionic *N*,*N*,*P*-ligand catalyst that enables the highly asymmetric amination of unactivated prochiral secondary alkyl radicals. The key to achieving efficient enantiodiscrimination between the two alkyl groups lies in the carefully designed chiral ligands, which create a confined environment. The success of the corresponding asymmetric C–H amination establishes a preliminary foundation for future developments in this area and opens the door to incorporating other radical precursors. We anticipate that this strategy will pave the way for future asymmetric reactions involving more-complex unactivated prochiral alkyl radicals and diverse nucleophiles.

REFERENCES AND NOTES

1. T. Toraya, *Chem. Rev.* **103**, 2095–2127 (2003).
2. K. I. Öberg, *Chem. Rev.* **116**, 9631–9663 (2016).
3. D. P. Curran, N. A. Porter, B. Giese, *Stereochemistry of Radical Reactions: Concepts, Guidelines, and Synthetic Applications* (VCH, 1996).
4. A. Studer, D. P. Curran, *Angew. Chem. Int. Ed.* **55**, 58–102 (2016).
5. A. Y. Chan *et al*., *Chem. Rev.* **122**, 1485–1542 (2022).
6. M. C. Leech, K. Lam, *Nat. Rev. Chem.* **6**, 275–286 (2022).
7. L. F. T. Novaes *et al*., *Chem. Soc. Rev.* **50**, 7941–8002 (2021).
8. R. M. Bullock *et al*., *Science* **369**, eabc3183 (2020).
9. S. Mondal *et al*., *Chem. Rev.* **122**, 5842–5976 (2022).
10. M. P. Sibi, S. Manyem, J. Zimmerman, *Chem. Rev.* **103**, 3263–3296 (2003).
11. L. Zhang, E. Meggers, *Acc. Chem. Res.* **50**, 320–330 (2017).
12. J. Großkopf, T. Kratz, T. Rigotti, T. Bach, *Chem. Rev.* **122**, 1626–1653 (2022).
13. C. K. Prier, D. A. Rankic, D. W. C. MacMillan, *Chem. Rev.* **113**, 5322–5363 (2013).
14. G. E. M. Crisenza, D. Mazzarella, P. Melchiorre, *J. Am. Chem. Soc.* **142**, 5461–5476 (2020).
15. R. S. J. Proctor, A. C. Colgan, R. J. Phipps, *Nat. Chem.* **12**, 990–1004 (2020).
16. C.-L. Wang *et al*., *Science* **382**, 1056–1065 (2023).
17. A. H. Cherney, N. T. Kadunce, S. E. Reisman, *Chem. Rev.* **115**, 9587–9652 (2015).
18. J. Choi, G. C. Fu, *Science* **356**, eaaf7230 (2017).
19. F. Wang, P. Chen, G. Liu, *Acc. Chem. Res.* **51**, 2036–2046 (2018).
20. X.-Y. Dong, Z.-L. Li, Q.-S. Gu, X.-Y. Liu, *J. Am. Chem. Soc.* **144**, 17319–17329 (2022).
21. W.-C. C. Lee, X. P. Zhang, *Angew. Chem. Int. Ed.* **63**, e202320243 (2024).
22. M. A. Emmanuel *et al*., *Chem. Rev.* **123**, 5459–5520 (2023).
23. L. Cheng *et al*., *Science* **381**, 444–451 (2023).
24. Y. Xu *et al*., *Nature* **625**, 74–78 (2024).
25. J. Schmidt, J. Choi, A. T. Liu, M. Slusarczyk, G. C. Fu, *Science* **354**, 1265–1269 (2016).
26. C. Chen, J. C. Peters, G. C. Fu, *Nature* **596**, 250–256 (2021).
27. Y. Yang, J. Liu, Z. Li, *Angew. Chem. Int. Ed.* **53**, 3120–3124 (2014).
28. S. V. Athavale *et al*., *J. Am. Chem. Soc.* **144**, 19097–19105 (2022).
29. Y. Xi *et al*., *J. Am. Chem. Soc.* **142**, 18213–18222 (2020).
30. B. Tao, G. C. Fu, *Angew. Chem. Int. Ed.* **41**, 3892–3894 (2002).
31. F.-H. Zhang, F.-J. Zhang, M.-L. Li, J.-H. Xie, Q.-L. Zhou, *Nat. Catal.* **3**, 621–627 (2020).
32. H. Zhou *et al*., *Nature* **605**, 84–89 (2022).
33. R. Chen, C. S. Kayrouz, E. McAmis, D. S. Clark, J. F. Hartwig, *Angew. Chem. Int. Ed.* **63**, e202407111 (2024).
34. M. Wang *et al*., *Nature* **631**, 556–562 (2024).
35. Y. Yang, S.-L. Shi, D. Niu, P. Liu, S. L. Buchwald, *Science* **349**, 62–66 (2015).
36. A. A. Koesoema *et al*., *Appl. Microbiol. Biotechnol.* **103**, 9543–9553 (2019).
37. B. Mitschke, M. Turberg, B. List, *Chem* **6**, 2515–2532 (2020).
38. T. C. Nugent, Ed., *Chiral Amine Synthesis: Methods, Developments and Applications* (Wiley, 2010).
39. Y.-F. Zhang *et al*., *J. Am. Chem. Soc.* **143**, 15413–15419 (2021).
40. J.-J. Chen *et al*., *Nature* **618**, 294–300 (2023).
41. Q. M. Kainz *et al*., *Science* **351**, 681–684 (2016).
42. R. E. Williams, H. M. Leatherwood, The Njarðarson Group (The University of Arizona), "Top 200 Small Molecule Drugs by Retail Sales in 2023" (2024); https://bpb-us-e2.wpmucdn.com/sites.arizona.edu/dist/9/130/files/2024/07/2023Top200SmallMoleculePosterV6.pdf.
43. X.-Y. Lv, R. Martin, *Org. Lett.* **25**, 3750–3754 (2023).
44. L. Caiger, H. Zhao, T. Constantin, J. J. Douglas, D. Leonori, *ACS Catal.* **13**, 4985–4991 (2023).
45. F. Sladojevich, A. Trabocchi, A. Guarna, D. J. Dixon, *J. Am. Chem. Soc.* **133**, 1710–1713 (2011).
46. Y. Tian *et al*., *Nat. Chem.* **16**, 466–475 (2024).
47. L.-L. Wang *et al*., *Nat. Synth.* **2**, 430–438 (2023).
48. N. Shiomi *et al*., *Org. Lett.* **19**, 74–77 (2017).
49. D. M. Haddleton *et al*., *Macromolecules* **32**, 2110–2119 (1999).
50. F.-L. Wang *et al*., *Nat. Chem.* **14**, 949–957 (2022).
51. H. Lee *et al*., *J. Am. Chem. Soc.* **144**, 4114–4123 (2022).
52. A. A. Thomas *et al*., *J. Am. Chem. Soc.* **140**, 13976–13984 (2018).
53. P. Shi, Y. Tu, D. Ma, C. Bolm, *Adv. Synth. Catal.* **365**, 1613–1617 (2023).
54. I. Schiffers *et al*., *Org. Process Res. Dev.* **26**, 2811–2822 (2022).
55. H. M. L. Davies, K. Liao, *Nat. Rev. Chem.* **3**, 347–360 (2019).
56. A. J. Sterling, N. R. Ciccia, Y. Guo, J. F. Hartwig, M. Head-Gordon, *J. Am. Chem. Soc.* **146**, 6168–6177 (2024).
57. M. Yamada *et al*., *Org. Process Res. Dev.* **25**, 327–336 (2021).
58. S. Xu, Q. Hao, H. Li, Z. Liu, W. Zhou, *Org. Process Res. Dev.* **21**, 585–589 (2017).
59. D. L. Hughes, *Org. Process Res. Dev.* **20**, 1855–1869 (2016).
60. J. Lusztyuk, B. Maillard, S. Deycard, D. A. Lindsay, K. U. Ingold, *J. Org. Chem.* **52**, 3509–3514 (1987).
61. J. C. Walton, *Acc. Chem. Res.* **31**, 99–107 (1998).
62. S. Winstein, N. J. Holness, *J. Am. Chem. Soc.* **77**, 5562–5578 (1955).
63. H. H. Jaffé, *Chem. Rev.* **53**, 191–261 (1953).
64. E. T. Denisov, *Russ. Chem. Bull.* **48**, 442–447 (1999).
65. S. T. Schneebeli, M. L. Hall, R. Breslow, R. Friesner, *J. Am. Chem. Soc.* **131**, 3965–3973 (2009).
66. D. M. Golden, L. W. Piszkiewicz, M. J. Perona, P. C. Beadle, *J. Am. Chem. Soc.* **96**, 1645–1653 (1974).

ACKNOWLEDGMENTS

The authors sincerely thank C. Yu and J. Dong from the School of Life Sciences, Southern University of Science and Technology (SUSTech), for their assistance in preparing the image of *Geotrichum candidum* acetophenone reductase shown in Fig. 1C. We also thank Q. Song from the Shenzhen Grubbs Institute and Guangming Advanced Research Institute, SUSTech, for his help with the ultraviolet-visible and fluorescence spectroscopic characterization. Additionally, we acknowledge the support provided by the SUSTech Core Research Facilities. **Funding:** Financial support from the National Key R&D Program of China (2021YFF0701604 to X.-Y.L.); the National Natural Science Foundation of China (22025103, 92256301, and 22331006 to X.-Y.L.; and 22122109 and 22271253 to X.H.); the Guangdong Innovative Program (2019BT02Y335 to X.-Y.L.); the Guangdong Major Project of Basic and Applied Basic Research (2023B0303000020 to X.-Y.L.); the Guangdong Basic and Applied Basic Research Foundation (2024A1515010324 to Y.-F.Z.); the Shenzhen Science and Technology Program (KQTD20210811090112004 to X.-Y.L. and Q.-S.G., and JCYJ20220818100600001 to X.-Y.L.); the Shenzhen Key Laboratory of Cross-Coupling Reactions (ZDSYS20220328104200001 to X.-Y.L.); the New Cornerstone Science Foundation through the XPLORER PRIZE (to X.-Y.L.); the High-Level of Special Funds (G03050K003 to X.-Y.L.); the High-Level Key Discipline Construction Project (G030210001 to X.-Y.L.); the Zhejiang Provincial Natural Science Foundation of China (LDQ23B020002 to X.H.); the Starry Night Science Fund of Zhejiang University Shanghai Institute for Advanced Study (SN-ZJU-SIAS-006 to X.H.); the CAS Youth Interdisciplinary Team (JCTD-2021-11 to X.H.); the Fundamental Research Funds for the Central Universities (226-2022-00140, 226-2022-00224, 226-2023-00115, and 226-2024-00003 to X.H); the State Key Laboratory of Clean Energy Utilization (ZJUCEU2020007 to X.H.); the State Key Laboratory of Physical Chemistry of Solid Surfaces (202210 to X.H.); the Leading Innovation Team grant from the Department of Science and Technology of Zhejiang Province (2022R01005 to X.H.); and the Open Research Fund of the School of Chemistry and Chemical Engineering of Henan Normal University (2024Z01 to X.H.) is acknowledged. Computational studies are supported by the Center for Computational Science and Engineering of SUSTech. **Author contributions:** Y.-F.Z., B.W., and Z.C. designed the experiments and analyzed the data; Y.-F.Z., B.W., Z.C., N.-Y.Y., J.-M.X., and J.L. performed the experiments; J.-R.L. and X.H. designed the DFT calculations, and J.-R.L. performed the DFT calculations; Y.-F.Z., J.-R.L., Q.-S.G., X.H., and X.-Y.L. wrote the manuscript; and X.-Y.L. conceived and supervised the project. **Competing interests:** The authors declare that they have no competing interests. **Data and materials availability:** Crystallographic data are available free of charge from the Cambridge Crystallographic Database Centre (CCDC) under CCDC 2383922 (for product **S1**). All other characterization data are found in the supplementary materials.

SUPPLEMENTARY MATERIALS

science.org/doi/10.1126/science.adu3996
Materials and Methods
Supplementary Text
Figs. S1 to S21
Tables S1 to S8
References (*67*–*98*)
NMR Spectra
HPLC Spectra
Data S1

Submitted 5 November 2024; accepted 25 February 2025
10.1126/science.adu3996

MARS GEOLOGY

Carbonates identified by the Curiosity rover indicate a carbon cycle operated on ancient Mars

Benjamin M. Tutolo[1]*, Elisabeth M. Hausrath[2], Edwin S. Kite[3], Elizabeth B. Rampe[4], Thomas F. Bristow[5], Robert T. Downs[6], Allan Treiman[7], Tanya S. Peretyazhko[8], Michael T. Thorpe[9,10,11], John P. Grotzinger[12], Amelie L. Roberts[13], P. Douglas Archer[8], David J. Des Marais[5], David F. Blake[5], David T. Vaniman[14], Shaunna M. Morrison[15,16], Steve Chipera[14], Robert M. Hazen[15], Richard V. Morris[4], Valerie M. Tu[17], Sarah L. Simpson[17], Aditi Pandey[4], Albert Yen[18], Stephen R. Larter[1], Patricia Craig[14], Nicholas Castle[14], Douglas W. Ming[4], Johannes M. Meusburger[5], Abigail A. Fraeman[18], David G. Burtt[10], Heather B. Franz[10], Brad Sutter[8], Joanna V. Clark[17], William Rapin[19], John C. Bridges[20], Matteo Loche[19], Patrick Gasda[21], Jens Frydenvang[22], Ashwin R. Vasavada[18]

Ancient Mars had surface liquid water and a dense carbon dioxide (CO_2)–rich atmosphere. Such an atmosphere would interact with crustal rocks, potentially leaving a mineralogical record of its presence. We analyzed the composition of an 89-meter stratigraphic section of Gale crater, Mars, using data collected by the Curiosity rover. An iron carbonate mineral, siderite, occurs in abundances of 4.8 to 10.5 weight %, colocated with highly water-soluble salts. We infer that the siderite formed in water-limited conditions, driven by water-rock reactions and evaporation. Comparison with orbital data indicates that similar strata (deposited globally) sequestered the equivalent of 2.6 to 36 millibar of atmospheric CO_2. The presence of iron oxyhydroxides in these deposits indicates that a partially closed carbon cycle on ancient Mars returned some previously sequestered CO_2 to the atmosphere.

The geomorphology of Mars demonstrates that the planet formerly hosted large quantities of liquid water on its surface, at least intermittently, which requires a higher temperature than at present (*1*, *2*). Climate models of ancient Mars indicate that to produce sufficiently warm conditions for stable liquid water, the atmosphere must have contained at least tens of millibars of atmospheric carbon dioxide (CO_2) (*1*, *2*) and potentially much more (several bars) (*3*–*5*). The current martian atmosphere contains only ~6 mbar CO_2 (*6*).

It has been estimated that volcanic outgassing would have provided the equivalent of 0.1 to 10 bar of CO_2 to Mars' early atmosphere (*7*, *8*). Much of this CO_2 (up to 3 bar) was subsequently lost to space (*6*), but enough CO_2 must have been present in the atmosphere at some point for liquid water to be stable. Under those conditions, reactions between liquid water and rock (aqueous alteration) are predicted to have produced sedimentary carbonates (*9*, *10*).

There have been several detections of carbonate minerals on Mars (*6*, *11*, *12*), but in lower quantities than were predicted (*10*, *11*, *13*). Carbonates have been identified in situ by using rovers, remotely by orbiters, and in martian meteorites (supplementary text). Those carbonates have a wide range of compositions and mineralogical contexts (*12*) but are mostly iron (Fe)–bearing carbonates with differing (but substantial) magnesium (Mg)–, calcium (Ca)–, and manganese (Mn)–carbonate components (*12*). The chemistry of carbonates can record their formation pathways (*14*, *15*). The measured compositions of martian carbonates are generally consistent with formation through aqueous alteration of basalt, which is supported by their colocation with primary basaltic minerals such as olivine and pyroxene (*12*). These properties have been interpreted as indicating that the dominant mode of carbonate mineral formation on Mars is direct, possibly hydrothermal, replacement of basaltic minerals rather than sedimentary processes (*12*).

Spectroscopic mapping of surface geology from orbit can be used to estimate global mineralogical inventories (*11*). Global deposits of carbonates on Mars are estimated to have sequestered the equivalent of 10 mbar to 1 bar of atmospheric CO_2 (*6*). These estimates span a wide range because few carbonate exposures have been identified from orbit (*16*). Either carbonate minerals are rare on the surface of Mars, or they are present in a form that eludes detection by reflectance and thermal emission spectroscopy. In either case, there is little evidence of the carbonates in sedimentary rocks that are predicted by climate and geochemical models.

Rover drill samples contain siderite

We searched for carbonates using data from the Curiosity rover, part of the Mars Science Laboratory mission, which is exploring Aeolis Mons (informally known as Mount Sharp) in Gale crater, Mars. In late 2022, the rover reached sedimentary strata containing magnesium sulfates (*17*), part of a sulfate-rich unit that had previously been mapped from orbit (*18*). The rover drilled four samples of these rocks (Fig. 1) in locations imaged with the Mast Camera (Mastcam) (*19*). Those samples were analyzed by using the rover's Chemistry and Mineralogy (CheMin) instrument, which uses x-ray diffraction to determine sample mineralogy.

Crystalline starkeyite ($MgSO_4{\cdot}4H_2O$) was present in the drill hole informally called Canaima, which was sampled at −3879 m elevation (relative to Mars mean radius) from the strata informally designated the Contigo member (lithologically distinct subdivision) of a larger sedimentary unit, informally designated the Mirador Formation (*17*). Curiosity then ascended onto a nearby prominent bench informally known as the Marker Band (*20*), which extends almost continuously around Mt. Sharp. Geologically, this is informally designated as the Amapari member of the Mirador Formation. The hard rocks of the wave-rippled strata of the Amapari member could not be drilled, but a drill sample informally named Tapo Caparo was obtained from the overlying thickly laminated strata, at −3853 m elevation (fig. S1) on sol 3752 (where mission sols are martian days elapsed since the rover landed). The Canaima and Tapo Caparo samples were obtained from sedimentary deposits that were laid down in a lacustrine (lakebed) environment. A further drill sample, informally named Ubajara, was acquired at −3826 m elevation on sol 3823, above a transition to sediments from a predominantly eolian (wind-blown) environment (Fig. 1). This unit, informally designated the Chenapau member of the Mirador Formation, has sedimentary features, such as sand sheets (fig. S2), that indicate there was a shallow water table that limited sand accumulation (*21*). Another drill sample, informally named Sequoia, was obtained from Chenapau sandstones at −3764 m elevation on sol 3980 (fig. S3).

[1]Department of Earth, Energy, and Environment, University of Calgary, Calgary, AB, Canada. [2]Department of Geoscience, University of Nevada–Las Vegas, Las Vegas, NV, USA. [3]Department of Geophysical Sciences, University of Chicago, Chicago, IL, USA. [4]Astromaterials Research and Exploration Science Division, NASA Johnson Space Center, Houston, TX, USA. [5]Exobiology Branch, NASA Ames Research Center, Moffett Field, CA, USA. [6]Department of Geosciences, University of Arizona, Tucson, AZ, USA. [7]Lunar and Planetary Institute, Universities Space Research Association, Houston, TX, USA. [8]Amentum, NASA Johnson Space Center, Houston, TX, USA. [9]Department of Astronomy, University of Maryland, College Park, MD, USA. [10]Solar System Exploration Division, NASA Godard Space Flight Center, Greenbelt, MD, USA. [11]Center for Research and Exploration in Space Science and Technology, NASA Goddard Space Flight Center, Greenbelt, MD, USA. [12]Division of Geological and Planetary Sciences, California Institute of Technology, Pasadena, CA, USA, Pasadena, CA, USA. [13]Department of Earth Science and Engineering, Imperial College London, London, UK. [14]Planetary Science Institute, Tucson, AZ, USA. [15]Earth and Planets Laboratory, Carnegie Institution for Science, Washington, DC, USA. [16]Department of Earth and Planetary Sciences, Rutgers University New Brunswick, Piscataway, NJ, USA. [17]Texas State University–Amentum Johnson Space Center Engineering, Technology, and Science II, NASA Johnson Space Center, Houston, TX, USA. [18]Jet Propulsion Laboratory, California Institute of Technology, Pasadena, CA, USA. [19]Institut de Recherche en Astrophysique et Planétologie, Université de Toulouse, CNRS, Centre National d'Études Spatiales, Toulouse, France. [20]Space Park Leicester, University of Leicester, Leicester, UK. [21]Los Alamos National Laboratory, Los Alamos, NM, USA. [22]Globe Institute, University of Copenhagen, Copenhagen K, Denmark.
*Corresponding author. Email: benjamin.tutolo@ucalgary.ca

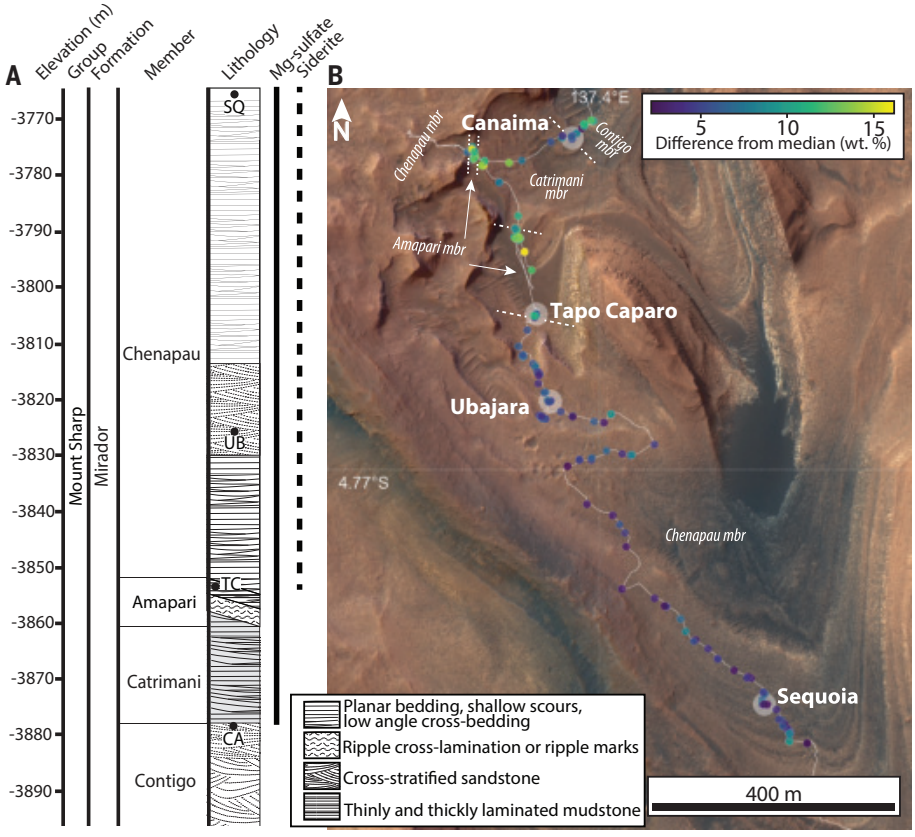

Fig. 1. Geological context of the drill samples. (**A**) Stratigraphic column indicating elevations and sedimentological interpretations of the 89-m vertical section traversed by the rover. Group, formation, and member designate the sedimentary units. Hatching styles indicate the lithology, as indicated in the legend. Black circles indicate drill sample locations: CA, Canaima; TC, Tapo Caparo; UB, Ubajara; and SQ, Sequoia. Vertical thick lines extend between sample elevations where Mg-sulfate minerals (solid line) and siderite (dashed line) have been detected. (**B**) Orbital optical image mosaic of Gale crater, overlain with Curiosity's traverse (white line) up Mt. Sharp. Member (mbr) boundaries correspond to the section in (A). The difference between ChemCam observation points and the median Chenapau bedrock composition (*19*) is plotted as colored circles (as indicated in the color bar) at locations where ChemCam analyses were performed. Chenapau member chemistry is homogeneous and closely resembles the chemistry of the upper section of the Amapari member, near the Canaima drill site.

Table 1. Mineralogical composition of the examined samples. Values of mineral and amorphous component abundance (in weight %) derived from the CheMin data and their 1σ uncertainties. Dashes indicate that the phase was below CheMin detection limit (<1 wt %).

Phase	Tapo Caparo	Ubajara	Sequoia
Plagioclase	15.3 ± 0.7	14.8 ± 1.2	21.1 ± 0.7
Pyroxene	8.7 ± 0.8	6.0 ± 0.8	13.9 ± 0.9
Quartz	–	0.9 ± 0.2	0.9 ± 0.2
Hematite	–	2.3 ± 0.7	2.4 ± 0.7
Goethite	–	1.2 ± 0.2	–
Akageneite	–	–	2.7 ± 0.6
Siderite	10.5 ± 0.5	4.8 ± 0.3	7.6 ± 0.4
Anhydrite	0.8 ± 0.2	0.5 ± 0.2	2.6 ± 0.3
Bassanite	1.5 ± 0.4	0.8 ± 0.1	–
Gypsum	–	2.3 ± 0.2	–
Starkeyite	–	6.4 ± 0.8	–
Kieserite	3.2 ± 0.4	–	5.8 ± 0.8
Amorphous	60 ± 12	60 ± 12	43 ± 13

We analyzed CheMin measurements of each of these four drill samples (figs. S4 to S7) (*19*), finding that the Tapo Caparo, Ubajara, and Sequoia samples contain crystalline siderite ($FeCO_3$) at respective abundances of 10.5 ± 0.5, 4.8 ± 0.3, and 7.6 ± 0.4 wt % (1σ uncertainties). The samples also contain basaltic minerals [the sodium (Na)–, Ca-, and aluminum (Al)–bearing silicate mineral plagioclase and the Ca- and Mg-bearing silicate mineral pyroxene], calcium sulfates, magnesium sulfates, different amounts of iron oxyhydroxides, and an unidentified x-ray amorphous material (Table 1, Fig. 2, and supplementary text). The abundance of siderite in these samples was sufficiently high for our analysis procedure (*19*) to determine the cation compositions of the carbonates (fig. S8). We found that the siderite is highly pure, with estimated formulas of $Fe_{0.97}Mg_{0.03}CO_3$, $Fe_{0.95}Mg_{0.05}CO_3$, and $FeCO_3$ for the Tapo Caparo, Ubajara, and Sequoia siderites, respectively (Fig. 2C).

We confirmed the siderite purity and accompanying mineralogy using the Sample Analysis at Mars (SAM) instrument suite, which combusts samples to produce gases and performs evolved gas analysis (EGA) to determine their chemistry (*19*). EGA of these samples by use of SAM shows that all three exhibit a similar CO_2 release, caused by carbonate mineral thermal decomposition, at temperatures >100°C lower than would be expected from Mg- or Ca-carbonates (fig. S9). The SAM results are consistent with the formulas calculated from the CheMin data for all three samples.

Siderite deposition requires fluid supersaturation

The abundance and composition of the carbonates in the drill samples indicates a sedimentary pathway for carbonate formation and preservation on Mars. Siderite has been theoretically predicted to be a primary, early-forming sedimentary mineral on Mars (*12*, *22*). The nearly pure $FeCO_3$ compositions we found are unlike the Ca- and Mg-rich carbonates that were previously identified in martian samples (Fig. 2C).

The siderite and sulfates in the analyzed sediments were deposited by fluids. We constrained properties of the fluid by considering the mineralogy and geological context of the samples in a geochemical framework (*19*). Like other carbonates (*23*), siderite is much more soluble in an aqueous solution if carbonic acid (H_2CO_3) is more abundant than its dissociation product, bicarbonate (HCO_3^-) (Fig. 3). To allow precipitation, any siderite-forming solution must therefore have substantial alkalinity (effectively, the sum of HCO_3^- and CO_3^{2-} concentration in equivalents units) at neutral or basic pH, depending on the partial pressure of CO_2 (P_{CO_2}) in the solution (Fig. 3). This P_{CO_2} might or might not have been representative of atmospheric P_{CO_2} at the time the siderite

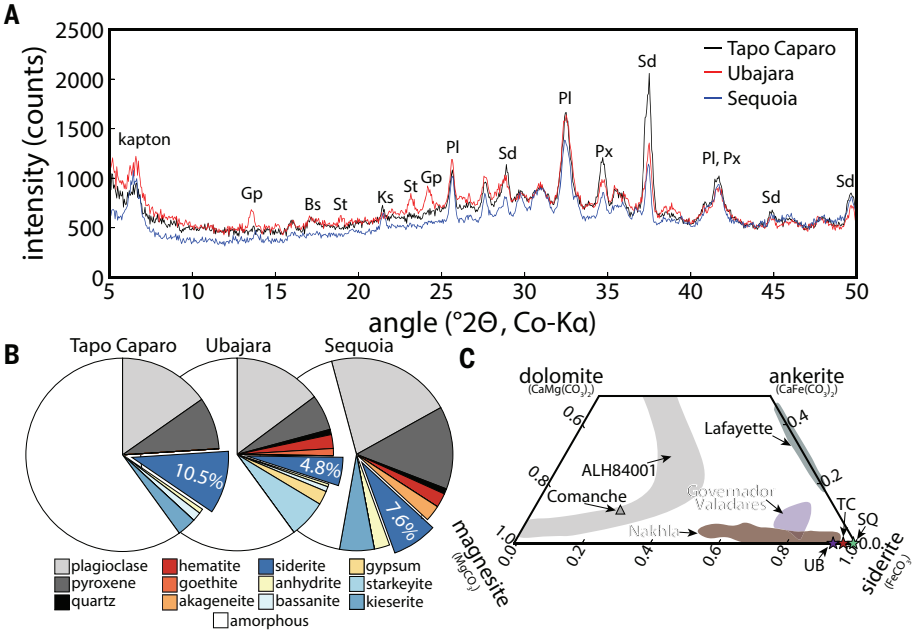

Fig. 2. Mineralogy of the samples and composition of the siderite. (**A**) X-ray diffraction patterns measured with CheMin from three samples (as indicated in the legend). Intensity is plotted as a function of the 2θ diffraction angle, in degrees, corresponding to CheMin's Cobalt (Co) Kα x-ray source (*19*). Peaks are labeled with the identified minerals: Sd, siderite; Gp, gypsum; Px, pyroxene; St, starkeyite; Bs, bassanite; Ks, kieserite; and Pl, plagioclase. A peak due to the Kapton window on the CheMin cell is also labeled. (**B**) Pie charts showing the calculated mineralogical and amorphous phase abundances in the Tapo Caparo, Ubajara, and Sequoia samples. Colors indicate minerals. The siderite wedges are offset and labeled with their abundance. (**C**) The carbonate compositions of the investigated samples (stars, labeled as in Fig. 1A) compared with shaded regions corresponding to the composition of carbonates previously identified in martian meteorites (ALH84001, Lafayette, Nakhla, and Governador Valadares) and at the Comanche outcrop in Gusev Crater (*12*) on a ternary diagram for the Ca, Mg, and Fe carbonate system.

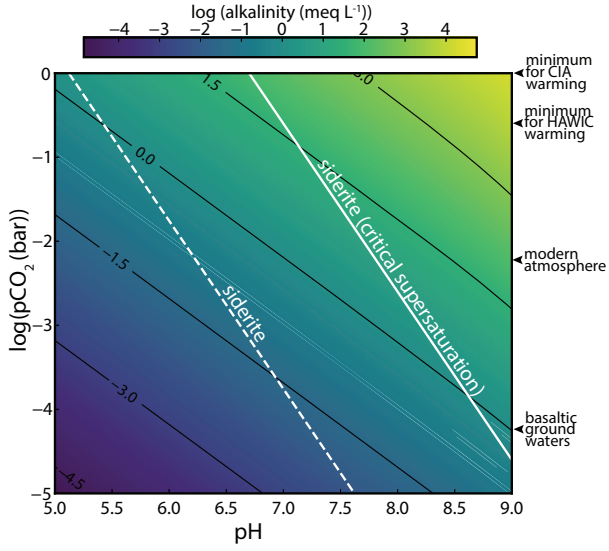

Fig. 3. Thermodynamic requirements for siderite formation. The dashed white line indicates the minimum pH required for siderite precipitation as a function of P_{CO_2}, determined from our thermodynamic solubility calculations (*19*). The thick white line is the same threshold but for the experimentally measured critical supersaturation, which incorporates kinetic inhibition of siderite precipitation (*35*). Color indicates the corresponding alkalinity in milliequivalents per liter (meq L^{-1}); thin black lines are contours labeled with the corresponding values. Black arrowheads indicate the minimum atmospheric P_{CO_2} theoretically predicted to stabilize liquid water in collision-induced absorption (CIA) (*3*) and high-altitude water ice cloud (HAWIC) (*2*) scenarios, and the modern martian atmosphere (*6*). Also indicated is the maximum P_{CO_2} measured in Icelandic basaltic groundwaters (*24*), which is much lower than Earth's atmospheric P_{CO_2} (*19*).

was deposited; less alkalinity is required to precipitate siderite at lower P_{CO_2} typical of basaltic groundwaters (*24*) than at the theoretically predicted P_{CO_2} of the ancient martian atmosphere (Fig. 3). Because siderite contains Fe in its chemically reduced state, the siderite-forming solutions must also have been less oxidized than the modern martian surface and atmosphere, in which the stability of oxidized Fe is demonstrated by the prevalence of oxidized (red) Fe. Isotopic analysis of the siderite shows that it is enriched in heavy isotopes of C and O, relative to both the modern and predicted ancient Mars atmospheres (*25*). Because siderite is preferentially produced in reducing, lower-than-atmospheric P_{CO_2} solutions, we propose that it formed in subsurface pore spaces that were not in direct contact with the atmosphere.

The composition of the siderite provides further constraints on its formation conditions. Because dissolved Mn^{2+} is easily incorporated into siderite (*15*), the lack of measurable Mn^{2+} in the analyzed siderites indicates that the precipitating solution contained little or no Mn^{2+}. Olivines and pyroxenes in martian meteorites usually contain substantial Mn^{2+} (*26*), which would be released alongside Fe^{2+} during basalt dissolution. We therefore infer that the siderite did not form through direct replacement of basaltic minerals. Similarly, the negligible Mg^{2+} contents of the siderite are consistent with formation at low temperature (*14*, *15*). The absence of Ca^{2+} in the siderite indicates a high Fe^{2+}/Ca^{2+} ratio in the precipitating solution at the time of siderite formation (*14*, *15*). The drill samples also contain Ca-sulfate minerals, which require substantial Ca^{2+} and SO_4^{2-} in the solution. We therefore infer that the siderites and sulfates formed from solutions with substantially different Fe^{2+}/Ca^{2+} ratios, or at different times from an evolving solution. This ratio could fall over time if a substantial fraction of Fe was removed through siderite precipitation, leaving Ca still in solution (fig. S10). Sulfates have been prevalent along Curiosity's traverse of Mt. Sharp, and at least some of the sulfates in these drill samples might have formed after the siderite, either through evaporation during early diagenesis (postdepositional changes to the sediment) (*27*) or as veins filling fractures during later diagenesis (*28*, *29*).

Evaporation drove siderite precipitation

Dissolution of basalt could have provided the divalent cations (Fe^{2+}, Ca^{2+}, and Mg^{2+}) required to form the sulfate and carbonate minerals, whereas atmospheric CO_2 and sulfur dioxide (SO_2) could have provided the major anions HCO_3^- and SO_4^{2-}. Even after these solutes were dissolved in the fluid, another mechanism is required to reach sufficient supersaturation for nucleation and growth of the carbonate

and sulfate minerals (or their precursors) to occur. The most straightforward mechanism is evaporation of the water in Gale crater, which is consistent with the stratigraphic transition from shallow lacustrine to shallow water-table eolian deposition (Fig. 1). Gale crater is a closed-basin lake system (*30*, *31*), and other samples collected within the crater contain abundant highly soluble salts that require extensive evaporation for deposition (*9*, *22*, *27*, *32*). Alternative mechanisms to concentrate solutes, such as brine freezeout, could have had a similar overall effect (*22*). Although we cannot eliminate brine freezeout as a potential mechanism, sedimentological criteria (*30*) imply that it is unlikely to have occurred in Gale crater.

We used the concept of chemical divides, which relates sequences of mineral precipitation during evaporation to the chemistry of the evaporating waters (*22*, *33*), to interpret the origin of the sampled mineralogy. Because it is the least soluble, siderite is expected to be the first evaporite mineral to precipitate during evaporation of martian aqueous solutions, except those with highly acidic or sulfate-rich compositions (*9*, *22*). Early siderite formation exhausts the alkalinity, which prevents precipitation of other carbonates such as calcite ($CaCO_3$) or magnesite ($MgCO_3$). Continued evaporation leads to the formation of Ca-sulfate phases, such as anhydrite ($CaSO_4$) or gypsum ($CaSO_4{\cdot}2H_2O$). Further evaporation yields hydrous Mg-sulfates such as kieserite ($MgSO_4{\cdot}H_2O$), epsomite ($MgSO_4{\cdot}7H_2O$), or meridianiite ($MgSO_4{\cdot}11\ H_2O$), depending on temperature (*17*, *22*). Because siderite formation occurs at an earlier stage of evaporative concentration than the precipitation of hydrous Mg-sulfates, the formation of the latter through evaporation of Fe^{2+}-bearing solutions implies an earlier siderite-forming step (*22*). If Fe^{2+} had remained in solution when the Mg-sulfates formed, we expect the simultaneous precipitation of Fe-sulfates such as melanterite ($FeSO_4{\cdot}7H_2O$), which have not been detected (our CheMin data set an upper limit of $\lesssim$1 wt % in the samples) (*22*). The evaporation sequence we expect (fig. S10) is consistent with the measured compositions of the drill samples.

We confirmed the consistent chemical composition of the 89 m of analyzed strata using the Chemistry and Camera (ChemCam) instrument, which uses laser pulses to remotely estimate the chemistry of rocks encountered along the rover's traverse more frequently than is possible by using drill samples (*19*). These analyses demonstrate that the analyzed section of the Mirador Formation is chemically homogeneous and differs from the underlying Mt. Sharp stratigraphy (Fig. 1). This implies that the fluids that deposited carbonate and sulfates were long-lived and affected a substantially thick portion of the Mt. Sharp stratigraphy.

Theoretical models indicate that P_{CO_2} must have been higher on ancient Mars, to stabilize liquid water on the surface long enough to deposit the stratigraphically lower sediments that were previously investigated by Curiosity (*30*). The onset of siderite deposition therefore does not record the beginning of elevated atmospheric P_{CO_2}. Carbonate deposition in Gale crater was likely triggered by a change in the fluid within the crater. We hypothesize that changing global environmental conditions might have decreased water availability and diminished the role of sulfuric acid in mediating geochemical reactions. For identical mineral dissolution rates (for example, under identical pH and temperature), water-rock reactions become more effective at buffering water chemistry under more water-limited conditions because solution chemistry evolves more rapidly as minerals dissolve into smaller solution volumes. Sulfuric acid is thought to be the dominant mediator of water-rock interactions on Mars (*10*). Water-limited reactions would have been more effective at neutralizing acid, particularly if the aqueous solutions were not in direct contact with atmospheric SO_2. Even a low concentration of sulfuric acid in solution lowers the pH sufficiently to inhibit carbonate precipitation (*34*). We calculate (*19*) that siderite precipitation halts (Fig. 3) if solution pH is lower than occurred during sediment deposition in underlying Gale crater sediments [pH 5.2 to 5.6 (*35*)]. We therefore suggest that the appearance of siderite in sediments could mark when sulfuric acid was neutralized by basalt-driven alkalinity generation. Any process that neutralizes sulfuric acid could have led to siderite precipitation (Fig. 3) while also leaching the Mg^{2+} and Ca^{2+} required to trigger sulfate deposition during subsequent evaporation.

Implications for global sulfate-bearing strata

Orbital data have been used to map sulfate-bearing sedimentary strata, similar to those observed in Mt. Sharp, across the planet (*36*). Spectral absorption features associated with carbonate minerals have not been reported in orbital observations of Mt. Sharp's sulfate-bearing strata (*37*). These sulfate-bearing sediments were not expected to be carbonate-bearing. We suggest that the carbonates we identified were invisible to orbital investigation, perhaps owing to dust cover or mixing with other phases, such as Mg-sulfates. Whatever the reason for this discrepancy, if other sulfate deposits on Mars also contain carbonate at similar abundances to those we measured at Gale crater, they might also have eluded detection from orbit.

If the mineralogy of the Mt. Sharp sulfate sediments we investigated is representative of global deposits, they could contain a substantial reservoir of carbon. We considered two scenarios to estimate the amount of CO_2 that these rocks might have sequestered (fig. S11) (*19*). In the first scenario, we assumed that the 89 m of strata investigated by Curiosity represent a brief, carbonate-precipitating interlude and multiplied this thickness by the area of global sulfate strata (*19*). In this case, global sulfate strata contain the equivalent of 2.6 to 5.7 mbar of sequestered CO_2—a similar amount to that contained in the modern martian atmosphere. In the second scenario, we assumed that siderite persists throughout the full volume of global sulfate sediments (*19*). In this case, global sulfate strata could contain the equivalent of 16 to 36 mbar of atmospheric CO_2; the latter value is six times Mars' current atmospheric CO_2 pressure. If that amount of CO_2 was present in the ancient atmosphere, it would have provided sufficient pressure for stable surface liquid water on early Mars because the increased atmospheric pressure suppresses evaporative cooling (*38*, *39*). However, a few tens of millibar of atmospheric CO_2 is inadequate by itself to stabilize liquid water on the early martian surface because it would not provide sufficient warming to raise surface temperatures (*40*–*43*). Because erosion has reduced the size of global sulfate deposits, the values of area and volume used in these calculations are likely to be underestimates (*19*).

Diagenesis returned carbon to the atmosphere

Once formed, siderite can decompose to Fe-oxyhydroxides, releasing CO_2, through changes in environmental parameters, such as pH, P_{CO_2}, redox state, or the flux of ionizing radiation (supplementary text). The differences in Fe-bearing minerals in the otherwise compositionally and geologically (Fig. 1) similar Mg-sulfate–rich Canaima, Tapo Caparo, Ubajara, and Sequoia samples indicates differing degrees of post-depositional siderite destruction and provides a record of an ancient martian carbon cycle, which has not been evident in previously investigated strata (*13*, *27*). The Canaima sample contained no detectable siderite but abundant Fe-oxydydroxides in the form of hematite (α-Fe_2O_3) and goethite (α-FeOOH) (*17*). The Tapo Caparo sample was taken from a location separated from Canaima by the Marker Band, which was impenetrable by Curiosity's drill and therefore perhaps impermeable to water. Tapo Caparo contained abundant siderite and no detectable hematite or goethite. Higher up in the stratigraphy, the Ubajara and Sequoia samples contained less siderite than did the Tapo Caparo sample but abundant hematite with either goethite (in Ubajara) or akageneite (β-FeOOH, in Sequoia) (Table 1). Because these ferric Fe-bearing minerals cannot form from the anoxic solutions that would have precipitated siderite (*44*), their presence indicates that diagenetic transformations caused (at least partial) siderite destruction, Fe-oxyhydroxide formation, and

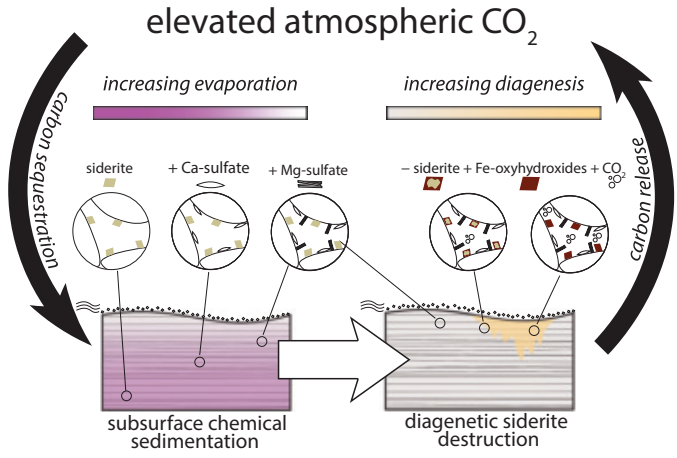

Fig. 4. Schematic illustration of our proposed carbon cycle on early Mars. Evaporation of water (pink shading) from subsurface pore spaces initially deposits siderite, which sequesters atmospheric CO_2 (black downward arrow). Increasing levels of evaporation deposit Ca-sulfate and Mg-sulfate minerals. Wind-blown (eolian) sedimentation at the ground surface (gray dots) moves the location of evaporation and chemical sedimentation upward with time. After some time (white arrow), infiltration of siderite-undersaturated fluids (yellow shading) partially destroys the previously precipitated siderite, forming Fe-oxyhydroxides and releasing previously sequestered CO_2 back into the atmosphere (black upward arrow).

therefore CO_2 release from the Mg-sulfate–bearing strata (Fig. 4). Sulfate-rich, siderite-undersaturated fluids, such as those that formed postdepositional jarosite [$(H_3O^+, K^+, Na^+)Fe_3(SO_4)_2(OH)_6$] in underlying strata (*45*), could have driven this process of carbonate destruction. SAM EGA analyses indicate the presence of Fe-sulfates at abundances below the CheMin detection limit in the investigated samples (fig. S12), which is consistent with this scenario.

Sulfate-bearing formations elsewhere on Mars, mapped by using orbital data, might have experienced a similar sequence of carbonate formation and destruction. Siderite has not been detected in those other deposits, but Fe oxyhydroxides associated with sulfate-bearing strata have been identified in the Valles Marineris and Terra Meridiani formations (*46*). Those oxyhydroxides were hypothesized to have formed from siderite, possibly by acidic groundwaters (*46*). If that interpretation is correct, decomposition of siderite occurred in multiple locations and released CO_2 into the atmosphere, recycling CO_2 that was originally sequestered during siderite formation. Diagenetic carbonate destruction observed elsewhere on Mars (*47*), in martian meteorites (*48*), and in sandstones on Earth (*44*) yields nearly identical reaction products to those we found in Gale crater and are observed globally in orbital data (supplementary text). We therefore conclude that in situ, orbital, and terrestrial analog evidence all indicate that postdepositional alteration of siderite closed the loop in Mars' carbon cycle, by returning CO_2 to the atmosphere (Fig. 4). Yet the persistence of siderite long after deposition indicates that postdepositional siderite destruction was incomplete, and more carbon was sequestered than was subsequently released. The ancient martian carbon cycle was thus imbalanced, in contrast with Earth's, which has remained balanced over geologic time (*49*).

REFERENCES AND NOTES

1. E. S. Kite, L. J. Steele, M. A. Mischna, M. I. Richardson, *Proc. Natl. Acad. Sci. U.S.A.* **118**, e2101959118 (2021).
2. R. A. Urata, O. B. Toon, *Icarus* **226**, 229–250 (2013).
3. R. Wordsworth *et al.*, *Nat. Geosci.* **14**, 127–132 (2021).
4. R. M. Ramirez *et al.*, *Nat. Geosci.* **7**, 59–63 (2014).
5. R. Wordsworth *et al.*, *Geophys. Res. Lett.* **44**, 665–671 (2017).
6. B. M. Jakosky, *Planet. Space Sci.* **175**, 52–59 (2019).
7. B. D. Stanley, M. M. Hirschmann, A. C. Withers, *Geochim. Cosmochim. Acta* **75**, 5987–6003 (2011).
8. H. Lammer *et al.*, *Space Sci. Rev.* **174**, 113–154 (2013).
9. D. C. Catling, *J. Geophys. Res.* **104** (E7), 16453–16469 (1999).
10. S. M. McLennan, J. P. Grotzinger, J. A. Hurowitz, N. J. Tosca, *Annu. Rev. Earth Planet. Sci.* **47**, 91–118 (2019).
11. B. L. Ehlmann, C. S. Edwards, *Annu. Rev. Earth Planet. Sci.* **42**, 291–315 (2014).
12. J. C. Bridges, L. J. Hicks, A. H. Treiman, in *Volatiles in the Martian Crust*, J. Filiberto, S. P. Schwenzer, Eds. (Elsevier, 2019), pp. 89–118.
13. T. F. Bristow *et al.*, *Proc. Natl. Acad. Sci. U.S.A.* **114**, 2166–2170 (2017).
14. C. S. Romanek *et al.*, *Geochim. Cosmochim. Acta* **73**, 5361–5376 (2009).
15. R. Sengupta, N. J. Tosca, S. A. Robinson, *Geochim. Cosmochim. Acta* **271**, 1–15 (2020).
16. C. S. Edwards, B. L. Ehlmann, *Geology* **43**, 863–866 (2015).
17. S. J. Chipera *et al.*, *J. Geophys. Res. Planets* **128**, e2023JE008041 (2023).
18. R. Anderson, J. F. I. Bell, *Mars* **5**, 76–128 (2010).
19. Materials and methods are available as supplementary materials.
20. C. M. Weitz *et al.*, *J. Geophys. Res. Planets* **127**, e2022JE007211 (2022).
21. G. Kocurek, J. Nielson, *Sedimentology* **33**, 795–816 (1986).
22. N. J. Tosca, S. M. McLennan, *Earth Planet. Sci. Lett.* **241**, 21–31 (2006).
23. B. M. Tutolo, A. Awolayo, C. Brown, *Environ. Sci. Technol.* **55**, 11906–11915 (2021).
24. S. Arnorsson, I. Gunnarsson, A. Stefansson, A. Andresdottir, A. E. Sveinbjörnsdóttir, *Geochim. Cosmochim. Acta* **66**, 4015–4046 (2002).
25. D. G. Burtt *et al.*, *Proc. Natl. Acad. Sci. U.S.A.* **121**, e2321342121 (2024).
26. J. J. Papike, J. M. Karner, C. K. Shearer, P. V. Burger, *Geochim. Cosmochim. Acta* **73**, 7443–7485 (2009).
27. W. Rapin *et al.*, *Nat. Geosci.* **12**, 889–895 (2019).
28. M. Nachon *et al.*, *J. Geophys. Res. Planets* **119**, 1991–2016 (2014).
29. J. L'Haridon *et al.*, *Icarus* **311**, 69–86 (2018).
30. J. P. Grotzinger *et al.*, *Science* **350**, aac7575 (2015).
31. W. Rapin *et al.*, *Geology* **49**, 842–846 (2021).
32. J. A. Berger *et al.*, *J. Geophys. Res. Planets* **125**, e2020JE006536 (2020).
33. H. P. Eugster, L. A. Hardie, "Saline Lakes" in *Lakes: Chemistry, Geology, Physics*, A. Lerman, Ed. (Springer, 1978), pp. 237–293.
34. A. G. Fairén, D. Fernández-Remolar, J. M. Dohm, V. R. Baker, R. Amils, *Nature* **431**, 423–426 (2004).
35. N. J. Tosca, I. A. M. Ahmed, B. M. Tutolo, A. Ashpitel, J. A. Hurowitz, *Nat. Geosci.* **11**, 635–639 (2018).
36. J. P. Grotzinger, R. E. Milliken, in *Sedimentary Geology of Mars*, SEPM Special Publications, vol. 102, J. R. Grotzinger, R. E. Milliken, Eds. (SEPM Society for Sedimentary Geology, 2012), pp. 1–48.
37. A. A. Fraeman *et al.*, *J. Geophys. Res. Planets* **121**, 1713–1736 (2016).
38. A. P. Ingersoll, *Science* **168**, 972–973 (1970).
39. M. H. Hecht, *Icarus* **156**, 373–386 (2002).
40. S. W. Squyres, J. F. Kasting, *Science* **265**, 744–749 (1994).
41. R. Wordsworth *et al.*, *Icarus* **222**, 1–19 (2013).
42. M. Turbet, H. Tran, *J. Geophys. Res. Planets* **122**, 2362–2365 (2017).
43. E. S. Kite *et al.*, *Sci. Adv.* **8**, eabo5894 (2022).
44. H. Yoshida *et al.*, *Sci. Adv.* **4**, eaau0872 (2018).
45. P. E. Martin *et al.*, *J. Geophys. Res. Planets* **122**, 2803–2818 (2017).
46. J. P. Bibring *et al.*, *Science* **317**, 1206–1210 (2007).
47. J. Carter, C. Viviano-Beck, D. Loizeau, J. Bishop, L. Le Deit, *Icarus* **253**, 296–310 (2015).
48. J. D. Piercy, J. C. Bridges, L. J. Hicks, *Geochim. Cosmochim. Acta* **326**, 97–118 (2022).
49. C. T. A. Lee, H. Jiang, R. Dasgupta, M. Torres, in *Deep Carbon: Past to Present*, B. N. Orcutt, I. Daniel, R. Dasgupta, Eds. (Cambridge Univ. Press, 2019), pp. 313–357.
50. T. Bristow, B. M. Tutolo, Data from: In situ evidence of an active carbon cycle on ancient Mars. *Astrobiology Habitable Environment Database* (2024); https://doi.org/10.48667/tvxy-6a39.

ACKNOWLEDGMENTS

Mastcam mosaics were processed by the Mastcam team at Malin Space Science Systems. We thank J. Sneed and D. P. Mayer for help in calculating global stratum volumes. We acknowledge the support of the Jet Propulsion Laboratory engineering and management teams and Mars Science Laboratory science team members who participated in tactical and strategic operations, without whom the data presented here could not have been collected. **Funding:** B.M.T. acknowledges funding from the Canadian Space Agency, grant 22EXPMSLCA. E.M.H., E.S.K., and M.T.T. acknowledge funding from NASA grants 80NSSC22K0656 (E.M.H.), 80NSSC22K0731 (E.S.K.), and 80GSFC21M0002 (M.T.T.). T.F.B. acknowledges support for CheMin operations provided by NASA's Mars Exploration Program. A.L.R. acknowledges funding from the Science and Technology Funding Council of the United Kingdom, grant ST/W507520/1. J.C.B. acknowledges funding from the UK Space Agency. P.G. acknowledges support for ChemCam activities from the NASA Mars Exploration Program, grant R-00727-24-0.2. A portion of this research was carried out by A.Y., A.A.F., and A.R.V. at the Jet Propulsion Laboratory, California Institute of Technology, under a contract with NASA (80NM0018D0004). **Author contributions:** B.M.T. wrote the manuscript. B.M.T., E.M.H., E.B.R., T.F.B., R.T.D., A.T., T.S.P., M.T.T., D.J.D.M., D.F.B., D.T.V., S.M.M., S.C., R.M.H., R.V.M., V.M.T., S.L.S., A.P., A.Y., P.C., N.C., D.W.M., and J.M.M. processed, analyzed, and interpreted the CheMin data. P.D.A., D.G.B., H.B.F., B.S., and J.V.C. led the interpretation of the SAM data. A.L.R. and J.P.G. led the stratigraphic interpretation. J.F. led the ChemCam data interpretation. J.C.B., A.T., R.V.M., D.W.M., W.R., and H.B.F. assisted with comparisons to prior martian carbonate identifications. A.A.F. led the analysis and interpretation of orbital data. B.M.T., E.M.H., A.T., D.G.B., T.S.P., S.R.L., W.R., M.L., and P.G. interpreted geochemical pathways to the observed mineralogical assemblages. E.S.K. led the sulfate volume and area calculations and discussed the implications for Mars atmospheric evolution. A.R.V. managed the project and guided the mission. All coauthors commented on the results and

revised the text. **Competing interests:** The authors declare that they have no competing interests. **Data and materials availability:** The Curiosity data are archived in NASA's Planetary Data System (PDS). The MastCam images used to produce the drill site mosaics are available from PDS at https://planetarydata.jpl.nasa.gov/img/data/msl/msl_mmm/data_MSLMST. Text lists (.lst) of the constituent images that compose the mosaics are provided at the Astrobiology Habitable Environment Database (AHED) repository (*50*). The ChemCam spectra are available from PDS at https://pds-geosciences.wustl.edu/msl/msl-m-chemcam-libs-4_5-rdr-v1/mslccm_1xxx/data. Information for extracting the specific spectra used (target name, sol, spacecraft clock identifications), details about analysis locations, and the calculated Euclidian distances are included in the AHED repository (*51*). The CheMin diffraction data were level 4 data products archived in PDS at https://pds-geosciences.wustl.edu/msl/msl-m-chemin-4-rdr-v1/mslcmn_1xxx/data/rdr4. We used the .lbl and .csv files containing (in their file names) the following values of the spacecraft clock: Tapo Caparo 730910626, Ubajara 737119969, and Sequoia 751061408. The derived mineral abundances are level 5 data products archived in PDS at https://pds-geosciences.wustl.edu/msl/msl-m-chemin-4-rdr-v1/mslcmn_1xxx/data/rdr5, with the corresponding spacecraft clock identifications. These data are also archived in the Gale crater Mineralogy and Geochemistry database at https://odr.io/CheMin#/search/display/84/eyJkdF9pZCI6IjQzIn0/1. The SAM EGA data are available in PDS at https://pds-geosciences.wustl.edu/msl/msl-m-sam-2-rdr-l0-v1/mslsam_1xxx/data. We used the level 1b data for samples eid25719 (Tapo Caparo 1), eid25723 (Tapo Caparo 2), eid25729 (Ubajara), eid25743 (Sequoia 1), and eid25746 (Sequoia 2). The modified FULLPAT software used in our CheMin data analysis, the code we used to calculate siderite chemical formulas, and the code we used to calculate sulfate strata volume are archived in the AHED repository (*50*).

SUPPLEMENTARY MATERIALS

science.org/doi/10.1126/science.ado9966
Materials and Methods
Supplementary Text
Figs. S1 to 12
Table S1
References (*51*–*122*)
Data S1 and S2

Submitted 1 March 2024; accepted 25 February 2025
10.1126/science.ado9966

PLANT SCIENCE

Bacterial pathogen deploys the iminosugar glycosyrin to manipulate plant glycobiology

Nattapong Sanguankiattichai[1,2], Balakumaran Chandrasekar[1]†, Yuewen Sheng[3], Nathan Hardenbrook[4], Werner W. A. Tabak[5], Margit Drapal[6], Farnusch Kaschani[7], Clemens Grünwald-Gruber[8], Daniel Krahn[9], Pierre Buscaill[1], Suzuka Yamamoto[10], Atsushi Kato[10], Robert Nash[11], George Fleet[12], Richard Strasser[13], Paul D. Fraser[6], Markus Kaiser[5], Peijun Zhang[3,4]*, Gail M. Preston[1]*, Renier A. L. van der Hoorn[1]*

The extracellular space (apoplast) in plants is a key battleground during microbial infections. To avoid recognition, the bacterial model phytopathogen *Pseudomonas syringae* pv. *tomato* DC3000 produces glycosyrin. Glycosyrin inhibits the plant-secreted β-galactosidase BGAL1, which would otherwise initiate the release of immunogenic peptides from bacterial flagellin. Here, we report the structure, biosynthesis, and multifunctional roles of glycosyrin. High-resolution cryo–electron microscopy and chemical synthesis revealed that glycosyrin is an iminosugar with a five-membered pyrrolidine ring and a hydrated aldehyde that mimics monosaccharides. Glycosyrin biosynthesis was controlled by virulence regulators, and its production is common in bacteria and prevents flagellin recognition and alters the extracellular glycoproteome and metabolome of infected plants. These findings highlight a potentially wider role for glycobiology manipulation by plant pathogens across the plant kingdom.

The extracellular space in plant tissues (the apoplast) is an important molecular battleground during plant-pathogen interactions (*1*). This microenvironment is colonized by bacteria, fungi, and oomycetes that likely evolved various strategies to avoid recognition, suppress immune responses, and manipulate host physiology. Previous work on interactions between *Nicotiana benthamiana* plants and the model bacterial pathogen *Pseudomonas syringae* revealed a role for plant apoplastic β-galactosidase BGAL1 in plant immunity (*2*). BGAL1 contributes to the hydrolytic release of immunogenic peptides from glycosylated flagella of *P. syringae* that activate plant defenses (*2*). During infection, *P. syringae* pv. *tomato* DC3000 (*Pto*DC3000) produces a small molecule inhibitor of BGAL1 (*2*), which we named glycosyrin. We report the molecular structure of glycosyrin, elucidate its biosynthesis and regulation, and clarify its impact on plant glycobiology.

Glycosyrin biosynthesis gene cluster is activated by virulence regulators

To identify genes required for glycosyrin biosynthesis, we transformed *Pto*DC3000 Δ*hopQ1-1* (*3*) (wild type for glycosyrin production in this work) with *lacZ* encoding the β-galactosidase from *Escherichia coli*, which is routinely used for blue staining with X-gal (5-bromo-4-chloro-3-indoyl-β-D-galactopyranoside). We then performed Tn*5*-transposon mutagenesis and selection on virulence-inducing medium containing X-gal and identified darker blue colonies of glycosyrin-deficient mutants (Fig. 1A). The loss of glycosyrin was confirmed in activity assays with purified LacZ and a fluorogenic substrate (fig. S1) and transposon insertion sites were identified for 140 glycosyrin-deficient mutants (data S1). These Tn*5* insertion sites concentrated in four virulence gene regulators (*hrpR*, *hrpS*, *hrpL*, and *rhpS*) and one putative glycosyrin biosynthesis gene cluster (*gsn*, locus tags PSPTO_0834-0838, new NCBI locus tags PSPTO_RS04425-RS04445; Fig. 1, B and C). The deletion mutant lacking the *gsn* cluster (Δ*gsn*) was unable to produce the inhibitor, and transformation of this mutant with a plasmid carrying the *gsn* cluster restored inhibitor production (Fig. 1D). Glycosyrin production was also established in *E. coli* upon transformation with the plasmid carrying the *gsn* cluster (Fig. 1D). Thus, the *gsn* gene cluster is necessary and sufficient for glycosyrin production in bacteria.

The *gsn* cluster contains five genes (*gsnABCDE*, Fig. 1C). *gsnA* encodes an alcohol dehydrogenase (Pfam PF00107, PF08240) and *gsnB* encodes a reductase (PF01872). The Δ*gsnA* and Δ*gsnB* mutants were unable to produce the inhibitor, indicating that these two genes are indispensable (fig. S2, A and B). *gsnC* encodes a HAD family phosphatase (PF13419) and *gsnE* encodes an MFS family transporter (PF07690), possibly involved in the export of glycosyrin or transport of other metabolites related to biosynthesis. The Δ*gsnC* or Δ*gsnE* mutants had partially reduced glycosyrin production (fig. S2C), likely because the genome encodes many HAD and MFS members that tend to act promiscuously and redundantly (*4*, *5*). Finally,

[1]Department of Biology, University of Oxford, Oxford, UK. [2]Department of Microbiology, Faculty of Science, Mahidol University, Bangkok, Thailand. [3]Diamond Light Source, Harwell Science and Innovation Campus, Didcot, UK. [4]Division of Structural Biology, Wellcome Trust Centre for Human Genetics, University of Oxford, Oxford, UK. [5]ZMB Chemical Biology, Faculty of Biology, University of Duisburg-Essen, Essen, Germany. [6]Department of Biological Sciences, Royal Holloway University of London, Egham, UK. [7]Analytics Core Facility Essen (ACE), Chemical Biology, Faculty of Biology, Universität Duisburg-Essen, ZMB, Essen, Germany. [8]Core Facility Mass Spectrometry, BOKU University, Vienna, Austria. [9]Leibniz Institut für analytische Wissenschaften ISAS e. V., Dortmund, Germany. [10]Department of Hospital Pharmacy, University of Toyama, Toyama, Japan. [11]Institute of Biological, Environmental and Rural Sciences/Phytoquest Limited, Aberystwyth, UK. [12]Chemistry Research Laboratory, Department of Chemistry, University of Oxford, Oxford, UK. [13]Institute of Plant Biotechnology and Cell Biology, Department of Biotechnology and Food Science, BOKU University, Vienna, Austria.
***Corresponding author. Email: peijun.zhang@diamond.ac.uk (P.Z); gail.preston@biology.ox.ac.uk (G.M.P.); renier.vanderhoorn@biology.ox.ac.uk (R.A.L.v.d.H.)**
†Present address: Department of Biological Sciences, Birla Institute of Technology and Science, Pilani, Pilani, India.

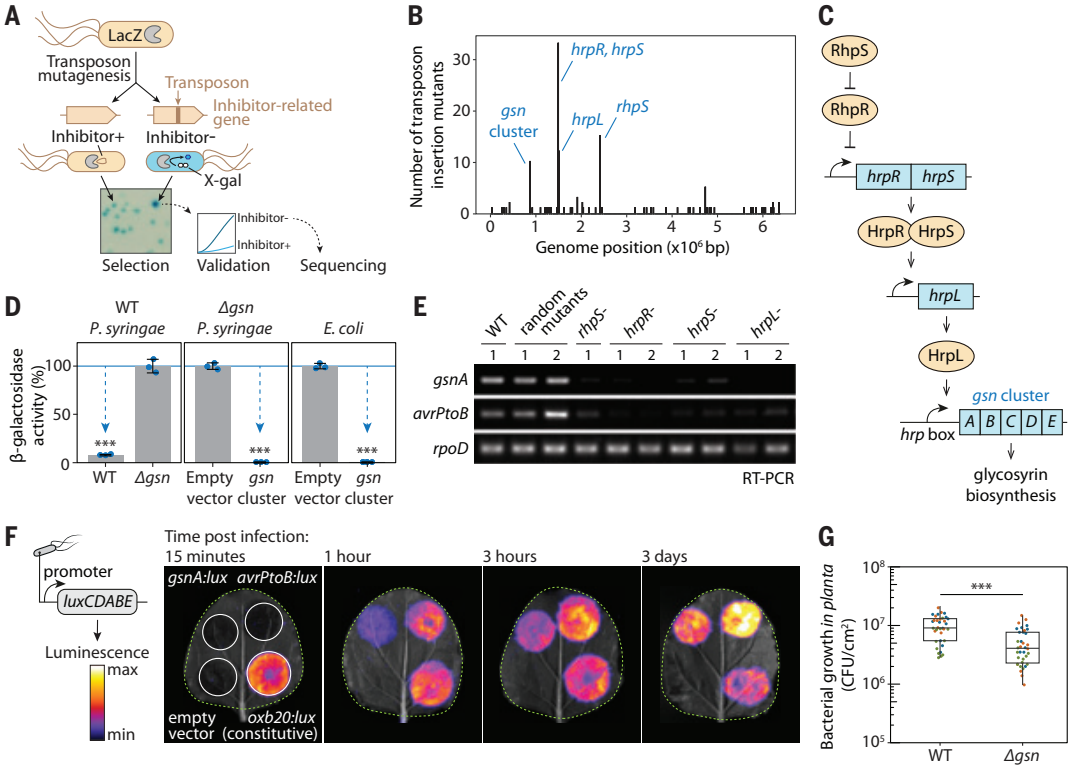

Fig. 1. Glycosyrin biosynthesis gene cluster and its regulators identified by forward genetics. (**A**) A genetic screen for glycosyrin-deficient mutants. *P. syringae* expressing LacZ β-galactosidase was used to create a random transposon insertion mutant library. When plated onto minimal medium supplemented with X-gal, glycosyrin-deficient mutants could not inhibit LacZ, resulting in a darker blue color. These candidates were confirmed in an enzymatic assay and transposon insertion sites determined by sequencing. (**B**) Histogram of the identified transposon insertion sites along the length of the genome, highlighting genes required for glycosyrin production. (**C**) The *gsn* gene cluster confers glycosyrin biosynthesis under the control of virulence gene regulators RhpS, HrpR, HrpS, and HrpL. The promotor of the *gsn* cluster contains a HrpL binding site (*hrp* box). (**D**) The *gsn* cluster confers glycosyrin biosynthesis in *P. syringae* and *E. coli*. Supernatants from bacterial cultures in minimal medium were tested for inhibitor using the FDG hydrolysis assay with LacZ. β-galactosidase activity is reported as a percentage relative to the mean of the no-inhibitor-control (Δ*gsn* or empty vector). Arrows highlight inhibition. Data are mean ± SD (n = 3). Asterisks indicate significant difference compared to no-inhibitor-control ($P < 0.001$) from Welch's t-test. (**E**) *gsn* gene expression is dependent on *hrpR*, *hrpS*, *hrpL*, and *rhpS*. RNA from bacteria grown in minimal medium was used for RT-PCR to monitor transcript levels of *gsnA*, *avrPtoB* (type III secreted effector) and *rpoD* (reference gene). (**F**) The *gsn* cluster is transcribed during infection. Bacteria carrying various promoter:*luxCDABE* reporter constructs were infiltrated into *N. benthamiana* leaves and luminescence was imaged at different time points. Signals displayed are scaled to the maximum and minimum within each image. (**G**) *gsn* cluster contributes to virulence. Bacterial strains were spray-inoculated onto *N. benthamiana* leaves and the colony forming units per square centimeter were quantified at three days post inoculation. Results from three independent experiments with 12 replicates each are plotted in different colors. Asterisks indicate significant difference ($P <$ 0.001) from two-way analysis of variance (ANOVA) with experiments as blocks.

gsnD encodes a protein with a domain of unknown function (DUF1349, PF07081) and has a concanavalin A-like fold (fig. S3A), which is present in some lectins, glycosidases, and REE1, a protein implicated in regulating galactose metabolism (*6*). However, the Δ*gsnD* mutant produced similar inhibitor levels compared to wild-type (WT) bacteria (fig. S2C).

The promoter of the *gsn* gene cluster contains the *hrp* box, a conserved binding site for transcription factor HrpL (*7*), which is transcriptionally regulated by HrpR/S and RhpS (*8*) (Fig. 1C). RhpS, HrpR/S, and HrpL are master regulators of virulence genes induced during plant infection, including type-III effectors such as *avrPtoB* (*8*). Indeed, expression of the *gsn* cluster was impaired in *rhpS*, *hrpR/S*, and *hrpL* mutants, similar to *avrPtoB* (Fig. 1E). Consequently, as demonstrated with a *gsn:lux* reporter strain, the *gsn* cluster was transcribed from the initial to late stages of infection (Fig. 1F), consistent with inhibitor production during infection (*2*). When compared with WT bacteria, the Δ*gsn* mutant had reduced growth in *N. benthamiana* (Fig. 1G) but not in vitro (fig. S4A), indicating that the *gsn* cluster contributes to virulence during infection. This is also consistent with reduced virulence for a *gsnA* mutant on *Arabidopsis thaliana* described previously (*7*). The virulence role of the *gsn* cluster, however, was not observed in the *bgal1-1* mutant of *N. benthamiana* (fig. S4B), suggesting that BGAL1 is the main virulence target of glycosyrin under the tested conditions.

The *gsn* cluster is present in many strains across the major phylogroups of *P. syringae* (fig. S5A), but the phylogeny of *gsnA* is incongruent with that of *P. syringae* (fig. S5B). The *gsn* cluster is flanked by transposable elements and located downstream of $tRNA^{Lys}$ loci (fig. S5, A and C), which are typical for integrase sites (*9*). The *gsn* cluster also has a lower GC content than its neighboring regions and the genomic average (fig. S5D). These findings suggest that the *gsn* cluster has been dispersed in *P. syringae* through horizontal gene transfer.

Strains carrying the *gsn* cluster produced the inhibitor whereas strains lacking the cluster did not (fig. S5E). The *hrp* box in the *gsn* cluster promoter is also conserved across *P. syringae* (fig. S5F). These data suggest that different strains produce glycosyrin during infection of various plants. Indeed, the bean pathogen *P. syringae* pv. *phaseolicola* 1448A carries the *gsn* cluster and also inhibits apoplastic β-galactosidase activity during infection of

Phaseolus vulgaris (common bean), its native host plant (fig. S22E).

GsnA homologs (alcohol dehydrogenases) are present in diverse bacterial species in different gene clusters with similar gene functions (fig. S6), some of which are known to produce distinct iminosugars, potent glycosidase inhibitors with sugar-like structures containing a nitrogen instead of oxygen in the ring (fig. S6) (*10*–*12*). However, unlike previously characterized gene clusters, the *gsn* cluster also encodes GsnB (homolog of reductase RibD) (fig. S6), suggesting that glycosyrin is produced by a different metabolic pathway.

Glycosyrin is a hydrated iminosugar mimicking galactose

To elucidate the molecular structure of glycosyrin, we immobilized His-tagged LacZ on a metal affinity resin to capture glycosyrin from the crude secretome of the glycosyrin-producing WT strain until LacZ saturation. Subsequent washing and elution with imidazole yielded a LacZ-glycosyrin complex with a high degree of inhibitor saturation (Fig. 2, A and B). Using cryo–electron microscopy (cryo-EM), we resolved the structure of the LacZ-glycosyrin complex at 1.9 Å resolution and detected an electron density in the active site that was absent in the negative control generated using the secretome of the Δ*gsn* mutant (Fig. 2, C and D, and fig. S7). This density revealed that glycosyrin consists of a five-membered ring with three defined chiral centers: two with putative hydroxyls and one with a putative branching geminal diol group, which likely forms upon hydration of an aldehyde group (Fig. 2D). We next chemically synthesized this molecule and obtained a 1.4-Å resolution structure of its complex with LacZ, which is identical to the native glycosyrin (Fig. 2D and fig. S7), confirming the structure of glycosyrin.

Because glycosyrin binding to LacZ is noncovalent (fig. S8A), we analyzed soluble metabolites extracted from the captured LacZ-glycosyrin complex to further validate the glycosyrin structure using gas chromatography-mass spectrometry (GC-MS) (fig. S8B). The peaks of the synthetic glycosyrin standard were identical to those detected in native glycosyrin and absent in the Δ*gsn*-derived sample (fig. S8C) and these spectra were consistent with the identified structure (figs. S8C and S14). We detected the same glycosyrin signals in apoplastic fluid extracted from *N. benthamiana* leaves infected with WT but not Δ*gsn* mutant *P. syringae* (fig. S8D).

Glycosyrin binds to the enzyme active site and closely mimics the orientation of hydroxyl groups of galactose (Fig. 2E) (*13*). The hydrated aldehyde allows the five-membered glycosyrin ring to mimic the conformation of the six-membered galactose ring. Additionally, the protonated nitrogen of glycosyrin electrosta-

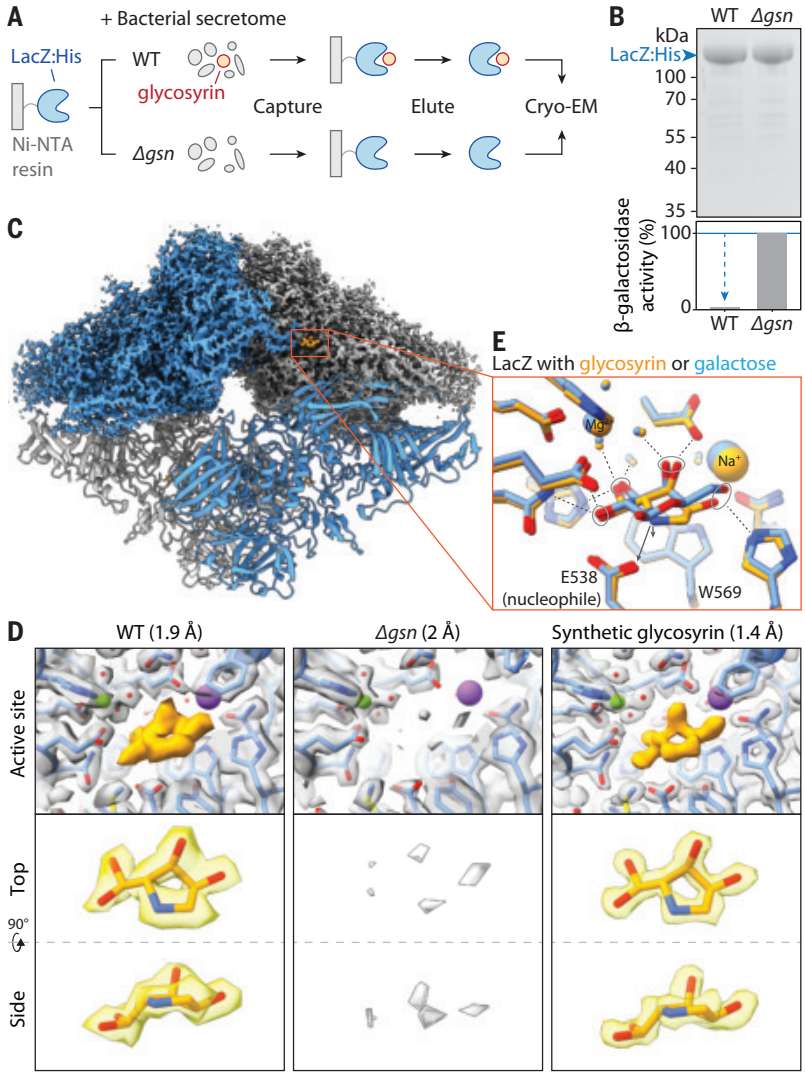

Fig. 2. Glycosyrin structure and mechanism revealed by high-resolution cryoEM. (**A**) LacZ-glycosyrin complex capture and downstream analyses. The Histidine-tagged β-galactosidase from *E. coli* (LacZ:His), immobilized on Ni-NTA beads, was used to capture glycosyrin from the crude bacterial secretomes of glycosyrin-producing *P. syringae* (wild type) or the glycosyrin-deficient mutant (Δ*gsn*, negative control). After washing, the complex was eluted and used for cryo-EM. (**B**) Captured LacZ was saturated with glycosyrin. (Top) Total protein stain of eluted samples separated on SDS-PAGE. (Bottom) β-galactosidase activity of each sample measured by the FDG hydrolysis assay showing inhibition of the wild type compared with Δ*gsn* samples. (**C**) Structure of LacZ-glycosyrin complex from cryo-EM. The density map is shown for the top half of the structure and a fitted model is shown for the bottom half. Each monomer of the LacZ tetramer is colored differently. Glycosyrin is colored orange. (**D**) Structure of glycosyrin revealed by cryo-EM. (Top) Structures of the LacZ complex captures from WT or Δ*gsn* strains and of LacZ incubated with synthetic glycosyrin. Density maps with fitted protein structures show the enzyme active site in the presence and absence of glycosyrin (orange). The resolution of each structure is shown in brackets. (Bottom) Extracted density map with fitted structure of glycosyrin from top and side view. (**E**) Glycosyrin mimics galactose binding in the active site. Overlay of structures of the LacZ active site and side chains of interacting residues in complex with glycosyrin (orange) or galactose (blue) showing similarity of overall binding pose and positioning of hydroxyl groups (circled). A positive charge on the protonated nitrogen of glycosyrin will add additional electrostatic interactions with the negatively charged catalytic glutamic acid (E538) and cation-pi interaction with the aromatic tryptophan (W569), represented by arrows. The stick representation of the molecular structure is colored by heteroatoms (red, oxygen; blue, nitrogen); hydrogen is not shown. Dashed lines represent hydrogen bonds. Small spheres represent water.

tically interacts with the conserved catalytic glutamic acid (E538) and establishes a cation-pi interaction with the aromatic tryptophan (W569) (Fig. 2E). Similar interactions were predicted for active site of BGAL1 (fig. S9). Indeed, inhibition assays showed that synthetic glycosyrin was a potent inhibitor of both LacZ and BGAL1, with an IC_{50} below that of 1-deoxygalactonojirimycin and galactostatin, two well-known iminosugars with 6-membered rings that inhibit β-galactosidases (fig. S10).

Glycosyrin biosynthesis branches from purine pathway

To resolve the biosynthesis pathway of glycosyrin, we first focused on GsnB because it is specific to the *gsn* cluster in our comparative genomics analysis (fig. S6). GsnB is homologous to RibD reductase, which functions in the riboflavin synthesis pathway (fig. S11A). The Alphafold2-predicted structure of GsnB contains conserved active site pockets similar to those in the crystal structures of RibD in complex with the substrate analog ribose-5-phosphate and cofactor NADPH (*14*) (fig. S11B), suggesting that GsnB could act on a similar substrate. This GsnB substrate likely also contains an amine group because the *gsn* cluster lacks an aminotransferase, unlike other clusters containing GsnA homologs (fig. S6).

Considering that glycosyrin is a 5-carbon sugar-like molecule, we hypothesized that 5-phosphoribosyl-1-amine (PRA) might be a substrate of GsnB (Fig. 3A and fig. S11C). Structural modeling also predicted NADPH and PRA binding in the active site pockets of GsnB (fig. S11D). PRA is produced by PurF from 5-phosphoribosyl-1-pyrophosphate (PRPP) and is used by PurD in purine synthesis (Fig. 3A) (*15*). Indeed, when grown on purines to complement for purine deficiency (fig. S12A), the Δ*purF* mutant was unable to produce glycosyrin, unlike the Δ*purD* mutant (Fig. 3B). Notably, the Δ*purD* mutant produced more glycosyrin than WT bacteria (fig. S12B), likely because more PRA is available for glycosyrin production in the absence of PurD (Fig. 3A). Thus, the purine intermediate PRA is the precursor for glycosyrin biosynthesis.

Given the reductase activity of RibD (fig. S11A), we speculated that GsnB could similarly reduce PRA into 1-amino-1-deoxy-D-ribitol-5-phosphate (1ADRP) using cofactor NADPH (Fig. 3C and fig. S11C). Subsequently, the putative phosphatase GsnC might remove the phosphate of 1ADRP to produce 1-amino-1-deoxy-D-ribitol (1ADR). Structural modeling of GsnC indeed predicts the binding of 1ADRP with its phosphate close to the conserved catalytic aspartic acid residues and cofactor Mg^{2+}, consistent with the expected phosphatase catalytic mechanism (fig. S13) (*16*). Finally, the putative oxidase GsnA might oxidise the secondary hydroxyl group in 1ADR to produce the ketose 5-amino-5-deoxy-L-ribulose (5ADR) (Fig. 3C). 5ADR can spontaneously convert into the detected hydrated glycosyrin (Fig. 3D), as explained below.

To confirm the enzymatic steps of glycosyrin biosynthesis, we produced and purified four enzymes (PurF, GsnB, GsnC, and GsnA, fig. S15C) and incubated them with the predicted substrate PRPP and cofactors. β-galactosidase inhibitor was produced from the mixture with all four enzymes but not when any of the four enzymes was omitted (Fig. 3E), Thus these enzymes are necessary and sufficient for glycosyrin biosynthesis in vitro.

To verify the order of these reactions, we first produced intermediates from each enzymatic step in vitro and then heat-inactivated the enzymes. We were then able to produce the inhibitor from these intermediates by adding the subsequent enzymes and cofactors in the expected order (Fig. 3F). Furthermore, using GC-MS, the intermediates (PRA, 1ADRP, and 1ADR) were detected after each enzymatic step and these intermediates were depleted upon the addition of subsequent enzymes (fig. S15). To confirm the final enzymatic step, we also detected glycosyrin formation from synthetic 1ADR by GsnA (figs. S16 and S17B), an NAD^+-dependent oxidase (fig. S17C). Notably, the pink color of purified GsnA indicated that cobalt ion is a preferred cofactor, which was confirmed in vitro (fig. S17D), unlike the annotation of this alcohol dehydrogenase family as being zinc-dependent (*17*). Structural modeling predicted the binding of 1ADR to GsnC such that the catalytic threonine residue and cofactors NAD^+ and Co^{2+} are in close proximity to the hydroxyl group to be oxidized on 1ADR (fig. S17F) (*18*). Taken together, these results confirmed the biosynthesis pathway of glycosyrin (Fig. 3, A and C).

We thus propose a chemical conversion pathway for the final steps of glycosyrin formation (Fig. 3D). First, the amine and ketone groups in 5ADR will react to produce the cyclic imine form of glycosyrin. This imine substructure will undergo a spontaneous Heyns rearrangement (*19*), resulting in the aldehyde form of glycosyrin. This aldehyde is then hydrated to yield the hydrate form (Fig. 3D). To confirm that this pathway occurs spontaneously, we chemically synthesized both the imine and aldehyde derivatives of glycosyrin (fig. S18) and found that, upon removing the protecting group in water, they both spontaneously converted into the hydrate form, detected by both LC-MS and NMR as the major product (Fig. 3G and fig. S19). In addition, GC-MS analysis of glycosyrin produced in vitro by GsnA from 1ADR detected both imine and aldehyde forms of glycosyrin because GC-MS was performed under anhydrous conditions (fig. S16). Thus, spontaneous chemical conversions generate the hydrate form of glycosyrin.

Glycosyrin manipulates plant glycobiology

The originally identified target of glycosyrin is BGAL1, which acts in plant defense by facilitating the release of immunogenic peptides from glycosylated flagellin protein (*2*). BGAL1 also removes the terminal β-D-galactose from N- and O-glycans of transiently expressed recombinant proteins (*20*). Taking advantage of a terminal β-D-galactose-specific lectin called RCAI (*21*), we found that apoplastic fluids isolated from the *bgal1-1* mutant contained RCAI-positive proteins (Fig. 4A), indicating that BGAL1 also processes endogenous plant glycoproteins. Notably, RCAI-positive glycoproteins also accumulated in WT plants upon infection with WT *P. syringae*, more than with the Δ*gsn* mutant, whereas no differential RCAI-positive glycoproteins were observed in *bgal1-1* mutant plants (Fig. 4A). These findings indicated that this modification of the host glycoproteome occurs through BGAL1 inhibition by glycosyrin. *N*-glycan analysis of the apoplastic proteome revealed that glycosyrin production during infection suppressed the accumulation of *N*-glycans that are likely produced by BGAL1 (fig. S20G). We also purified RCAI-positive proteins from the apoplast of infected plants and found that FLA17 (Fasciclin-like arabinogalactan protein17, NbL16 g25050) was differentially glycosylated upon infection without showing differential protein accumulation (fig. S20 and data S2).

Moreover, untargeted metabolomics of apoplastic fluid from plants infected with WT and Δ*gsn P. syringae* revealed that glycosyrin also triggered the accumulation of galactosylglycerol (873 ± 150 μM) and trehalose (46 ± 12 μM) in the apoplast of leaves infected with WT *P. syringae* (Fig. 4B, fig. S21, and data S3 and S4). These metabolites were not consumed by *P. syringae* in vitro (fig. S21D). Their accumulation was independent of BGAL1 (fig. S21A), suggesting that glycosyrin may target other glycosidases involved in glycoside processing.

Indeed, glycosyrin inhibited several other glycosidases, including other β-galactosidases and β-glucosidases during infection of *N. benthamiana* leaves (fig. S22, A to C) and in apoplastic fluids (fig. S22D), as well as other plant α- and β-glucosidases (figs. S22E and S23). Thus, glycosyrin is a multifunctional iminosugar produced by *P. syringae* that manipulates different host glycosidases and influences various aspects of plant glycobiology during infection (Fig. 4C).

Discussion

We resolved the molecular structure of glycosyrin and its biosynthesis and regulation and discovered its additional impact on plant glycobiology. Amongst many identified natural iminosugars and derived synthetic analogs (*10*), glycosyrin is distinct as it carries an aldehyde substituent attached to the heterocyclic ring. The hydrated form of the aldehyde is stable at physiological conditions and allows glycosyrin

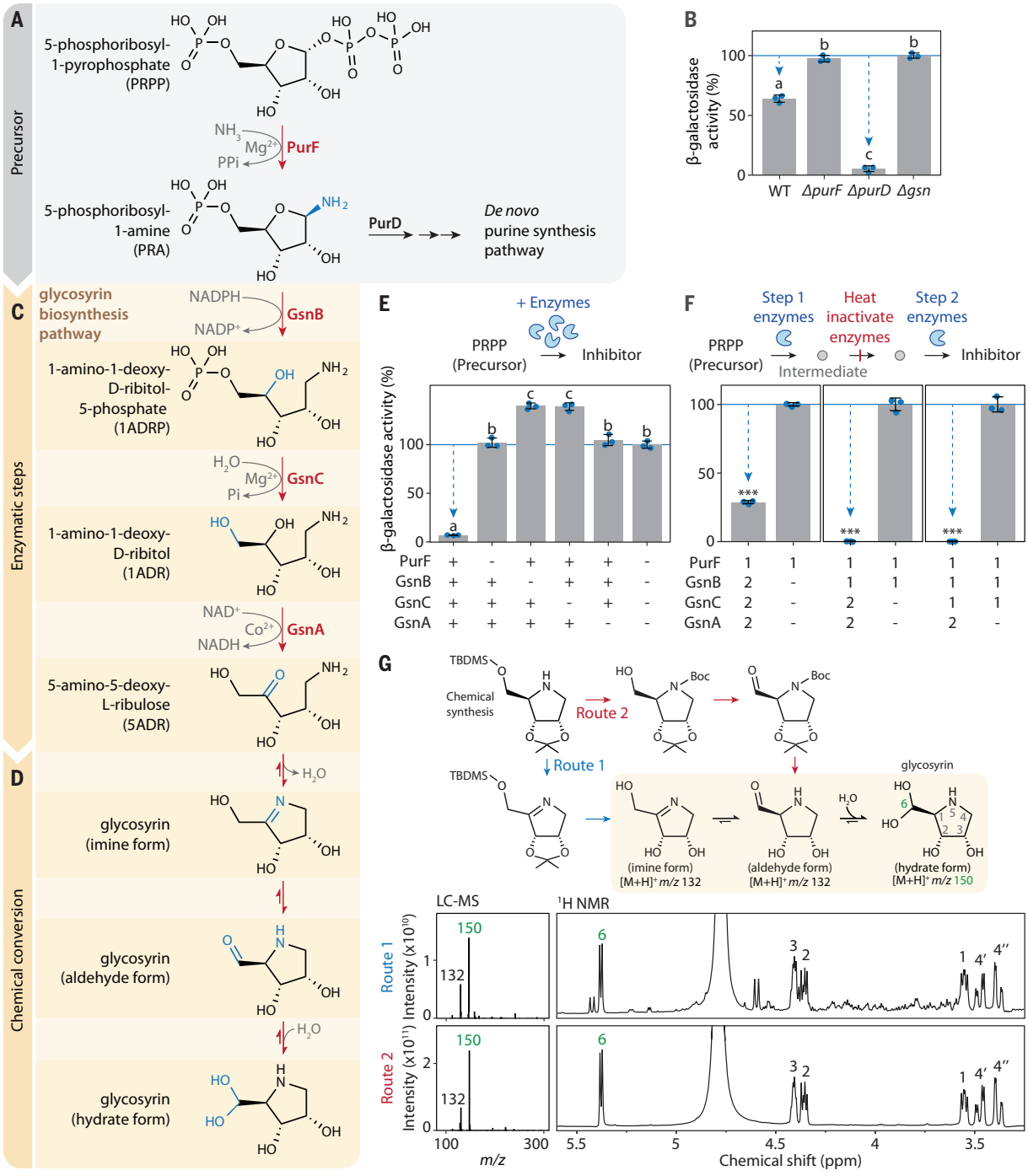

Fig. 3. Glycosyrin biosynthesis branches off from purine biosynthesis pathway. (**A**) Glycosyrin biosynthesis starts from PRA, an intermediate in the purine synthesis pathway. (**B**) *purF* but not *purD* is required for glycosyrin biosynthesis. Bacterial strains (WT or knockout mutants Δ*purF*, Δ*purD*, Δ*gsn*) were grown in virulence-inducing MG medium containing purines overnight. (**C**) Three *gsn*-encoded enzymes convert PRA into 5ADR. (**D**) A chemical conversion pathway of 5ADR into the hydrate form of glycosyrin. (**E**) PurF, GsnB, GsnC, and GsnA are required and sufficient for the biosynthesis of glycosyrin from PRPP in vitro. PRPP was mixed with and without purified enzymes and their cofactors. (**F**) PurF, GsnB, GsnC, and GsnA act consecutively in glycosyrin biosynthesis. PRPP was mixed with purified enzymes and their cofactors in two separate steps: In the first step [1], enzymes added to produce an intermediate followed by heat inactivation of the enzymes; in the second step [2], enzymes were added to complete glycosyrin biosynthesis. (B, E, and F) Inhibitor production was tested in an FDG hydrolysis assay with LacZ. β-galactosidase activity is reported as a percentage relative to the mean of no-inhibitor-control [Δ*gsn* for (B); all enzymes omitted for (E); enzyme 2 omitted for (F)]. Arrows highlight inhibition. Data are mean ± SD (n = 3). Different letters indicate groups with significant difference ($P < 0.001$) from one-way ANOVA and post-hoc Tukey HSD test. Asterisks indicate significant difference ($P < 0.001$) from Welch's t-test. (**G**) Both imine and aldehyde forms of glycosyrin spontaneously convert into the hydrate form in water. (Top) Chemical synthesis of glycosyrin using two routes, through imine or aldehyde forms. (Bottom) Products were analyzed with LC-MS (left) and ^{1}H-NMR (right), showing the spectra that correspond to the hydrate form. Positions within the structure of the hydrate form are numbered and labeled on the corresponding signals in NMR spectra.

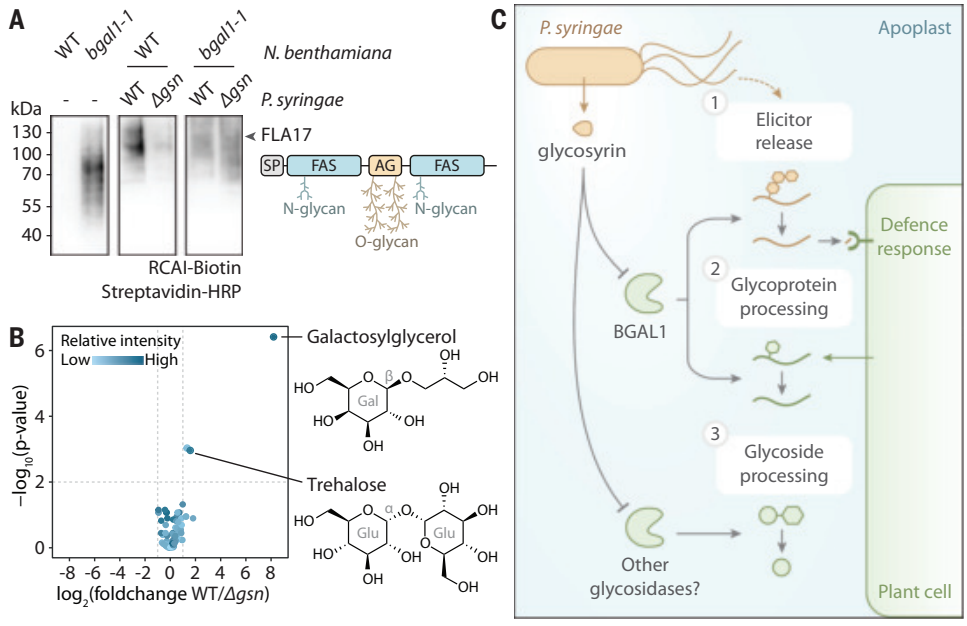

Fig. 4. Glycosyrin manipulates multiple aspects of extracellular plant glycobiology. (**A**) Accumulation of RCAI-positive glycoproteins in the apoplast upon infection is dependent on BGAL1 and glycosyrin production. Proteins were extracted by acetone precipitation of apoplastic fluids from *N. benthamiana* [WT or BGAL1 knockout mutant (*bgal1-1*)] with or without infection by *P. syringae* (WT or Δ*gsn*), then separated on SDS-PAGE, and blotted and probed with the RCAI lectin to detect galactose. FLA17 (fasciclin-like arabinogalactan protein17, NbL16g25050) was identified as the differentially accumulating glycoprotein (fig. S20). FLA17 sequence features: signal peptide (SP), fasciclin domain (FAS, PF02469) with putative N-glycosylation sites, and disordered region with arabinogalactan protein motif (AG) for O-glycosylation. The full gel with loading control is shown in fig. S20B. (**B**) Glycosyrin-dependent accumulation of galactosylglycerol and trehalose in the apoplast. Volcano plot of soluble metabolites detected by GC-MS of apoplastic fluids from leaves infected with WT or Δ*gsn* mutant (data S3). Glucoside components are shown with galactose (Gal), glucose (Glu), and bond configuration (α or β). (**C**) *P. syringae* produces glycosyrin to manipulate multiple aspects of glycobiology inside host plants by inhibiting plant glycosidases in the apoplast. [1] One major target of glycosyrin is BGAL1, the β-galactosidase that was previously shown to initiate the release of immunogenic fragments from flagellin (*2*). [2] Inhibition of BGAL1 by glycosyrin also interrupts apoplastic glycoprotein processing resulting in the accumulation of galactose-containing glycoproteins. [3] Glycosyrin also disrupts processing of glycosides by glycosidases other than BGAL1, resulting in the accumulation of specific glycosides in the apoplast.

to efficiently mimic galactose. Glycosyrin and its derivatives may have medicinal applications because iminosugars are used to treat type-II diabetes and Fabry disease (*22*, *23*). The glycosyrin biosynthesis pathway is distinct among iminosugars because it uses reductase GsnB to convert an intermediate from the purine biosynthesis pathway. By contrast, biosynthesis of other iminosugars starts with an aminotransferase acting on a sugar-phosphate precursor (*11*, *12*, *24*, *25*). The presence of GsnA homologs in biosynthesis gene clusters in diverse bacterial genomes indicates the iminosugar biosynthesis is common in bacteria.

In plants, glycosyrin inhibits BGAL1, which acts in plant immunity against bacteria that carry modified viosamine (mVio) in the O-glycan that decorates flagellin (*2*). The fact that the virulence role of glycosyrin in *Pto*DC3000 is dependent on BGAL1 and that BGAL1 suppresses bacterial growth only of strains producing mVio (*2*) indicates that at the tested conditions, glycosyrin promotes bacterial growth by avoiding the recognition of the flagellin elicitor. However, there are many strains that lack the mVio transferase gene (*vioT*) and can still produce glycosyrin, indicating that these strains may produce glycosyrin for a different purpose.

Glycosyrin also changes the host glycoproteome during infection. *N*-glycan analysis indicated that glycosyrin increases the accumulation of putative BGAL1 products and high-mannose, the latter being consistent with previous findings with *Pto*DC3000-infected *Arabidopsis* (*26*, *27*). Differential *N*-glycosylation might disturb the function of proteins such as receptor kinase MIK2, which carries an *N*-glycan that is essential for complex formation with coreceptor BAK1 (*28*). Glycosyrin also causes differential glycosylation of FLA17, which carries O-linked arabinogalactans (*29*), an obvious substrate for apoplastic β-galactosidases (*30*). FLA proteins are implicated in cell wall development and remodeling as well as in cell-to-cell communication and adhesion (*31*, *32*). It is also likely that glycosyrin changes cell wall properties directly by inhibiting β-galactosidases (*33*–*35*).

Glycosyrin production also triggers an accumulation of galactosylglycerol and trehalose in the apoplast, which is independent of BGAL1 and may result from inhibition of other glycosidases. Galactosylglycerol may originate from galactolipids in the thylakoid membrane, which are also precursors of the immune signaling molecule azelaic acid (*36*, *37*). Although pathogens often induce accumulation of host-derived sugars and metabolites in the apoplast as nutrient sources (*38*, *39*), trehalose and galactosylglycerol are not consumed by *P. syringae* in vitro. However, these glycosides are well-known osmolytes (*40*, *41*) and may thus contribute to the aqueous apoplast that promotes virulence (*42*, *43*). Elevated trehalose levels may also dampen plant defense responses to promote *P. syringae* infection (*44*). In addition, by inhibiting β-glucosidases, glycosyrin may also prevent the activation of defense-related glucosides, such as salicylic acid–glucoside and cyanogenic glucosides (*45*). Thus, there are many additional mechanisms through which glycosyrin may promote virulence.

Glycosyrin production is widely distributed in *P. syringae* infecting diverse host plants, including almonds, olives, leeks, tomatoes, and beans. Homologous iminosugar biosynthesis gene clusters are also present in other plant pathogens such as *Acidovorax* and *Erwinia* and in plant-associated bacteria such as *Kosakonia*, *Bacillus*, and *Paenibacillus*. Taken together with the fact that glycosyrin can inhibit multiple glycosidases and that this inhibition is difficult to avoid because glycosyrin closely mimics monosaccharide substrates, it is likely that glycosidase inhibition is a common strategy used by these bacteria to manipulate the glycobiology of host plants.

REFERENCES AND NOTES

1. G. Doehlemann, C. Hemetsberger, *New Phytol.* **198**, 1001–1016 (2013).
2. P. Buscaill *et al.*, *Science* **364**, eaav0748 (2019).
3. C. F. Wei *et al.*, *Plant J.* **51**, 32–46 (2007).
4. D. Drew, R. A. North, K. Nagarathinam, M. Tanabe, *Chem. Rev.* **121**, 5289–5335 (2021).
5. E. Kuznetsova *et al.*, *J. Biol. Chem.* **281**, 36149–36161 (2006).
6. I.-D. Choi, M.-Y. Jeong, M.-S. Ham, H.-C. Sung, C.-W. Yun, *Biochem. Biophys. Res. Commun.* **377**, 395–399 (2008).
7. M. Vencato *et al.*, *Mol. Plant Microbe Interact.* **19**, 1193–1206 (2006).
8. Y. Xie, X. Shao, X. Deng, *Environ. Microbiol.* **21**, 4465–4477 (2019).

9. K. P. Williams, *Nucleic Acids Res.* **30**, 866–875 (2002).
10. A. A. Watson, G. W. J. Fleet, N. Asano, R. J. Molyneux, R. J. Nash, *Phytochemistry* **56**, 265–295 (2001).
11. C. Nuñez, N. A. Horenstein, *J. Nat. Prod.* **82**, 3401–3409 (2019).
12. L. F. Clark, J. V. Johnson, N. A. Horenstein, *ChemBioChem* **12**, 2147–2150 (2011).
13. D. H. Juers *et al*., *Biochemistry* **40**, 14781–14794 (2001).
14. P. Stenmark, M. Moche, D. Gurmu, P. Nordlund, *J. Mol. Biol.* **373**, 48–64 (2007).
15. Y. Zhang, M. Morar, S. E. Ealick, *Cell. Mol. Life Sci.* **65**, 3699–3724 (2008).
16. A. Gohla, *Biochim. Biophys. Acta Mol. Cell Res.* **1866**, 153–166 (2019).
17. J. Mistry *et al*., *Nucleic Acids Res.* **49**, D412–D419 (2021).
18. S. B. Raj, S. Ramaswamy, B. V. Plapp, *Biochemistry* **53**, 5791–5803 (2014).
19. Z. Wang, "Heyns Rearrangement" in *Comprehensive Organic Name Reactions and Reagents* (2010).
20. R. Kriechbaum *et al*., *Plant Biotechnol. J.* **18**, 1537–1549 (2020).
21. Y. Itakura *et al*., *J. Biochem.* **142**, 459–469 (2007).
22. R. J. Nash, A. Kato, C. Y. Yu, G. W. Fleet, *Future Med. Chem.* **3**, 1513–1521 (2011).
23. B. G. Winchester, *Tetrahedron Asymmetry* **20**, 645–651 (2009).
24. R. Miyauchi, C. Ono, T. Ohnuki, Y. Shiba, *Appl. Environ. Microbiol.* **82**, 6414–6422 (2016).
25. H. E. Beal, N. A. Horenstein, *AMB Express* **11**, 120 (2021).
26. S. J. Kim, D. D. Bhandari, R. Sokoloski, F. Brandizzi, *Plant J.* **116**, 541–557 (2023).
27. G. Beihammer *et al*., *Glycoconj. J.* **40**, 97–108 (2023).
28. H. Wu *et al*., *Nat. Plants* **10**, 1984–1998 (2024).
29. A. Leszczuk, P. Kalaitzis, J. Kulik, A. Zdunek, *BMC Plant Biol.* **23**, 45 (2023).
30. E. Nguema-Ona *et al*., *Front. Plant Sci.* **5**, 499 (2014).
31. Y. Ma *et al*., *Plant Physiol.* **192**, 119–132 (2023).
32. X. Wu *et al*., *BMC Plant Biol.* **20**, 305 (2020).
33. J. Sampedro *et al*., *Plant Physiol.* **158**, 1146–1157 (2012).
34. T. Kotake *et al*., *Plant Physiol.* **138**, 1563–1576 (2005).
35. G. H. Dean *et al*., *Plant Cell* **19**, 4007–4021 (2007).
36. C. Wang *et al*., *Sci. Adv.* **4**, eaar4509 (2018).
37. Q. M. Gao *et al*., *Cell Rep.* **9**, 1681–1691 (2014).
38. F. El Kasmi, D. Horvath, T. Lahaye, *Curr. Opin. Plant Biol.* **44**, 98–107 (2018).
39. X. Zhu *et al*., *Nat. Microbiol.* **8**, 1561–1573 (2023).
40. B. C. Freeman, C. Chen, G. A. Beattie, *Environ. Microbiol.* **12**, 1486–1497 (2010).
41. N. Pade, N. Linka, W. Ruth, A. P. M. Weber, M. Hagemann, *New Phytol.* **205**, 1227–1238 (2015).
42. C. Roussin-Léveillée, D. Mackey, G. Ekanayake, R. Gohmann, P. Moffett, *Nat. Rev. Microbiol.* **22**, 360–372 (2024).
43. X. F. Xin, B. Kvitko, S. Y. He, *Nat. Rev. Microbiol.* **16**, 316–328 (2018).
44. X. Wang, Y. Du, D. Yu, *J. Integr. Plant Biol.* **61**, 509–527 (2019).
45. A. V. Morant *et al*., *Phytochemistry* **69**, 1795–1813 (2008).
46. M. Drapal, N. Sanguankiattichai, P. Fraser, R. A. L. Van der Hoorn, HighRes HILIC-MS of apoplastic fluids of N. benthamiana, V2, Mendeley Data (2025); https://data.mendeley.com/datasets/kbmbn6hvn7/2.

ACKNOWLEDGMENTS

We thank P. Bota for GC-MS maintenance and training; U. Pyzio for plant care; S. Rodgers, C. O'Brien, and P. Bowman for technical support; G. Yi for summarizing cryoEM data; and B. Mooney and J. Huang for feedback on the manuscript. We thank Diamond Light source for access and support of the cryoEM facilities at the UK National Electron Bio-Imaging Centre (eBIC), proposals NT21004, NT29812, and BI28713. Computation was performed at the Diamond Light Source and the Oxford Biomedical Research Computing (BMRC) facility, a joint development between the Wellcome Centre for Human Genetics and the Big Data Institute (BDI) supported by Health Data Research UK and the NIHR Oxford Biomedical Research Centre. **Funding:** This work was funded by the following: BBSRC grant BB/T015128/1 (to N.S., G.M.P., and R.A.L.v.d.H.), BB/R017913/1 (to P.B. and R.A.L.v.d.H.) and BB/W013932/1 (to R.A.L.v.d.H. and P.D.F.); ERC Advanced Grant 101019324 (to R.A.L.v.d.H.) and 101021133 (to P.Z.); National Institutes of Health U54AI170791-7522 (to P.Z.); UK Wellcome Trust Investigator Award 206422/Z/17/Z (to P.Z.); Wellcome Trust Core Award Grant 203141/Z/16/Z (to P.Z.); Oxford Interdisciplinary Bioscience DTP BB/M011224/1 (to N.S. and G.M.P.); Royal Thai Government Scholarship (to N.S.); European Union through HORIZON MSCA GLYCO-N training network (to M.K.); Japanese Society for the Promotion of Science (JSPS KAKENHI) JP24K09706 (to A.K.). **Author contributions:** Conceptualization: N.S., B.C., G.M.P., and R.A.L.v.d.H. Methodology: N.S., B.C., D.K., G.M.P., R.A.L.v.d.H., Y.S., N.H., P.Z., W.W.A.T., M.K., M.D., P.D.F., S.Y., A.K., F.K., C.G., and R.S. Investigation: N.S., B.C., D.K., P.B., Y.S., N.H., W.W.A.T., M.D., S.Y., A.K., R.N., G.F., F.K., C.G., and R.S. Funding acquisition: A.K., P.D.F., M.K., P.Z., G.M.P., and R.A.L.v.d.H. Supervision: A.K., P.D.F., M.K., P.Z., G.M.P., and R.A.L.v.d.H. Writing – original draft: N.S. and R.A.L.v.d.H. Writing – review & editing: all authors. **Competing interests:** The authors declare no competing interests. **Data and materials availability:** All data are available in the manuscript, supplementary materials, and cited references. The cryoEM density maps and corresponding atomic models have been deposited in the EMDB and PDB, respectively. The accession codes are EMDB-19182 and PDB 8RI7 for LacZ with native inhibitor (WT); EMDB-19181 and PDB 8RI6 for LacZ with Δ*gsn* negative control; EMDB-19183 and PDB 8RI8 for LacZ with synthetic glycosyrin. The high-resolution HILIC-MS data have been deposited in Mendeley Data (*46*). The mass spectrometry proteomics data for the on-bead digestions have been deposited to the ProteomeXchange Consortium via the PRIDE (*47*) partner repository (https://www.ebi.ac.uk/pride/archive/) with the dataset identifier PXD059601. Materials are available upon request.

SUPPLEMENTARY MATERIALS

science.org/doi/10.1126/science.adp2433
Materials and Methods
Figs. S1 to S23
Tables S1 to S6
References (*47*–*104*)
Data S1 to S4
MDAR Reproducibility Checklist

Submitted 14 March 2024; resubmitted 13 January 2025
Accepted 21 February 2025
10.1126/science.adp2433

STRUCTURAL BIOLOGY

Structure of human PINK1 at a mitochondrial TOM-VDAC array

Sylvie Callegari[1,2]*, Nicholas S. Kirk[1,2], Zhong Yan Gan[1,2]†, Toby Dite[1,2], Simon A. Cobbold[1,2], Andrew Leis[1,2], Laura F. Dagley[1,2], Alisa Glukhova[1,2,3,4,5]*, David Komander[1,2]*

Mutations in the ubiquitin kinase PINK1 cause early-onset Parkinson's disease, but how PINK1 is stabilized at depolarized mitochondrial translocase complexes has remained poorly understood. We determined a 3.1-angstrom resolution cryo–electron microscopy structure of dimeric human PINK1 stabilized at an endogenous array of mitochondrial translocase of the outer membrane (TOM) and voltage-dependent anion channel (VDAC) complexes. Symmetric arrangement of two TOM core complexes around a central VDAC2 dimer is facilitated by TOM5 and TOM20, both of which also bind PINK1 kinase C-lobes. PINK1 enters mitochondria through the proximal TOM40 barrel of the TOM core complex, guided by TOM7 and TOM22. Our structure explains how human PINK1 is stabilized at the TOM complex and regulated by oxidation, uncovers a previously unknown TOM-VDAC assembly, and reveals how a physiological substrate traverses TOM40 during translocation.

Mutations in the protein kinase PARK6/PINK1 lead to early-onset forms of Parkinson's disease (EOPD) (*1*). PINK1 is a ubiquitin and Parkin kinase (*2*–*7*) and functions as an early sensor and transducer of mitochondrial damage signaling (*8*–*10*). In healthy mitochondria, PINK1 is translocated across the outer mitochondrial membrane (OMM) via the translocase of the outer membrane (TOM) complex, inserted into the inner mitochondrial membrane (IMM) via the translocase of the inner membrane (TIM)23 complex, cleaved by the IMM protease PARL, and retrotranslocated and degraded by the proteasome (*10*). Depolarization leads to stalled import into the IMM, and PINK1 is stabilized at the OMM, where the kinase domain becomes activated, and triggers mitophagy by generating phospho-ubiquitin to recruit and initiate activation of the E3 ubiquitin ligase Parkin. Full activation of Parkin by PINK1 phosphorylation unleashes its E3 ligase activity and leads to ubiquitination of many OMM proteins (*11*–*14*). The assembled carpet of short-chain ubiquitin and phospho-ubiquitin signals (*15*–*18*) initiates mitophagy of the damaged mitochondrion.

Multiple structures of isolated kinase domains of PINK1 from insects have provided molecular details about PINK1 activation (*19*–*21*), which has been biochemically confirmed in human PINK1 (*3*, *12*, *21*, *22*). However, human PINK1 has resisted structural characterization, and the PINK1 N terminus (residues 1 to 115), which contains many patient mutations (*23*), has

[1]Walter and Eliza Hall Institute of Medical Research, Parkville, Victoria, Australia. [2]Department of Medical Biology, University of Melbourne, Melbourne, Victoria, Australia. [3]Department of Biochemistry and Pharmacology, The University of Melbourne, Melbourne, Victoria, Australia. [4]Drug Discovery Biology, Monash Institute of Pharmaceutical Sciences, Monash University, Parkville, Victoria, Australia. [5]ARC Centre for Cryo-electron Microscopy of Membrane Proteins, Monash Institute of Pharmaceutical Sciences, Monash University, Parkville, Victoria, Australia.
***Corresponding author. Email: callegari.s@wehi.edu.au (S.C.); glukhova.a@wehi.edu.au (A.G.); dk@wehi.edu.au (D.K.)**
†Present address: MRC Laboratory of Molecular Biology, Cambridge, UK.

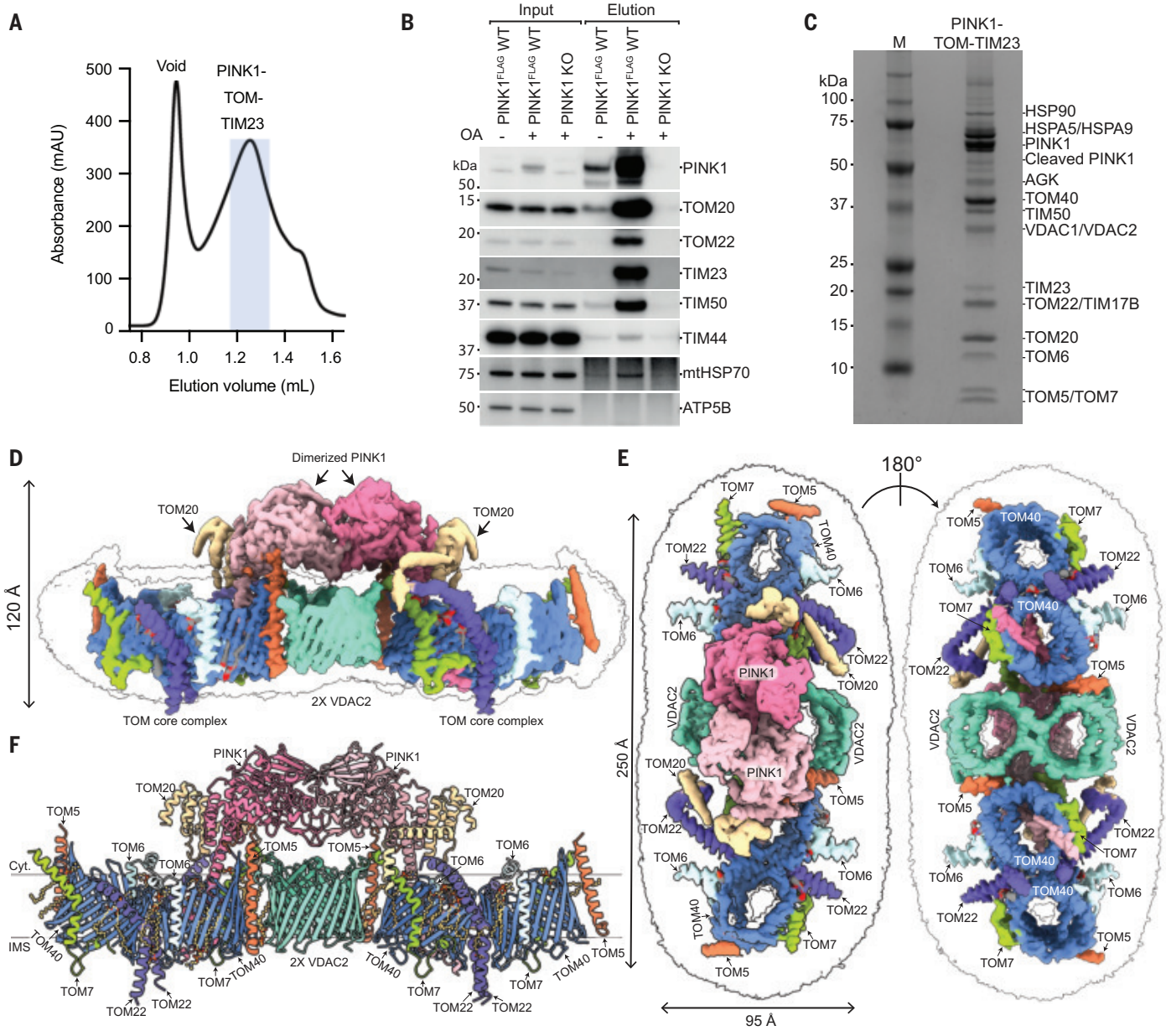

Fig. 1. Cryo-EM analysis of purified human PINK1-translocase complexes from mitochondria resolves dimerized PINK1 bound to a TOM-VDAC array. (**A**) SEC profile of the purified PINK1-TOM-TIM23 complex. mAU, milli–absorbance unit. (**B**) The isolated PINK1-3×FLAG complex was run on a NuPAGE 4-12% Bis-Tris gel, Western blotted, and probed using the indicated antibodies. *N* = 2 independent experiments. KO, knockout (deletion); WT, wild type. (**C**) After SEC, fractions of PINK1-3×FLAG complexes containing both TOM and TIM23 components were pooled and loaded on a NuPAGE 4-12% Bis-Tris gel and stained using Instant Blue SafeStain (Expedeon). Prominent bands were excised, trypsin-digested, and identified using liquid chromatography–MS. See data S1. M, marker. (**D** and **E**) A 3.1-Å resolution cryo-EM reconstruction of dimerized PINK1 bound to a TOM-VDAC array within a micelle is shown (D) along the membrane plane and (E) from the cytosol and from the IMS. A composite density map is depicted, assembled from the density map of the overall refined complex (with all components colored) and overlaid with the outline of the unsharpened cryo-EM map of the micelle. The cryo-EM map of the micelle was generated using ChimeraX by segmenting the unsharpened density map to remove PINK1, thereby isolating the micellar region surrounding the TOM-VDAC array. (**F**) The atomic model of the PINK-TOM-VDAC array, viewed along the membrane plane.

remained unresolved. A structure of full-length PINK1 at mitochondria is crucial to develop and understand PINK1 activators and treat Parkinson's disease (*24*–*26*).

Mechanisms of mitochondrial protein import have been intensely studied over the past 5 decades, yet many questions remain (*27*–*30*). The TOM complex is the main entry gate for all ~1500 proteins that are imported into the mitochondria as unfolded precursors. Yet how these precursors pass through the TOM complex after recognition by the presequence receptors TOM20 and TOM22 has not been resolved, nor has it been established how mitochondrial presequence-containing precursors are handed over from the TOM to the TIM23 complex (*30*). PINK1 is stabilized on the OMM after depolarization, but how and why is unclear (*10*). A ~700-kDa PINK1-TOM complex was reported in 2012 (*31*, *32*), and TOM7 (*33*), TOM20 (*34*, *35*), and, more recently, the TIM23 complex (*34*, *36*)

were shown to be functionally important in PINK1 stabilization.

In this work, we report the structure of human PINK1 arrested after depolarization at an endogenous mitochondrial import array comprising TOM and VDAC2 channels. The structure explains how PINK1 interacts with five TOM complex components, VDAC2, and phospholipids; unveils how a physiological presequence import substrate traverses the OMM; and rationalizes EOPD patient mutations. The structural role for VDAC channels in forming mitochondrial import arrays may illuminate how mitophagy is initiated.

Characterization of stabilized PINK1 on human mitochondria

To understand human PINK1 stabilization, we studied PINK1 in its endogenous environment on depolarized mitochondria. We realized that an unknown 100-kDa band arising from hydrogen peroxide treatment in our earlier work (*21*) was indeed an adduct between Cys^{40} of PINK1 and TIM50 (fig. S1). This observation indicated that PINK1 could be used to trap a TOM-TIM23 supercomplex, as has since been reported (*34*, *36*).

For biochemical and structural studies, we exploited a scalable Expi293 (Thermo) human cell expression system, in which we expressed 3xFLAG-tagged wild-type human PINK1. Stabilization of PINK1 by oligomycin–antimycin A (OA) treatment for 3 hours was followed by mitochondrial isolation, membrane solubilization in digitonin, PINK1 immunoprecipitation, and a final size exclusion chromatography (SEC)

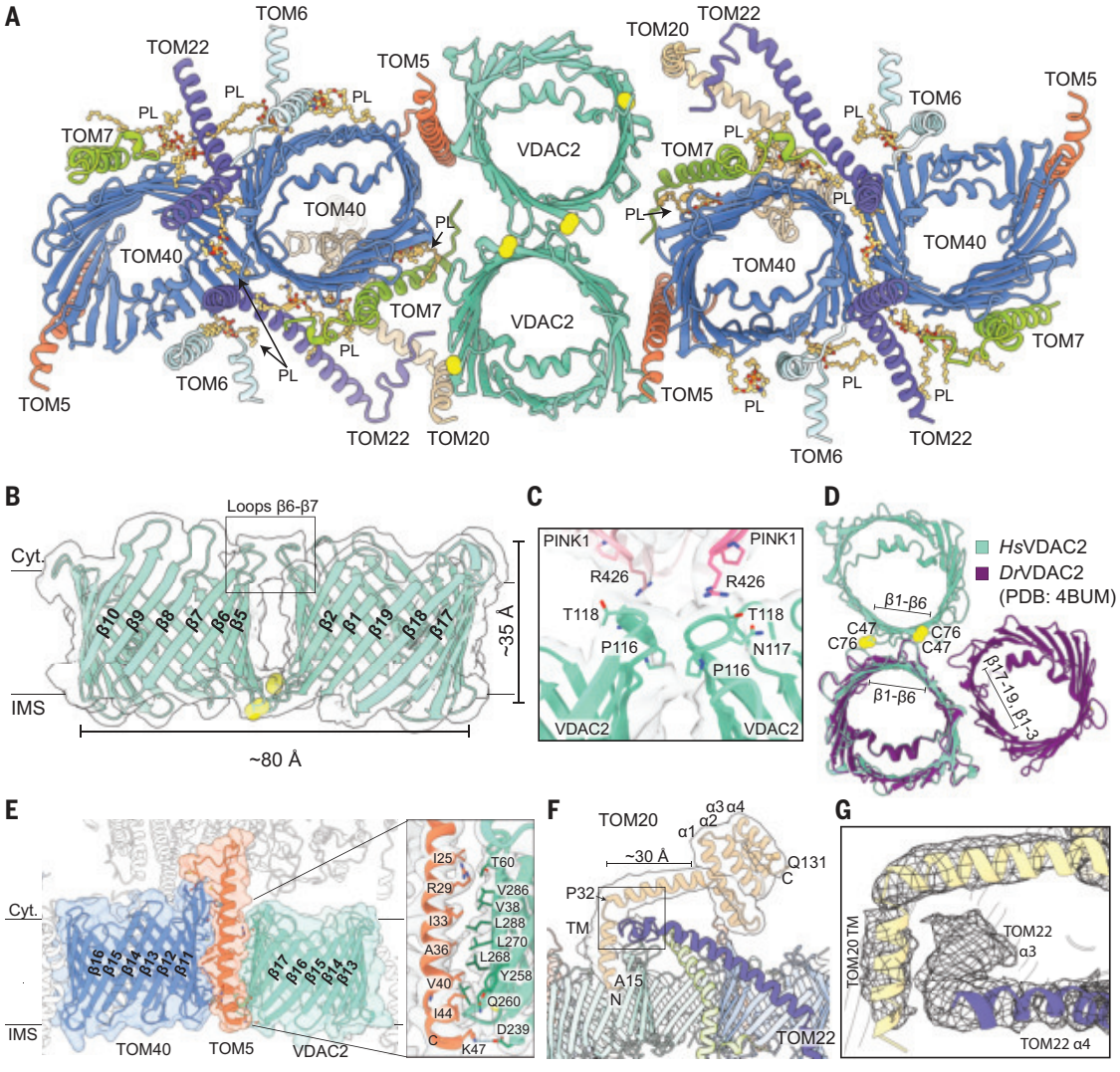

Fig. 2. PINK1 co-isolates with a distinctive TOM-VDAC2 assembly. (**A**) Atomic model of the TOM-VDAC array as viewed from the IMS. PINK1 has been removed from the model to emphasize the composition of the TOM-VDAC assembly. Phospholipids (PLs) are numbered (see fig. S5). (**B**) Model of the isolated VDAC2 dimers viewed along membrane plane and overlayed on the cryo-EM density. Disulfide bonds are shown as yellow spheres. Also see fig. S6. Cyt., cytosol. (**C**) Inset from (B) showing a close-up of the VDAC2 β6-β7 loop and its interaction with PINK1. Interacting residues are shown. (**D**) Model of VDAC2 homodimer from this structure overlayed on the model of the previously published zebrafish VDAC2 dimer (*44*). The view is from the IMS, and disulfide bonds are shown as yellow spheres. (**E**) Atomic model of TOM5 connecting the TOM40 barrel to VDAC2 viewed along the membrane plane. The inset shows a close-up of the TOM5-VDAC2 interaction interface. The side chains of interacting residues are shown, and hydrogen bonds are indicated by dotted blue lines. (**F**) Model of TOM20 along the membrane plane overlayed on the density for TOM20. PINK1 is removed from the model to more clearly depict TOM20. (**G**) Close-up view of the interaction between TOM20 and TOM22 in the cytosolic space, overlayed on the cryo-EM density (in mesh). The TOM22 α3 helix could not be confidently modeled and so only the density is shown. The side-view tool in ChimeraX was used to enhance visualization of the interacting helices. Single-letter abbreviations for the amino acid residues are as follows: A, Ala; C, Cys; D, Asp; E, Glu; F, Phe; G, Gly; H, His; I, Ile; K, Lys; L, Leu; M, Met; N, Asn; P, Pro; Q, Gln; R, Arg; S, Ser; T, Thr; V, Val; W, Trp; and Y, Tyr.

step that resulted in a single peak (Fig. 1A and fig. S2A). Fractions within the peak were composed of a 750-kDa complex, as measured by mass photometry (Fig. 1A and fig. S2B), which was further characterized by Western blotting (Fig. 1B), activity assays (fig. S2C), and mass spectrometry (MS) (Fig. 1C and data S1). Chemical cross-linking MS (XL-MS) analysis of the purified complex mapped more than 250 intraprotein cross-links and more than 35 cross-links between complex components (data S2). A network of cross-links was observed between PINK1 and TOM components, including TOM7, TOM40, and TOM20. The N terminus of PINK1 formed cross-links with TIM50 and TIM17B, and further intriguing cross-links were detected between TOM40 and the intermembrane space (IMS) domain of TIM50, corroborating the notion of a stabilized TOM-TIM23 supercomplex (fig. S3 and table S1). MS analysis of purified complex components also identified mitochondrial proteins not initially expected to be part of a PINK1-TOM-TIM23 supercomplex, including mitochondrial voltage-dependent anion channels (VDAC1, VDAC2, and VDAC3), acylglycerol kinase (AGK), and chaperones (Hsp90, mtHsp60, and mtHsp70) (Fig. 1C and data S1).

Large-scale purification from Expi293 (Thermo) cells generated a complex in detergent micelles at sufficient concentration (4 mg/ml) to perform cryo–electron microscopy (cryo-EM) single-particle analysis. Immediately apparent within the two-dimensional (2D) classes were large, regular protein assemblies. The dominant species present was revealed to be an oval-shaped disc with six pores (fig. S4A). High-resolution 3D reconstruction resulted in a cryo-EM map with a global resolution of 3.1 Å (local resolution range of 2 to 13 Å) (Fig. 1, D and E). Further symmetry expansion and local refinement resolved one-half of the complex with a global resolution of 2.7 Å (local resolution of 2 to 6 Å). The transmembrane domain of TOM20 was also resolved using 3D variability and local refinement to 3.3 Å (local resolution of 2 to 13 Å) (fig. S4B).

The complete complex reconstruction (Fig. 1, D to F) includes two TOM core complexes, each comprising two copies of TOM40, TOM7, TOM6, TOM5, and TOM22 and one copy of TOM20 (*29*). The two TOM core complexes are arranged symmetrically around a central VDAC2 dimer, connected by TOM5. Human PINK1 kinase domains form a symmetric dimer, as observed in previous insect structures (*20*, *21*), that sits atop the VDAC dimer and is held in position by interactions with TOM5 and extensive contacts with TOM20, which forms a helical brace for the PINK1 kinase dimer. The PINK1 N termini are threaded into the barrel of the VDAC-proximal TOM40 channels and exit into the IMS guided by TOM7 and TOM22 (Fig. 1, D to F). The high-resolution structure also resolves 18 lipid molecules, some of which contact PINK1 (fig. S5).

The TOM-VDAC array

An assembly of TOM and VDAC complexes (Fig. 2A) has not previously been reported and provides insights into arrangements of endogenous OMM complexes. Individually, the structures of the two TOM core complexes are similar to previous structures of the human TOM complex (*37*–*40*) (fig. S6), including the location of lipid molecules (figs. S5 and S6B). For a comparison of our TOM complex structure with published TOM structures across species, see fig. S6. Our larger structure reveals new roles for TOM5 and illuminates TOM20-TOM22 interactions. This complex structure additionally provides a high-resolution reconstruction of human VDAC2, a VDAC channel with specific roles in apoptosis (*41*, *42*) (Fig. 2B). The rationale for modeling a VDAC2 dimer is explained in the supplementary text and depicted in fig. S7.

VDAC dimers and oligomers can form through a variety of interfaces (*43*). Our VDAC2 dimer forms through symmetric interactions of β sheets 1 to 6, which, on the IMS side, juxtapose Cys residues in exposed loops that form disulfide bonds within the oxidative environment of the IMS (Fig. 2, B and D, fig. S7B, and supplementary text). On the cytosolic side, a π-π interaction between symmetric Pro^{116} residues on the β6-β7 loop is further braced by PINK1 Arg^{426} (Fig. 2C). A previous crystal structure of a zebrafish VDAC2 dimer (Fig. 2D) (*44*) formed symmetrically through β strands 17 to 19, 1, and 3. In our structure, this hydrophobic VDAC2 surface is occupied by TOM5 on both molecules and is further strengthened by a salt bridge (TOM5-Lys^{47}:VDAC2-Asp^{239}) (Fig. 2E and fig. S8). VDAC2 Asp^{239} and the hydrophobic residues are largely conserved across all three VDAC isoforms (fig. S9).

TOM20 is a dynamically associated accessory subunit of the TOM complex that serves as a presequence receptor (*29*). How TOM20 engages with the TOM core complex upon presequence recognition and then interacts with TOM22 to enable presequence entry into the TOM40 barrel remains unclear. Previous studies used cross-linking to stabilize and visualize TOM20 and achieved low local resolution reconstruction for these components (*37*, *38*). Our structure has enabled high-resolution reconstruction of TOM20 and TOM22 in an arrested state of the TOM complex with a stalled substrate.

Consistent with some previous reports (*38*, *45*), but contrary to others (*37*), only one TOM20 molecule per TOM core complex was observed. In our structure, TOM20 is resolved from residues 15 to 131 (Fig. 2F), and residues 15 to 24 are inserted into the membrane, between VDAC2 and TOM22, some 50 Å away from previously reported locations (*38*) (fig. S10A). The cytoplasmic portion of TOM20 begins at Asp^{25}, as a helical extension of the transmembrane domain. This helix then kinks at Pro^{32} and continues to Ala^{52}, culminating in the helical presequence binding domain that binds PINK1 (Fig. 2F). The kinked arrangement of TOM20 is cantilevered by the α3 and α4 helices of TOM22, likely through multiple aromatic and van der Waals interactions, which, however, could not be confidently modeled in the final reconstruction (Fig. 2G). We were unable to model the α1 and α2 helices of TOM22; we instead show that a previously published assignment of the TOM22 α1 and α2 helices (*37*) in fact coincides with our density for the transmembrane domain of TOM20 (fig. S10B). Using 3D variability analysis (3DVA), we resolved multiple conformations of the entire TOM20 N terminus (fig. S11). In one 3DVA cluster, TOM20 extends toward the IMS side of the micelle and contacts the VDAC barrel (fig. S11). These analyses highlight the mobility of the TOM20 transmembrane region, explaining the difficulty in capturing this mobile TOM component (*37*, *38*). Hence, the arrested substrate PINK1 locks TOM20 (and TOM22) in a most peripheral location on the TOM complex close to VDAC2; in active, translocating TOM complexes, TOM20 and TOM22 locations may be distinct.

Structure of human PINK1

We resolved in our structure residues 63 to 581 of human PINK1, with residues 70 to 110 located within the TOM40 barrel (Fig. 3A). The cytosolic portion of PINK1, from residue 110 to the C terminus, folds into the anticipated extended kinase domain, similar to insect PINK1 orthologs (*20*, *21*) (Fig. 3B). Moreover, PINK1 kinase domains form a symmetric dimer, stabilized by an intermolecular disulfide at Cys^{166}, at the tip of the kinase P-loop, which is also similar to insect *Pediculus humanus* PINK1 (*Ph*PINK1) Cys^{169}-linked dimers (*21*) (Fig. 3, A and B). Dimerization is essential for PINK1 to trans-autophosphorylate (on Ser^{202} in *Ph*PINK1, or Ser^{228} in human PINK1), which in *Ph*PINK1 induces conformational changes in the N-lobe, including αC helix kinking and ordering of insertion-3 to form the ubiquitin binding site (*21*, *46*). However, for *Ph*PINK1 to phosphorylate ubiquitin, the dimer must disassociate (*21*).

In our structure, human PINK1 adopts an active kinase conformation, with aligned C- and R-spines, and displays a kinked αC helix (*47*), suggesting that trans-autophosphorylation has taken place (Fig. 3, C and D). However, density around Ser^{228} was too weak to model confidently and was therefore modeled in the unphosphorylated state. Folding of insertion-3 is induced by phosphorylation (*21*, *46*), yet in our structure, insertion-3 remains disordered. Indeed, all three kinase domain insertions in human PINK1 (*19*) are disordered and were not modeled (Fig. 3C).

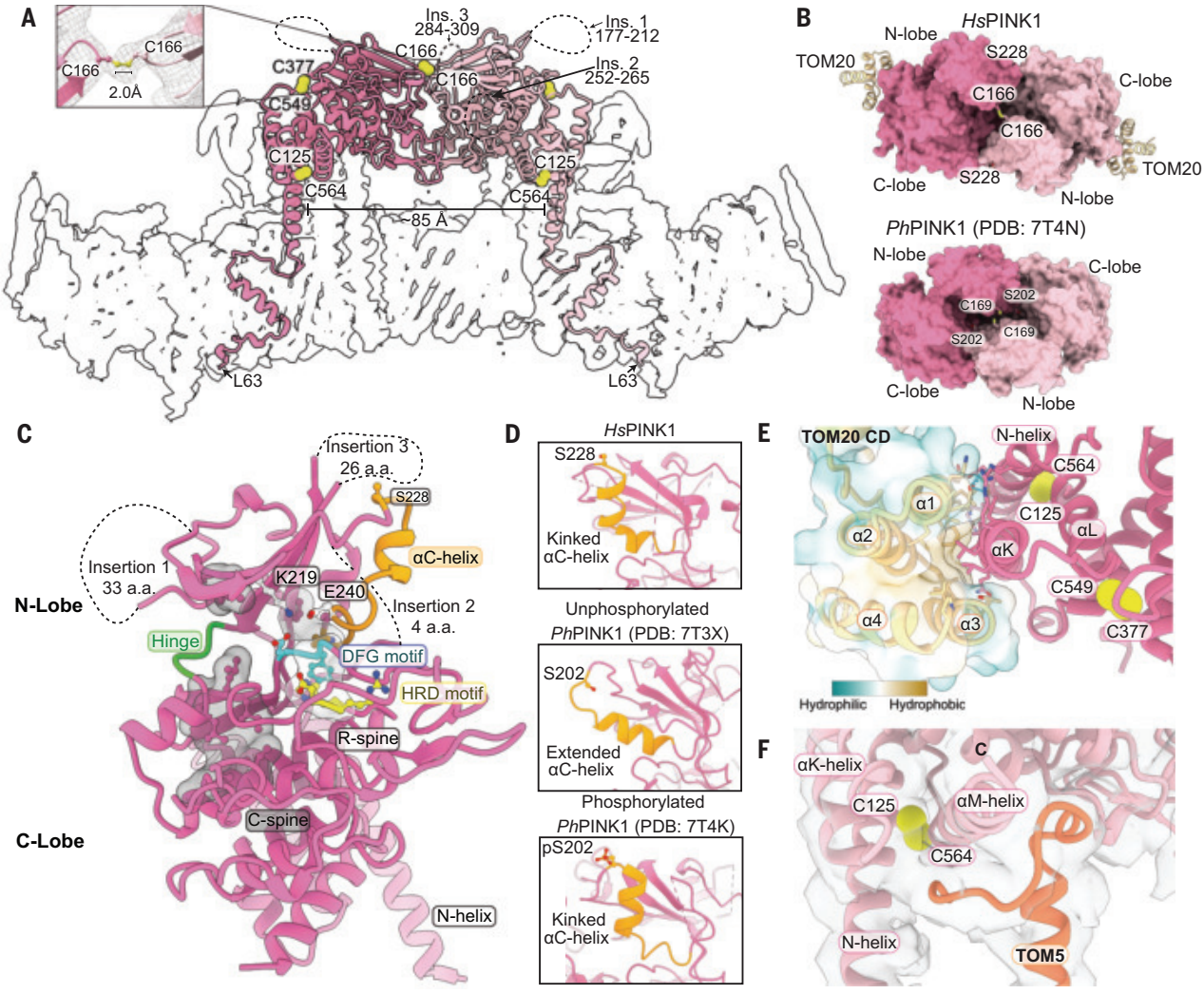

Fig. 3. Disulfide bonds stabilize a postactivation, but preactive, PINK1 dimer. (**A**) Atomic model of PINK1 dimer overlayed on an outline of the density of the TOM-VDAC array. Disulfide bonds are depicted as yellow spheres. Dashed lines indicate unmodeled residues. The inset depicts the cryo-EM density (mesh) for the disulfide bond between PINK1 Cys^{166} and PINK1 Cys^{166} on the respective PINK1 molecules. (**B**) Surface rendered models of the PINK1 dimer from this structure of *Homo sapiens* (*Hs*PINK1) and previously published *Ph*PINK1 (*21*), as viewed from the top. TOM20 in the *Hs*PINK1 model is shown in ribbon form. (**C**) Typical active kinase features of *Hs*PINK1. Colored atoms are part of the following motifs: HRD (yellow), DGF (blue), the αC helix (orange) in the kinked conformation, and the hinge region (green), with the catalytic spine (gray surface) and regulatory spine (white surface) in the aligned active conformation. Disordered loops are depicted as dotted lines. a.a., amino acids. (**D**) Close-up view of the kinked αC helix for *Hs*PINK1 in our structure, alongside the straight αC helix in the published unphosphorylated *Ph*PINK1 [Protein Data Bank (PDB) ID 7T3X] and the kinked αC helix in phosphorylated *Ph*PINK1 (PDB ID 7T4K). (**E**) Close-up view of PINK1 bound to TOM20. For TOM20, the atomic model is shown within the surface model, colored to depict hydrophobicity. Disulfide bonds are shown as yellow spheres. (**F**) Close-up view of the interaction between the kinase lobe of PINK1 and the N terminus of TOM5. Only side chains for interacting residues that could be confidently modeled are shown. Disulfide bonds are depicted as yellow spheres.

Closer examination of the dataset revealed substantial mobility in the kinase domains in particular. Indeed, the high-resolution reconstruction was obtained from approximately one-third of all particles, reflecting those with Cys^{166} cross-links, according to 3D classification without alignment. In the remaining approximately two-thirds of particles, dimers still formed with locked-in-place C-lobes but disordered kinase N-lobes. In these particles, PINK1 molecules are likely not disulfide-linked and are able to dissociate, which is a prerequisite for ubiquitin phosphorylation. Alternatively, this large set of particles could simply represent air-water interface–damaged particles.

Together, the overall structure of the human PINK1 kinase domain is highly consistent with structures and biochemistry performed for *Ph*PINK1 and *Tribolium castaneum* PINK1 (*Tc*PINK1) (*20*, *21*, *46*, *48*) and confirms many aspects of the PINK1 activation cascade. We interpret our structure as a postphosphorylation or activation (kinked αC helix) yet preactive (cross-linked dimer) state of the ubiquitin kinase PINK1.

Interactions of the human PINK1 dimer with the TOM-VDAC array

Two additional intramolecular disulfides further stabilize PINK1 on the TOM-VDAC array: between Cys^{125}, a residue mutated in EOPD on the kinase domain N helix, and Cys^{564} on the C-terminal αM helix; as well as between Cys^{549} on the αL helix and Cys^{377} in the β7-β8 loop. Both disulfides lock the kinase N helix (residues 106 to 134) to the C lobe and intrinsically reinforce the kinase domain (Fig. 3, A and E). The kinase dimer position on the TOM-VDAC array is further locked-down by interactions

with TOM20 and TOM5, holding it firmly in position.

TOM20 directly binds the PINK1 C lobe αK helix (residues 524 to 543) in the hydrophobic presequence binding groove and forms additional hydrogen bonds with the PINK1 N helix (Fig. 3E and fig. S12). These interactions have recently been suggested by AlphaFold modeling (*34*, *35*). Overall, TOM20 provides an elaborate brace around the locked-down PINK1 dimer (Fig. 1E).

A surprising and prominent second interaction exists between the cytosolic N-terminal portion of TOM5 and the C-lobe of PINK1. TOM5 residues 1 to 15 are intimately connected with a previously unappreciated C-lobe groove formed by the αM helix of PINK1 and the C-lobe core. Hence, TOM5 not only provides crucial TOM-VDAC interactions but also appears to play a role in orienting and supporting the kinase domain above the TOM-VDAC array (Fig. 3F). Together, TOM20 and TOM5, along with the cross-linked αM, L, K, and N helices, appear to be responsible for restricting the orientation and flexibility of PINK1 on the surface of mitochondria, promoting dimerization and activation (*21*).

PINK1 passage through TOM40

The locked-down conformation of the PINK1 dimer spans a distance of ~85 Å between residues that enter TOM40, which does not fit within a single TOM core complex (<80-Å distance between TOM40 barrels), explaining the observation of a TOM-VDAC array (Fig. 3A). As a result, only one of the TOM40 barrels is occupied in each TOM core complex.

Our structure resolves a physiological substrate, PINK1, within the TOM40 barrel at 2.75-Å resolution, illuminating the path of a presequence substrate in a human TOM40 barrel (Fig. 4, A and B). Cross-linking in yeast had mapped multiple routes for substrates to traverse the Tom40 barrel, following nonoverlapping pathways along the inner lining of the barrel (*49*–*53*). In our structure, the kinase N helix (residues 107 to 135) enters the TOM40 barrel at Arg^{119}. Within TOM40, the PINK1 transmembrane domain (residues 76 to 105) forms a long loop (residues 96 to 105) that skirts the TOM40 barrel before traversing the channel via a short helix (residues 76 to 91). Four residues (92 to 96) that include Cys^{92} and Cys^{96}, are mobile and were not modeled. Cys^{92} is interesting because its role as a patient mutation has remained obscure (*32*, *54*, *55*).

PINK1 interacts with TOM40 via five surface segments, namely "entrance," "patch-1," "patch-2," "N-terminal segment," and "exit" (Fig. 4A). The cytosolic entrance for PINK1 is located on the cytosolic rim of TOM40, along β9 to β11. The PINK1 N helix makes further interactions with the TOM7 N terminus (Lys^{7}) and, more intriguingly, also with a phospholipid, PL4 (fig. S5),

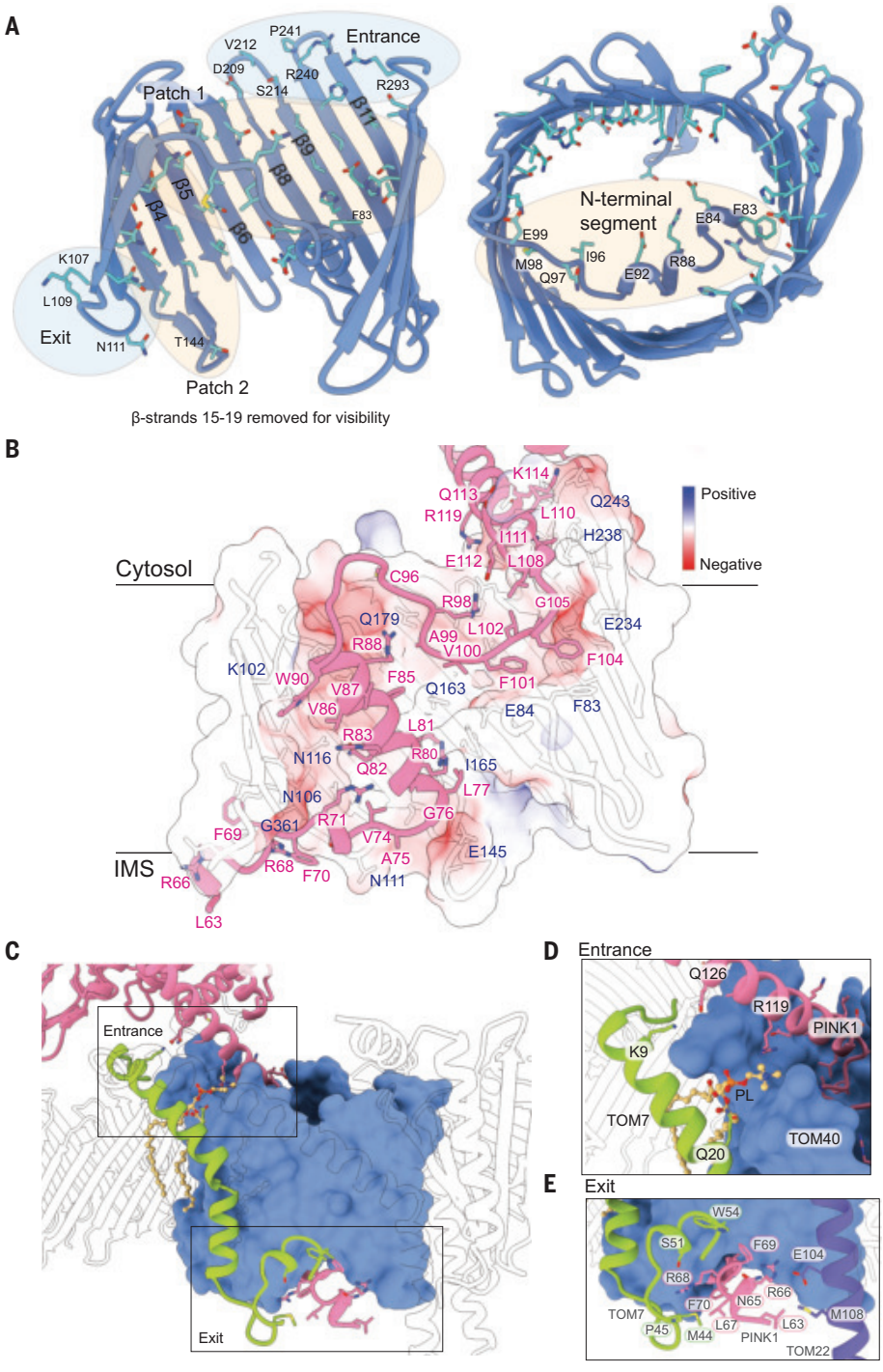

Fig. 4. PINK1 illuminates a path for mitochondrial presequence substrates through the TOM40 barrel. (**A**) Atomic model of the asymmetric TOM40 barrel containing PINK1 along the membrane plane and viewed from the cytosol. Side chains for residues that interact with PINK1 are shown. For visualization inside the barrel, β strands 15 to 19, which are not contacted by PINK1, were removed. The indicated patches mark the different interaction regions of PINK1 through the barrel. (**B**) Surface electrostatic potential of the asymmetric TOM40 barrel, along the membrane plane, containing PINK1. A ribbon model is used to depict PINK1. Interacting side chains are shown. The side-view tool in ChimeraX was used to segment the TOM40 barrel to enable visualization inside. (**C**) Interactions of PINK1 upon entrance and exit of the TOM40 barrel. TOM40 is shown as a surface-rendered model, whereas PINK1 and TOM7 are in ribbon form. (**D**) A close-up view of the PINK1 entrance into the TOM40 barrel from (C). PL indicates the phospholipid, shown in stick form. (**E**) A close-up view of the PINK1 exit tunnel through the TOM40 barrel from (C). Interacting side chains are shown.

which forms hydrogen bonds via its phosphate head group with both PINK1 Arg^{119} and TOM7 Gln^{20} (Fig. 4, C and D). Phospholipids at the TOM complex have previously been reported to be required for TOM complex stability and for binding of precursor substrates to the TOM complex (*56*), but a direct interaction between a substrate and phospholipid at the TOM complex has not been noted. Three additional charged interactions (PINK1 Arg^{119}, Lys^{114}, Glu^{114} with TOM20 Asp^{209}, Glu^{243}, Arg^{293}) and hydrophobic contacts via PINK1 Leu^{108} and Leu^{110} stabilize PINK1 entry into the TOM40 barrel (Fig. 4, A to D).

Patch-1 in the TOM40 barrel forms a channel along the curvature of the barrel, parallel to the membrane. Although it presents a net–negatively charged surface, patch-1 binds a mostly hydrophobic PINK1 motif (sequence GRAVFLAFG, residues 97 to 105; Fig. 4B). In particular, TOM40 Glu^{234}, located within an acidic patch just below the entrance, forms hydrogen bonds with the backbone amides of Phe^{104} and Gly^{105}. Patch-2 forms a path down the channel and is also lined with acidic residues. This site is occupied by a short PINK1 helix (residues 76 to 91), which follows along β strands 4 and 5 toward the IMS before protruding into the barrel β3-β4 loop of TOM40, stabilized by TOM40 Glu^{145}. The TOM40 N-terminal segment, a short helix within the pore (Fig. 4A, right), harnesses PINK1 as it traverses patch-1 and patch-2, forming multiple interactions along its length. Here, TOM40 Phe^{83}, situated within a pocket in patch-1, forms a π-π stack with PINK1 Phe^{104}, and TOM40 Glu^{92} forms hydrogen bonds with PINK1 Arg^{80}.

PINK1 exits TOM40 between strands β1 and β19, interacting with the TOM40 C terminus at Gly^{361} (Fig. 4, A and B). On the IMS rim of the TOM40 barrel, PINK1 forms hydrophobic and cation-π interactions between PINK1 Phe^{69} and TOM40 Val^{105} and Lys^{107}, and a β sheet–like H-bonding network between the β1 strand of TOM40 and the PINK1 backbone between Arg^{68} and Phe^{70} (Fig. 4E). Further detailed analysis of changes within the TOM40 barrel, with and without a substrate, can be found in the supplementary text and fig. S13.

We resolved six PINK1 residues (63 to 69) emerging from TOM40, and interestingly, these are guided out of the barrel by TOM22 and TOM7. TOM22 interacts with PINK1 through a salt bridge between TOM22 Glu^{104} and invariant PINK1 Arg^{66} as well as through a hydrophobic contact (TOM22 Met^{108}: PINK1 Leu^{63}) (Fig. 4E). Similarly, the saxophone shape of TOM7 at the IMS side creates a pocket for Arg^{68} of PINK1, which forms three hydrogen bonds: with the backbone carbonyls of TOM7 Pro^{45} and TOM40 Leu^{109} and with the side chain of TOM7 Ser^{51}. The "elbow" of TOM7 is further stabilized by van der Waals interactions between PINK1 Leu^{67} and TOM7 Pro^{45} (Fig. 4E). Importantly, both TOM7-interacting residues, PINK1 Arg^{68} and Leu^{67}, are mutated in EOPD patients. TOM7 is known to be an important component of PINK1 stabilization (*35*, *57*). Deletion of TOM7 in human cells leads to continuous PINK1 import and cleavage (by OMA1) in depolarized conditions (*33*), and our structure explains how TOM7 guides the entrance and exit of PINK1 through the TOM complex and into mitochondria.

Conclusion: Model for PINK1 stabilization on the TOM-VDAC array

Our structure of human PINK1 trapped as an import intermediate, apart from providing a structural explanation for PINK1 stabilization at the TOM complex and patient mutations in EOPD (fig. S14), answers the long-standing question of how a physiological presequence import substrate traffics through the human TOM complex. Unexpectedly, we also elucidated the architecture of a human VDAC2 dimer, which is the central component of the observed TOM-VDAC array, revealing a previously unknown role for the long-standing small TOM subunit TOM5 (*58*). The yeast homolog of VDAC, porin, has been shown to be linked to protein import through its role in the mitochondrial carrier pathway and the mitochondrial intermembrane space assembly (MIA) pathway (*59*, *60*). Yeast porin has the ability to regulate oligomerization of yeast Tom40 by sequestering Tom22, and a complexome profiling study observed TOM-porin and TOM-VDAC complexes in yeast and human mitochondria, respectively (*59*–*61*). Our study now implicates TOM-VDAC association in PINK1 mitophagy. It is unclear how common a feature the TOM-VDAC array is for the OMM landscape and whether it has roles in mitochondrial protein import in mammalian cells.

VDACs are the most abundant components of the OMM overall and also the earliest and most abundantly ubiquitinated proteins on the OMM (*18*). Mapping of reported ubiquitination sites onto VDAC2 (*18*) in the complex structure (fig. S15) revealed that ubiquitination would disrupt the complex. However, a ubiquitinated VDAC may become a prime substrate for TOM-associated monomeric PINK1 (Fig. 5). The role of VDAC in PINK1-mediated mitophagy has been debated, although the discussion has largely centered on VDAC1 (*62*, *63*). It has since been shown that depletion of all VDAC isoforms compromises Parkin recruitment to mitochondria (*64*) and that VDAC isoforms can

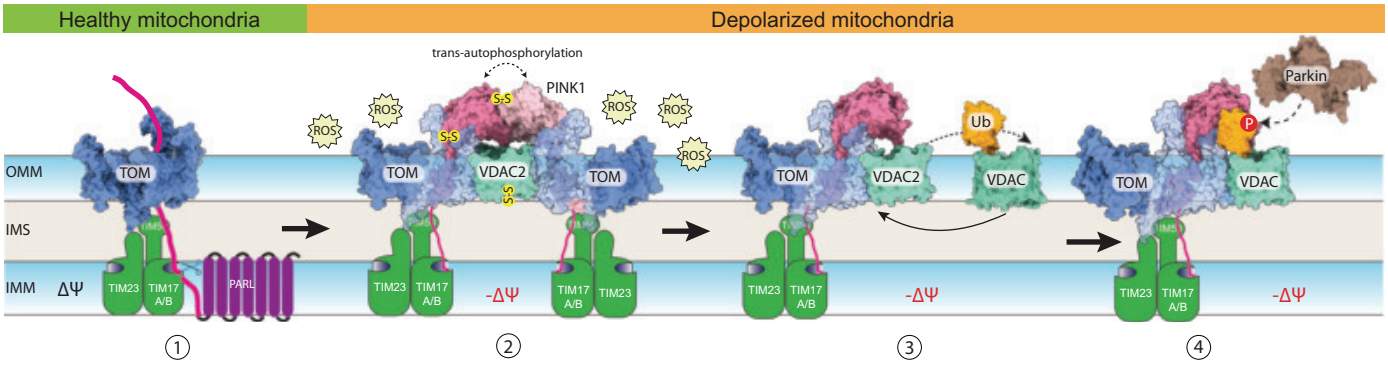

Fig. 5. Model for PINK1 stabilization and proposed role of VDAC in the initiation of PINK1/Parkin mitophagy. Model of PINK1 stabilization and activity. 1) In healthy mitochondria, PINK1 is imported into the IMM in a membrane potential dependent (ΔΨ) manner via the TOM-TIM23 presequence pathway, before cleavage by PARL and retrotranslocation. 2) In depolarized mitochondria, PINK1 import into the IMM is blocked. The PINK1 kinase domain folds on the OMM. Simultaneously, ROS also stimulate VDAC2 dimerization in the IMS, as well as the dimerization of PINK1 molecules on separate TOM complexes. The PINK1-TOM-VDAC array thus assembles, and PINK1 is trans-autophosphorylated. 3) As the initial burst of ROS dissipates and the redox environment becomes more reductive, the array and the PINK1 dimers dissociate. The associated VDACs can then either become ubiquitinated (Ub) by a nearby E3 ligase or, because folded activated PINK1 can bind ubiquitin, the in situ VDAC could be exchanged for an already ubiquitinated VDAC via avidity effects. 4) Ubiquitinated VDAC then becomes the prime PINK1 substrate, and the resulting phospho-ubiquitin recruits Parkin in close proximity to PINK1 to enable Parkin phosphorylation.

even form a complex with Parkin (*65*). However, it was not expected that VDAC is a part of the PINK1 stabilization complex (*31*, *32*, *35*), and it remains to be determined whether VDAC2 has a role for PINK1 stabilization or activity.

To arrive at the stage of PINK1 entrapment visualized in our reconstruction, numerous preceding import steps would have taken place (Fig. 5). The PINK1 N-terminal presequence would be recognized by TOM complex receptors, including TOM20 and TOM22, which would facilitate the import of the PINK1 N terminus through the TOM40 barrel; it would then exit at an exit tunnel comprising TOM40, TOM7, and TOM22 (Fig. 4E). A similar exit for presequence substrates has been suggested in yeast (fig. S13E) (*49*–*51*, *53*, *66*). The presequence would be picked up by TIM23 complex components TIM50 and TIM17B, which copurify and form cross-links with PINK1 (Fig. 1C and fig. S3) and which lead to cleavage and degradation of PINK1 in healthy mitochondria (Fig. 5). Depolarization would have inactivated the driving force for TIM23 translocation, blocking PINK1 import through the IMM and resulting in the accumulation of folded PINK1 bound to the TOM complex.

For PINK1 to become a ubiquitin kinase and signal mitochondrial dysfunction, it needs to dimerize and trans-autophosphorylate (*20*, *21*). PINK1 dimerization cannot occur within the same TOM core complex; it requires two TOM core complexes to assemble on a central VDAC dimer (Fig. 5). TOM5 plays integral roles to connect the TOM40 and VDAC β barrels and further provides a cytosolic docking site for PINK1. Also, TOM20, at the periphery of the TOM core complex in our structure and in close proximity to VDAC2, provides an elaborate brace for the PINK1 dimer, which, as a result, is highly constrained on the OMM surface. Oxidation and disulfide bond formation clearly contributed to the high-resolution structure presented here (Fig. 5). These oxidation events were not engineered [no cross-linkers or exogenous reactive oxygen species (ROS) for structural studies, SEC in presence of reducing agents] and likely reflect modification by endogenous ROS after depolarization. It is tempting to speculate that PINK1 oxidation is enhanced by VDAC channels exuding ROS during depolarization.

Dimerization prevents PINK1 from acting as a ubiquitin kinase (*21*), and to signal mitochondrial stress, the PINK1 dimer has to open, which, for our structure, would require reductive resolution of the Cys^{166} disulfide bridge. The resulting TOM-bound monomeric, active PINK1 may destabilize the TOM-VDAC array. At this point, ubiquitinated VDAC molecules would be presented with two docking sites: Whereas TOM5 can bind the VDAC barrel, TOM-associated PINK1 would bind and phosphorylate ubiquitin attached to VDAC. This model is consistent with earlier observations of VDAC-dependent Parkin recruitment (*64*, *65*). Parkin recruitment to phospho-ubiquitinated VDAC, would locate Parkin in close proximity to PINK1, streamlining Parkin activation by PINK1 (Fig. 5).

Next, we shall attempt to visualize PINK1 as an active ubiquitin kinase on mitochondria, as well as complete our structural studies of the PINK1-TOM-TIM23 supercomplex, which appeared to be present in a small number of particles but requires further stabilization. Our structure also provides multiple unexplored avenues to stabilize PINK1 on mitochondria to develop much needed treatment options for Parkinson's disease patients.

REFERENCES AND NOTES

1. E. M. Valente *et al*., *Science* **304**, 1158–1160 (2004).
2. L. A. Kane *et al*., *J. Cell Biol.* **205**, 143–153 (2014).
3. C. Kondapalli *et al*., *Open Biol.* **2**, 120080 (2012).
4. A. Kazlauskaite *et al*., *Biochem. J.* **460**, 127–141 (2014).
5. F. Koyano *et al*., *Nature* **510**, 162–166 (2014).
6. T. Wauer *et al*., *EMBO J.* **34**, 307–325 (2015).
7. A. Ordureau *et al*., *Mol. Cell* **56**, 360–375 (2014).
8. J. W. Harper, A. Ordureau, J.-M. Heo, *Nat. Rev. Mol. Cell Biol.* **19**, 93–108 (2018).
9. M. F. Schmidt, Z. Y. Gan, D. Komander, G. Dewson, *Cell Death Differ.* **28**, 570–590 (2021).
10. D. P. Narendra, R. J. Youle, *Nat. Cell Biol.* **26**, 1639–1651 (2024).
11. S. A. Sarraf *et al*., *Nature* **496**, 372–376 (2013).
12. T. Wauer, M. Simicek, A. Schubert, D. Komander, *Nature* **524**, 370–374 (2015).
13. C. Gladkova, S. L. Maslen, J. M. Skehel, D. Komander, *Nature* **559**, 410–414 (2018).
14. V. Sauvé *et al*., *Nat. Struct. Mol. Biol.* **25**, 623–630 (2018).
15. K. N. Swatek *et al*., *Nature* **572**, 533–537 (2019).
16. O. Antico *et al*., *Sci. Adv.* **7**, eabj0722 (2021).
17. A. Ordureau *et al*., *Mol. Cell* **77**, 1124–1142.e10 (2020).
18. A. Ordureau *et al*., *Mol. Cell* **70**, 211–227.e8 (2018).
19. H. I. Woodroof *et al*., *Open Biol.* **1**, 110012 (2011).
20. S. Rasool *et al*., *Mol. Cell* **82**, 44–59.e6 (2022).
21. Z. Y. Gan *et al*., *Nature* **602**, 328–335 (2022).
22. A. Kumar *et al*., *eLife* **6**, e29985 (2017).
23. A. M. Pickrell, R. J. Youle, *Neuron* **85**, 257–273 (2015).
24. N. T. Hertz *et al*., *Cell* **154**, 737–747 (2013).
25. N. Hertz *et al*., Research Square rs.3.rs-4356493 [Preprint] (2024); https://doi.org/10.21203/rs.3.rs-4356493/v1.
26. Z. Y. Gan *et al*., *Sci. Adv.* **10**, eadj7408 (2024).
27. N. Pfanner, B. Warscheid, N. Wiedemann, *Nat. Rev. Mol. Cell Biol.* **20**, 267–284 (2019).
28. J. D. Busch, L. F. Fielden, N. Pfanner, N. Wiedemann, *Mol. Cell* **83**, 890–910 (2023).
29. Y. Araiso, K. Imai, T. Endo, *Annu. Rev. Biochem.* **91**, 679–703 (2022).
30. S. Callegari, L. D. Cruz-Zaragoza, P. Rehling, *Biol. Chem.* **401**, 709–721 (2020).
31. M. Lazarou, S. M. Jin, L. A. Kane, R. J. Youle, *Dev. Cell* **22**, 320–333 (2012).
32. K. Okatsu *et al*., *J. Biol. Chem.* **288**, 36372–36384 (2013).
33. S. Sekine *et al*., *Mol. Cell* **73**, 1028–1043.e5 (2019).
34. M. A. Eldeeb *et al*., *Proc. Natl. Acad. Sci. U.S.A.* **121**, e2313540121 (2024).
35. O. G. Raimi *et al*., *Sci. Adv.* **10**, eadn7191 (2024).
36. S. Akabane *et al*., *Cell Rep.* **42**, 112454 (2023).
37. J. Su *et al*., *Proc. Natl. Acad. Sci. U.S.A.* **119**, e2200158119 (2022).
38. J. Su *et al*., *PNAS Nexus* **3**, pgae269 (2024).
39. W. Wang *et al*., *Cell Discov.* **6**, 67 (2020).
40. Z. Guan *et al*., *Cell Discov.* **7**, 22 (2021).
41. E. H.-Y. Cheng, T. V. Sheiko, J. K. Fisher, W. J. Craigen, S. J. Korsmeyer, *Science* **301**, 513–517 (2003).
42. H. L. Glover, A. Schreiner, G. Dewson, S. W. G. Tait, *Nat. Cell Biol.* **26**, 1434–1446 (2024).
43. T. Hosaka *et al*., *Protein Sci.* **26**, 1749–1758 (2017).
44. J. Schredelseker *et al*., *J. Biol. Chem.* **289**, 12566–12577 (2014).
45. P. Ornelas *et al*., *Proc. Natl. Acad. Sci. U.S.A.* **120**, e2301447120 (2023).
46. A. F. Schubert *et al*., *Nature* **552**, 51–56 (2017).
47. S. S. Taylor, A. P. Kornev, *Trends Biochem. Sci.* **36**, 65–77 (2011).
48. K. Okatsu *et al*., *Sci. Rep.* **8**, 10382 (2018).
49. T. Shiota *et al*., *Science* **349**, 1544–1548 (2015).
50. X. Zhou *et al*., *Nat. Struct. Mol. Biol.* **30**, 1996–2008 (2023).
51. K. Tucker, E. Park, *Nat. Struct. Mol. Biol.* **26**, 1158–1166 (2019).
52. Y. Araiso *et al*., Cryo-EM structure of the translocator of the outer mitochondrial membrane, Protein Data Bank (2019); https://doi.org/10.2210/pdb6jnf/pdb.
53. T. Bausewein *et al*., *Cell* **170**, 693–700.e7 (2017).
54. M. Iguchi *et al*., *J. Biol. Chem.* **288**, 22019–22032 (2013).
55. K. Okatsu *et al*., *Nat. Commun.* **3**, 1016 (2012).
56. J. J. Hoffmann, T. Becker, *Int. J. Mol. Sci.* **23**, 5274 (2022).
57. K. K. Maruszczak, M. Jung, S. Rasool, J.-F. Trempe, D. Rapaport, *J. Mol. Med.* **100**, 747–762 (2022).
58. K. Dietmeier *et al*., *Nature* **388**, 195–200 (1997).
59. L. Ellenrieder *et al*., *Mol. Cell* **73**, 1056–1065.e7 (2019).
60. H. Sakaue *et al*., *Mol. Cell* **73**, 1044–1055.e8 (2019).
61. C. S. Müller *et al*., *Mol. Cell. Proteomics* **15**, 669–681 (2016).
62. D. Narendra, L. A. Kane, D. N. Hauser, I. M. Fearnley, R. J. Youle, *Autophagy* **6**, 1090–1106 (2010).
63. S. Geisler *et al*., *Nat. Cell Biol.* **12**, 119–131 (2010).
64. Y. Sun, A. A. Vashisht, J. Tchieu, J. A. Wohlschlegel, L. Dreier, *J. Biol. Chem.* **287**, 40652–40660 (2012).
65. S. Callegari *et al*., *Autophagy* **13**, 201–211 (2017).
66. Y. Araiso, T. Endo, *Biophys. Physicobiol.* **19**, e190022 (2022).
67. Y. Perez-Riverol *et al*., *Nucleic Acids Res.* **50**, D543–D552 (2022).
68. S. Okuda *et al*., *Nucleic Acids Res.* **45**, D1107–D1111 (2017).

ACKNOWLEDGMENTS

We thank M. Lazarou, G. Dewson, T. Nguyen, and W. Tan (Walter and Eliza Hall Institute of Medical Research) for helpful advice. We acknowledge use of the facilities at the Ian Holmes Imaging Centre, Bio21 Institute. **Funding:** This work was funded by National Health and Medical Research Council Investigator grant GNT1178122 (D.K.), an Australian Government Research Training Program Fellowship (Z.Y.G.), The Hugh Christopher Middendorp Testamentary Trust (S.C.), and a CSL Centenary Fellowship (A.G.). **Author contributions:** Conceptualization: S.C., D.K.; Methodology: S.C., N.S.K., Z.Y.G., T.D., S.A.C., A.L., L.F.D., A.G.; Cryo–EM data collection: N.S.K., A.L.; Structural modeling and refinement: N.S.K., A.G.; Investigation: S.C., N.S.K., Z.Y.G., T.D., S.A.C., A.L., L.F.D., A.G.; Visualization: S.C., N.S.K.; Funding acquisition: S.C., D.K., A.G.; Supervision: S.C., D.K., A.G.; Writing – original draft: S.C., N.S.K., D.K.; Writing – review & editing: All authors. **Competing interests:** D.K. is founder, shareholder, and scientific advisory board member of Entact Bio and Proxima Bio. All other authors declare no competing interests. **Data and materials availability:** Coordinates and EM density maps have been submitted to the Protein Data Bank and EM Data Bank for the entire complex (9EIH, EMD-48083), the symmetry expanded portion of the complex (9EII, EMD-48084), and the symmetry expanded with extended TOM20 helix (9EIJ, EMD-48085). The MS proteomics data related to in-gel digests have been deposited to the ProteomeXchange Consortium via the PRIDE partner repository (dataset identifier PXD058526) (*67*). The cross-linking MS data have been deposited to the ProteomeXchange Consortium (*68*) via jPOST with accession number JPST003503.

SUPPLEMENTARY MATERIALS

science.org/doi/10.1126/science.adu6445
Materials and Methods
Supplementary Text
Figs. S1 to S15
Tables S1 and S2
References (*69*–*84*)
MDAR Reproducibility Checklist
Data S1 and S2

Submitted 9 December 2024; accepted 27 February 2025
Published online 13 March 2025
10.1126/science.adu6445

BATTERIES

Fatigue of Li metal anode in solid-state batteries

Tengrui Wang[1]†, Bo Chen[1]†, Yijie Liu[2]†, Zhenyou Song[1], Zhongqiang Wang[1], Yuwei Chen[1], Qian Yu[1], Jiayun Wen[1], Yiming Dai[1], Qi Kang[1], Fei Pei[3], Rong Xu[4], Wei Luo[1]*, Yunhui Huang[3]*

Solid-state lithium metal batteries (SSBs) are promising for electric vehicles because of their potential to provide high energy density and enhanced safety. However, these batteries face short-circuit challenges caused by uncontrolled lithium dendrite growth during cycling. Using operando scanning electron microscopy and phase-field simulations, we determined that failure of SSBs is closely linked to the fatigue of the lithium metal anode, which markedly contributes to interface degradation and dendrite growth in SSBs. This fatigue follows the Coffin-Manson equation in mechanics, indicating that it is an innate characteristic. Clarifying the essential role of fatigue provides a physical basis for understanding failures of SSBs and paves the way to extending their lifespan.

Solid-state Li metal batteries (SSBs), which integrate a high-capacity Li metal anode (LMA) with a nonflammable inorganic solid-state electrolyte (SSE) and a high-voltage cathode, have emerged as a promising choice to simultaneously offer both high energy density and high safety (*1*–*4*). To meet practical performance levels, SSBs need to deliver a current density >10.0 mA/cm^2, a capacity exceeding 5.0 mAh/cm^2, and a long lifespan of >1000 cycles (*5*). Although meeting one of the conditions is relatively straightforward, fulfilling all of them concurrently is a challenge. In particular, SSBs encounter rapid failures caused by Li dendrite growth upon cycling, which is one of the major obstacles to their commercialization (*6*–*11*).

Understanding the mechanisms of SSB failures is a crucial focus for both scientific and industrial inquiry (*12*–*14*). Suboptimal interface contact has been considered the main reason for failures of SSBs, because voids at the interface cause current constriction and overpotential increase, which induces Li dendrite formation (*15*, *16*). However, short circuiting still occurs even when the initial Li-SSE interfacial resistance has been minimized to levels lower than those in liquid cells (*17*). Kinetics theory reveals that the voids can accumulate during Li stripping at high current and capacity because Li^+ cannot adequately replenish the Li loss at the interface (*18*–*20*). Although enhanced Li-ion diffusion speed through interface engineering and high stack pressure can suppress kinetics-limited void accumulation, they cannot prevent interface degradation and short failure during cycling (*21*, *22*). The unexpected interface decay and failure of SSBs seem counterintuitive given that the loss of Li under this condition is completely restored with Li^+ diffusion or Li deformation (*23*). More recent studies posit that SSB failure is highly linked to mechanics, because SSEs may not accommodate volume changes or relieve stress as effectively as liquid electrolytes (*24*, *25*). The substantial stress generated from Li deposition can drive crack growth in SSEs and induce Li dendrite formation (*26*–*28*). Methods such as ion implantation or implementing soft interfaces have been suggested to mitigate the cracking of SSEs (*29*, *30*). Nevertheless, the occurrence of short circuiting due to Li dendrites remains inevitable. Critical stripping current (CSC) and critical current density (CCD) are two commonly used metrics for evaluating the capability of Li dendrite suppression (*7*, *20*). Although the above-mentioned mechanistic theories can achieve high CCD or CSC, it is still not well understood why SSBs cycling at a current density much lower than CSC or CCD still encounter interface degradation and Li dendrite growth.

Fatigue is a widespread, long-standing, and critical issue for metallic materials exposed to cyclic loadings, being responsible for >80% of engineering failures (*31*). The fatigue from cyclic loading induces cracks and fractures of a material at stress levels below its ultimate tensile strength (*32*). Therefore, a high ultimate tensile strength does not guarantee that a metallic material has a long-term cycling life (*33*). Similarly, both CSC and CCD represent the maximum current that the solid-state cells can tolerate, which can be akin to the "ultimate tensile strength" for SSBs. A high CSC or CCD does not necessarily reflect the long-term cycling capability of SSBs because these metrics do not consider fatigue. As a metallic material, LMA should also undergo fatigue when subjected to cyclic mechanical loading during cycling; however, this remains an unexplored topic.

In this work, we have unveiled how Li metal fatigue gives rise to the failure of SSBs upon cycling. The verification of Li metal fatigue in SSBs clarifies the previously inexplicable phenomenon and offers an opportunity to establish a quantitative correlation among current density, capacity, mechanical properties of LMA, and lifespans of SSBs. Fatigue of the Li metal anode during electrochemical cycling also reshapes our knowledge of SSB failure and provides insights into the rational design of the Li metal anode.

Interface evolution characterizations with operando scanning electron microscope

Because garnet-type $Li_{6.5}La_3Zr_{1.5}Ta_{0.5}O_{12}$ (LLZTO) exhibits exceptional stability toward LMA, it was used as the model SSE in this work (*34*). The properties of as-prepared LLZTO SSEs are illustrated in fig. S1. Symmetric Li|LLZTO|Li cells (coin-cell type) were assembled and evaluated under stripping current densities (CSC tests; Fig. 1A), step-increasing cyclic currents (CCD tests; Fig. 1B), and long-term cyclic current density (Fig. 1C). The stripped capacity reached 11.5 mAh/cm^2 at 0.5 mA/cm^2, and in situ electrochemical impedance spectroscopy (EIS) results suggest that the potential increase originates from the rising interfacial impedances (fig. S2) (*19*). The CCD of the Li|LLZTO|Li cell is 1.0 mA/cm^2 at room temperature. However, during long-term cycling, the cell still experienced a potential increase starting at the 60th cycle and short circuited at the 145th cycle despite the capacity being only 1.2% (0.25 mAh/cm^2) of the largest stripped capacity (21.3 mAh/cm^2) and having a low current density that was only one-tenth of the CCD (0.1 mA/cm^2). The partial enlargement of the charging curve at 0.1 mA/cm^2 suggests a stable interface without void formations during stripping at such a condition (fig. S3). This puzzling phenomenon underscores the crucial role of cyclic currents. We then replaced LLZTO with other SSEs, including sulfide-based Li_6PS_5Cl (LPSC), β-Li_3PS_4 (β-LPS), and polymer-based polyethylene, to assemble Li-Li symmetric cells, and used the $Na_3Zr_2Si_2PO_{12}$ SSE for fabricating Na-Na symmetric cells. We observed that short circuit occurred even when the cyclic current was much lower than the CCD and CSC (see supplementary note I and figs. S4 to S8).

To understand the failure mechanisms, operando techniques are essential for tracking the interface evolutions (*22*, *35*). By connecting the custom-designed sample stage in a scanning electron microscope (SEM) with an external electrochemical workstation, real-time observations of interfacial evolutions during charging and discharging were enabled (Fig. 1D; for details, see supplementary note II and figs. S9 and

[1]Institute of New Energy for Vehicles, School of Materials Science and Engineering, Tongji University, Shanghai, China. [2]School of Electrical Engineering, Southwest Jiaotong University, Chengdu, China. [3]State Key Laboratory of Material Processing and Die & Mould Technology, School of Materials Science and Engineering, Huazhong University of Science and Technology, Wuhan, Hubei, China. [4]State Key Laboratory for Strength and Vibration of Mechanical Structures, Department of Engineering Mechanics, Xi'an Jiaotong University, Xi'an, China.
*Corresponding author. Email: weiluo@tongji.edu.cn (W.L.); huangyh@hust.edu.cn (Y.H.)
†These authors contributed equally to this work.

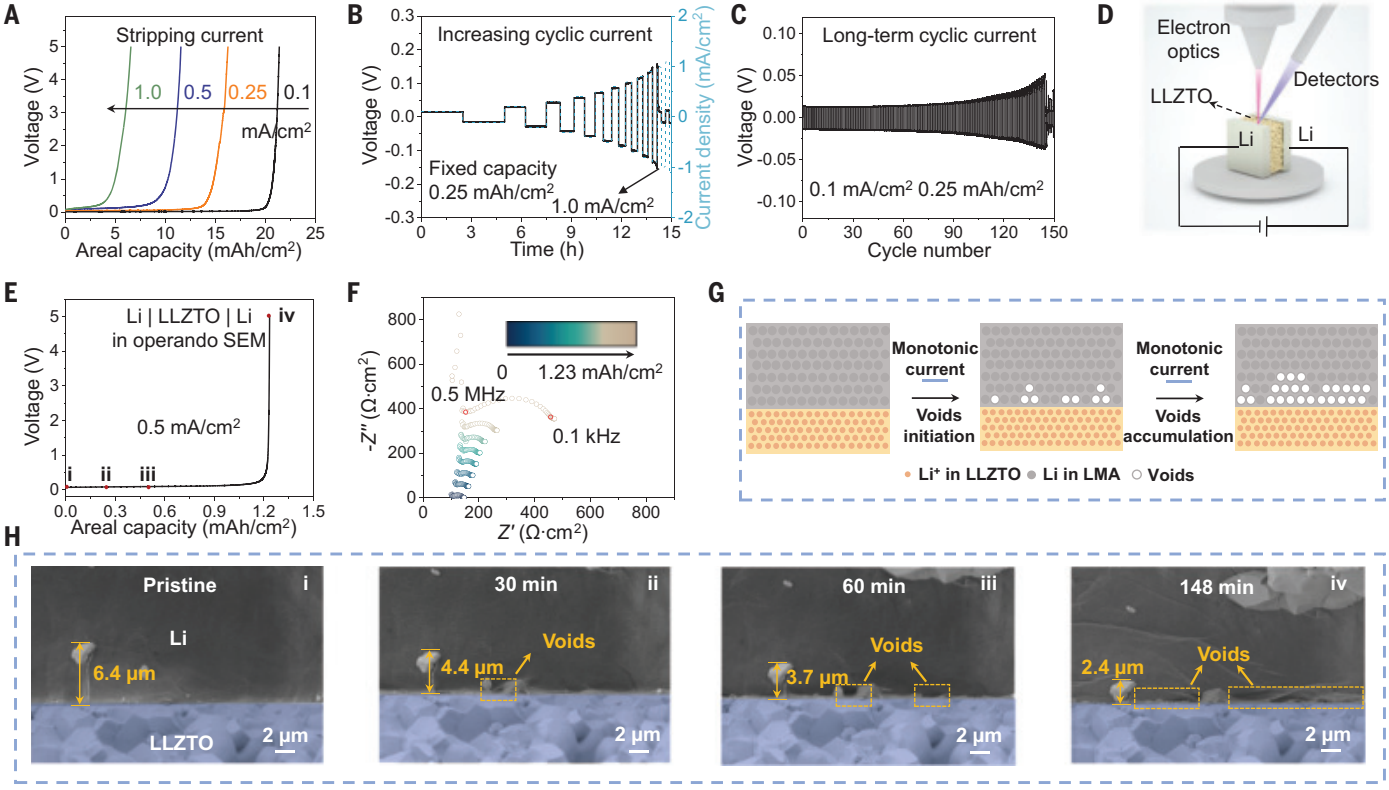

Fig. 1. Electrochemical performances of Li|LLZTO|Li symmetric cells and operando SEM imaging of LMA|LLZTO interface. (**A**) Voltage profiles of Li|LLZTO|Li cells at stripping currents of 0.1, 0.25, 0.5, and 1.0 mA/cm^2. The stripped capacities reached 21.3, 16.2, 11.5, and 6.5 mAh/cm^2, respectively. (**B**) Voltage evolutions of a symmetric cell at step-increasing currents with a fixed capacity of 0.25 mAh/cm^2. The cell ultimately short circuited at 1.0 mA/cm^2. (**C**) Long-term cycling stability at 0.1 mA/cm^2 and 0.25 mAh/cm^2. (**D**) Schematic of the operando SEM experiment. (**E** and **F**) Voltage profile (E) and corresponding in situ EIS profiles (F) of a Li|LLZTO|Li cell in operando SEM. (**G**) Illustration of interface failure process during stripping. (**H**) Operando SEM images of the LMA-LLZTO interface evolutions during stripping shown in Fig. 2E.

S10). We then observed the dynamic evolution process of the LMA-LLZTO interface under a stripping current (Fig. 1E). Initially, the cell voltage remained relatively stable, but eventually experienced a sharp polarization inflection toward the end, which stems from the escalating interfacial impedance during the stripping process (Fig. 1F and fig. S11). Before stripping, Li showed an intimate contact with LLZTO (Fig. 1H). As the stripping process advanced, LMA moved toward LLZTO side. After 30 min, small voids appeared, gradually grew up, and finally connected with each other. On the plating side, the plated Li formed a column shape and gradually grew while maintaining an intimate interfacial contact (fig. S12). The underlying physical process is illustrated in Fig. 1G. During Li stripping, a Li atom undergoes electron loss and transforms into Li^+, traversing the LMA-LLZTO interface and creating a vacancy (*23*). As stripping proceeds, vacancies accumulate at the interface, leading to void formation and subsequent voltage increase.

Fatigue of LMA

To further reveal the role of cyclic current, it is crucial to mitigate the void formation induced by limited kinetics (*19*, *20*). Therefore, a low current density of 0.1 mA/cm^2 and an ultralow capacity of 0.0083 mAh/cm^2 (5-min charging and discharging) were selected (Fig. 2A). The galvanostatic charge-discharge curve confirms that the potential remains stable in each stripping or plating cycle, indicating the absence of voids due to sluggish Li^+ transfer. Unexpectedly, even at such a moderate condition, the voltage showed a noticeable increase after 350 cycles. The corresponding interface evolution processes of LMA are depicted in Fig. 2C. In the initial 10 cycles, there was minimal change in LMA. Between the 10th and 30th cycle, partial defects emerged, as indicated by the arrows. As cycling progressed, the number of defects increased and they grew in size. By the 150th cycle, the defects further proliferated, and slip bands appeared, causing a slight increase in the cell's voltage. Until the 350th cycle, small voids were observed and the voltage showed an increase compared with the first cycle. Because the observation range of SEM is relatively limited for high resolution, we took SEM images from different locations to demonstrate the universality of our observations (figs. S13 and S14). These changes are consistent with the increases in the cell's voltage and illustrate the effects of cycling current, indicating a distinctive failure mechanism compared with that under the stripping current. This phenomenon became more pronounced at an increased current density of 0.25 mA/cm^2 (fig. S15).

Figure 2D shows specific charge-discharge curves of a cell cycling at 0.1 mA/cm^2 and 0.25 mAh/cm^2. The voltage was initially stable before 60 cycles, indicating a consistent stripping and plating cycle. However, after 90 cycles, the voltage increase accelerated, and the shape of the voltage curve changed, transitioning from horizontal to inclined upward. This suggests that the interface had turned from a stable to an unstable state (*19*). As shown in fig. S3, void formation during the stripping process under the same condition has been ruled out. Thus, this transition from steady state to non–steady state should be attributed to the results of cyclic current. Figure 2E illustrates the voltage changes of SSBs during cycling. The fluctuations in voltage of SSBs here represent the volume changes of voids (*19*, *20*), which was further confirmed by EIS and x-ray microcomputed tomography (see supplementary note III and figs. S16 to S18).

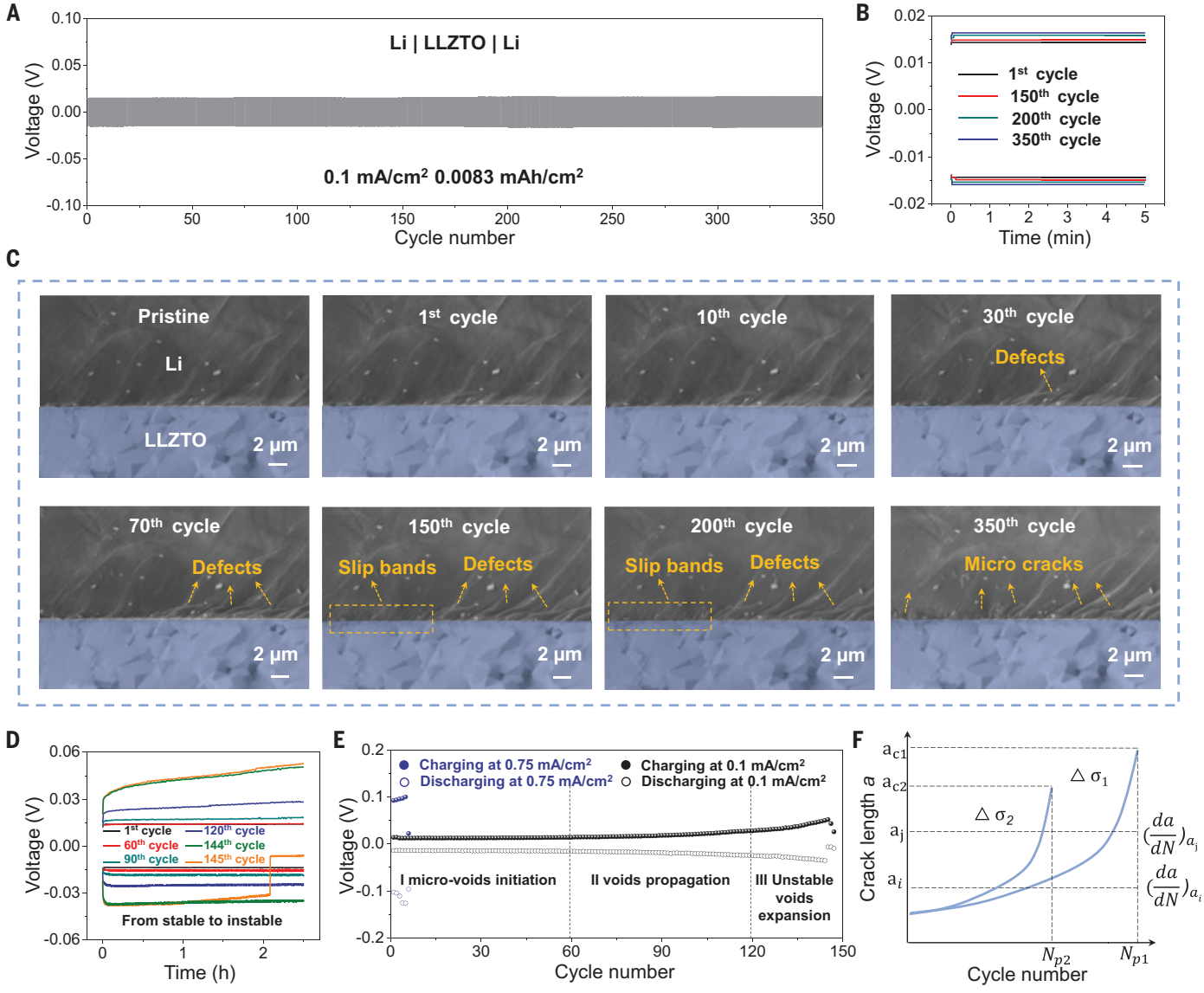

Fig. 2. Operando SEM analysis of LMA-LLZTO interface under cyclic currents and failure analysis. (**A**) Voltage profiles of a Li|LLZTO|Li symmetric cell in operando SEM under a cyclic current of 0.1 mA/cm^2. The charging and discharging times are both 5 min. At such a current density and capacity (0.0083 mAh/cm^2), the impacts of Li^+ diffusion are almost eliminated. (**B**) Four typical charge-discharge curves from (A). (**C**) Corresponding operando SEM images of LMA during cycling. Interface degradations can be clearly observed during cycling. (**D**) Charge-discharge curves for specific cycles of a Li|LLZTO|Li cell cycling at 0.1 mA/cm^2 and 0.25 mAh/cm^2. (**E**) Voltage evolution curves of symmetric cells at 0.1 mA/cm^2 (black circle) and 0.75 mA/cm^2 (blue circle). Solid circles represent charging voltage, and hollow circles represent discharging voltage. A sudden voltage drop indicates short circuit. (**F**) Typical fatigue crack propagation curve of a metallic material.

The growth of voids formed during cycling in LMA closely resembles fatigue crack growth in metallic materials. A typical fatigue crack propagation curve of a metallic material in mechanics is presented in Fig. 2F. Both the crack length (a) and the slope (da/dN) increase with the cycle number (N) (*36*). When the fatigue test reaches a certain cycle, da/dN increases to infinity, indicating the final fracture induced by fatigue. Moreover, a higher cyclic stress results in a faster slope increase and shorter cycle lives, similar to the effects of increasing the current density on the cycle life of SSBs. The analogous patterns of voltage cycle number curve and the evolution of crack lengths in metallic fatigue suggest a shared fatigue-driven failure mode. According to the theory of metallic fatigue, the lifespan of the SSBs can be divided into three stages: (i) microvoid initiation, (ii) void propagation, and (iii) unstable void expansion (Fig. 2E and fig. S19).

Quantitative relationship between mechanics and electrochemistry

Because of Li metal's high reactivity, prior studies have rarely evaluated its fatigue behavior. We designed a set of methods and in situ visualized mechanical testing of Li metal in a SEM (fig. S20). The in situ tensile testing and fatigue testing directly verified that Li metal experiences fatigue when it undergoes cyclic stress lower than its tensile strength (fig. S21). Moreover, simulated results of current and stress distributions within the LMA demonstrated that it would go through cyclic stress during electrochemical cycling (fig. S22), satisfying the conditions of LMA fatigue (*31*, *33*). Both the electrochemical performances and the operando SEM observations suggest that the fatigue-induced failure of LMA is intensified by increasing both current density and capacity (see supplementary note IV and figs. S23

to S25). This is similar to the influence of stress and strain on the fatigue life of metals in mechanics, where the Coffin-Manson equation describes the relationship between the fatigue life of a material and the magnitude of plastic strain that it experiences (for details, see supplementary note V) (*37*, *38*). The Coffin-Manson equation is

$$\frac{\Delta\varepsilon_t}{2} = \frac{\sigma'_f}{E_v^*}(2N_f)^b + \varepsilon'_f(2N_f)^c$$

where $\Delta\varepsilon_t$ is the plastic strain, σ'_f is the fatigue strength coefficient, E_v^* is the effective elastic modulus, N_f is the cycling number required to reach fatigue failure, ε'_f is an empirical constant known as the fatigue ductility coefficient, and b and c are the fatigue strength exponent and fatigue ductility exponent, respectively. According to this equation, the fatigue life of metallic materials is determined by plastic strain, stress, and their mechanical properties. To apply this equation in SSBs, we first explicated the relationship between current density (capacity) and stress (plastic strain). Figure 3A shows the stress as a function of current density (CD) calculated with phase-field simulations (for details, see supplementary note VI). The stress generated on LMA exhibits an exponential growth with a power law exponent of 4.2 in relation to the current density. According to the simulation of Li deposition process, the normalized capacity (Q) and plastic deformation of LMA exhibit a positive linear correlation with a power law exponent of almost 1.0 (fig. S26 and Fig. 3B). We could also obtain a similar relationship between that plastic deformation and capacity from the operando SEM observations (fig. S27). These correlations enable the application of the Coffin-Manson equation in SSBs. In addition to current density and capacity, σ'_f and ε'_f of LMA are essential mechanical parameters in this equation. Although it is challenging to directly obtain these parameters through experiments due to the significant instability of LMA in the air, we can use ultimate tensile strength and fracture strain in tensile testing to approximately represent σ'_f and ε'_f, respectively (fig. S28). We then used the Coffin-Manson equation to simulate the degradation processes of SSBs (see supplementary note VI). Figures S29 to S31 illustrate the simulated morphology changes of LMA during cycling at 0.1 mA/cm^2 and 0.25 mAh/cm^2, as well as the corresponding current distributions and stress distributions evolutions, respectively. Simulation results indicated that voids were initiated by 50 cycles and gradually grew within 50 to 120 cycles, leading to concentrations of current and stress. After 120 cycles, the voids significantly grew up. The void growth increased the interface resistance and could be tracked in the calculated voltage evolution curves (Fig. 3C). Figure S32 and Fig. 3D illustrate the experimentally obtained and calculated cycle life of SSBs as a function of current density. In addition, the curves depicting changes in cycle life with capacity are presented in fig. S33 and Fig. 3E. The similar statistical patterns of the experimental and calculated results link the failures of SSBs with LMA fatigue.

Theoretically, enhancing the fatigue strength of metallic materials can effectively improve fatigue lifespan (*31*, *39*). We used the relationship to investigate the influence of LMA's fatigue strength on the lifespans of SSBs. Figure S34 and Fig. 3F show that the cycle life of SSBs can be greatly enhanced by tripling the preset fatigue strength. To verify this, we fabricated a $Li_{20}Zn$ alloy anode, which shows a slightly lower Li^+ diffusion coefficient but three times higher mechanical strength compared with pristine Li (fig. S35). As expected, the as-assembled $Li_{20}Zn$|LLZTO|$Li_{20}Zn$ symmetric cell delivered an enhanced lifespan of 249 cycles compared with that of the Li|LLZTO|Li cell (145 cycles), which is close to the theoretically predicted value of 282 cycles. The improved cycling stability of $Li_{20}Zn$ anode could also be verified in full cells (fig. S36). To investigate the origination of enhanced electrochemical performances, we also conducted fatigue testing of $Li_{20}Zn$ alloy and pristine Li (fig. S37). Under the same stress, the fatigue life of the $Li_{20}Zn$ alloy was more than three times that of Li. A kinetically ultrasluggish Li_4Mg alloy anode can also verify the essential role of high fatigue resistance. The Li^+ diffusion coefficient of Li_4Mg (0.17×10^{-11} cm^2/s) is only ~7.8% of that of pristine Li (2.2×10^{-11} cm^2/s), whereas its mechanical strength is 25.4 times higher than pristine Li (fig. S38) (*40*). Contrary to traditional viewpoints based on kinetics, the cycle life of a Li_4Mg|LLZTO|Li_4Mg symmetric cell was >500 cycles (2500 hours) without short circuit, surpassing that of Li and $Li_{20}Zn$ (fig. S39). The Li^+ diffusion coefficients, mechanical strength, and cycling stability of Li, $Li_{20}Zn$, and Li_4Mg are shown in Fig. 3, G, H, and I, respectively. The cycling stability of SSBs showed a strongly positive correlation with the fatigue resistance

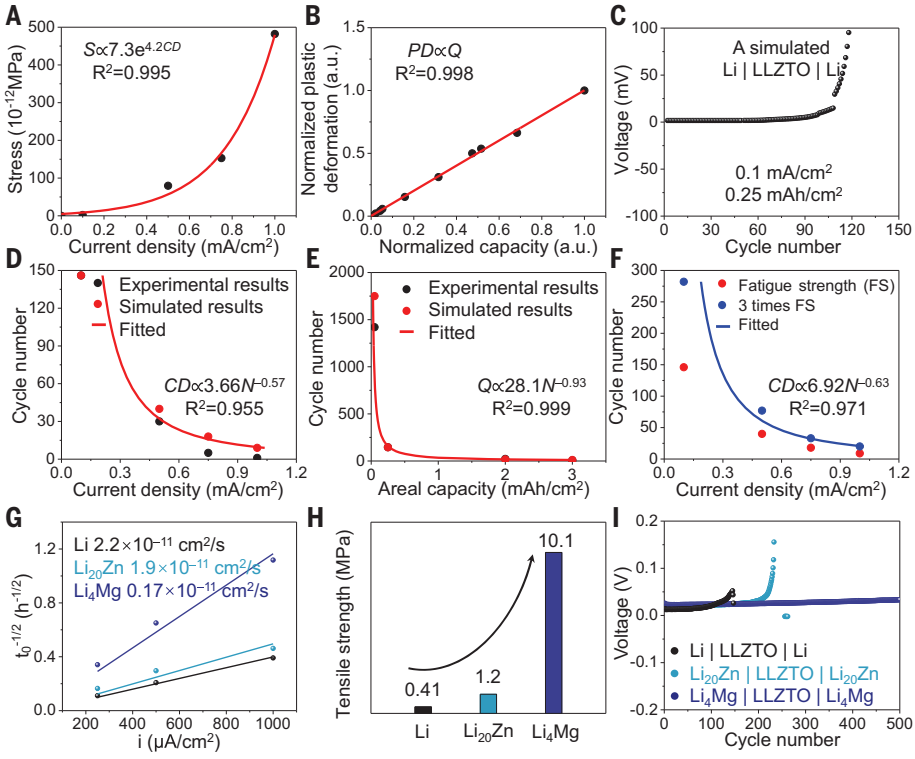

Fig. 3. Quantitative analysis of SSB failure. (**A** and **B**) Correlation between calculated stress (S) and CD (A) and normalized PD and normalized capacity (Q) (B) obtained from theoretical calculation. R^2 is coefficient of determination of fitting results. (**C**) Simulated voltage evolution curves of a Li|LLZTO|Li symmetric cell at 0.1 and 0.25 mAh/cm^2. (**D** and **E**) Statistical relationship between CD and cycle number (N) (D) and Q and N (E). Each data point is an N value obtained from experiments or simulations. The fitted curve of simulated results shows that the cycle life decreases proportionally with increasing CD, following a power law. Moreover, cycle number N is inversely proportional to Q. (**F**) Effects of fatigue strength (FS) on the cycle life of SSBs. Enhancing the FS of LMA can increase the cycle life of SSBs. (**G**) Li^+ diffusion coefficient of Li (2.2×10^{-11} cm^2/s), $Li_{20}Zn$ (1.9×10^{-11} cm^2/s), and Li_4Mg (0.17×10^{-11} cm^2/s). (**H**) Tensile strength of Li, $Li_{20}Zn$, and Li_4Mg. (**I**) Voltage evolution curves of Li|LLZTO|Li, $Li_{20}Zn$|LLZTO|$Li_{20}Zn$, and Li_4Mg|LLZTO|Li_4Mg cells.

of LMA. The fatigue-driven mechanism not only provides insights for enhancing the cycling stability, but also offers pathways to reducing the pressure requirement of SSBs, which is a core challenge for practically meaningful SSBs (*41*). The influences of stacked pressures on LMA fatigue are discussed in supplementary note VII and figs. S40 to S42. Enhanced fatigue strength can improve the cycling stability of SSBs at an ultralow pressure of 0.025 MPa (fig. S42).

SSBs failure mechanisms driven by fatigue of LMA

Fatigue-driven LMA-SSE interface failures can be categorized into three modes: (i) defect fatigue–dominated failure, (ii) kinetic fatigue–dominated failure, and (iii) fatigue-dominated failure. The interface between LMA and SSE with poor contact can be classified into mode (i). Initial defects at interface can increase local current density and the stress concentration of LMA, thus accelerating interface degradation (fig. S43 and Fig. 4A). For the initially well fabricated LMA-SSE interface, degradation under high and low current densities manifests differently. High currents would cause the accumulation of Li vacancies and the generation of microvoids during individual stripping processes due to the limited diffusion speed of Li^+ (*19*, *20*). In subsequent cycling, interface degradation is exacerbated due to both limited kinetics and LMA fatigue, thereby resulting in rapid interface degradation and SSBs failures within a few cycles [mode (ii), Fig. 4B]. Conversely, even if Li^+ diffusion speed is sufficient to prevent void formation (*21*, *23*), cyclic stress imposed by cyclic current will induce LMA fatigue. The microvoids induced by LMA fatigue ultimately contribute to interface degradation in long-term cycling [mode (iii), Fig. 4C]. In short, fatigue of LMA would occur when exposed to cyclic current regardless of the initial interface status and current density. To achieve demanded cycling stability, simultaneously enhancing fatigue strength and the Li^+ diffusion coefficient of LMA should be an effective strategy (fig. S44).

In materials mechanics, tensile strength represents the maximum stress that a material can withstand. For practical applications, fatigue limit, defined as the stress below which the material can endure an infinite number of cycles without fatigue failure, is vital. For SSBs, both CSC and CCD are analogous to "ultimate tensile strength" and denote the maximum current that the cell can tolerate, which cannot effectively evaluate long-term cycling performances because they do not take fatigue into consideration. Thus, we propose using the fatigue-limited current (FLC) as a metric to evaluate LMA fatigue behaviors and SSB electrochemical properties. FLC is defined as the current at which fatigue-induced failure is absent under specific capacities, capacity retention, and cycle numbers (fig. S45). For instance, an ideal FLC for SSB should be >10.0 mA/cm^2 under the conditions of 5.0 mAh/cm^2 and 1000 cycles. Compared with CCD and CSC, FLC is a more practical indicator for evaluating the long-term cycling performance of SSBs.

We also investigated the influences of Li metal's microstructure on fatigue, LMA fatigue in anode-less or anode-free SSBs, and the relationship between LMA fatigue and cathode fatigue (see supplementary notes VIII to X and figs. S46 to S48, respectively).

Conclusions

In this work, we have shown through operando SEM, simulations, and electrochemical analysis that the fatigue of LMA is a universal phenomenon in SSBs and is critical for understanding SSB failure upon long-term cycling. We found that LMA fatigue in SSBs follows a mechanics equation, indicating that it is an innate characteristic. We successfully quantified the relationship between mechanics and electrochemistry and established a quantitative correlation among current density, capacity, mechanical property, and cycle life in SSBs. Although research on metal fatigue has been conducted for nearly 180 years, our present work endows fatigue with new meaning in SSBs and successfully leverages it to address

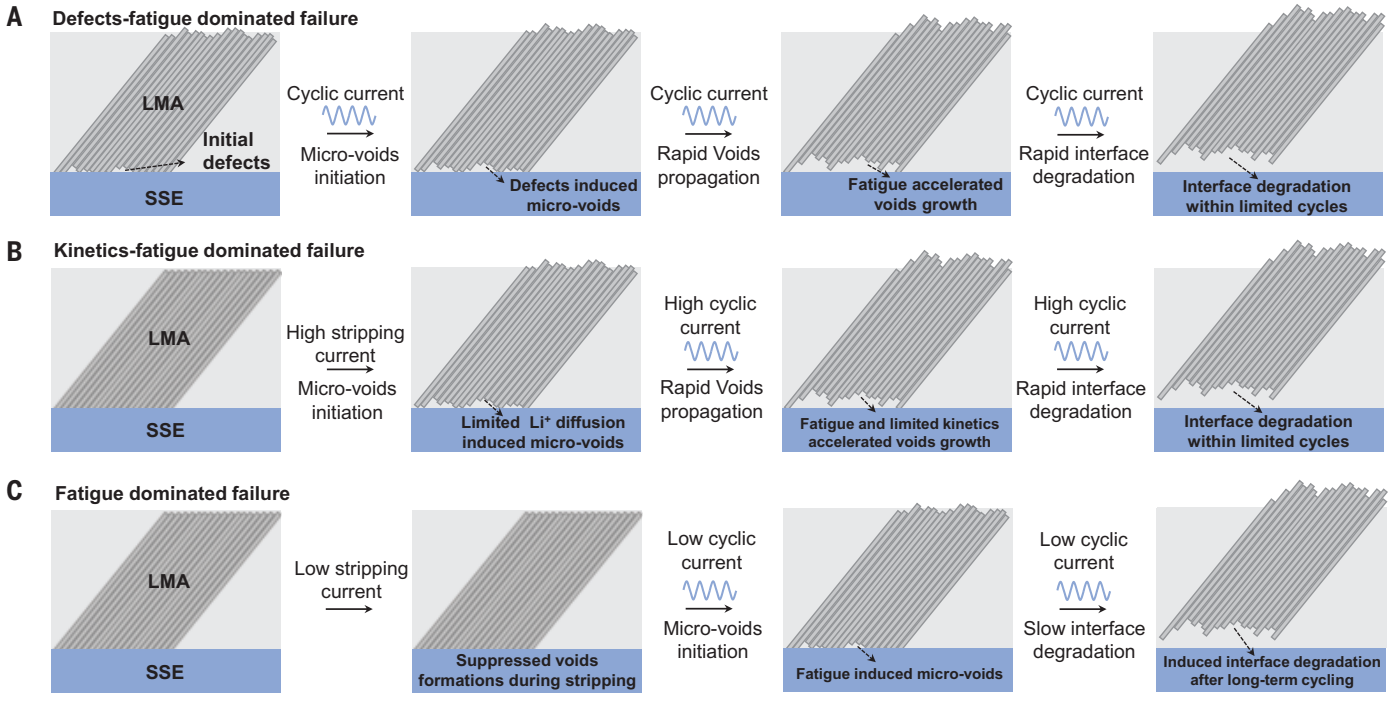

Fig. 4. SSB failure mechanisms driven by fatigue of LMA. (**A**) Defects fatigue–dominated failure mode. This mode occurs at interface with poor contact. (**B**) Kinetics fatigue–dominated failure, which shows up in interfaces with initially intimate contact and cycling at high current densities. (**C**) Fatigue-dominated failure, which shows up in interfaces with initially intimate contact and cycling at low current densities.

challenges such as suppressing LMA failure and increasing the cycle life.

REFERENCES AND NOTES

1. B. Dunn, H. Kamath, J.-M. Tarascon, *Science* **334**, 928–935 (2011).
2. N. Kamaya *et al*., *Nat. Mater.* **10**, 682–686 (2011).
3. D. H. S. Tan *et al*., *Science* **373**, 1494–1499 (2021).
4. J. Liang, X. Li, K. R. Adair, X. Sun, *Acc. Chem. Res.* **54**, 1023–1033 (2021).
5. J. Liu *et al*., *Nat. Energy* **4**, 180–186 (2019).
6. T. Fuchs *et al*., *Adv. Energy Mater.* **12**, 2201125 (2022).
7. S. Sarkar, V. Thangadurai, *ACS Energy Lett.* **7**, 1492–1527 (2022).
8. M. Bay *et al*., *Adv. Energy Mater.* **10**, 1902899 (2020).
9. R. J. Y. Park *et al*., *Nat. Energy* **6**, 314–322 (2021).
10. L. E. Marbella *et al*., *Chem. Mater.* **31**, 2762–2769 (2019).
11. J. A. Lewis *et al*., *ACS Appl. Mater. Interfaces* **14**, 4051–4060 (2022).
12. F. Han *et al*., *Nat. Energy* **4**, 187–196 (2019).
13. L. Zhou, N. Minafra, W. G. Zeier, L. F. Nazar, *Acc. Chem. Res.* **54**, 2717–2728 (2021).
14. X. Liu *et al*., *Nat. Mater.* **20**, 1485–1490 (2021).
15. H. Wan *et al*., *Nat. Energy* **8**, 473–481 (2023).
16. X. Han *et al*., *Nat. Mater.* **16**, 572–579 (2017).
17. S. Lee *et al*., *Sci. Adv.* **8**, eabq0153 (2022).
18. T. Krauskopf *et al*., *Joule* **3**, 2030–2049 (2019).
19. T. Krauskopf, H. Hartmann, W. G. Zeier, J. Janek, *ACS Appl. Mater. Interfaces* **11**, 14463–14477 (2019).
20. J. Kasemchainan *et al*., *Nat. Mater.* **18**, 1105–1111 (2019).
21. V. Raj *et al*., *Nat. Mater.* **21**, 1050–1056 (2022).
22. Z. Ning *et al*., *Nature* **618**, 287–293 (2023).
23. T. Krauskopf, F. H. Richter, W. G. Zeier, J. Janek, *Chem. Rev.* **120**, 7745–7794 (2020).
24. S. Kalnaus, N. J. Dudney, A. S. Westover, E. Herbert, S. Hackney, *Science* **381**, eabg5998 (2023).
25. Y. Chen *et al*., *Nature* **578**, 251–255 (2020).
26. L. Ye, X. Li, *Nature* **593**, 218–222 (2021).
27. G. McConohy *et al*., *Nat. Energy* **8**, 423 (2023).
28. C. D. Fincher *et al*., *Joule* **6**, 2794–2809 (2022).
29. Y. Qi, C. Ban, S. J. Harris, *Joule* **4**, 2599–2608 (2020).
30. H. Huo *et al*., *Nat. Commun.* **12**, 176 (2021).
31. C. Dan *et al*., *Nat. Mater.* **22**, 1182–1188 (2023).
32. W. Schütz, *Eng. Fract. Mech.* **54**, 263–300 (1996).
33. J. C. Stinville *et al*., *Science* **377**, 1065–1071 (2022).
34. Y. Zhu, X. He, Y. Mo, *ACS Appl. Mater. Interfaces* **7**, 23685–23693 (2015).
35. J. A. Lewis *et al*., *Nat. Mater.* **20**, 503–510 (2021).
36. S. Ishihara *et al*., *Fatigue Fract. Eng. Mater. Struct.* **33**, 294–302 (2010).
37. B.-R. You, S.-B. Lee, *Int. J. Fatigue* **18**, 235–244 (1996).
38. D. Sornette, T. Magnin, Y. Brechet, *Europhys. Lett.* **20**, 433–438 (1992).
39. Z. Qu *et al*., *Nature* **626**, 999–1004 (2024).
40. J. Aspinall *et al*., *Nat. Commun.* **15**, 4511 (2024).
41. X. Hu *et al*., *Nat. Rev. Mater.* **9**, 305–320 (2024).

ACKNOWLEDGMENTS

We thank G. Qu, T. Chen, and Y. Liao from Tongji University; Y. Chen and L. Li from Shanghai Jiao Tong University; and G. Wu from Southwest Jiaotong University for their assistance and discussion and X. Chen for help with schematic design.
Funding: This work was supported by the Shanghai Pilot Program for Basic Research and Xiaomi Young Talents Program.
Author contributions: T.W., W.L., and Y.H. conceived the idea and designed the experiments. T.W. analyzed data. T.W., B.C., Y.L., R.X., W.L., and Y.H. wrote and edited the paper. T.W., B.C., and Q.Y. conducted the operando SEM experiments. Y.L. performed simulations. T.W. and Y.D. provided schematic design. T.W., Z.S., and Z.Q.W. fabricated the alloy anode and conducted the mechanical experiments. T.R.W., Y.C., J.W., and F.P. performed the electrochemical tests and the fabrications of SSEs. Q.K. and R.X. provided valuable discussions. All authors have given approval to the manuscript.
Competing interests: The authors declare no competing interests. **Data and materials availability:** All data are available in the main text or the supplementary materials.

SUPPLEMENTARY MATERIALS

science.org/doi/10.1126/science.adq6807
Materials and Methods
Figs. S1 to S48
Table S1
References (*42*–*50*)
Supplementary Notes I to X

Submitted 26 May 2024; resubmitted 31 October 2024
Accepted 13 February 2025
10.1126/science.adq6807

ENVIRONMENTAL SCIENCE

Global soil pollution by toxic metals threatens agriculture and human health

Deyi Hou[1,2]*†, Xiyue Jia[1]†, Liuwei Wang[1], Steve P. McGrath[3], Yong-Guan Zhu[4,5], Qing Hu[6], Fang-Jie Zhao[7], Michael S. Bank[8,9], David O'Connor[10], Jerome Nriagu[11]

Toxic metal pollution is ubiquitous in soils, yet its worldwide distribution is unknown. We analyzed a global database of soil pollution by arsenic, cadmium, cobalt, chromium, copper, nickel, and lead at 796,084 sampling points from 1493 regional studies and used machine learning techniques to map areas with exceedance of agricultural and human health thresholds. We reveal a previously unrecognized high-risk, metal-enriched zone in low-latitude Eurasia, which is attributed to influential climatic, topographic, and anthropogenic conditions. This feature can be regarded as a signpost for the Anthropocene era. We show that 14 to 17% of cropland is affected by toxic metal pollution globally and estimate that between 0.9 and 1.4 billion people live in regions of heightened public health and ecological risks.

Soil provides the basis for nearly 95% of food consumed by human beings (*1*). As the human population continues to grow and living standards improve, global food production needs to increase by 35 to 56% by 2050 (*2*). This puts substantial pressure on nonrenewable soil resources, the degradation of which already threatens the livelihoods of 1.3 billion people globally (*3*). The United Nations Food and Agriculture Organization (FAO) warns that 90% of global soil resources may be at risk by 2050, owing to soil erosion, excessive usage of fertilizers and pesticides, and industrial pollution (*4*, *5*). Often overlooked in the matter of soil quality is soil pollution by toxic heavy metals and metalloids (herein "toxic metals"), which reduces crop yields and results in unsafe food. Even though some metals such as cobalt (Co) and copper (Cu) are essential in small amounts for biological functioning, their bioaccumulation in organisms, including crops, can render them toxic in the human food chain. Furthermore, toxic metals are nondegradable and therefore accumulate over decadal timescales in soils (*6*–*8*).

Global soil pollution by toxic metals has been studied for decades (*9*); however, quantitative estimates of their impact on soil quality and spatially explicit mapping of soil pollution on a global scale are lacking. A few regional and country-scale investigations have provided concerning data on this issue. For instance, a national survey in China found that 19% of agricultural soils exceeded soil quality standards, with arsenic (As, a metalloid), cadmium (Cd), Cu, and nickel (Ni) accounting for the majority of exceedances (*10*). A study on toxic metals across 27 European countries showed that 28% of soils exceeded thresholds (*11*).

There are two main sources of toxic metals in soil: geogenic and anthropogenic. Toxic metals are ubiquitous in bedrocks, which are the natural soil parent materials, and occur in varying concentrations. Some types of parent rock (e.g., basalt and shale), as well as primary minerals (e.g., pyrite, sphalerite), contain elevated levels of As, Cd, Cu, and Ni that result from the high affinity of sulfur for these metals (*8*, *12*). During the geologic weathering and soil-forming processes, toxic metals are continuously released from soil parent materials (*13*, *14*). Some toxic metals may also be transported in the atmosphere after volcanic emissions and wind erosion and subsequently deposited in surface soil (*13*, *15*). Because of translocation and transformation mechanisms

[1]School of Environment, Tsinghua University, Beijing, China. [2]State Key Laboratory of Regional Environment and Sustainability, Tsinghua University, Beijing, China. [3]Rothamsted Research, Sustainable Soils and Crops, Harpenden, United Kingdom. [4]Research Center for Eco-Environmental Sciences, Chinese Academy of Sciences, Beijing, China. [5]Institute of Urban Environment, Chinese Academy of Sciences, Xiamen, China. [6]Engineering Innovation Centre (Beijing), Southern University of Science and Technology, Shenzhen, China. [7]College of Resources and Environmental Sciences, Nanjing Agricultural University, Nanjing, China. [8]Institute of Marine Research, Bergen, Norway. [9]Department of Environmental Conservation, University of Massachusetts Amherst, Amherst, MA, USA. [10]School of Real Estate and Land Management, Royal Agricultural University, Cirencester, UK. [11]School of Public Health, University of Michigan, Ann Arbor, MI, USA.
***Corresponding author. Email: houdeyi@tsinghua.edu.cn**
†These authors contributed equally to this work.

occurring during pedogenesis, toxic metals may accumulate in soil because of fixation in crystal lattices—binding with clay minerals through electrostatic forces—or complexation with organic matter and iron (Fe) oxyhydroxides, which can lead to a high natural background of toxic metal concentrations in certain soil environments (*12*, *16*, *17*).

Anthropogenic sources of toxic metals in the pedosphere include agricultural, household, and industrial activities. Substantial metal contamination of soils commenced at the beginning of the Anthropocene (e.g., Bronze Age), particularly as a result of metal mining and processing (*13*, *18*). Mining activities transfer huge quantities of rock, often with high metal concentrations, from the underground to the surface. This leads to soil pollution by leachate and runoff from mining waste, irrigation of cropland with polluted water, wind-eroded waste rocks, and atmospheric deposition originating from metal smelters (*6*, *19*). Metal pollution at a given location may be transported across long distances, as evidenced by ice cores recovered from Greenland, which reveal that intensive mining and smelting activities in the Greek and Roman times caused pronounced pulse in metal contamination at hemispheric scales (*20*). Elevated toxic metal contents are also embedded in industrial infrastructure (including machinery, bridges, transport systems, cables, and buildings) and agricultural and household products (such as phosphorus fertilizers, paints, and batteries), which can contribute considerably to the toxic metal burden in soil ecosystems (*21*).

The spatial distribution of toxic metals in soil depends on a dynamic and complex balance between input and output processes. The main output pathways include leaching, soil erosion by surface runoff, plant uptake, and crop harvest (*13*, *17*, *22*). Redistribution of toxic metals may occur in the vertical dimension of soil profiles because of soil-plant interactions. The plant-pump effect, for instance, transports toxic metals from deeper soil (e.g., C horizons) to surficial soil (e.g., O horizons), where they accumulate (*17*). Toxic metals in soil may also migrate at regional scales because of biovolatization, wind-borne soil suspension, forest fires, and other perturbances (*13*, *15*). On the basis of these migration mechanisms, it has been suggested that certain environmental and socioeconomic factors, including topography, climate, soil texture, and human activities, may be used as predictors to evaluate toxic metal distribution across large spatial scales (*11*, *23*–*25*).

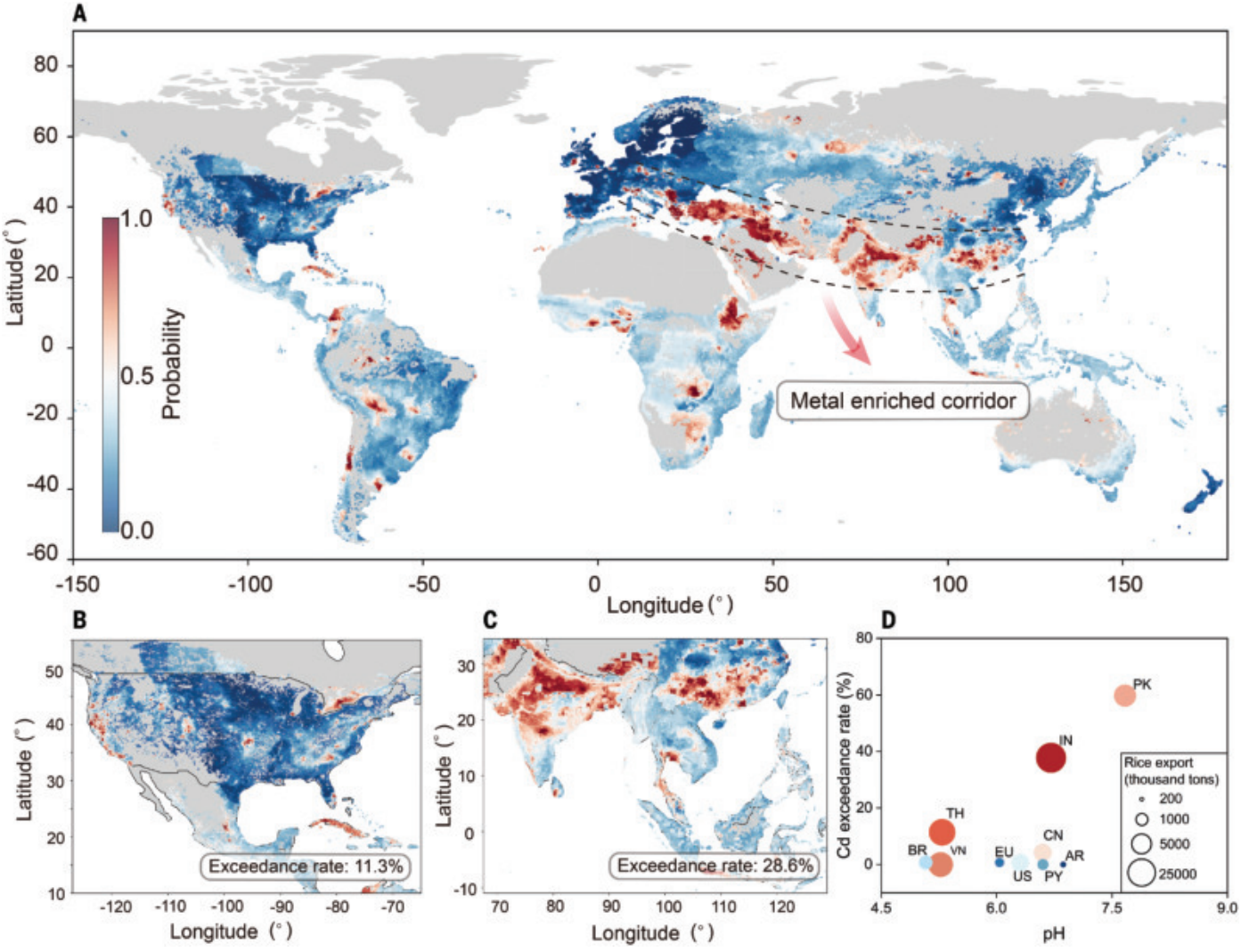

Fig. 1. Global soil pollution by toxic metals exceeding agricultural thresholds (AT). (**A**) Aggregate distribution of exceedance of arsenic, cadmium, cobalt, chromium, copper, nickel, and lead; color code shows the maximum probability of exceedance among the seven metals. (**B** and **C**) Zoomed-in sections of globally important food production areas. (**D**) Predicted Cd exceedance rates and average soil pH indicative of Cd mobility in the major rice export countries. Country abbreviation: IN, India; TH, Thailand; VN, Vietnam; PK, Pakistan; CN, China; US, United States; BR, Brazil; PY, Paraguay; EU, European Union; AR, Argentina.

The combination of recent developments in machine learning technologies and the availability of expansive measurement data now make it possible to undertake a systematic assessment of global soil pollution for seven toxic metals: As, Cd, Co, chromium (Cr), Cu, Ni, and lead (Pb). We hypothesized that soil pollution, on a global scale, would be governed by both direct and indirect effects of biogeophysical and anthropogenic factors. Using machine learning models, we identified and analyzed multilayered and nonlinear relationships and developed a robust and spatially explicit, continuous prediction of toxic metal exceedances on the basis of sparsely distributed global data.

Global toxic metal exceedances

We have compiled 796,084 datapoints of soil concentrations of the key toxic metals from 1493 regional studies covering diverse climate zones, geologic settings, and land use types (figs. S1 and S2) (*26*). Data quality assurance procedures were followed to ensure that the data were reliable and representative of regional metal concentrations, and appropriate analytical methods were used to ensure robust measurements (*26*). Samples collected from studies focusing on contaminated sites were excluded to avoid bias toward highly enriched localized areas. Soil concentrations in 10 km by 10 km pixels were converted to binary data by using a set of agricultural thresholds (AT) and human health and ecological thresholds (HHET) derived from country thresholds (table S1) (*26*). Five sets of predictive variables, namely climatic, geological, soil textural, topographic, and socioeconomic, were included as proxies of natural and anthropogenic processes governing metal abundance in soil. Extremely randomized trees (ERT) was selected as the best-performing machine learning model (*27*). The models were validated with an independent dataset, which verified high model precision and accuracy unrelated to numerical overfitting. The models were then used to project data onto a soil pollution map on a global scale, excluding any permafrost and desert areas (*26*).

Globally, our model estimates that 14 to 17% (95% confidence interval) of surface soils exceed the AT for at least one toxic metal in cropland areas (Fig. 1). Probabilities of individual metal exceedance vary geographically (figs. S4 to S10). The global exceedance rate of Cd is the highest, reaching 9.0% (−1.9%/+1.5%). Cadmium exceedance for agricultural soil is the most notable in northern and central India, Pakistan, Bangladesh, southern China, southern parts of Thailand and Cambodia, Iran, Türkiye, Ethiopia, Nigeria, South Africa, Mexico, and Cuba. Both anthropogenic sources and geogenic enrichment likely contributed to the elevated Cd concentrations in these regions (*6*, *8*, *28*, *29*). The exceedance rates of Ni and Cr reach 5.8% (−1.8%/+1.1%) and 3.2% (−0.7%/+1.6%), respectively. Their exceedance is the most prevalent in the Middle East, subarctic Russia, and eastern Africa, likely due to high geogenic background as well as mining activities (*28*, *30*). Soil As exceedance occurred at a rate of 1.1% (−0.04%/+0.3%) and was the most notable in southern and southwestern China, south and Southeast Asia, West Africa, and central parts of South America, which coincides with observed and predicted areas of high As concentration in groundwater (*14*). The exceedance rate of Co is 1.1% (−0.1%/+2.9%)

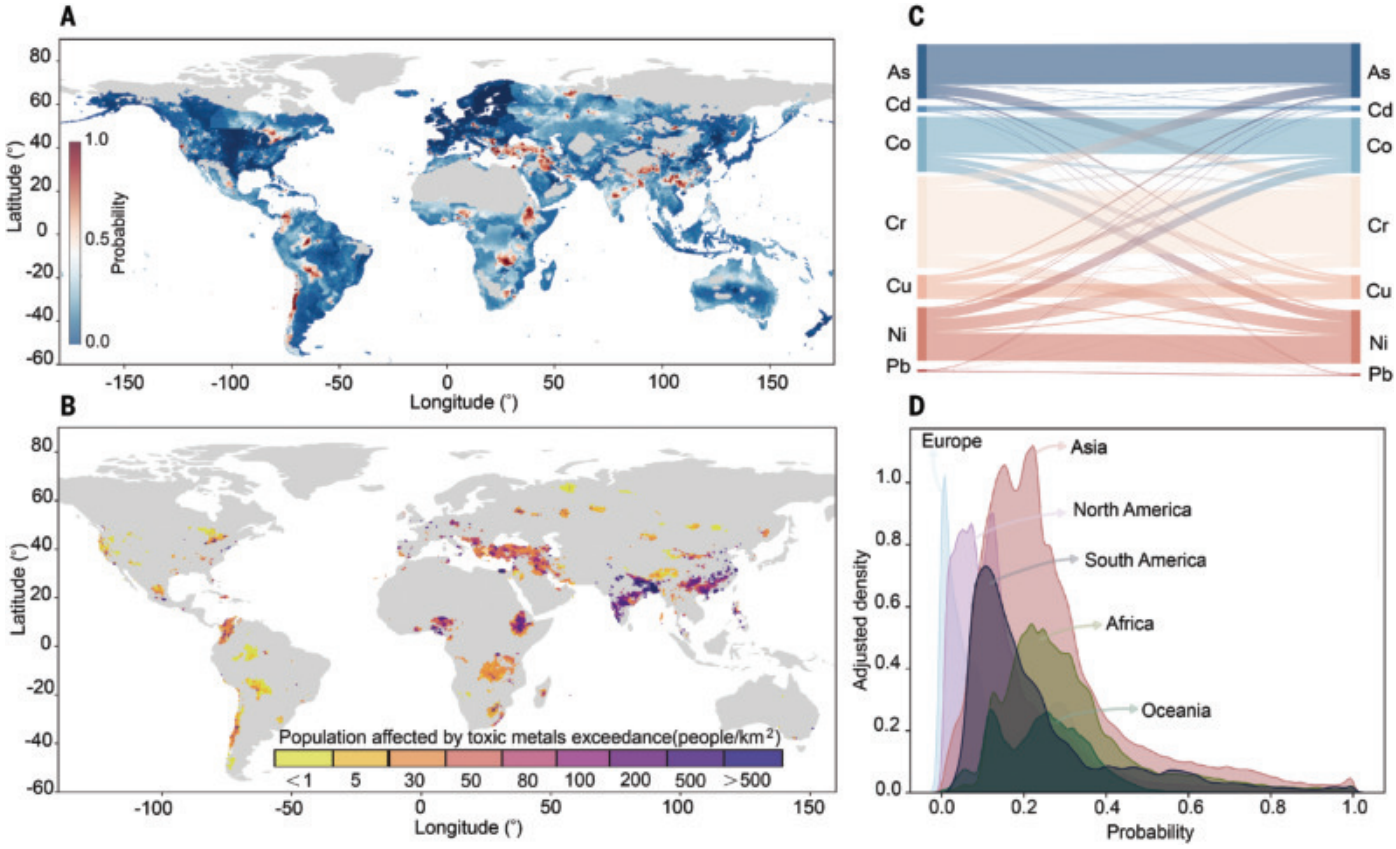

Fig. 2. Global distribution of soil toxic metals exceeding human health and ecological thresholds (HHET). (**A**) Map of metal concentration exceedance. (**B**) Population density in areas with >0.5 probability of metal exceeding ecological and human health threshold. (**C**) Combined soil pollution by toxic metals, with line width in the Sankey diagram showing the proportion of all dual comingled pollution. (**D**) Density histogram showing the relative frequency of exceedance probability of various continents, adjusted by area of each continent.

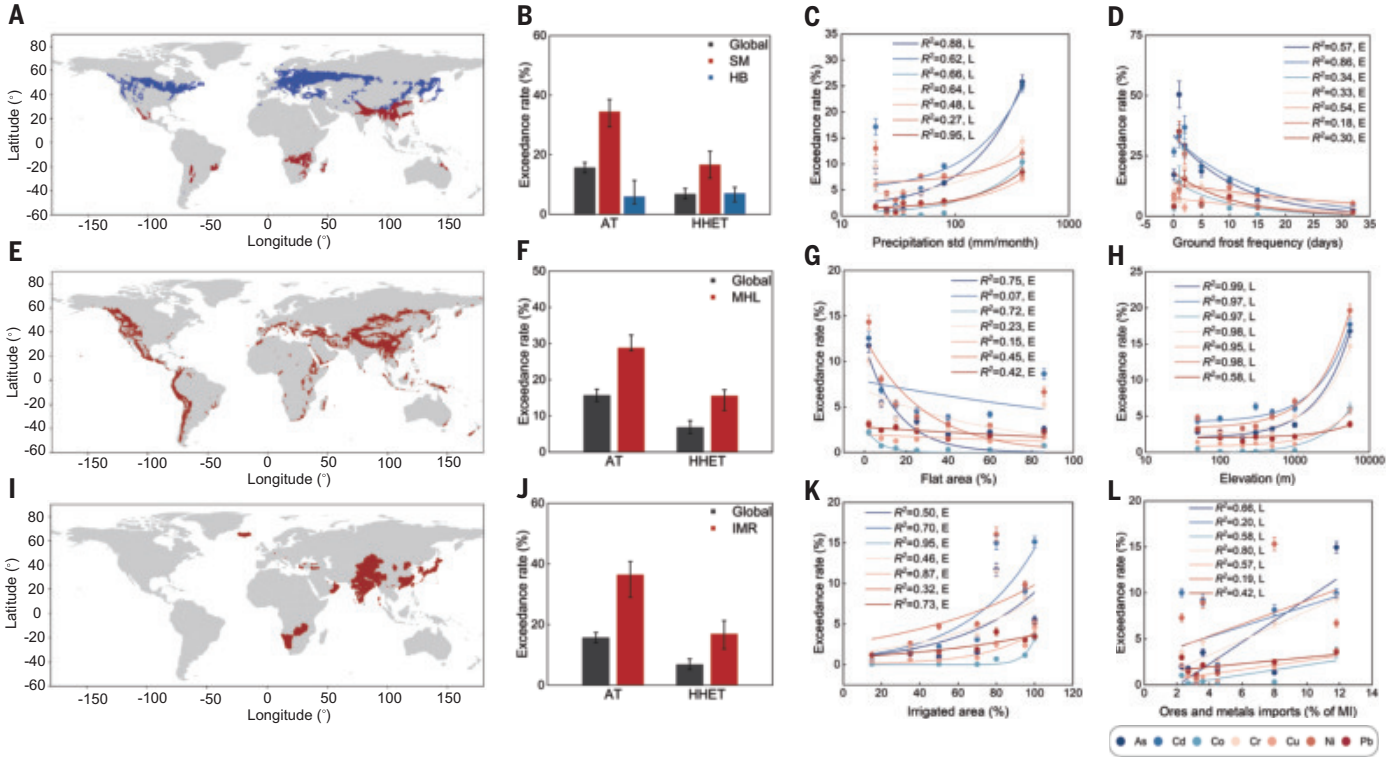

Fig. 3. Natural and anthropogenic drivers of soil metal exceedance. (**A**) Global distribution of subtropical monsoon (SM) (red) and hemiboreal (HB) (blue) climate zones. (**B**) Exceedance rate in global, SM, and HB climate zones. (**C**) Exceedance rate increases as precipitation increases. (**D**) Exceedance rate decreases as ground frost frequency increases. (**E**) Global distribution of hilly mountain areas (HMA), with <2% of area sloped between 0.005 and 0.02, >10% of area sloped between 0.3 and 0.45, and elevation >1000 m above mean sea level. (**F**) Exceedance rate in HMA is significantly higher than the global average. (**G**) Exceedance rate decreases as proportion of flat land increases. (**H**) Exceedance rate increases as elevation increases. (**I**) Global distribution of irrigated and mineral-rich regions (IMR), with proportion of irrigation >90% and ores and metals imports >5% of merchandise imports (MI). (**J**) Exceedance rate in IMR compared with global average. (**K**) Exceedance rate increases as the proportion of irrigation increases. (**L**) Exceedance rate increases as the proportion of ores and metals imports increases. Regression lines are shown in (C), (D), (G), (H), (K), and (L), with "L" indicating linear regression and "E" indicating exponential regression. Error bars represent 95% confidence interval derived from bootstrap method.

and was the most prevalent in Zambia, the Democratic Republic of the Congo, and Ethiopia, likely the result of mining-related activities (*31*). Globally, 6.8% (−1.7%/+1.9%) of surficial soil exceeded HHET, with a similar or smaller exceedance than AT exceedance owing to generally less stringent threshold values (Fig. 2 and figs. S11 to S17).

Soil pollution by toxic metals has considerable impacts on food production and food safety. We estimate that 242 million ha (−26/+27 million ha), or 16% of global cropland, is affected by toxic metal exceedances. Among the areas most at risk, southern China, northern and central India, and the Middle East are well documented to have elevated toxic metal concentrations in their soils (*32*–*34*). Limited data exist for Africa, and the prediction will require more soil sampling and analysis for verification (*35*).

By overlaying the human health and ecological risk map over global population distribution in 2020, it is estimated that 0.9 to 1.4 billion people live in the high-risk areas (Fig. 2B). However, it should be noted that the actual risks posed by soil metals are dependent upon their mobility, overall bioavailability, and human exposure pathway dynamics (*36*, *37*). Exposure and toxic effects also depend on individual dietary habits and food deprivation, as well as the degree of co-occurrence of multiple elements (Fig. 2C). Moreover, international trade of food products originating from high-risk countries may lead to a spillover effect and dispersion of such risks (Fig. 1D).

Our study identified a notable high-risk zone in low-latitude Eurasia and across southern Europe, the Middle East, South Asia, and southern China. This belt coincides with the geographical distribution of several ancient cultures, including ancient Greek civilizations, the Roman Empire, Persian culture, ancient India, and Yangtze River Chinese culture (fig. S25). This intercontinental "metal-enriched corridor" is attributed to a combination of anthropogenic and environmental factors (discussed below). Because metals do not degrade, this zone can be regarded as a keystone indicator of the Anthropocene era.

Natural and anthropogenic drivers

Several environmental drivers affect the global distribution of toxic metal exceedances. Near-surface temperature, precipitation, and potential evapotranspiration have the strongest positive effects (*38*), likely contributing to relatively high metal exceedance in southern China, India, the Middle East, Central America, and Central Africa. Such conditions accelerate the weathering processes that release metals from soil parent materials and enhance the enrichment of metals in clay minerals and iron oxides or aluminum oxides (*22*). By contrast, the frequency of ground frosts and wet day frequencies show the strongest negative effects (*38*). This may be due to weak weathering-induced influx and strong leaching-related efflux of metals (*39*), as well as weak plant-pump effects limiting vertical enrichment (*17*). The subtropical monsoon climate zones, which are important for global agriculture, tend to be hot and

humid despite the dry season. This climate zone has a metal exceedance rate of 34% (−5%/+4%) for the AT, substantially higher than the global average of 15.7%. By contrast, the metal exceedance rate in the cold and humid hemiboreal climate zone is much lower at 6.0% (−2.4%/+5.5%) (Fig. 3B). We also found that high elevation and steep slope landscapes correspond to more prevalent metal exceedance (Fig. 3, E to G) owing to the topography affecting rock weathering, soil formation, and erosion, and therefore influencing the leaching and accumulation of metals (*40*–*42*). In mountainous areas with a low percentage of flat areas and high percentage of steep slopes, the metal exceedance rat e is 15% (−4%/+2%) for HHET and 29% (−1%/+3%) for AT, nearly twice the global averages.

Socioeconomic factors are also important drivers governing global toxic metal distribution patterns. Proxies of mining intensity, as identified by ores and metals exports, mineral rents, mineral depletion, and ores and metals imports, were the strongest socioeconomic predictors of toxic metal exceedances, highlighting the major contribution of mining and smelting to metal accumulation in soils at a global scale (*6*, *43*, *44*). The proportion of irrigated land was also found to be a strong predictor of metal exceedance, which is consistent with previous reports that irrigation water contaminated by industrial activities can cause widespread contamination of agricultural soils (*6*, *8*, *19*). In areas with intensive mining activities and a high percentage of surface irrigation (Fig. 3, I to L), the metal exceedance rate was 17% (−5%/+4%) for HHET and 36% (−7%/+4%) for AT, more than twice the global average. Although irrigation with groundwater extracted from arsenic-bearing aquifers in the region south of the Himalayas resulted in hot spots of As in soils (*8*), in general, the use of groundwater for irrigation is a strong predictor of toxic metal nonexceedance on a global scale. This suggests that groundwater may generally contain lower levels of toxic metals than other irrigation water sources, thus serving as a carrier of metal efflux rather than influx, except in areas with high geogenic background or serious anthropogenic pollution (*45*).

We used structural equation modeling (SEM) to assess the causal links between irrigation, mining, plant pumping, weathering, leaching, and exceedance rate and hazard level (Fig. 4, A and B, and fig. S22) and found that weathering and plant pumping contribute substantially to the concentrations of As, Cd, Co, and Cu in soil. Furthermore, SEM results verified that anthropogenic processes, including mining and irrigation, provided substantial contributions for most of the toxic metals. Although many effects are exerted through direct influencing pathways, a considerable portion of the influences may be exerted indirectly (Fig. 4C). Indirect pathways account for 96, 87, 62, and 62% of the net effect of mining on hazard level for As, Cd, Co, and Cu. These SEM results were in good accordance with the complex importance features of the machine learning models (Fig. 4D) and support our hypothesis that soil toxic metal enrichment is governed by

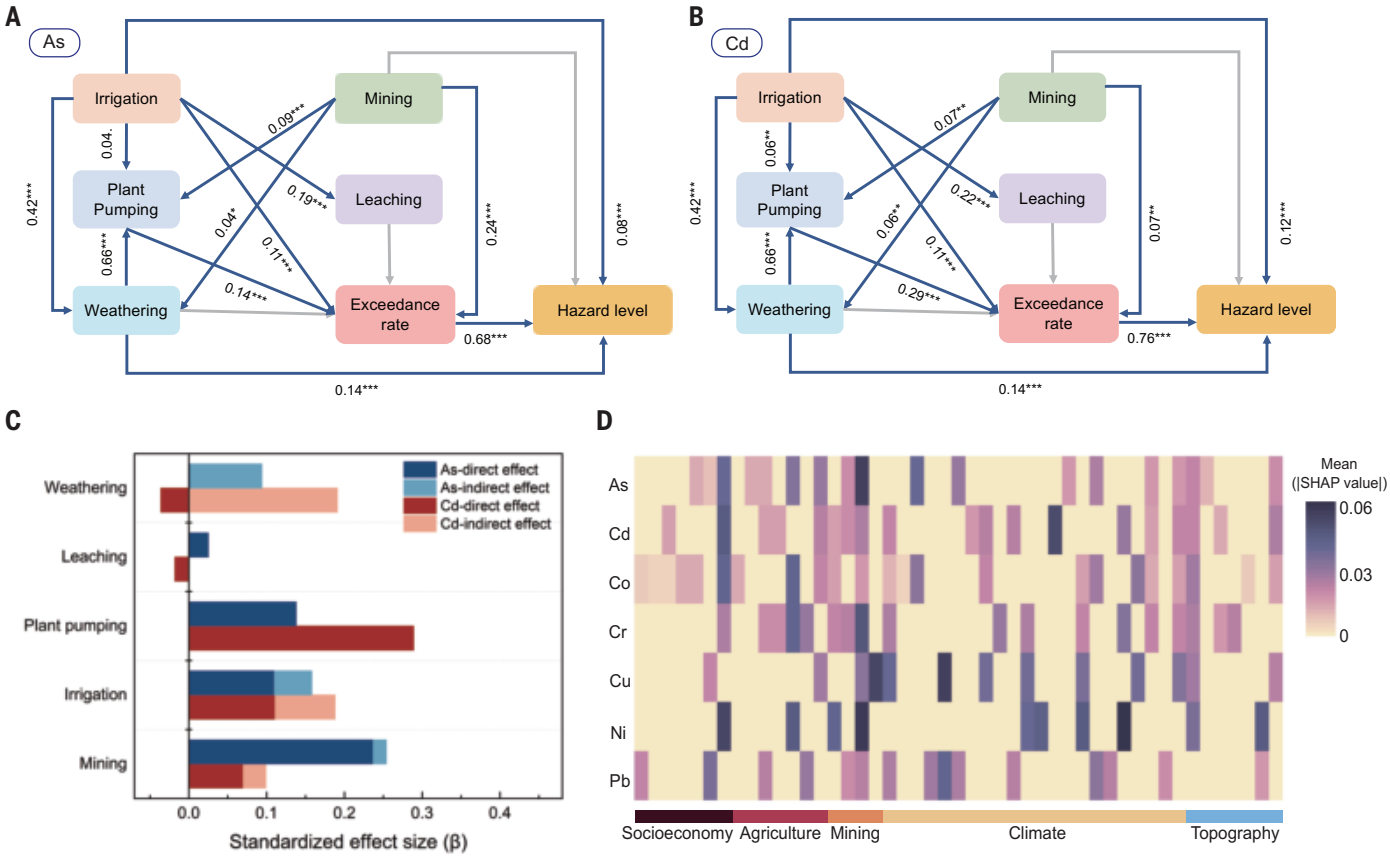

Fig. 4. Relationships among soil metal exceedance and underlying processes. (**A**) Structural equation modeling (SEM) of irrigation, mining, plant pumping effect, leaching, and weathering on exceedance rate and hazard level of As [n = 2149, χ^2 = 4.45, bootstrap P = 0.41, root mean square error of approximation (RMSEA) = 0.04, standardized root mean squared residual (SRMR) = 0.009, goodness-of-fit index (GFI) = 0.999]. $^{**}P < 0.001$, $^{***}P < 0.01$, $^{*}P < 0.05$, $^{.}P < 0.1$. (**B**) SEM of Cd [n = 2379, χ^2 = 0.57, bootstrap P = 0.95, RMSEA = 0.00, SRMR = 0.003, GFI = 1.000]. (**C**) Summed direct effect and indirect effects. The direct effect reflects the degree of standard deviation change in dependent variables with each one standard deviation change in a directly linked predictive variable, and indirect effect reflects the magnitude of associated change through an indirect link. (**D**) Feature importance assessed by Shapley additive explanations (SHAP) (materials and methods 1.4.4). The larger the Shapley value, the more important a variable on the x axis is (*38*).

the interplay of a wide range of biogeophysical and socioeconomic variables at broad spatiotemporal scales.

Discussion

Our model results show that soil contamination is occurring on a global scale, posing major risks to both ecosystems and human health (*7*, *46*) and threatening water quality and food security (*6*, *8*). The model prediction includes both known soil pollution areas and previously undocumented areas of concern (figs. S23 and S24). Some of these regions, such as Southern China and the Middle East, have been reported previously, but we were able to delineate the risk zones continuously on a global scale. Our machine learning models used data from the public domain to provide an assessment of regional soil pollution, and the results show that the technique is a useful screening tool that can complement traditional soil pollution–mapping methods. There is an ongoing global initiative on soil pollution prevention and restoration under the United Nations Environment Programme (UNEP) and the FAO (*35*, *47*). Our results suggest that international aid should be allocated to facilitate soil pollution surveys in data-sparse regions such as sub-Saharan Africa.

Recent large-scale studies in Europe found a mysterious trend north of the 55° latitude line, which demarcates high-metal soils in the south from the low-metal soils in the north (*11*, *48*). This phenomenon had been attributed to the coincidental match with the maximum extent of the last glaciation; however, the overall mechanism and drivers remain unclear. Our results now reveal that the toxic metal–enriched area across southern Europe is part of a more extensive transcontinental metal-enriched corridor spanning across low-latitude Eurasia (Fig. 1A). We postulate that this corridor of long-lasting legacy of human influence was formed as the result of strong weathering of metal-enriched parent rocks (*12*, *49*) and plant-pumping effects (*13*, *17*), a lower degree of leaching associated with precipitation and terrain (*12*), and a long history of mining and smelting activities occurring since ancient civilizations began (*8*).

Our models were validated by using a series of uncertainty analyses (*26*) (figs. S18 to S21). Mapping the extent of spatial extrapolation showed that our dataset provides a good coverage of most environmental conditions, with the least-represented pixels and highest proportion of extrapolation in Southeast Asia, Russia, and Africa. Due to lack of sampling data in developing countries and remote regions, our model still has relatively high degrees of uncertainty in northern Russia, central India, and Africa (fig. S2). Moreover, metal concentrations in soil have high spatial heterogeneity and may vary considerably over short distances. The present study is based on average metal concentrations on a 10-km grid, which is more reflective of diffusive and regional pollution rather than site-specific conditions. The data may be sufficient for risk screening purposes but are inadequate to support risk mitigation. Soil remediation needs to rely upon site-specific delineation of lateral and vertical extent of soil pollution, as well as a better understanding of metal sources, fate and transport dynamics, and bioavailability (*12*).

Soil pollution can have a profound impact on global food security and public health. For the millions of people making a living on the 14 to 17% of globally polluted cropland, the bioaccumulation of toxic metals in crops and farm animals can affect biodiversity and productivity, cause detrimental health effects, and exacerbate poverty. The collateral effects on the global food chain are unknown at this time, especially in the context of how global trade dynamics may affect the distribution of contaminated agricultural products. These large areas of toxic metal enrichment are expected to continue to increase owing to the growth in demand for critical metals required to support the net zero "green transition" and the development of photovoltaic devices, wind turbines, and electric vehicle batteries (*50*, *51*). We hope that the global soil pollution data presented in this report will serve as a scientific alert for policy-makers and farmers to take immediate and necessary measures to better protect the world's precious soil resources.

REFERENCES AND NOTES

1. Food and Agriculture Organization of the United Nations, "Healthy soils are the basis for healthy food production" (FAO, 2015).
2. M. van Dijk, T. Morley, M. L. Rau, Y. Saghai, *Nat. Food* **2**, 494–501 (2021).
3. United Nations Convention to Combat Desertification, *Global Land Outlook* (UNCCD, 2017).
4. Food and Agriculture Organization of the United Nations, *Status of the World's Soil Resources* (FAO, 2015).
5. Food and Agriculture Organization of the United Nations, "Saving our soils by all earthly ways possible" (FAO, 2022).
6. D. Hou *et al*., *Nat. Rev. Earth Environ.* **1**, 366–381 (2020).
7. O. Coban, G. B. De Deyn, M. van der Ploeg, *Science* **375**, abe0725 (2022).
8. Food and Agriculture Organization of the United Nations and United Nations Environment Programme, *Global Assessment of Soil Pollution* (FAO and UNEP, 2021).
9. A. Kabata-Pendias, *Trace Elements in Soils and Plants* (CRC Press, 2000).
10. Ministry of Environmental Protection of the People's Republic of China, "National soil contamination survey report" (MEP, 2014).
11. G. Tóth, T. Hermann, G. Szatmári, L. Pásztor, *Sci. Total Environ.* **565**, 1054–1062 (2016).
12. B. J. Alloway, Ed., *Heavy Metals in Soils: Trace Metals and Metalloids in Soils and their Bioavailability* (Springer Dordrecht, ed. 3, 2013).
13. A. A. Meharg, C. Meharg, *Environ. Sci. Technol.* **55**, 7757–7769 (2021).
14. J. Podgorski, M. Berg, *Science* **368**, 845–850 (2020).
15. J. O. Nriagu, *Nature* **338**, 47–49 (1989).
16. X. Liu *et al*., *Nat. Rev. Earth Environ.* **3**, 461–476 (2022).
17. M. Imseng *et al*., *Environ. Sci. Technol.* **52**, 1919–1928 (2018).
18. S. Hong, J.-P. Candelone, C. C. Patterson, C. F. Boutron, *Science* **272**, 246–249 (1996).
19. M. G. Macklin *et al*., *Science* **381**, 1345–1350 (2023).
20. S. Hong, J.-P. Candelone, C. C. Patterson, C. F. Boutron, *Science* **265**, 1841–1843 (1994).
21. J. O. Nriagu, J. M. Pacyna, *Nature* **333**, 134–139 (1988).
22. M. Imseng *et al*., *Environ. Sci. Technol.* **53**, 4140–4149 (2019).
23. L. R. Lado, T. Hengl, H. I. Reuter, *Geoderma* **148**, 189–199 (2008).
24. S. Maas *et al*., *Environ. Pollut.* **158**, 2294–2301 (2010).
25. Y. Hu, H. Cheng, *Environ. Sci. Technol.* **47**, 3752–3760 (2013).
26. Materials and methods are available as supplementary materials.
27. P. Geurts, D. Ernst, L. Wehenkel, *Mach. Learn.* **63**, 3–42 (2006).
28. British Geological Survey, *World Mineral Production 2016–2020* (BGS, 2022).
29. A. Kubier, R. T. Wilkin, T. Pichler, *Appl. Geochem.* **108**, 1–16 (2019).
30. BGS, "Mineral profile: Nickel" (British Geological Survey, 2008).
31. G. Gunn, Ed., *Critical Metals Handbook* (John Wiley & Sons, 2013).
32. H. Chen, Y. Teng, S. Lu, Y. Wang, J. Wang, *Sci. Total Environ.* **512-513**, 143–153 (2015).
33. N. Gupta *et al*., *Environ. Toxicol. Pharmacol.* **82**, 103563 (2021).
34. M. Amini, M. Afyuni, N. Fathianpour, H. Khademi, H. Flühler, *Geoderma* **124**, 223–233 (2005).
35. United Nations Environment Assembly, "Managing soil pollution to achieve sustainable development," UNEA3/6 (Third Session, Resolution 6) (UNEA, 2018).
36. G. Liu *et al*., *Geoderma* **312**, 104–113 (2018).
37. G. Lin *et al*., *J. Hazard. Mater.* **480**, 135876 (2024).
38. D. Hou *et al*., Global soil pollution by toxic metals threatens agriculture and human health, Dryad (2025); https://doi.org/10.5061/dryad.83bk3jb2z.
39. F. Meite *et al*., *Sci. Total Environ.* **616–617**, 500–509 (2018).
40. W. E. Dietrich, J. T. Perron, *Nature* **439**, 411–418 (2006).
41. C. Boente *et al*., *Catena* **208**, 105730 (2022).
42. Q. Ding, G. Cheng, Y. Wang, D. Zhuang, *Sci. Total Environ.* **578**, 577–585 (2017).
43. A. S. Vega *et al*., *Appl. Geochem.* **141**, 105230 (2022).
44. E. Saljnikov *et al*., *Environ. Geochem. Health* **41**, 2265–2279 (2019).
45. T. Gleeson, M. Cuthbert, G. Ferguson, D. Perrone, *Annu. Rev. Earth Planet. Sci.* **48**, 431–463 (2020).
46. United Nations Environment Programme, *Towards a Pollution-Free Planet: Background Report* (UNEP, 2017).
47. Food and Agriculture Organization of the United Nations, *Soil Pollution: A Hidden Reality* (FAO, 2018).
48. C. Reimann, P. de Caritat, GEMAS Project Team, NGSA Project Team, *Sci. Total Environ.* **416**, 239–252 (2012).
49. H. S. Moghadam *et al*., *J. Petrol.* **58**, 2143–2190 (2017).
50. K. Bhuwalka *et al*., *Environ. Sci. Technol.* **55**, 10097–10107 (2021).
51. A. Farina, A. Anctil, *Resour. Conserv. Recycling* **176**, 105938 (2022).

ACKNOWLEDGMENTS

We thank the anonymous reviewers for their constructive comments and the many providers of data used in our models. **Funding:** This work was supported by National Natural Science Foundation of China grant 42225703 (D.H.) and National Key Research and Development Program of China grant 2020YFC1808000 (D.H.). **Author contributions:** Conceptualization: D.H., X.J., S.P.M., Y.-G.Z, Q.H., F.-J.Z., M.S.B., D.O., J.N.; Funding acquisition: D.H.; Investigation: D.H., X.J., L.W.; Methodology: D.H., X.J., L.W., S.P.M., F-J.Z., D.O.; Project administration: D.H., L.W.; Visualization: D.H., X.J.; Supervision: D.H.; Writing – original draft: D.H., X.J.; Writing – review & editing: D.H., S.P.M., Y.-G.Z., Q.H., F.-J.Z., M.S.B., D.O., J.N. **Competing interests:** The authors declare that they have no competing interests. **Data and materials availability:** Data and code generated during this study are publicly available and can be accessed at (*38*). **License information:** Copyright © 2025 the authors, some rights reserved; exclusive licensee American Association for the Advancement of Science. No claim to original US government works. https://www.science.org/about/science-licenses-journal-article-reuse

SUPPLEMENTARY MATERIALS

science.org/doi/10.1126/science.adr5214
Materials and Methods
Figs. S1 to S27
Tables S1 to S10
References (*52–128*)

Submitted 4 July 2024; resubmitted 19 November 2024
Accepted 5 March 2025
10.1126/science.adr5214

NEUROSCIENCE

Distinct synaptic plasticity rules operate across dendritic compartments in vivo during learning

William J. Wright[1,2,3,4,5]*, Nathan G. Hedrick[1,2,3,4,5], Takaki Komiyama[1,2,3,4,5]*

Synaptic plasticity underlies learning by modifying specific synaptic inputs to reshape neural activity and behavior. However, the rules governing which synapses will undergo different forms of plasticity in vivo during learning and whether these rules are uniform within individual neurons remain unclear. Using in vivo longitudinal imaging with single-synapse resolution in the mouse motor cortex during motor learning, we found that apical and basal dendrites of layer 2/3 (L2/3) pyramidal neurons showed distinct activity-dependent synaptic plasticity rules. The strengthening of apical and of basal synapses is predicted by local coactivity with nearby synapses and activity coincident with postsynaptic action potentials, respectively. Blocking postsynaptic spiking diminished basal synaptic potentiation without affecting apical plasticity. Thus, individual neurons use multiple activity-dependent plasticity rules in a compartment-specific manner in vivo during learning.

The ability to acquire and adapt behavior through the process of learning is one of the most fundamental functions of the brain. Learning acts to modify neural circuits to reorganize their functional output in a way that leads to behavioral adaptation. Synaptic plasticity is thought to underlie this process by modifying specific synaptic inputs to transform neural activity. Although the molecular and cellular mechanisms underlying the induction and expression of synaptic plasticity have been extensively detailed (*1*–*3*), it remains unclear how specific synapses are selected to undergo different forms of plasticity during learning, often referred to as the credit assignment problem.

Previous in vitro studies have identified numerous potential activity-dependent rules directing synaptic plasticity. The most prevalent of these rules are Hebbian in nature, whereby coincident presynaptic input and postsynaptic spiking drives synapse-specific plasticity (*4*, *5*). However, many different varieties of Hebbian rules, as well as non-Hebbian rules, have been demonstrated (*6*–*9*). Furthermore, many of these rules have been found within the same neural populations, which makes it unclear whether and how neurons may use these different rules in vivo during learning.

Most neurons in the brain have elaborate dendritic arbors that receive most of their excitatory synaptic inputs. These dendrites are not uniform and can be subdivided into compartments with distinct anatomical and biophysical properties (*10*, *11*), which likely influence how different activity patterns engage the biochemical processes underlying synaptic plasticity. Therefore, it is possible that individual neurons use multiple activity-dependent plasticity rules in a compartment-specific manner, which may afford neurons with greater encoding capacity (*12*). Using in vivo two-photon imaging to simultaneously image synaptic activity and neural output, we investigated the plasticity rules of individual synapses along the apical and basal dendrites of layer 2/3 (L2/3) pyramidal neurons in the primary motor cortex (M1) as mice learned a motor task over the course of days.

[1]Department of Neurobiology, University of California San Diego, La Jolla, CA, USA. [2]Center for Neural Circuits and Behavior, University of California San Diego, La Jolla, CA, USA. [3]Department of Neurosciences, University of California San Diego, La Jolla, CA, USA. [4]Halıcıoğlu Data Science Institute, University of California San Diego, La Jolla, CA, USA. [5]Kavli Institute for Brain and Mind, University of California San Diego, La Jolla, CA, USA.
*Corresponding author. Email: wjwright@ucsd.edu (W.J.W.); tkomiyama@ucsd.edu (T.K.)

Compartment-specific functional synaptic organization

To investigate synaptic function and plasticity in vivo during learning, we trained mice in a well-established motor learning task that induces synaptic plasticity in L2/3 neurons of M1 (*13*–*15*). Mice learned to press a lever beyond a set threshold in response to an auditory cue to receive a water reward (Fig. 1, A and B). Over 2 weeks of training, mice displayed an increase in success rate, a decrease in reaction time, and an increase in movement stereotypy within and across sessions (Fig. 1, C to E, and fig. S1) that is indicative of motor learning. This learning is accompanied by the emergence of reproducible spatiotemporal activity in M1 L2/3 excitatory neurons (*13*). To simultaneously monitor the input activity onto individual synapses and neural output in these neurons, we coexpressed the glutamate sensor iGluSnFR3 (*16*) and the red-shifted calcium indicator RCaMP2 (*17*) in a sparse subset of L2/3 pyramidal neurons in M1 and performed longitudinal in vivo two-photon imaging (Fig. 1, A, C, and F). When expressed postsynaptically, iGluSnFR3 reports presynaptic glutamate release received by the postsynaptic dendritic spine and thus serves as a proxy for single-synapse activity. Global dendritic calcium events encompassing the entire dendritic segment within the field of view in apical dendrites largely reflect somatic activity in these neurons (*15*), which contrasts with hippocampal CA1 pyramidal neurons (*18*, *19*). By reanalyzing these previously published data, we confirmed that this is also true for basal dendrites (fig. S2). Therefore, this approach allowed us to reliably monitor the input activity of individual synapses in conjunction with postsynaptic neural output in actively behaving mice (Fig. 1, F and G, and fig. S3, A and B).

We first sought to determine whether synaptic inputs in distinct dendritic compartments display any differences in their functional organization by imaging the distal apical or basal dendrites of L2/3 neurons as mice underwent motor learning (Fig. 1H and fig. S3D). A significantly larger portion of apical spines encoded movement-related information [movement-related spines (MRSs) showing significantly more activity during movements versus non–movement-related spines (nonMRSs); see materials and methods] compared with basal spines (Fig. 1I; fig. S4, A to D; and fig. S5). However, the temporal dynamics of MRSs around movement periods was relatively similar across apical and basal dendrites, with most spines' activity onset preceding movement (Fig. 1, J to L, and fig. S5).

Given that spatiotemporally clustered synaptic activity engages dendritic electroactive processes [e.g., *N*-methyl-D-aspartate (NMDA) spikes] to have a disproportionately strong effect on postsynaptic activity (*20*, *21*), we next examined the degree of functional clustering of synaptic inputs along the apical and basal dendrites. To do so, we measured the coactivity between spines along the same dendrite, which were defined as periods where spines were simultaneously active (fig. S3C and materials and methods). Furthermore, to remove the potential influence of overall activity rates on coactivity measurements, we normalized all coactivity rates by subtracting out the coactivity rate expected by chance (materials and methods). Apical spines displayed significantly greater coactivity rates with other nearby (<20 μm away) spines along the same dendrite compared with basal spines (Fig. 1, M and N, and fig. S5). In addition, a greater fraction of apical spines' total activity was coactive with that of their neighbors, and when coactive, apical spines were coactive with a greater number of other spines (fig. S4, E and F, and fig. S5). When looking separately at MRSs and nonMRSs, we found that the greater local synaptic coactivity observed in apical dendrites was selective for MRSs (Fig. 1O and fig. S5). Notably, these differences between apical and basal dendrites likely did not arise from artifacts owing to differences in imaging depth because spines in both compartments displayed similar densities, sizes, event

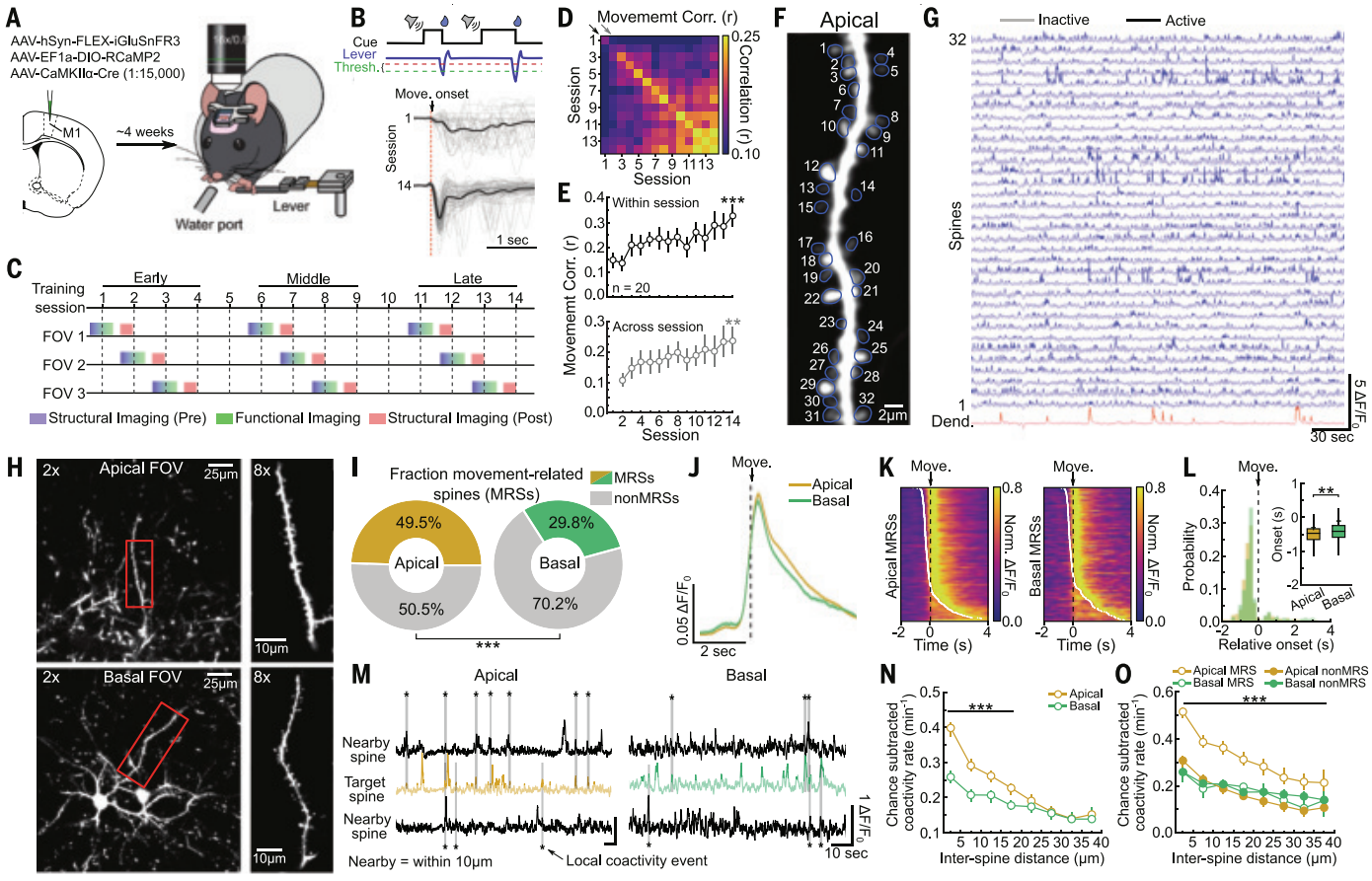

Fig. 1. Compartment-specific functional synaptic organization. (**A**) Schematic of experimental setup. (**B**) (Top) Task structure. (Bottom) Example lever traces from day 1 and day 14 of training. Gray lines show individual trials, and the black line is the mean of all trials. (**C**) Diagram of behavioral and imaging schedule. FOV, field of view. (**D**) Correlation of rewarded movements within and across sessions (n = 20 mice). (**E**) The average movement correlation increases both within (top; Pearson's correlation, $P = 1.5 \times 10^{-4}$) and across (bottom; Pearson's correlation, $P = 4.8 \times 10^{-3}$) training sessions (n = 20 mice). (**F**) Example image of an apical dendrite coexpressing iGluSnFR3 and RCaMP2 with individual spine regions of interest (ROIs) labeled. See fig. S3 for basal dendrite example. (**G**) Example individual spine iGluSnFR3 traces (blue) and dendritic RCaMP2 trace (red) from the dendrite in (F). Active portions of the traces are demarcated in darker colors. $\Delta F/F_0$, change in fluorescence. (**H**) Example images of basal (top) and apical (bottom) FOVs. (**I**) Fraction of MRSs is greater in apical dendrites compared with basal ($P = 9.2 \times 10^{-27}$; Fisher's exact test). (**J**) Averaged activity around movement periods of apical and basal MRSs. (**K**) Trial-averaged activity of individual apical (left) and basal (right) MRSs around movement periods. White dots denote activity onset. (**L**) The activity onset of apical spines occurs earlier preceding movements compared with basal spines (aligned rank transform, $P = 6.64 \times 10^{-4}$). (**M**) Example traces showing local coactivity between spines and their neighbors (<10 μm). Gray bars with asterisks denote coactive periods. (**N**) Apical spines have greater coactivity rates with nearby spines compared with basal spines (aligned rank transform; group main effect, $P = 1.1 \times 10^{-43}$; distance main effect, $P < 1 \times 10^{-308}$, group:distance interaction, $P = 1.7 \times 10^{-23}$; Mann-Whitney U post hoc test, ***$P < 0.001$). (**O**) Apical MRSs have greater coactivity rates with nearby spines compared with all other groups (aligned rank transform; group main effect, $P = 1.2 \times 10^{-70}$; distance main effect, $P < 1 \times 10^{-308}$; group:distance interaction, $P = 1.8 \times 10^{-33}$; Mann-Whitney U post hoc, ***$P < 0.001$, apical MRSs versus all other groups). Sample sizes are as follows: Apical: 1510 total spines, 747 MRSs, 763 nonMRSs, 57 dendrites, and 10 mice. Basal: 1323 total spines, 394 MRSs, 929 nonMRSs, 51 dendrites, and 12 mice. Data from all neurons across all sessions are included. See fig. S5 for separate analysis of movement-related and non–movement-related neurons. Line plots represent medians ± bootstrap 95% confidence intervals (CIs). Box and whisker plots represent medians and interquartile ranges (the plus signs indicate means, and whiskers are 1.5× interquartile ranges). See table S1 for detailed statistics. For this and all figures, P values are as follows: *$P < 0.05$; **$P < 0.01$; ***$P < 0.001$.

amplitudes, and noise levels (fig. S3, E to I). Together, these results suggest that apical synapses in L2/3 pyramidal neurons are organized into task-related functional clusters, whereas this tendency is much weaker for basal synapses.

Apical plasticity is associated with local synaptic coactivity

The functional organization of synapses is likely shaped by plasticity-dependent refinement over time. Therefore, the differences that we have observed in the functional organization of synapses along the apical and basal dendrites suggest that distinct synaptic plasticity rules may operate in these compartments that differentially favor clustered activity. To test this idea, we next investigated the activity-dependent rules that direct synaptic plasticity during learning. We performed structural imaging in two adjacent days before each of the behavioral training sessions and functional imaging during training on the first of the 2 days (Fig. 1C). The goal was to identify functional features on day 1 that predicted structural plasticity identified on day 2. Because the spine area serves as a reliable proxy for postsynaptic strength (*22*–*24*), we longitudinally tracked changes in spine area over adjacent days and identified spines undergoing structural long-term potentiation (sLTP) (>1.5×; materials

and methods) and structural long-term depression (sLTD) (<0.75×; materials and methods) (Fig. 2A). To validate the accuracy of our in vivo spine area measurements, we reanalyzed our previously published data from correlated light and electron microscopy (CLEM) experiments (*14*) and found that our in vivo estimates of spine area strongly correlated with spine volumes measured with electron microscopy (EM) (Fig. 2, B and C).

We first examined the time course of structural plasticity over the course of learning by reanalyzing previously published data that performed structural imaging of spines longitudinally every day in mice trained in the lever-press task and control mice without training (*25*). We found that, in both apical and basal dendrites, the rate of sLTP was higher in training animals compared with no-training animals only during the first few days of training (fig. S6, A and C). Similarly, in our current dataset, sLTP was higher in the early session compared with middle and late sessions (fig. S6, E and G). These results suggest that learning-related sLTP occurs primarily during the early phase of training in our task. Additionally, the fraction of spines undergoing sLTP in the early sessions tended to be greater in neurons that better encoded movements on subsequent days [movement-related neurons (MRNs); fig. S7, A and D], which suggests that sLTP contributes to learning-related changes in the neuronal firing properties. On the basis of these findings, we focused the rest of our investigation on the early stage of training when most learning-related plasticity occurred.

Because we observed more pronounced functional clustering of synapses in apical versus basal dendrites, we hypothesized that local synaptic coactivity may be a driving force for plasticity in apical dendrites. We found that apical spines that exhibited sLTP during the first few days of training displayed greater levels of coactivity with nearby spines in the previous day compared with spines undergoing sLTD or those remaining stable (Fig. 2, D and E). Consistently, the local coactivity rate of spines positively correlated with their subsequent changes in spine area (Fig. 2F). Furthermore, movement-related neurons, which had higher rates of sLTP compared with non–movement-related neurons, had correspondingly higher local coactivity rates (fig. S7C). Notably, we observed that synaptic coactivity rates decreased over the course of training, similar to the decrease of the rate of sLTP (fig. S6, E and I), which further suggests that coactivity promotes sLTP in apical dendrites. If coactivity between nearby synapses promotes sLTP, then we might expect sLTP events to spatially cluster with one another. We therefore measured the distance from each spine to the nearest sLTP event. We found that the distance between sLTP spines was smaller than the distance from other spine types to sLTP (Fig. 2G) while also being smaller than expected by chance (Fig. 2H), indicating spatial clustering of sLTP. By contrast, the distance from spines undergoing sLTD to the nearest sLTP spines was greater than expected by chance, but sLTD spines themselves did not spatially cluster (Fig. 2H and fig. S8, B and C). The elevated levels of local coactivity rates of sLTP spines could arise from sLTP spines specifically having elevated local coactivity rates. Alternatively, sLTP spines could exist in dendritic domains with generally elevated coactivity. To distinguish these possibilities, we compared the local coactivity of spines undergoing different forms of plasticity with that of their stable neighbors (<10 μm; materials and methods and Fig. 2I). Spines undergoing sLTP had greater local coactivity rates compared with their stable neighbors (Fig. 2J), which suggests that local coactivity promotes sLTP in apical dendrites in a spine-specific manner.

In contrast to apical dendrites, we did not find a strong association between synaptic plasticity in basal dendrites and coactivity with nearby spines (Fig. 2K), and the correlation between local coactivity rate and subsequent change in spine area was weak (Fig. 2M). We also did not observe any spatial clustering between any plasticity events (Fig. 2, N and O, and fig. S5, C and D) or any differences in their coactivity relative to that of their stable neighbors (Fig. 2, P and Q). Taken together, these results suggest that local synaptic coactivity promotes learning-related sLTP in apical, but not basal, dendrites.

Somatic activity directs plasticity in basal dendrites

Traditional Hebbian theories of plasticity postulate that the coincidence of action potentials of pre- and postsynaptic neurons promotes the strengthening of the connection between them (*4*, *5*). Therefore, we investigated the influence of the coincidence of synaptic input and somatic activity (referred to here as coincident activity) on plasticity. For both apical and basal dendrites, we observed that coincident activity was most prevalent during the early stage of learning, when most learning-related plasticity occurred (fig. S9). However, in apical dendrites, we found that the rate of synaptic activity coinciding with somatic activity did not correlate with subsequent spine area changes (Fig. 3, A and B), nor did we observe any differences in coincident activity between spines undergoing sLTP and sLTD during the first few days of training (Fig. 3C), which indicates that the rate of coincident activity does not direct learning-related plasticity in apical dendrites. Because spike timing–dependent models emphasize the importance of the relative timing of synaptic to somatic activity in directing plasticity, we next looked for differences in the timing of the onset of synaptic activity relative to somatic activity. However, we were unable to detect any differences in the relative onset timing of synaptic activity in sLTP versus sLTD spines (Fig. 3, D to F), which argues against a spike timing–dependent mechanism. We note, however, that the temporal resolution of our methodology may be insufficient to detect small differences.

In contrast to apical dendrites, we found that the rate of coincident activity in basal dendrites positively correlated with subsequent spine area changes (Fig. 3, G and H). We also observed that basal sLTP spines had elevated coincident activity rates—whereas sLTD spines had lower coincident activity rates—compared with activity in stable spines (Fig. 3I). Similar to apical dendrites, however, we did not observe any differences in the timing of the onset of synaptic activity relative to somatic activity between spines undergoing different forms of plasticity (Fig. 3, J and K). Together, these results suggest that synaptic activity coinciding with somatic output serves to direct learning-related plasticity in basal dendrites, indicative of Hebbian plasticity, whereas this is not the case in apical dendrites.

Blocking somatic activity selectively disrupts basal plasticity

The results above suggest that basal synaptic plasticity depends critically on somatic activity of the postsynaptic neuron, whereas apical plasticity does not. We sought to test this directly by blocking postsynaptic action potentials and examining the effects on synaptic plasticity. We used a soma-targeted variant of the hyperpolarizing potassium channel Kir2.1, which acts to hyperpolarize the neuron and suppresses action potential firing (Fig. 4A and fig. S10A) (*26*). Using calcium imaging, we validated that this construct blocks nearly all somatic calcium activity in a cell-autonomous manner (Fig. 4, A and B, and fig. S10, B and C).

We sparsely coexpressed this construct with iGluSnFR3 in M1 L2/3 neurons to examine its effects on synaptic plasticity in apical and basal dendrites as mice underwent motor learning (fig. S11, A to F). It may be expected that blocking somatic activity would trigger homeostatic synaptic upscaling. However, we observed that spines in both apical and basal dendrites had overall smaller areas (fig. S11, G and I), which argues against homeostatic upscaling and is consistent with previous studies using similar constructs (*27*). Nevertheless, we observed higher event rates as well as higher spine density in basal dendrites (fig. S11, H and J), which suggests some form of homeostatic compensation.

Blocking somatic activity did not change the fraction of spines undergoing sLTP or sLTD in apical dendrites (Fig. 4, C to E). In marked contrast, basal plasticity was strongly affected by blocking somatic activity, such that the fraction of sLTP spines was substantially reduced,

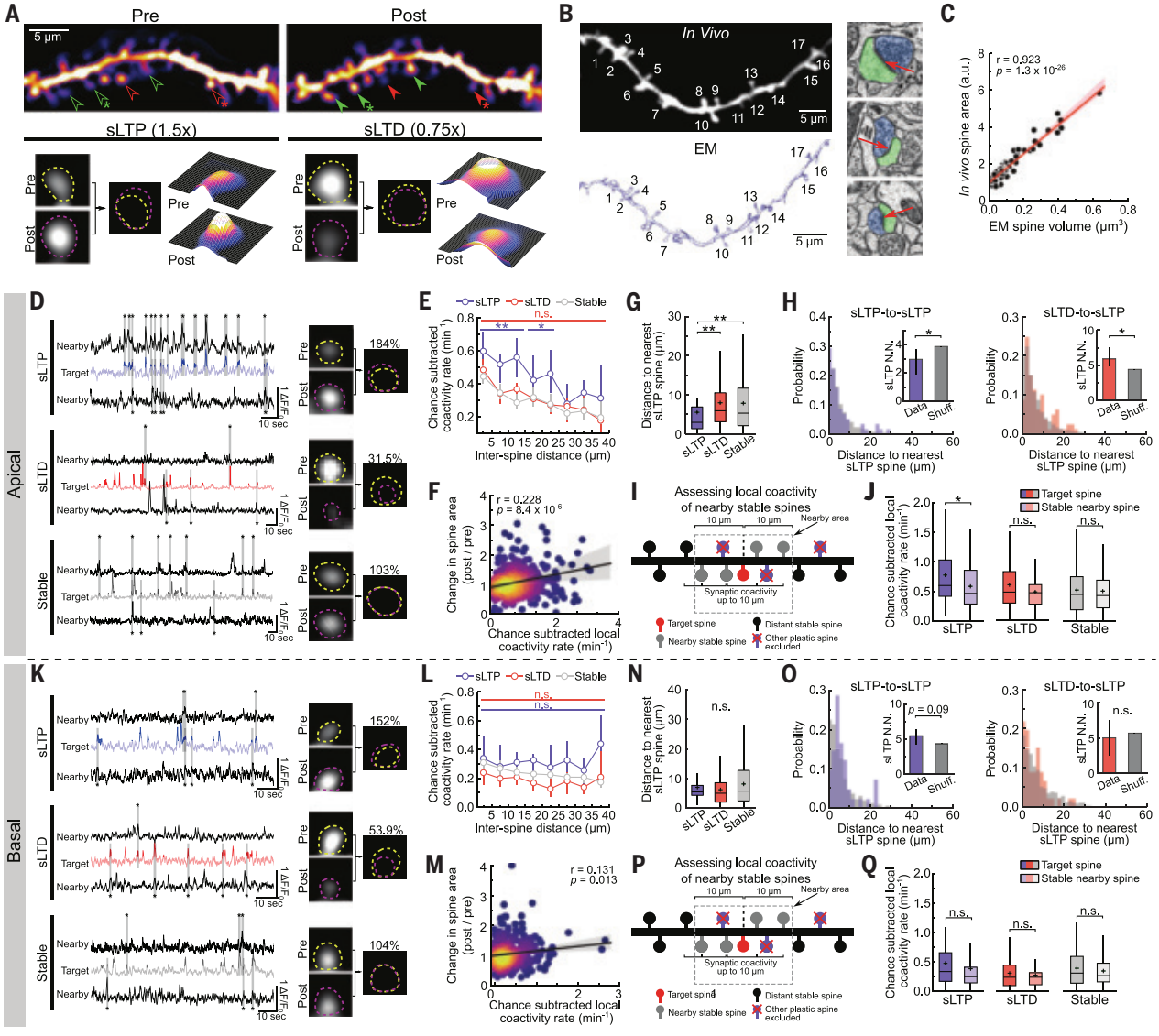

Fig. 2. Apical plasticity is associated with local synaptic coactivity. (**A**) (Top) Example images of the same dendrite across 2 days. Green and red arrows indicate spines undergoing sLTP and sLTD, respectively. (Bottom) Example spines undergoing sLTP (left) and sLTD (right) from the dendrite shown above marked with an asterisk. (**B**) Example dendrite imaged in vivo (top) and its EM reconstruction (bottom). (Right) EM images of individual synapses with the postsynaptic density (PSD) indicated by red arrows. Blue and green shading denote pre- and postsynaptic compartments. Data are from Hedrick *et al*. (*14*). (**C**) Spine areas estimated in vivo correlated with spine volumes measured by EM (Pearson's correlation, $P = 1.3 \times 10^{-26}$). a.u., arbitrary units. (**D**) Example traces showing local coactivity of spines undergoing different forms of plasticity with nearby (<10 µm) spines in apical dendrites. (**E**) Apical spines undergoing sLTP have greater coactivity rates specifically with nearby spines compared with other plasticity groups [aligned rank transform; group main effect, $P = 7.76 \times 10^{-3}$; distance main effect, $P = 3.76 \times 10^{-22}$; group:distance interaction, $P = 1.49 \times 10^{-3}$; Mann-Whitney *U* post hoc test; blue, $^{**}P < 0.01$, $^{*}P < 0.05$, sLTP versus stable; red, n.s. (not significant) $P > 0.05$ LTD versus stable]. (**F**) The local coactivity rate of apical spines correlates with their subsequent spine area change (Pearson's correlation, $P = 8.4 \times 10^{-6}$). (**G**) The nearest distance between apical spines undergoing sLTP is smaller than the distance between sLTP and other plasticity events (aligned rank transform, $P = 0.005$; Mann-Whitney *U* post hoc, $^{**}P < 0.01$). (**H**) The distance between apical sLTP events is closer than expected by chance (left; $P = 0.044$), whereas the distance between sLTD and sLTP events is larger than expected by chance (right; $P = 0.022$). N.N., nearest neighbor. (**I**) Schematic illustrating how the local coactivity of nearby stable spines was assessed. (**J**) The local coactivity of spines undergoing sLTP is greater than their nearby (<10 µm) stable spines (Mann-Whitney *U*; sLTP versus nearby, $P = 0.041$; sLTD versus nearby, $P = 0.218$; stable versus nearby, $P = 0.972$). (**K**) Same as (D), but for basal spines. (**L**) There are no distance-dependent differences in the coactivity rates between spines for different plasticity groups (aligned rank transform; group main effect, $P = 0.133$; distance main effect, $P = 1.67 \times 10^{-15}$; group:distance interaction, $P = 0.072$; Mann-Whitney *U* post hoc; blue, n.s. $P > 0.05$, LTP versus stable; red, n.s. $P > 0.05$, LTD versus stable). (**M**) The local coactivity of basal spines displays a weak but significant correlation with their spine area change (Pearson's correlation, $P = 0.013$). (**N**) No differences in the nearest distance between spines undergoing sLTP and other plasticity events in basal dendrites (aligned rank transform, $P = 0.488$). (**O**) The distance between basal sLTP events trends toward being greater than expected by chance (left; $P = 0.09$), but the distance between sLTD and sLTP events is the same as expected by chance (right; $P = 0.739$). (**P**) Same as (I) but for basal. (**Q**) There is no difference in local coactivity between plastic spines and their neighbors (Mann-Whitney *U*; sLTP versus nearby, $P = 0.211$; sLTD versus nearby, $P = 0.908$; stable versus nearby, $P = 0.448$). Sample sizes are as follows: Apical: 60 sLTP spines, 89 sLTD spines, 226 stable spines, 19 dendrites, and 10 mice. Basal: 45 sLTP spines, 70 sLTD spines, 251 stable spines, 17 dendrites, and 12 mice. Data included come only from early training session. Line and bar plots represent medians ± bootstrap 95% CIs. Box and whisker plots represent medians and interquartile ranges (the plus signs indicate means, and whiskers are 1.5× interquartile ranges). See table S1 for detailed statistics.

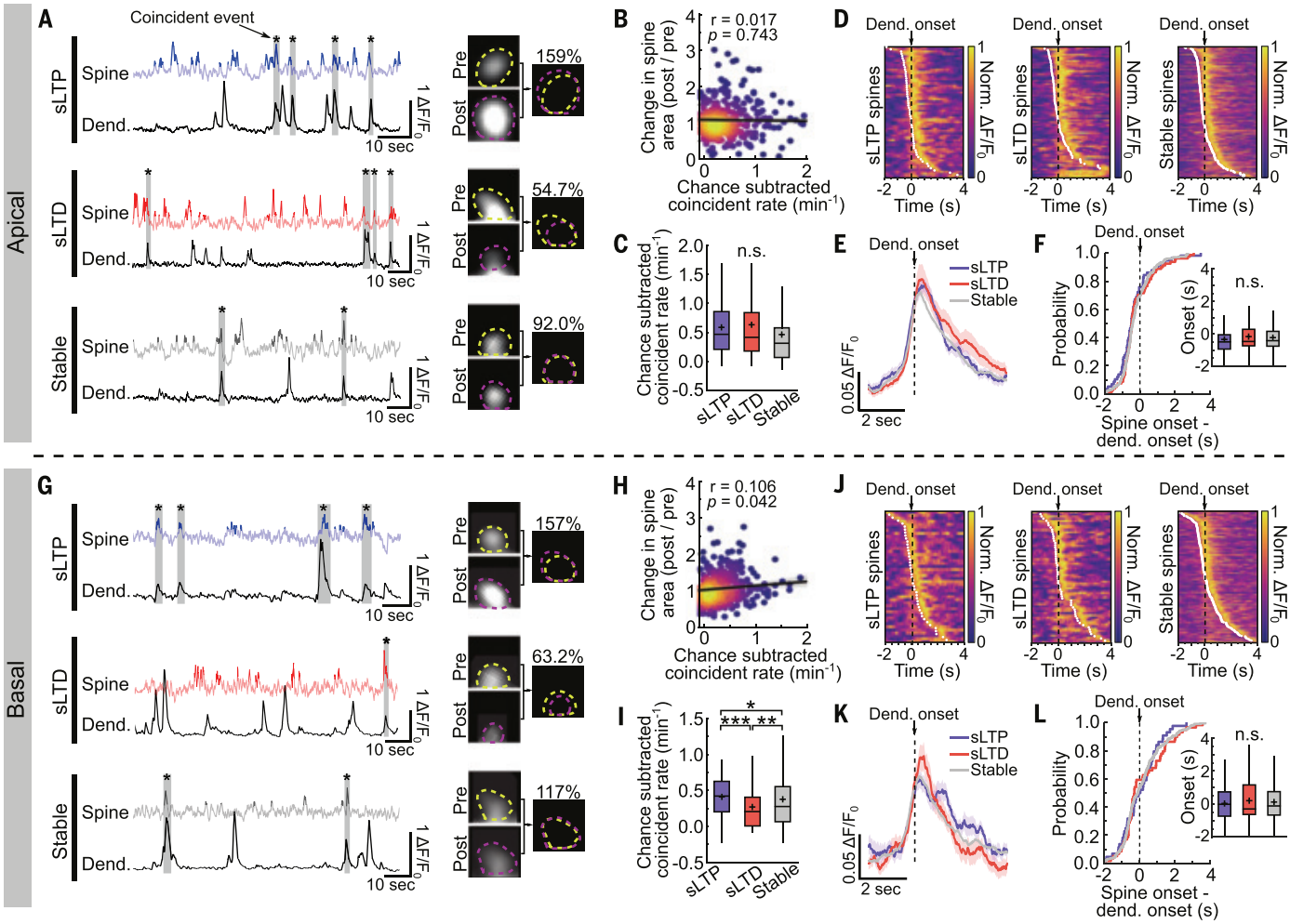

Fig. 3. Somatic activity directs basal plasticity. (**A**) Example traces showing spine activity coinciding with dendritic activity for spines undergoing different forms of plasticity in apical dendrites. Spine-dendrite coincident activity is marked by gray bars with asterisks. (**B**) Coincident activity rate of apical spines does not correlate with their spine area change (Pearson's correlation, P = 0.743). (**C**) There are no differences in the coincident activity rate of apical spines undergoing sLTP, undergoing sLTD, or remaining stable (aligned rank transform, P = 0.10). (**D**) Trial-averaged activity of individual apical spines undergoing sLTP (left), undergoing sLTD (middle), or remaining stable (right) when coactive with their parent dendrite. White dots denote activity onset. (**E**) Averaged spine activity during coincident activity events of apical spines undergoing different forms of plasticity. (**F**) There is no difference in the onset timing of apical spine activity relative to dendritic activity between spines undergoing different forms of plasticity (aligned rank transform, P = 0.507). (**G**) Same as (A) but for basal dendrites. (**H**) Coincident activity rate of basal spines correlates with their spine area change (Pearson's correlation, P = 0.042). (**I**) Basal spines undergoing sLTP have higher coincident activity rates, whereas spines undergoing sLTD have lower coincident activity rates compared with stable spines (aligned rank transform, P = 0.012; Mann-Whitney U post hoc, $^{***}P < 0.001$, $^{**}P < 0.01$, $^{*}P < 0.05$). (**J** and **K**) Same as (D) and (E) but for basal spines. (**L**) There is no difference in the onset timing of basal spine activity relative to dendritic activity between spines undergoing different forms of plasticity (aligned rank transform, P = 0.918). Sample sizes are as follows: Apical: 60 sLTP spines, 89 sLTD spines, 226 stable spines, 19 dendrites, and 10 mice. Basal: 45 sLTP spines, 70 sLTD spines, 251 stable spines, 17 dendrites, and 12 mice. Data included come only from early sessions. Box and whisker plots represent medians and interquartile ranges (plus signs indicate means, and whiskers are 1.5× interquartile ranges). See table S1 for detailed statistics.

accompanied by a twofold increase in sLTD spines (Fig. 4, F to H). This effect was consistent regardless of the distance from the soma (fig. S12). Collectively, these results are consistent with the notion that apical plasticity is primarily regulated by local synaptic coactivity, whereas basal plasticity is critically dependent on somatic activity.

Discussion

We investigated the activity-dependent rules directing the plasticity of individual synapses in vivo during learning. Previous studies that have examined the functional properties of individual synapses undergoing plasticity in vivo have typically used optogenetics to artificially induce plasticity and thus have investigated the properties of predefined plasticity rules (e.g., spike timing–dependent plasticity and behavioral timescale synaptic plasticity) (*28*, *29*). By contrast, by examining the endogenous activity patterns associated with synaptic plasticity, we sought to reveal activity-dependent plasticity rules that are at play during physiological learning. With this approach, we found that individual neurons use different plasticity rules in different dendritic compartments during learning, with plasticity in apical dendrites driven by local synaptic coactivity and plasticity in basal dendrites regulated by neural output.

Our findings are consistent with previous in vitro studies that have suggested that local heterosynaptic mechanisms may preferentially operate in distal dendrites (*7*, *30*–*32*), whereas spike timing–dependent mechanisms dominate

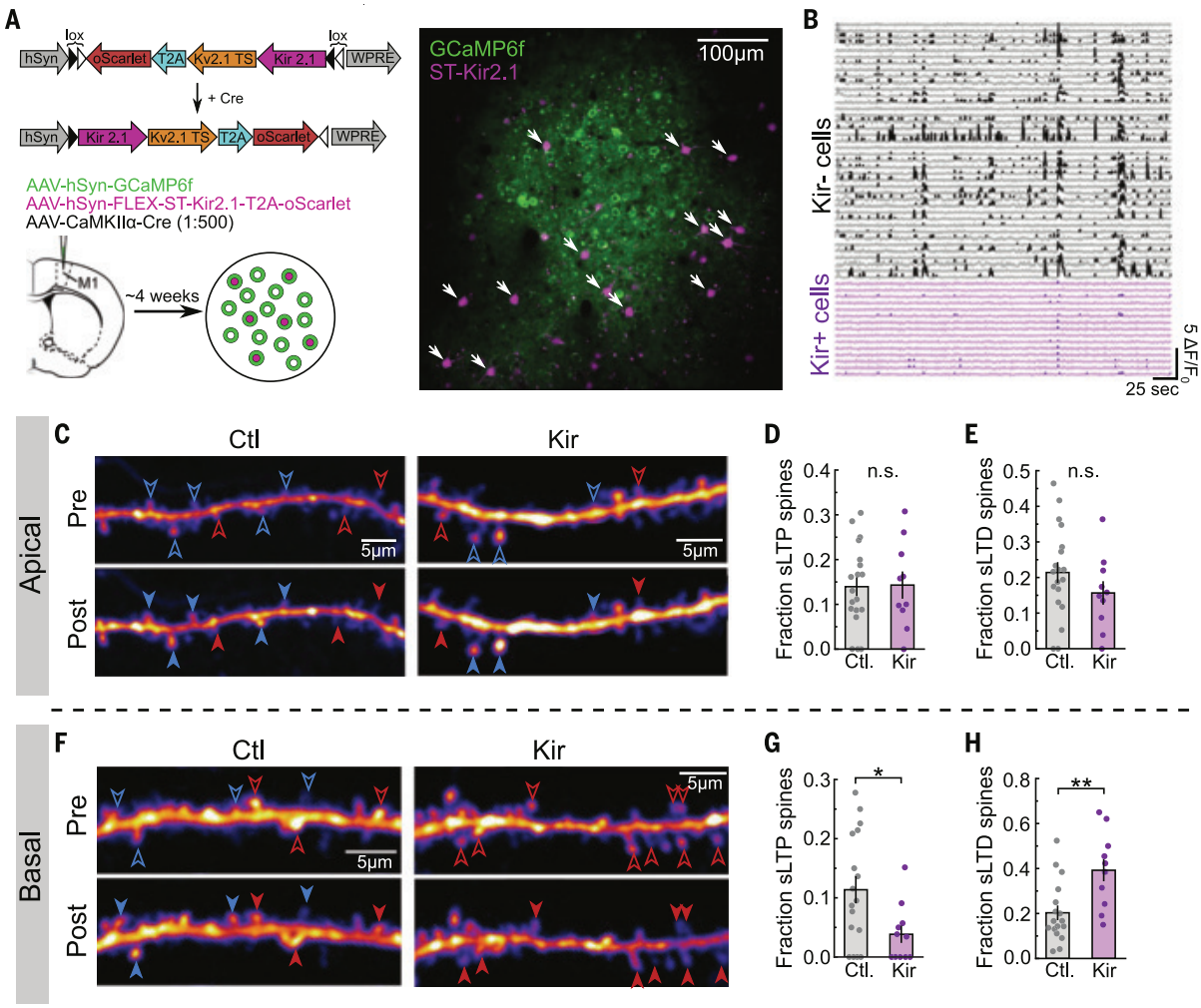

Fig. 4. Blocking somatic activity selectively disrupts basal plasticity. (**A**) (Left) Schematic of the ST-Kir2.1 construct and expression strategy for population imaging. (Right) Example in vivo image of neurons expressing GCaMP6f and ST-Kir2.1. (**B**) Calcium traces of neurons in (A) showing little to no activity in Kir2.1-expressing neurons. (**C**) Example images across 2 days of apical dendrites from control and Kir2.1 mice. Blue and red arrows denote spines undergoing sLTP and sLTD, respectively. (**D** and **E**) There is no difference between control versus Kir2.1 in the fraction of apical spines undergoing sLTP [(D) Mann-Whitney *U*, $P = 0.87$] or sLTD [(E) Mann-Whitney *U*, $P = 0.141$]. (**F**) Same as (C) but for basal dendrites. (**G** and **H**) ST-Kir2.1 expression decreases the fraction of basal spines undergoing sLTP [(H) Mann-Whitney *U*, $P = 0.037$] and increases the fraction of basal spines undergoing sLTD [(I) Mann-Whitney *U*, $P = 0.004$] compared with controls. Sample sizes are as follows: Apical: 19 control dendrites from 10 mice, 10 Kir2.1-expressing dendrites from 7 mice. Basal: 17 control dendrites from 11 mice, 11 Kir2.1-expressing dendrites from 5 mice. Data included come only from early sessions. Bar plots represent means ± SEMs. Box and whisker plots indicate medians and interquartile ranges (plus signs indicate means, and whiskers are 1.5× interquartile ranges). See table S1 for detailed statistics.

in proximal dendrites (*32*–*35*). Furthermore, our results are also consistent with previous in vivo studies linking calcium activity in basal dendrites to changes in neural firing properties, suggestive of Hebbian plasticity (*18*, *36*). These differences in plasticity rules likely arise from the differences in the anatomical and biophysical properties of these dendritic compartments. For example, distal dendrites have greater electrical impedance that enhances local depolarization and calcium influx from synaptic inputs (*37*, *38*). This may allow local synaptic coactivity to more strongly depolarize the dendrite and trigger localized (<20 μm) calcium release from intracellular stores to induce plasticity in apical but not basal dendrites (*19*, *39*). By contrast, back-propagating action potentials decay along the length of the dendrite (*40*–*42*) (fig. S3J) and thus may be less effective in regulating plasticity at distal dendritic locations. Therefore, the different learning rules that we observe in these different synaptic populations may simply be a result of their distance from the soma. However, additional differences between dendritic compartments exist, such as synaptic receptor composition and other subcellular properties (*43*–*45*), that may also influence how different activity patterns regulate plasticity. Future studies will be needed to define the mechanisms that govern the compartment-specific utilization of these plasticity rules in vivo.

Although we demonstrated different plasticity rules in apical and basal dendrites, these are likely not the only rules at play in these compartments. For instance, inhibitory and neuromodulatory signaling modulate the induction and expression of synaptic plasticity (*25*, *36*, *46*–*48*) and therefore likely work together with the activity-dependent rules that we report in this work to regulate plasticity during learning. Our observation that learning-related plasticity occurs preferentially during the early phases of learning may be a result of elevated cholinergic signaling and disinhibition

that also occur at this time acting to open a plasticity window (*49*). This also raises the possibility that under different behavioral contexts that engage other signaling pathways, such as stress, the manner through which these activity-dependent rules operate in different dendritic compartments may change.

The utilization of distinct activity-dependent rules likely reflects the computational functions that different dendritic compartments have evolved to perform. In apical dendrites, we found that locally coactive synapses strengthen. This aligns with previous studies that have demonstrated the roles of local synaptic coactivity in regulating synapse formation and elimination during development and adulthood (*14*, *15*, *50*, *51*), and together, these observations suggest a shared function of different forms of synaptic plasticity in apical dendrites to promote the formation of functional clusters. As a result, apical dendrites may act to bind different inputs into functional clusters to nonlinearly integrate diverse streams of information through the engagement of dendritic nonlinearities. We found strong functional clustering in apical dendrites (Fig. 1, N and O). Meanwhile, the Hebbian mechanisms prevalent in basal dendrites may serve to tie neurons encoding similar information together into functional ensembles and contribute to reliable pattern completion. By detailing how individual neurons use different activity-dependent synaptic plasticity rules in vivo, our work provides insights into how learning acts to shape the functional properties of neural circuits to modify behavior.

REFERENCES AND NOTES

1. R. L. Huganir, R. A. Nicoll, *Neuron* **80**, 704–717 (2013).
2. R. C. Malenka, M. F. Bear, *Neuron* **44**, 5–21 (2004).
3. J. Nishiyama, R. Yasuda, *Neuron* **87**, 63–75 (2015).
4. Y. Dan, M. M. Poo, *Neuron* **44**, 23–30 (2004).
5. N. Caporale, Y. Dan, *Annu. Rev. Neurosci.* **31**, 25–46 (2008).
6. K. P. Lamsa, J. H. Heeroma, P. Somogyi, D. A. Rusakov, D. M. Kullmann, *Science* **315**, 1262–1266 (2007).
7. J. P. Weber *et al*., *Nat. Commun.* **7**, 11380 (2016).
8. K. C. Bittner, A. D. Milstein, C. Grienberger, S. Romani, J. C. Magee, *Science* **357**, 1033–1036 (2017).
9. C. D. Harvey, K. Svoboda, *Nature* **450**, 1195–1200 (2007).
10. M. Häusser, N. Spruston, G. J. Stuart, *Science* **290**, 739–744 (2000).
11. N. Spruston, *Nat. Rev. Neurosci.* **9**, 206–221 (2008).
12. J. Bono, C. Clopath, *Nat. Commun.* **8**, 706 (2017).
13. A. J. Peters, S. X. Chen, T. Komiyama, *Nature* **510**, 263–267 (2014).
14. N. G. Hedrick *et al*., *Nat. Neurosci.* **25**, 726–737 (2022).
15. N. G. Hedrick, W. J. Wright, T. Komiyama, *Sci. Adv.* **10**, eadk0540 (2024).
16. A. Aggarwal *et al*., *Nat. Methods* **20**, 925–934 (2023).
17. M. Inoue *et al*., *Nat. Methods* **12**, 64–70 (2015).
18. M. E. J. Sheffield, D. A. Dombeck, *Nature* **517**, 200–204 (2015).
19. J. K. O'Hare *et al*., *Science* **375**, eabm1670 (2022).
20. G. J. Stuart, N. Spruston, *Nat. Neurosci.* **18**, 1713–1721 (2015).
21. G. Major, M. E. Larkum, J. Schiller, *Annu. Rev. Neurosci.* **36**, 1–24 (2013).
22. M. Matsuzaki *et al*., *Nat. Neurosci.* **4**, 1086–1092 (2001).
23. M. Matsuzaki, N. Honkura, G. C. R. Ellis-Davies, H. Kasai, *Nature* **429**, 761–766 (2004).
24. U. V. Nägerl, N. Eberhorn, S. B. Cambridge, T. Bonhoeffer, *Neuron* **44**, 759–767 (2004).
25. S. X. Chen, A. N. Kim, A. J. Peters, T. Komiyama, *Nat. Neurosci.* **18**, 1109–1115 (2015).
26. C. González *et al*., in *Comprehensive Physiology*, Y. S. Prakash, Ed. (Wiley, ed. 1, 2012), pp. 2087–2149.
27. M. Xue, B. V. Atallah, M. Scanziani, *Nature* **511**, 596–600 (2014).
28. S. El-Boustani *et al*., *Science* **360**, 1349–1354 (2018).
29. K. C. Gonzalez *et al*., *Nature* **637**, 1152–1160 (2025).
30. Á. Magó, J. P. Weber, B. B. Ujfalussy, J. K. Makara, *J. Neurosci.* **40**, 2593–2605 (2020).
31. M. Sandler, Y. Shulman, J. Schiller, *Neuron* **90**, 1028–1042 (2016).
32. P. J. Sjöström, M. Häusser, *Neuron* **51**, 227–238 (2006).
33. U. Gordon, A. Polsky, J. Schiller, *J. Neurosci.* **26**, 12717–12726 (2006).
34. J. J. Letzkus, B. M. Kampa, G. J. Stuart, *J. Neurosci.* **26**, 10420–10429 (2006).
35. R. C. Froemke, M. M. Poo, Y. Dan, *Nature* **434**, 221–225 (2005).
36. M. E. J. Sheffield, M. D. Adoff, D. A. Dombeck, *Neuron* **96**, 490–504.e5 (2017).
37. M. T. Harnett, J. K. Makara, N. Spruston, W. L. Kath, J. C. Magee, *Nature* **491**, 599–602 (2012).
38. K. Holthoff, D. Tsay, R. Yuste, *Neuron* **33**, 425–437 (2002).
39. P. J. Dittmer, M. L. Dell'Acqua, W. A. Sather, *Proc. Natl. Acad. Sci. U.S.A.* **116**, 13611–13620 (2019).
40. K. Svoboda, W. Denk, D. Kleinfeld, D. W. Tank, *Nature* **385**, 161–165 (1997).
41. K. Svoboda, F. Helmchen, W. Denk, D. W. Tank, *Nat. Neurosci.* **2**, 65–73 (1999).
42. A. T. Landau *et al*., *eLife* **11**, e76993 (2022).
43. M. Lafourcade *et al*., *Neuron* **110**, 1532–1546.e4 (2022).
44. C. E. Yaeger *et al*., *Cell Rep.* **43**, 114638 (2024).
45. D. M. Virga *et al*., *Nat. Commun.* **15**, 2142 (2024).
46. T. Hayama *et al*., *Nat. Neurosci.* **16**, 1409–1416 (2013).
47. S. Yagishita *et al*., *Science* **345**, 1616–1620 (2014).
48. S. Z. Hong *et al*., *Nat. Commun.* **13**, 3202 (2022).
49. C. Ren *et al*., *Neuron* **110**, 2334–2350.e8 (2022).
50. J. Winnubst, J. E. Cheyne, D. Niculescu, C. Lohmann, *Neuron* **87**, 399–410 (2015).
51. D. Niculescu *et al*., *Cell Rep.* **24**, 2063–2074 (2018).
52. W. Wright, Wright et al., 2025, version 1, data set, Zenodo (2024). doi:10.5281/zenodo.15047046.

ACKNOWLEDGMENTS

We thank B. Morales, D. Arakelyan, A. Medina, and E. Hall for technical assistance and the rest of the members of the Komiyama laboratory, especially J. Li, for discussions on the project and manuscript. **Funding:** This work was supported by the following funding sources: National Institutes of Health (grants R01 MH128746, R01 DC018545, R01 NS125298, and R01 NS091010 to T.K.; grant T32 NS007220 to W.J.W.), the National Science Foundation (grant 2024776 to T.K.), the Simons Collaboration on the Global Brain Pilot Award (T.K.), and the Eric and Wendy Schmidt AI in Science Fellowship (W.J.W.). **Author contributions:** Conceptualization: W.J.W., T.K.; Data curation: W.J.W.; Formal analysis: W.J.W.; Funding acquisition: W.J.W., T.K.; Investigation: W.J.W.; Methodology: W.J.W., T.K.; Project administration: T.K.; Resources: N.G.H.; Software: W.J.W.; Supervision: T.K.; Validation: W.J.W.; Visualization: W.J.W.; Writing – original draft: W.J.W., T.K.; Writing – review & editing: W.J.W., N.G.H., T.K. **Competing interests:** The authors declare that they have no competing interests. **Data and materials availability:** All data needed to evaluate the conclusions in the paper are present in the paper and/or the supplementary materials. Data and code to reproduce the findings in this paper have been uploaded to Zenodo (*52*).

SUPPLEMENTARY MATERIALS

science.org/doi/10.1126/science.ads4706
Materials and Methods
Figs. S1 to S12
Table S1
References (*53*–*58*)
MDAR Reproducibility Checklist
Movies S1 and S2

Submitted 14 August 2024; accepted 18 February 2025
10.1126/science.ads4706

By **Troy Christopher Dildine**

Not a 'DEI hire'

"Dad, here's your Bible. Do you think I can take 30 minutes to go to the gym? Here's the phone in case you need me." I was visiting my childhood home, working remotely on my postdoctoral research while I helped care for my father, who has several physical disabilities—a periodic routine to provide my mother some relief. I began to run on the treadmill, stride after mindless stride, when Fox News on the gym TV brought me back to the present. "We have 1 hour and 7 minutes left in our countdown before all agencies need to terminate all diversity-related positions!" I stopped the treadmill and saw an email from my supervisor at the National Institutes of Health (NIH) saying we needed to talk. My phone buzzed. "I'm sure you know what this call is about."

That was it. It was only Day 2 of President Donald Trump's new administration and I was terminated from my part-time role as a scientific diversity adviser at NIH, amid the narrative that those of us working on diversity, equity, and inclusion (DEI) were hired without merit.

It's a mindset I've encountered throughout my training. Growing up in an underresourced rural community, of mixed racial background, I did well in school and wanted to pursue higher education—though I had few examples to follow. I made it to a top university but faced and witnessed persistent dispiriting comments. "You're only here because of affirmative action," one fellow student said to me. I overhead a professor say to a Haitian refugee, "This is a tough class; you should consider taking something easier. Do you need me to speak Creole?" Even when such comments were not directed at me, I heard the message: People like us didn't deserve to be there.

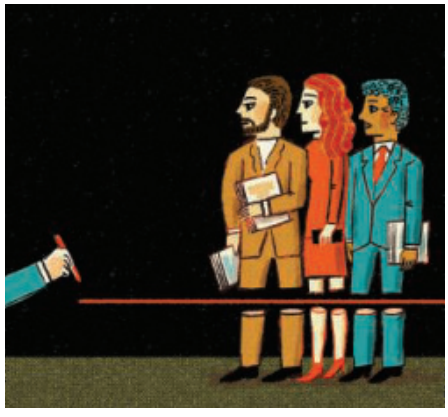

"Perseverance can only take me so far."

But amid the dejection, I also found determination. I believed I could work harder than my peers and achieve my goal: becoming a professor, studying equity, and advocating for vulnerable student populations. I also found fulfillment as a volunteer, participating in outreach and DEI-related activities, including mentoring underresourced high school students interested in the sciences and pushing for efforts to diversify faculty.

I went on to a Ph.D. studying disparities in how people feel pain and how providers assess it. Even as my research progressed successfully, I met doubters. But my hard-fought self-confidence and a carefully cultivated network of mentors helped me push toward my goal. I also created a diversity group at the NIH institute where I was doing my Ph.D., running weekly meetings and regular events to discuss DEI-related issues in medicine and support researchers from historically underrepresented groups. When I completed my Ph.D. and moved on to a postdoc, I continued my diversity work at NIH, with the blessing of my new university and NIH administrators. It felt like all the pieces were coming together—until it all began to fall apart about 2 years later, in the first week of the new administration.

First came the loss of my job as a diversity adviser. Days later came more bad news. I had spent months preparing an NIH grant proposal. But when I called the program officers, they advised me to pivot away from the health equity research I was proposing, which focused on how discrimination and stigma affect chronic pain. Such research might be less likely to be funded under the new administration, they said. I spent the 2 weeks prior to the deadline, including three sleepless nights, reworking my application to look at social isolation, stress, and psychophysiological responses as they relate to pain. I'm still holding out hope it might get funded. But I can't ignore the fact that my updated proposal no longer speaks directly to the passions that originally spurred me to pursue a Ph.D.

Despite the narratives currently rampaging in the United States that people of color are "DEI hires" lacking merit, I am finally confident in my abilities as a scientist. However, perseverance can only take me so far. I feel fortunate to have the relative privileges I do, but I feel my chances of becoming an academic scientist are dwindling. In this transitional stage of my career, I don't have 4 years to hunker down and wait it out. ■

Troy Christopher Dildine is a postdoc at Stanford University.

ILLUSTRATION: ROBERT NEUBECKER

QUALITY CONTENT FOR THE GLOBAL SCIENTIFIC COMMUNITY

Multiple ways to stay informed on issues related to your research

Posters

Podcasts

Sponsored Collection Booklets

Sponsored Feature

Webinars

Science AAAS

Brought to you by the *Science*/AAAS Custom Publishing Office.

Scan the code and start exploring the latest advances in science and technology innovation!

Science.org/custom-publishing

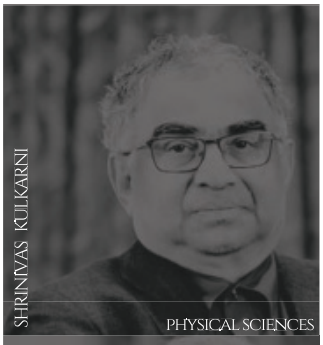

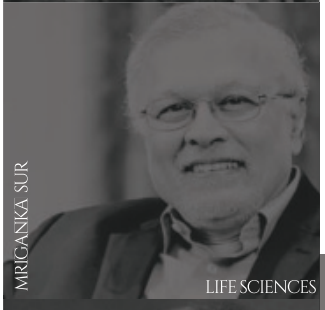

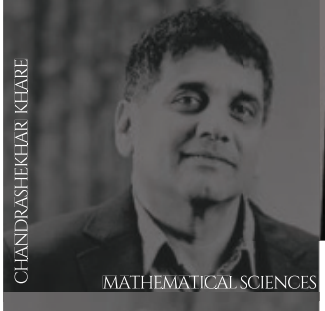

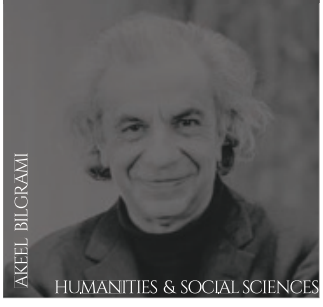

JURY CHAIRS 2025

Infosys Prize

Inspire Progress

NOMINATE NOW

Have a candidate in mind? Please write to us at **ISF@infosys.com**

The Infosys Science Foundation calls for nominations for the Infosys Prize 2025. The Infosys Prize is given for an invention, innovation or distinct achievement.

Nominees must be of Indian origin working anywhere in the world or anyone whose work impacts India and must be 40 years or younger as of November 1, 2025 to be eligible. The nominators will be invited to the nomination council. Self nominations will not be accepted.

You can find the statutes and other criteria for the prize on **www.infosysprize.org**.